Magma differentiation processes and volatile contents beneath the Shatsky Rise oceanic plateau: constraints from mineral, glass and melt inclusion compositions combined with thermodynamic and experimental modeling

Von der Naturwissenschaftlichen Fakultät

der Gottfried Wilhelm Leibniz Universität Hannover

zur Erlangung des Grades

Doktorin der Naturwissenschaften

Dr. rer. nat.

genehmigte Dissertation

von

Dipl.-Geow. Anika Husen

geboren am 27.02.1986, in Reinbek

2014

Referent: Prof. Dr. François Holtz

Korreferent: Prof. Dr. Karsten Haase

Tag der Promotion: 09.10.2014

Acknowledgements

<u>Abstract</u>

During Expedition 324, the Integrated Ocean Drilling Program recovered tholeiitic basalts at the Shatsky Rise oceanic plateau. The collected natural glasses contain 5 to 8.7 wt% MgO. Compared to mid-ocean ridge basalts (MORB), they are high in FeO (Fe_8: 10.3) and low in SiO_2 and Na_2O (Na_8: 1.9) contents, indicating melt generation at high amounts of partial melting and in great depth. Furthermore, the CaO/Al_2O_3 ratios in the evolved glasses from Shatsky Rise are higher respectively to MORB implying low pressure cotectic fractionation. However, the basaltic glasses from Shatsky Rise show differentiation trends similar to those of other oceanic plateaus, as e.g. Ontong Java and Kerguelen.

Pressures and temperatures of magma storage were estimated for 40 naturally quenched glasses (5-6.5 wt% MgO) from a profile of 150 m length drilled at the Tamu Massif, one of three massifs of the Shatsky Rise. Based on the glass major element compositions (electron microprobe) and glass H_2O contents (infrared spectroscopy), conditions of multiple saturation (liquid+olivine+plagioclase+clinopyroxene) were simulated using the COMAGMAT program. The calculated pressures and temperatures range from 240 MPa to 1 atm and from 1150 to 1100°C, and indicate polybaric crystallization in a shallow magma reservoir (<6 km). Along the drilled profile, we identified two complete cycles of magma injection in the reservoir with subsequent fractionation and eruption followed by a time of magmatic inactivity. The most MgO-rich samples of the Shatsky Rise were recovered at Ori Massif. In contrast to the evolved Tamu Massif glasses, they demonstrate fractionation at deeper levels because the simulated pressures of multiple saturation are ~650 MPa. This indicates that the magmas beneath Shatsky Rise evolved in a multilevel magma plumbing system.

Three synthetic compositions, representing different stages of the magma differentiation beneath the Shatsky Rise (8.6 wt% MgO, 8.0 wt% MgO, 6.4 wt% MgO), were used to conduct a complementary experimental study. The results were in agreement with the calculated magma storage conditions and showed that low pressures led to the high CaO/Al_2O_3 ratios in the Tamu Massif basalts. The natural differentiation trend is best reproduced by experiments at ~100 MPa considering the range of H_2O contents which was observed in the natural basaltic glasses (0.2-0.6 wt% H_2O). In addition, the experimental results also support the assumption that magma storage and fractionation occurred in different levels in the crust, because the natural liquid lines of descent cannot be reproduced via isobaric crystallization.

The systematic study of the influence of pressure and H_2O on basaltic phase relations demonstrated the significance of small amounts of H_2O during basaltic differentiation. The evaluation of recent geothermobarometers and thermodynamic models showed that magmatic temperatures and pressures are systematically overestimated due to negligence of the melt H_2O contents.

Keywords: COMAGMAT, IODP Expedition 324, magma differentiation, MORB, phase equilibria, Shatsky Rise, thermobarometry

Zusammenfassung

Die tholeiitischen Basalte des ozeanischen Plateaus Shatsky Rise wurden während der Expedition 324 des Integrated Ocean Drilling Programs erbohrt. Die natürlichen Gläser enthalten 5 bis 8.7 wt% MgO. Sie sind im Vergleich zu Mittelozeanischen Rücken Basalten (MORB) erhöht im Gehalt von FeO (Fe$_8$: 10.3) und niedriger im SiO$_2$- und Na$_2$O-Gehalt (Na$_8$: 1.9), was darauf schließen lässt, dass die Schmelzen bei höherem Aufschmelzgrad und in größerer Tiefe entstanden sind. Desweiteren sind die CaO/Al$_2$O$_3$ Verhältnisse in den entwickelten Gläsern des Shatsky Rise vergleichsweise hoch im Bezug auf MORBs, was wiederum ein Indiz für Fraktionierung bei kotektischen Bedingungen niedrigen Drucks ist. Generell zeigen die basaltischen Gläser des Shatsky Rise ähnliche Differenzierungstrends wie andere ozeanische Plateaus, z.B. Ontong Java und Kerguelen.

Für 40 natürliche Gläser (5-6.5 wt% MgO) wurden Druck- und Temperaturbedingungen für ein potentielles Magmareservoir berechnet. Die Proben stammen aus einem 150 m langen Profil, das am Tamu Massif, einem von drei Massiven des Shatsky Rise, erbohrt wurde. Mit Hilfe des COMAGMAT Modells, wurden für die gemessenen Zusammensetzungen der Gläser (Elektronenstrahl Mikrosonde) und deren H$_2$O-Gehalte (Infrarot Spektroskopie) Bedingungen simuliert, bei denen die Schmelzen im Gleichgewicht mit Olivin, Plagioklas und Klinopyroxen wären. Die daraus berechneten Druck- und Temperaturbedingungen von 240 MPa bis 1 atm und 1150-1100°C weisen auf polybare Kristallisation in einem flachen (<6 km) Magmareservoir hin. Die Proben mit dem höchsten MgO-Gehalt stammen vom Ori Massif, sie sprechen im Gegensatz zu den entwickelten Basalten des Tamu Massif für Fraktionierung bei ~650 MPa. Dies lässt auf ein System aus mehreren Magmakammern in unterschiedlicher Tiefe schließen.

Eine komplementäre experimentelle Studie dreier synthetischer Basalte, die unterschiedlich stark differenzierte Magmen des Shatsky Rise repräsentieren (8.6 wt% MgO, 8.0 wt% MgO, 6.4 wt% MgO), ist in guter Übereinstimmung mit der Simulation. Unter Einbeziehung der H$_2$O-Gehalte der natürlichen Gläser, zeigen die Ergebnisse, dass die hohen CaO/Al$_2$O$_3$ Verhältnisse in den Tamu Massif Basalten durch Differenzierung bei niedrigem Druck (<100 MPa) entstanden sein können. Desweiteren unterstützen die experimentellen Ergebnisse die Annahme, dass die Magmen des Shatsky Rise in unterschiedlichen Tiefen fraktioniert sind, weil nicht alle natürlichen Glaszusammensetzungen bei gleichem Druck reproduziert werden konnten.

Diese systematische Studie über den Einfluss von Druck und H$_2$O auf die Phasenbeziehungen in basaltischen Systemen hat die Bedeutung von niedrigen H$_2$O-Gehalten während der basaltischen Differentiation aufgezeigt. Die Vernachlässigung des Einflusses von H$_2$O bei den meisten Geothermobarometern führt zur systematischen Überschätzung der magmatischen Druck- und Temperaturbedingungen.

Schlagwörter: COMAGMAT, IODP Expedition 324, Magma Differenzierung, MORB, Phasengleichgewichte, Shatsky Rise, Thermobarometrie

Table of contents

Table of contents

Table of contents

Table of contents

Table of contents

<u>Objectives and Background</u>

This dissertation investigates the basaltic magma evolution by magma differentiation within the oceanic crust with special focus on basalts from the Shatsky Rise oceanic plateau. Although this plateau formed at a mid-ocean ridge (MOR) (Nakanishi et al., 1999), it has an expected crustal thickness of 30 km (Korenaga and Sager, 2012), which is four times the usual thickness of typical oceanic crust. This requires large volumes of basaltic magmas, which differentiate during their ascent through the crust. The presented data help to characterize the magma evolution beneath Shatsky Rise and contribute to the general understanding of the influence of pressure and the presence of small amounts of water on basaltic systems.

Basalts belong to the most abundant rocks on earth and build up the upper part of the oceanic crust. They are generated at different settings within the oceans or (less abundant) on the continents. The main basalt forming process occurs at MORs, where newly formed magmatic material is subsequently accreted to the older spreading lithosphere. Also, basalts appear in large igneous provinces (LIPs), which are enormous products of intraplate volcanism on continental or oceanic crust. Ocean islands and oceanic plateaus, like Shatsky Rise, belong to these LIPs and provide high volumes of basaltic rocks. Basalt formation is also known for settings of subduction zones, where the melts are generated by hydrous partial melting of upper mantle material. Basalts provide a link to mantle processes because their parental magmas originate in the mantle. Therefore, it is necessary to understand how the ascending melts are modified on their way to the surface.

1.   THE OCEANIC CRUST VOLCANISM

Oceanic crust is generated at MORs, where the lithosphere spreads apart (Hess, 1962). At the ridge axis, new crust is produced while fresh basaltic magmas erupt. The magma is originated in the asthenosphere, where it is formed by partial melting of the mantle material (1.5-2 GPa, <60 km; Bottinga et al., 1978; Bowen, 1956; Green & Ringwood, 1967; Kushiro et al., 1972; Presnall et al., 1979; Ringwood, 1975; Takahashi & Kushiro, 1983). The melting is initiated by upwelling of the mantle in the course of large scale mantle convection, which causes decompression melting. The generated melts ascend adiabatically and segregate from the host rock until they reach the oceanic crust. Here the melts accumulate in magma chambers (Fig. 0.1), where they partially crystallize and differentiate.

The thickness of the oceanic crust increases with distance to the spreading center, up to a typical thickness of 8-10 km. The model of a layered oceanic crust is based on the investigation of ophiolites, which are oceanic rocks being exposed on the continents driven by tectonic processes (Coleman, 1977). It is applicable for most fast spreading ridges, e.g. the East Pacific Rise (EPR). The observations in ophiolites in combination with seismic studies of recent MORs led to the model of the oceanic crust (Clague & Straley, 1977) shown in Fig. 0.1.

A sedimentary cover (Layer 1) overlies the uppermost igneous Layer 2, which consists of so called pillow lavas and sheeted dykes. The pyroclastic basaltic pillow lavas (Layer 2a) are erupted lava flows quenched by the sea water. The sheeted dykes are more slowly cooled diorites or microgabbros being chemically similar to basalts, but fine grained equigranular to aphanitic in texture. The Layer 3 is composed of gabbroic rocks. These are mostly coarse grained, equigranular and contain clinopyroxene (*Cpx*),

plagioclase (*Plag*), and olivine (*Ol*). They are assumed to be fractionated cumulates collected at the bottom of the magma chamber. By spreading of the lithosphere, these gabbros are transported away from the ridge axis. Below the gabbros, the Moho separates the oceanic crust from the upper mantle.
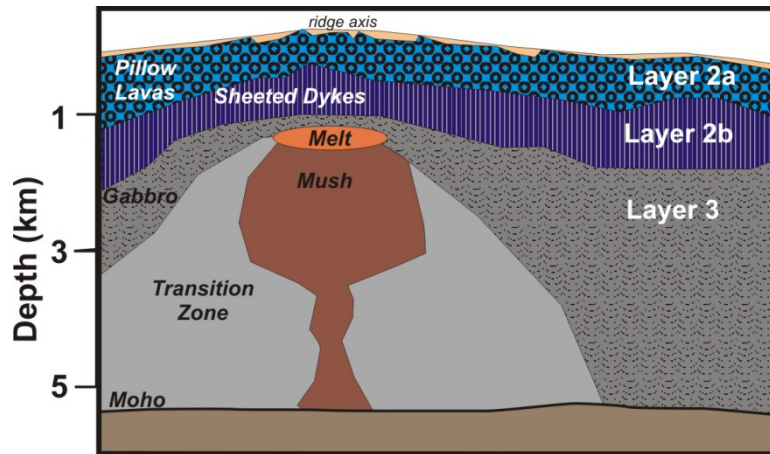
Figure 0.1: Schematic image of the layered model of the oceanic crust at a fast spreading MOR like East Pacific Rise (modified after Sinton & Detrick, 1992). The Layers 2 and 3 are indicated. Beneath the ridge axis, the continuous layering is interrupted: The melt lens is located in 1-2 km depth with a gradual transition to the underlying crystal mush zone (Sinton & Detrick, 1992). The degree of solidification increases with distance from the melt lens through the transition zone to the gabbroic rocks of Layer 3.

Besides at MORs, intraplate volcanism is also known for oceanic crust, where it forms ocean islands (e.g. like Hawaii, Marquesas Islands) and oceanic plateaus (e.g. Ontong Java, Kerguelen, Broken Ridge). The volcanic rocks forming these edifices are basaltic and similar to MORBs in their petrography, but they are chemically different. They originate in a (chemically) different and deeper hosted mantle source. As widely discussed in literature (e.g. Morgan, 1972; Wilson, 1963), ocean islands are associated with mantle plumes, where mantle material wells up accompanied by decompression partial melting (Coffin & Eldholm, 1994). The mantle plumes are expected to be static in their position, whereas the oceanic crust continuously moves driven by the spreading at MORs. When oceanic crust is progressively running over such a mantle plume, ocean island chains can be produced (e.g. Hawaii and Emperor, or Louisville seamount chain).

The interaction of these mantle plumes with active spreading centers is expected to result in topographic highs, e.g. Azores, Galapagos. These are morphologically different to MORs and the chemistry of the basalts formed at these topographic highs shows certain differences compared to normal MORBs.

2. MAGMA CHAMBERS - DIFFERENTIATION

Sinton & Detrick, 1992 used geophysical and petrographic data to characterize the model of the magma chambers beneath the EPR. They described magma chambers as large continuous mainly molten bodies. These are relatively narrow (<3 km) and thin (100 m-1 km) and overly a crystal mush zone (Fig. 0.1). During cooling of the magma, crystal fractionation causes a progressive change in melt composition. Thus, the basaltic rocks exposed on the ocean floor and in ophiolite complexes, show a wide compositional variability, although they follow clearly the main trend of tholeiitic differentiation. The melt composition variability of MORBs is explained by fractionation and subsequent replenishment within the magma chambers.

Based on geophysical observations, the position of the sub axial magma chamber is expected to be in shallow depth and located at the transition zone between the sheeted dykes and gabbros, which is consistent with the global low pressure fractionation trend displayed by MORB compositions. However, recent studies of crystallization conditions of MORBs showed that fractional crystallization occurs in various depth beneath MORs (Michael & Cornell, 1998; Herzberg, 2004; Villiger et al., 2007; Natland & Dick, 2009). According to Villiger et al. (2007) fractionation occurs immediately after the segregation from the partially molten mantle during the ascent to the surface. This is in agreement with models for oceanic crust formation presented by Korenaga & Kelemen (1998 and 2000). They described two models for the formation of the gabbros: (1) two sills, one

close to the Moho and one in shallow depth between the gabbros and the sheeted dykes, or (2) multiple small magma lenses which the ascending melts pass en route to the surface.

According to Purdy et al. (1992) the depth of the sub axial magma chamber is strongly correlated to the spreading rate. Higher magmatic flux induced by the higher spreading rates leads to more shallow magma chambers (Purdy et al., 1992).

Phase equilibria, experimental melting and crystallization studies in the last century showed that the mineral stabilities are, besides the melt composition, strongly dependent on the prevailing thermodynamic conditions, such as pressure, temperature, volatile content, and oxygen fugacity (e.g. Bender et al., 1978; Berndt et al., 2005; Feig et al., 2006; Feig et al., 2010; Grove et al., 1992; Walker et al., 1979). The investigation of conditions at which basaltic melts may have been formed is crucial for the understanding of the formation of the oceanic crust and especially for the location of one or several magma reservoirs. This is important in the case of Shatsky Rise, because although seismic studies investigate the upper crustal structure of the Shatsky Rise plateau (Sager et al., 2013; Expedition 324 Scientists, 2010), no recent model describes its whole crustal architecture.

3.   OBJECTIVES

This dissertation investigates the petrography of natural basalts and how the basaltic lavas were formed within the thick oceanic crust of the Shatsky Rise. The natural minerals and glasses of the Shatsky Rise basalts were analyzed and differentiation mechanisms under different conditions were investigated experimentally. The work is composed of three main parts:

Part I focuses on the characteristics of the natural samples recovered during the Integrated Ocean Drilling Program Expedition 324 and thermodynamic modeling to estimate the conditions, at which the basaltic magmas were stored and differentiated. The systematic core samples represent continuously stacked lava flows, thus, the drilled profile is correlated to time. Therefore, the data obtained from the natural samples give knowledge of time related melt evolution, and led to a model of the magma plumbing system beneath the Shatsky Rise.

Part II addresses crystallization experiments using the Shatsky Rise basaltic compositions. These provide detailed information on the influence of pressure, temperature and H_2O content on the mineral stabilities and liquid evolution. The investigated range of H_2O contents is very narrow, but representative for the range typical for MORBs. The experiments demonstrate the significant effect of small amounts of H_2O on the phase relations. The scientific outcomes contribute to the general understanding of MORB differentiation and can be also applied on Shatsky Rise in order to support the results of Part I.

Part III additionally describes the accuracy of recent thermodynamic models and geothermobarometers present in literature for basaltic compositions. The test using the experimental products described in Part II demonstrates that the presence of small amounts of H_2O leads to systematic overestimation of pressures and temperatures with the most models.

4.   REFERENCES

Bender, J. F., Hodges, F. N. & Bence, A. E. (1978). Petrogenesis of basalts from the project FAMOUS area: experimental study from 0 to 15 kbars. Earth and Planetary Science Letters 41, 277-302.

Berndt, J., Koepke, J. & Holtz, F. O. (2005). An Experimental Investigation of the Influence of Water and Oxygen Fugacity on Differentiation of MORB at 200MPa. Journal of Petrology 46, 135-167.

Bottinga, Y., Allegre, C. J. & Thompson, R. N. (1978). Partial Melting under Spreading Ridges [and Discussion]. Philosophical Transactions of the Royal Society of London. Series A, Mathematical and Physical Sciences 288, 501-525.

Bowen, N. L. (1956). The evolution of the igneous rocks. Dover Publicaations.

Clague, D. A. & Straley, P. F. (1977). Petrologic nature of the oceanic Moho. Geology 5, 133-136.

Coffin, M.F., and Eldholm, O. (1994), Large Igneous Provinces - crustal structure, dimensions, and external consequences. Reviews of Geophysics, 32(1), 1-36.

Coleman, R. G. (1977). Ophiolites: ancient oceanic lithosphere? Springer-Verlag.

Expedition 324 Scientists, E. (2010). Testing plume and plate models of ocean plateau formation at Shatsky Rise, northwest Pacific Ocean. IODP Prel. Rept 324.

Feig, S., Koepke, J. r. & Snow, J. (2006). Effect of water on tholeiitic basalt phase equilibria: an experimental study under oxidizing conditions. Contributions to Mineralogy and Petrology 152, 611-638.

Feig, S., Koepke, J. r. & Snow, J. (2010). Effect of oxygen fugacity and water on phase equilibria of a hydrous tholeiitic basalt. Contributions to Mineralogy and Petrology 160, 551-568.

Green, D. H. & Ringwood, A. E. (1967). The genesis of basaltic magmas. Contributions to Mineralogy and Petrology 15, 103-190.

Grove, T. L., Kinzler, R. J. & Bryan, W. B. (1992). Fractionation of mid-ocean ridge basalt (MORB). Mantle Flow and Melt Generation at Mid-Ocean Ridges. Washington, DC: AGU, 281-310.

Herzberg, C. (2004). Partial crystallization of mid-ocean ridge basalts in the crust and mantle. Journal of Petrology 45, 2389-2405.

Hess, H. (1962). History of Ocean Basins. Petrologic Studies A Volume to Honor A.F. Buddington, 599-620.

Korenaga, J. & Kelemen, P. B. (1998). Melt migration through the oceanic lower crust: a constraint from melt percolation modeling with finite solid diffusion. Earth and Planetary Science Letters 156, 1-11.

Objectives and Background

Korenaga, J. & Kelemen, P. B. (2000). Major element heterogeneity in the mantle source of the North Atlantic igneous province. Earth and Planetary Science Letters 184, 251-268.

Korenaga, J. and Sager, W.W., (2012), Seismic tomography of Shatsky Rise by adaptive importance sampling, Journal of Geophysical Research: Solid Earth, 117(B8), B08102.

Kushiro, I., Nakamura, Y., Akimoto, S. & Shimizu, N. (1972). Compositions of Coexisting Liquid and Solid-Phases Formed upon Melting of Natural Garnet and Spinel Lherzolites at High-Pressures - Preliminary Report. Earth and Planetary Science Letters 14.

Michael, P. J. & Cornell, W. C. (1998). Influence of spreading rate and magma supply on crystallization and assimilation beneath mid-ocean ridges: Evidence from chlorine and major element chemistry of mid-ocean ridge basalts. J. Geophys. Res. 103, 18325-18356.

Morgan, W. J. (1972). Deep Mantle Convection Plumes and Plate Motions. AAPG Bulletin 56, 203-213.

Nakanishi, M., Sager, W.W., and Klaus, A. (1999), Magnetic lineations within Shatsky Rise, northwest Pacific Ocean: Implications for hot spot-triple junction interaction and oceanic plateau formation, J. Geophys. Res., 104(B4), 7539-7556.

Natland, J. H., Dick, H. J.B. (2009) Paired melt lenses at the East Pacific Rise and the pattern of melt flow through the gabbroic layer at a fast-spreading ridge. Lithos 112, 73–86.

Presnall, D. C., Dixon, J. R., O'Donnell, T. H. & Dixons, S. A. (1979). Generation of Mid-ocean Ridge Tholeiites. Journal of Petrology 20, 3-35.

Purdy, G. M., Kong, L. S. L., Christeson, G. L. & Solomon, S. C. (1992). Relationship between spreading rate and the seismic structure of mid-ocean ridges. Nature 355, 815-817.

Ringwood, A. E. (1975). Compostion and petrology of the earth's mantle. London, New York, and Sydney (McGraw-Hill).

Sager, W.W., Kim, J., Klaus, A., Nakanishi, M., and Khankishieva, L.M. (1999), Bathymetry of Shatsky Rise, northwest Pacific Ocean: Implications for ocean plateau development at a triple junction, J. Geophys. Res., 104(B4), 7557-7576.

Sager, W. W., Zhang, J., Korenaga, J., Sano, T., Koppers, A. A. P., Widdowson, M. & Mahoney, J. J. (2013). An immense shield volcano within the Shatsky Rise oceanic plateau, northwest Pacific Ocean. Nature Geosci.

Sano, T., Shimizu, K., Ishikawa, A., Senda, R., Chang, Q., Kimura, J.I., Widdowson, M., and Sager, W.W. (2012), Variety and origin of magmas on Shatsky Rise, northwest Pacific Ocean, Geochemistry Geophysics Geosystems, 13, 25.

Scarfe, C. M. & Smith, D. G. W. (1977). Secondary minerals in some basaltic rocks from DSDP Leg 37. Canadian Journal of Earth Sciences 14, 903-910.

Sinton, J. M. & Detrick, R. S. (1992). Mid-ocean ridge magma chambers. Journal of Geophysical Research-Solid Earth 97, 197-216.

Takahashi, E. & Kushiro, I. (1983). Melting of a dry peridotite at high-pressures and basalt magma genesis. American Mineralogist 68, 859-879.

Villiger, S., Muentener, O. & Ulmer, P. (2007). Crystallization pressures of mid-ocean ridge basalts derived from major element variations of glasses from equilibrium and fractional crystallization experiments. Journal of Geophysical Research-Solid Earth 112.

Walker, D., Shibata, T. & Delong, S. E. (1979). Abyssal tholeiites from the oceanographer fracture-zone. 2. Phase-equilibria and mixing. Contributions to Mineralogy and Petrology 70, 111-125.

Wilson, J. T. (1963). A possible origin of the hawaiian islands. Canadian Journal of Physics 41, 863-870.

Part I: Geothermobarometry of Basaltic Glasses from the Tamu Massif, Shatsky Rise Oceanic Plateau

1.   ABSTRACT

We present the results of a petrological study of core samples from Tamu Massif (Site U1347), recovered during the Shatsky Rise Integrated Ocean Drilling Program (IODP) Expedition 324. The basaltic glasses from Site U1347 are evolved tholeiitic basalts containing 5.2 to 6.8 wt% MgO. They are principally located within the compositional field of mid-ocean ridge basalts (MORBs), but they have systematically higher FeO, lower Al_2O_3, SiO_2, and Na_2O concentrations, and the CaO/Al_2O_3 ratios are amongst the highest known for MORBs. In this sense, glasses from Site U1347 more closely resemble basaltic magmas from the Ontong Java Plateau (OJP), although they still

have lower SiO_2 concentrations. In contrast to MORB and similar to OJP, our fractionation corrected values of Na_2O and CaO/Al_2O_3 indicate more than 20 % of partial melting of the mantle during the generation of the parental magmas of Tamu Massif. The water contents in the glasses, determined by mid-infrared Fourier Transform Infrared (FTIR) spectroscopy, are MORB-like, and vary between 0.18 and 0.6 wt% H_2O. The calculated pressure-temperature (*P-T*) conditions at which the natural glasses represent cotectic olivine (*Ol*)-plagioclase (*Plag*)-clinopyroxene (*Cpx*) compositions range from 0.1 to 240 MPa and 1100 to 1150°C reflecting magma storage at shallow depth. The variation of the glass compositions and the modeled *P-T* conditions in correlation with the relative ages, indicate that there were at least two different magmatic cycles characterized by variations in eruptive styles (massive flows or pillow lavas), chemical compositions, volatile contents, and pre-eruptive *P-T* conditions. Each magmatic cycle represents the progressive differentiation in the course of polybaric crystallization after the injection of a more primitive magma batch. Magma crystallization and eruption episodes are followed by magmatic inactivity reflected in the core sequence by a sedimentary layer. Our data for Tamu Massif demonstrate that, similar to Ontong Java ocean plateau, crystallization beneath Shatsky Rise occurs at different crustal levels.

2.   INTRODUCTION

2.1.   The Shatsky Rise Large Igneous Province and IODP Expedition 324

Large igneous provinces (LIPs) are massive crustal emplacements of predominantly mafic extrusive and intrusive rocks. They appear as continental flood basalts, volcanic passive margins, oceanic plateaus, submarine ridges, seamount groups, and ocean basin flood basalts (Coffin and Eldholm, 1994). Different models are used to explain the extremely high magma production of LIPs: (1) the arrival of a potentially deep-sourced

mantle plume (Duncan and Richards, 1991), and (2) anomalous dynamics at mid-ocean ridges (MORs), e.g. at leaky transform faults, or at ridge reorganizations (Foulger, 2007). For many LIPs, in particular for ocean island chains, the hot spot model (1) is widely accepted. This model requires a deeper-sourced mantle plume compared to MORs (Zhang and Tanimoto, 1992). The mechanism underlying high LIP magma production is less established for large oceanic plateaus like e.g. the famous Ontong Java Plateau (OJP), which is the most studied oceanic plateau (e.g. pro plume head: Mahoney and Spencer (1991), Richards et al. (1991), Roberge et al. (2004), Clouard and Bonneville (2001), contra plume head: Fitton and Godard (2004)).

Besides Ontong Java and Kerguelen, Shatsky Rise is another large oceanic plateau. Unlike others, it was formed during a time of geomagnetic field reversals between Late Jurassic and Early Cretaceous, and its tectonic history recorded in magnetic lineations is relatively well reconstructed (Nakanishi et al., 1999). The plateau consists of three distinct massifs (from south to north Tamu, Ori, and Shirshov massifs, Fig. I.1). After Sager et al. (1999), they emerged as a result of interaction between a mantle plume and a propagating triple junction. The elongated shape of Shatsky Rise was best explained by the ridge tectonics, whereas the rise morphology was best explained by the plume head model, because the oldest and most voluminous Tamu Massif could be associated with the arrival of the plume head. The waning of magmatic activity with time in the younger massifs (Ori and then Shirshov) is explained by the decrease in magma production caused by the plume tail (Sager et al., 1999).

Part I: Geothermobarometry of Basaltic Glasses from the Tamu Massif, Shatsky Rise Oceanic Plateau
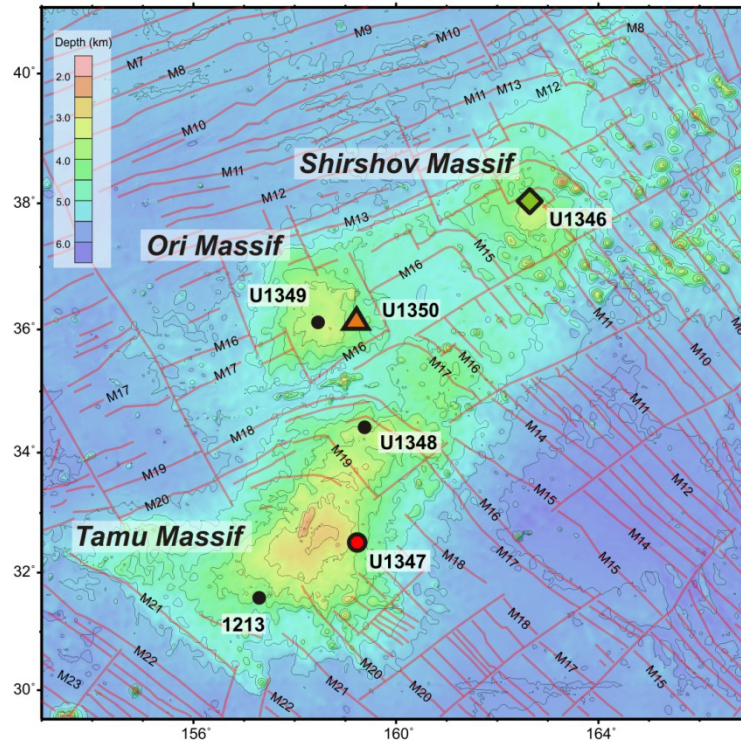
Figure I.1: Topography of Shatsky Rise. The map after Expedition 324 Scientists (2010) shows that Shatsky Rise consists of three Massifs. Marked are the magnetic lineations and fracture zones (red lines) (Nakanishi *et al.*, 1999), the IODP Expedition 324 drill sites (colored symbols), and ODP Site 1213 (blue dot). The depth below sea level is given by bluish to yellow colors (see legend).

Earlier petrological studies on Shatsky Rise magmatism are scarce in the literature. Tatsumi et al. (1998) presented the first analyses of dredged (highly altered) basalts; few of them demonstrated a high Nb/Y ratio. Mahoney et al. (2005) presented the first broader geochemical data from the Shatsky Rise igneous basement (Hole 1213B, Ocean Drilling Program (ODP) Leg 198) and classified those rocks as normal mid-ocean ridge basalt (N-MORB) tholeiites with compositional characteristics typical for East Pacific Rise (EPR). They interpreted whole rock high CaO/Al_2O_3 ratios and relatively high Fe and low Na values in the recovered samples (7.64-8.31 wt% MgO) to be indicative of high fractions of partial melting. Isotope data obtained for limited samples also revealed MORB-like signatures, contradicting the hypothesis that a mantle plume was involved (Mahoney et al., 2005).

Part I: Geothermobarometry of Basaltic Glasses from the Tamu Massif, Shatsky Rise Oceanic Plateau

In 2009, IODP Expedition 324 provided a new set of samples which now can be used to investigate the processes which led to the formation of this oceanic plateau. Five sites at three different massifs of Shatsky Rise were cored (U1346-U1350), and about 723 meters of igneous rocks were sampled (Sager et al., 2010). All three massifs were drilled and the core samples cover different stages of the tectonic history of the Shatsky Rise. Although the precise rock dating (e.g. Ar-Ar) is still in progress, the stratigraphic position of the core samples provide information on the relative emplacement time of the individual lava flows, which enables the reconstruction of dynamic processes proceeded in the magma reservoir(s).

Detailed post-cruise geochemical investigations of bulk rocks and fresh glasses form all five sites were recently presented by Sano et al. (2012). Three geochemical magma groups have been identified based on the glass compositions: normal-, low-Ti, and high-Nb-type basalts. The chemical compositions of the most voluminous normal-type basalts are similar to those of N-MORB with slight depletion in heavy rare earth elements (HREEs). The low-Ti type has slightly lower TiO_2, FeO, and MnO contents at a given MgO. The high-Nb basalts are characterized by distinctively high contents of Nb, K, and REEs, indicating that they are likely affected by an enriched source mantle. Based on geochemical modeling Sano et al. (2012) reported ~15% melting of a depleted mantle source in the presence of residual garnet, and emphasized that the melting zone was deeper than that of melting zones producing N-MORBs.

Sano et al. (2012) also argued that the final depth of the melting beneath Shatsky Rise was deeper than beneath MORs and the melting process stopped at the base of the pre-existing thick oceanic lithosphere. Independent geophysical studies identified a considerable thickening of the oceanic basement beneath the Shatsky plateau and

resolved a maximum thickness of the crust of 22 km (Den et al., 1969) to 30 km (Korenaga and Sager, 2012). This thick crust and the evolved character of the most basalts of the sites U1347 and U1350 imply that the parental magmas underwent extensive crystal fractionation en route to the surface which can be responsible for significant magmatic underplating in the course of Shatsky Rise plateau formation. Previous studies emphasized that beneath oceanic plateaus the chemical differentiation of basaltic magmas from their parental compositions might have occurred in shallow level magma chambers resulting in the formation of large volumes of fractionated cumulates (e.g. OJP basalts: Farnetani et al., 1996; Michael, 2000; Roberge et al., 2004).

Assuming that this mechanism of vertical stacking of successive shallow magma reservoirs (Michael, 2000) may play an important role in the formation of the Shatsky Rise, we conducted a study to (1) examine the role of fractional crystallization in the magma genesis, to (2) estimate the amount and depths of partial crystallization, and to (3) provide *P-T* estimates for distinctive magma types previously identified on the basis of their geochemical compositions. We present results of complementary petrographic and mineralogical investigations of the rocks from the Site U1347. Major element and volatile glass compositions determined in this study are used to simulate conditions of partial crystallization, to estimate the degree of partial melting of the mantle source, and to speculate on genetic relations between lavas from the different massifs of the Shatsky Rise.
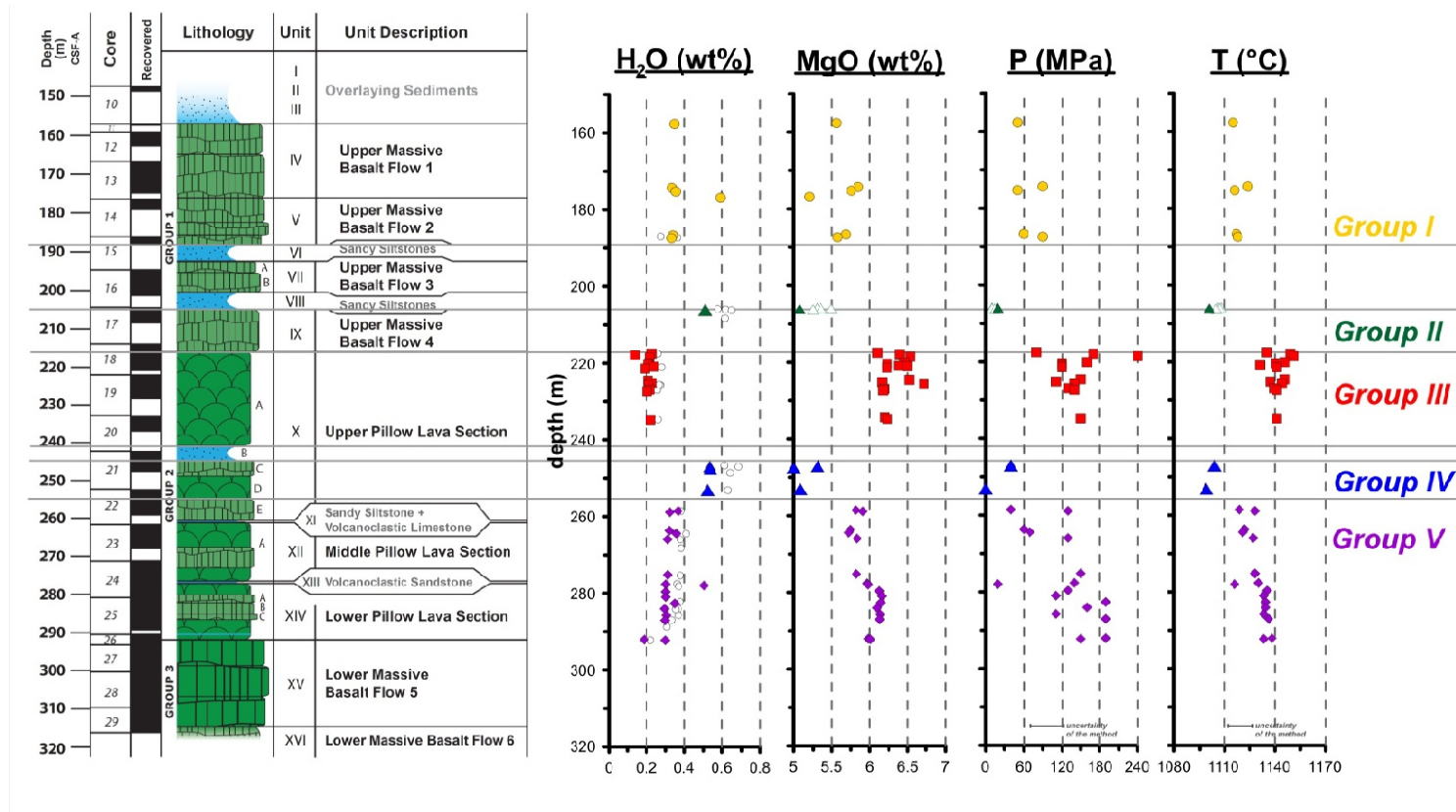
Figure I.2: Stratigraphic overview of Hole 1347A, combined with the measured H$_2$O (FTIR) and MgO (EPMA), compositions in the studied glasses. The modeled *P-T* conditions of *Ol+Plag+Cpx* multiple saturation along the core are shown. The Groups (I–V) which were discriminated along the profile are marked; they correlate well with the lithological units, with distinctive H$_2$O and major element concentrations as well as with simulated magma storage conditions. Filled and open symbols represent data from this study and Sano et al. (2012), respectively.

Part I: Geothermobarometry of Basaltic Glasses from the Tamu Massif, Shatsky
Rise Oceanic Plateau

2.2.   Site U1347 General Information

Site U1347 is located on the eastern flank of the Tamu Massif, which is the oldest

massif where Shatsky Rise volcanism has begun. Although only the uppermost crust of

the massif was penetrated by the drilling, the collected rocks provide important

information on the early processes which triggered the intense volcanism forming

Shatsky Rise. IODP Expedition 324 (Sager et al., 2010) cored into a ~ 160 m section of

volcanic lavas, dominated by thick (8-23m) massive basalt flows at the top and the base

of the hole, with a middle part comprised of alternating numerous pillow basalt inflation

units and thin (<1-2m) massive flows. This core provides samples which are less affected

by alteration (fresh glass rinds were frequently observed). Based on the on-board

macroscopic core description, the volcanic lava succession at Site U1347 was subdivided

into nine stratigraphic units (Fig. I.2, Tab. I.1). However, post-cruise geochemical studies

of the whole rocks and glasses of all Sites drilled on Shatsky Rise (Sano et al., 2012)

demonstrated that the magmas beneath Tamu Massif are quite homogeneous. Only a few

glass samples (at ~200-220 mbsf, stratigraphic Unit IX, Expedition 324 Scientists, 2010)

have slightly higher Nb/Ti and Zr/Ti ratios due to the lower TiO_2 contents (low-Ti type).

In contrast, the major volume of the Site U1347 lava pile (>92%) is composed of normal-

type basalt as described by Sano et al. (2012). In total, 41 samples representing the chilled

margins of pillow inflation units or massive flows were investigated in this study.

Part I: Geothermobarometry of Basaltic Glasses from the Tamu Massif, Shatsky Rise Oceanic Plateau

Table I.1: Stratigraphic and lithological lava units after Expedition 324 Scientists (2010), depth below sea floor (mbsf), flow morphology, petrography, glass H_2O concentrations (FTIR), and modeled *P-T* conditions of the 41 glass samples collected along the Hole U1347A, Tamu Massif, Shatsky Rise

sample		strati-graphic unit	litho-logical unit	depth	unit des-cription [a]	phenocryst phases [b]	H_2O	P	T
(core	interval)			(mbsf)			(wt%)	(MPa)	(°C)
Group I									
11R1	22.5/25	IV	4	157.62	mf	Pl*, Cpx*, Ol	0.35	60	1116
13R7	4/6.5	V	5	174.29	mf	Pl*, Cpx*	0.33	100	1125
13R7	98/100	V	5	175.24	mf	Pl*, Cpx*	0.35	60	1117
14R1	26/29	V	5	176.86	mf	Pl*, Cpx*	0.59	-	-
15R1	46/47.5	V	5	186.65	mf	Pl*, Cpx*, Ol	0.34	60	1117
15R1	119.5/121.5	VIIa	7	187.38	mf	Pl*, Cpx*, Ol	0.33	90	1118
Group II									
17R2	27.5/30	IX	11	206.09	mf	Pl*, Cpx*	0.51	20	1101
Group III									
18R3	91.5/94	Xa	12	217.48	mf	Pl*, Cpx*	0.23	90	1135
18R3	127/130	Xa	13	217.86	mf	Pl*, Cpx*	0.14	160	1149
18R4	46.5/48.5	Xa	14	218.51	mf	Pl*, Cpx*	0.22	200	1147
18R5	60/63	Xa	17	220.05	pl	Pl, Cpx	0.21	160	1145
18R5	88/92.5	Xa	17	220.33	pl	Pl*, Cpx*	0.21	140	1141
18R5	137.5/140	Xa	18	220.87	pl	Pl, Cpx	0.24	140	1142
18R6	47/51.5	Xa	19	221.37	pl	Pl*, Cpx*, Ol	0.19	130	1142
19R1	92/96	Xa	21	224.52	pl	Pl*, Cpx*	0.21	200	1148
19R2	22/25.5	Xa	23	225.11	pl	Pl*, Cpx*, Ol	0.23	130	1138
19R2	79.5/82.5	Xa	25	225.66	pl	Pl*, Cpx*, Ol	0.21	140	1145
19R3	57/62	Xa	28	226.86	pl	Pl, Cpx	0.22	140	1140
19R3	97/100	Xa	29	227.26	pl	Pl, Cpx, Ol	0.20	160	1142
20R1	109/111	Xa	30	234.29	pl	Pl*, Cpx*, Ol	-	-	-
20R2	9.5/11.5	Xa	32	234.72	pl	Pl*, Cpx*, Ol	0.22	160	1146
Group IV									
21R4	101/103.5	Xc	39	247	pl	Pl*, Cpx*, Ol	0.53	10	1100
21R5	25/28	Xc	40	247.51	mf	Pl*, Cpx*	0.54	0	1089
22R1	65/67	Xd	41	253.05	pl	Pl*, Cpx*	0.52	0	1099
Group V									
22R5	40/44	XI	44	258.5	pl	Pl, Cpx	0.37	50	1120
22R5	73/75.5	XII	46	258.82	pl	Pl*, Cpx*, Ol	0.32	140	1128
23R2	139/141	XII	48	263.62	pl	Pl, Cpx, Ol	0.32	80	1123
23R3	76/78	XII	50	264.37	pl	Pl*, Cpx*	0.36	80	1121
23R4	43/45	XII	52	265.48	pl	Pl, Cpx	-	-	-
23R4	85/89	XII	52	265.9	pl	Pl*, Cpx*, Ol	0.31	130	1127
24R3	107/108.5	XIV	55	275.16	pl	Pl, Cpx, Ol	0.31	150	1129
24R5	64/66	XIV	58	277.61	pl	Pl, Cpx	0.30	160	1132
24R5	96/98	XIV	58	277.93	pl	Pl, Cpx	0.50	35	1117
24R7	21/22	XIV	61	279.57	pl	Pl*, Cpx*	0.30	120	1132
24R8	54/56	XIV	63	280.94	pl	Pl, Cpx	0.30	140	1135
24R9	70/72	XIV	65	282.6	pl	Pl, Cpx, Ol	0.35	200	1134
25R3	10/13	XIV	67	283.98	pl	Pl, Cpx, Ol	0.30	170	1135
25R4	32/35.5	XIV	69	285.7	pl	Pl*, Cpx*, Ol	0.30	140	1135
25R5	27/32	XIV	71	287.01	pl	Pl, Cpx, Ol	0.30	205	1137
26R1	135/136.5	XIV	80	292.05	pl	Pl*, Cpx*	0.19	150	1136
26R2	2/4	XV	81	292.22	mf	Pl*, Cpx*	0.30	160	1133

[a] pillow lava (pl), massive flow (mf).
[b] olivine (Ol), plagioclase (Pl), and clinopyroxene (Cpx).
* mineral compositions are available in Husen et al. (2013) (Fig. I.3 and Fig. AI., PetDB).

Table I.2: Glass major Eeement compositions[a] (EPMA) of the 41 glass samples collected along the Hole U1347A, Tamu Massif, Shatsky Rise

Sample		SiO$_2$	TiO$_2$	Al$_2$O$_3$	FeO	MnO	MgO	CaO	Na$_2$O	K$_2$O	P$_2$O$_5$	S	Cl	Total
		(wt%	(wt%	(wt%	(wt%	(wt%	(wt%	(wt%	(wt%	(wt%	(wt%	(ppm	(ppm	
(core	interval)	(stdev))	(stdev))	(stdev))	(stdev))	(stdev))	(stdev))	(stdev))	(stdev))	(stdev))	(stdev))	(stdev))	(stdev))	
Group I														
11R1	22.5/25	50.54 (0.24)	2.46 (0.03)	13.14 (0.1)	14.63 (0.13)	0.24 (0.06)	5.57 (0.04)	10.55 (0.09)	2.35 (0.09)	0.26 (0.01)	0.18 (0.04)	524 (31)	77 (54)	100.11
13R7	4/6.5	50.55 (0.27)	2.23 (0.17)	13.3 (0.27)	14.23 (0.77)	0.26 (0.06)	5.86 (0.28)	10.82 (0.41)	2.31 (0.1)	0.24 (0.02)	0.15 (0.05)	434 (90)	143 (61)	100.12
13R7	98/100	50.47 (0.24)	2.41 (0.05)	13.01 (0.17)	14.55 (0.4)	0.3 (0.03)	5.8 (0.09)	10.54 (0.08)	2.35 (0.11)	0.26 (0.01)	0.25 (0.04)	558 (36)	80 (11)	99.25
14R1	26/29	50.48 (0.37)	2.6 (0.25)	12.69 (0.46)	15.65 (0.83)	0.29 (0.04)	5.21 (0.49)	10.16 (0.42)	2.41 (0.09)	0.28 (0.03)	0.17 (0.05)	583 (62)	117 (40)	99.42
15R1	46/47.5	50.75 (0.19)	2.37 (0.03)	13.1 (0.17)	14.59 (0.24)	0.24 (0.03)	5.69 (0.07)	10.48 (0.18)	2.34 (0.05)	0.26 (0.01)	0.12 (0.08)	508 (22)	86 (37)	99.47
15R1	119.5/121.5	50.44 (0.23)	2.48 (0.04)	13.12 (0.11)	14.82 (0.31)	0.26 (0.04)	5.58 (0.07)	10.46 (0.1)	2.35 (0.08)	0.26 (0.01)	0.15 (0.08)	590 (18)	119 (53)	100.30
Group II														
17R2	27.5/30	51.71 (0.25)	2.12 (0.04)	13.31 (0.12)	14.35 (0.18)	0.26 (0.03)	5.08 (0.04)	9.94 (0.11)	2.66 (0.08)	0.31 (0.01)	0.19 (0.03)	326 (26)	296 (49)	99.66
Group III														
18R3	91.5/94	50.62 (0.34)	2.07 (0.02)	13.49 (0.11)	13.48 (0.12)	0.22 (0.03)	6.1 (0.12)	11.4 (0.14)	2.25 (0.05)	0.21 (0.01)	0.11 (0.05)	361 (14)	117 (52)	99.83
18R3	127/130	50.41 (0.17)	2.11 (0.04)	13.54 (0.12)	12.93 (0.27)	0.28 (0.04)	6.39 (0.06)	11.55 (0.14)	2.35 (0.06)	0.2 (0.01)	0.2 (0.03)	323 (22)	86 (41)	99.28
18R4	46.5/48.5	50.01 (0.31)	2.04 (0.03)	13.59 (0.12)	13.36 (0.11)	0.19 (0.04)	6.59 (0.05)	11.42 (0.05)	2.37 (0.06)	0.23 (0.01)	0.16 (0.02)	364 (14)	115 (12)	100.00
18R5	60/63	50.11 (0.41)	2.05 (0)	13.47 (0.09)	13.33 (0.23)	0.09 (0.12)	6.49 (0.04)	11.65 (0.1)	2.36 (0.03)	0.23 (0.01)	0.18 (0.03)	380 (33)	117 (8)	99.40
18R5	88/92.5	50.66 (0.24)	2.05 (0.02)	13.62 (0.15)	13.21 (0.3)	0.22 (0.04)	6.23 (0.08)	11.39 (0.11)	2.23 (0.07)	0.21 (0.01)	0.13 (0.06)	346 (17)	99 (58)	99.58
18R5	137.5/140	50.48 (0.22)	2.31 (0.19)	13.39 (0.28)	14.05 (0.89)	0.25 (0.03)	5.88 (0.32)	10.93 (0.48)	2.28 (0.11)	0.24 (0.03)	0.13 (0.07)	480 (121)	123 (60)	100.06
18R6	47/51.5	50.59 (0.19)	2.07 (0.02)	13.58 (0.14)	13.26 (0.2)	0.21 (0.05)	6.23 (0.06)	11.46 (0.16)	2.22 (0.08)	0.21 (0.01)	0.13 (0.06)	361 (16)	102 (17)	100.04
19R1	92/96	50.08 (0.3)	2.01 (0.03)	13.35 (0.16)	13.33 (0.29)	0.04 (0.1)	6.53 (0.08)	11.75 (0.15)	2.46 (0.05)	0.22 (0.01)	0.19 (0.01)	350 (9)	119 (4)	99.30
19R2	22/25.5	50.61 (0.24)	2.05 (0.04)	13.59 (0.08)	13.42 (0.15)	0.24 (0.05)	6.17 (0.1)	11.34 (0.1)	2.19 (0.08)	0.21 (0.01)	0.12 (0.05)	368 (11)	121 (41)	100.56
19R2	79.5/82.5	50.48 (0.32)	2.13 (0.07)	13.36 (0.26)	13.38 (0.21)	0.22 (0.09)	6.72 (0.17)	11.48 (0.16)	2.01 (0.14)	0.21 (0.03)	-	-	-	99.87
19R3	57/62	50.54 (0.24)	2.1 (0.04)	13.58 (0.08)	13.4 (0.21)	0.18 (0.01)	6.2 (0.06)	11.33 (0.09)	2.26 (0.1)	0.2 (0)	0.15 (0.03)	364 (24)	110 (32)	100.21
19R3	97/100	50.61 (0.29)	2.05 (0.02)	13.63 (0.14)	13.41 (0.11)	0.21 (0.05)	6.18 (0.14)	11.29 (0.15)	2.24 (0.05)	0.21 (0)	0.12 (0.02)	365 (25)	101 (48)	100.14
20R1	109/111	50.48 (0.26)	2.1 (0.04)	13.44 (0.12)	13.43 (0.18)	0.26 (0.06)	6.2 (0.09)	11.45 (0.12)	2.25 (0.07)	0.22 (0.01)	0.12 (0.07)	367 (19)	137 (63)	99.68
20R2	9.5/11.5	50.42 (0.2)	2.1 (0.03)	13.45 (0.11)	13.59 (0.1)	0.22 (0.06)	6.23 (0.14)	11.29 (0.13)	2.32 (0.07)	0.21 (0.01)	0.12 (0.05)	378 (11)	124 (32)	100.06
Group IV														
21R4	101/103.5	50.18 (0.27)	2.5 (0.05)	13.2 (0.16)	14.9 (0.2)	0.35 (0.08)	5.33 (0.08)	10.34 (0.11)	2.62 (0.07)	0.28 (0.01)	0.2 (0.04)	501 (25)	492 (28)	99.08
21R5	25/28	50.77 (0.12)	2.43 (0.05)	13.12 (0.08)	15.19 (0.09)	0.25 (0.02)	5.01 (0.06)	10.18 (0.13)	2.51 (0.05)	0.28 (0.01)	0.16 (0.05)	476 (21)	499 (78)	99.93
22R1	65/67	50.93 (0.21)	2.43 (0.05)	13.1 (0.07)	15.06 (0.07)	0.28 (0.02)	5.09 (0.04)	10.04 (0.1)	2.58 (0.09)	0.27 (0.01)	0.13 (0.07)	465 (15)	545 (84)	99.91

Continued **Table I.2**

Sample		SiO$_2$	TiO$_2$	Al$_2$O$_3$	FeO	MnO	MgO	CaO	Na$_2$O	K$_2$O	P$_2$O$_5$	S	Cl	Total
		(wt%	(wt%	(wt%	(wt%	(wt%	(wt%	(wt%	(wt%	(wt%	(wt%	(ppm	(ppm	
(core	interval)	(stdev))	(stdev))	(stdev))	(stdev))	(stdev))	(stdev))	(stdev))	(stdev))	(stdev))	(stdev))	(stdev))	(stdev))	
Group V														
22R5	40/44	50.68 (0.06)	2.15 (0.03)	13.21 (0.06)	14.11 (0.24)	0.26 (0.03)	5.81 (0.14)	10.93 (0.18)	2.41 (0.07)	0.25 (0.01)	0.13 (0.07)	366 (19)	224 (35)	99.24
22R5	73/75.5	50.57 (0.09)	2.23 (0.03)	13.37 (0.12)	14.09 (0.13)	0.23 (0.03)	5.92 (0.04)	10.76 (0.07)	2.35 (0.1)	0.25 (0.01)	0.16 (0.06)	411 (20)	215 (37)	100.48
23R2	139/141	50.59 (0.26)	2.21 (0.03)	13.22 (0.11)	14.25 (0.25)	0.24 (0.03)	5.75 (0.08)	10.86 (0.07)	2.4 (0.06)	0.24 (0.01)	0.17 (0.05)	381 (29)	213 (27)	100.39
23R3	76/78	50.9 (0.25)	2.13 (0.02)	13.37 (0.14)	14.11 (0.1)	0.24 (0.05)	5.73 (0.1)	10.71 (0.1)	2.38 (0.11)	0.24 (0.01)	0.15 (0.05)	358 (23)	218 (57)	99.99
23R4	43/45	50.5 (0.17)	2.24 (0.03)	13.34 (0.1)	14.17 (0.09)	0.28 (0.04)	5.84 (0.13)	10.67 (0.09)	2.46 (0.05)	0.25 (0.01)	0.18 (0.03)	397 (16)	200 (53)	100.00
23R4	85/89	50.56 (0.17)	2.25 (0.03)	13.36 (0.08)	14.19 (0.11)	0.29 (0.04)	5.84 (0.15)	10.68 (0.11)	2.35 (0.05)	0.25 (0.01)	0.18 (0.03)	420 (17)	209 (56)	100.45
24R3	107/108.5	50.33 (0.19)	2.24 (0.03)	13.39 (0.11)	14.24 (0.07)	0.23 (0.07)	5.83 (0.05)	10.81 (0.18)	2.43 (0.06)	0.24 (0.01)	0.2 (0.05)	395 (12)	272 (37)	100.38
24R5	64/66	50.51 (0.35)	2.17 (0.03)	13.42 (0.14)	14.01 (0.25)	0.29 (0.03)	5.97 (0.09)	10.82 (0.08)	2.32 (0.02)	0.24 (0)	0.19 (0.04)	407 (23)	262 (69)	101.22
24R5	96/98	50.72 (0.15)	2.08 (0.04)	13.47 (0.13)	13.71 (0.38)	0.21 (0.04)	5.99 (0.2)	11.12 (0.29)	2.3 (0.09)	0.22 (0.01)	0.13 (0.04)	377 (14)	189 (42)	100.03
24R7	21/22	50.79 (0.3)	2.07 (0.04)	13.42 (0.17)	13.09 (0.39)	0.27 (0.04)	6.27 (0.15)	11.12 (0.07)	2.5 (0.09)	0.22 (0.01)	0.18 (0.03)	352 (15)	215 (19)	99.28
24R8	54/56	50.49 (0.49)	2.13 (0.05)	13.46 (0.14)	13.54 (0.15)	0.22 (0.03)	6.13 (0.05)	11.22 (0.05)	2.34 (0.05)	0.22 (0.02)	0.18 (0.04)	378 (31)	229 (18)	98.37
24R9	70/72	50.35 (0.28)	2.12 (0.02)	13.56 (0.15)	13.96 (0.07)	0.25 (0.04)	6.15 (0.11)	10.84 (0.09)	2.32 (0.06)	0.24 (0.01)	0.15 (0.04)	414 (34)	200 (72)	100.83
25R3	10/13	50.34 (0.27)	2.17 (0.02)	13.57 (0.11)	13.84 (0.12)	0.25 (0.05)	6.1 (0.24)	10.98 (0.03)	2.3 (0.1)	0.23 (0.01)	0.16 (0.03)	385 (12)	204 (46)	100.70
25R4	32/35.5	50.58 (0.15)	2.02 (0.03)	13.49 (0.2)	13.26 (0.33)	0.34 (0.08)	6.12 (0.05)	11.24 (0.07)	2.49 (0.07)	0.24 (0.01)	0.16 (0.05)	391 (19)	203 (16)	98.92
25R5	27/32	50.5 (0.1)	2.12 (0.06)	13.6 (0.05)	13.8 (0.28)	0.24 (0.03)	6.13 (0.06)	10.84 (0.07)	2.35 (0.08)	0.23 (0.01)	0.14 (0.04)	400 (12)	171 (55)	100.70
26R1	135/136.5	50.22 (0.22)	2.25 (0.04)	13.06 (0.16)	14.35 (0.37)	0.19 (0.06)	6.04 (0.07)	10.85 (0.08)	2.51 (0.08)	0.24 (0.01)	0.24 (0.03)	172 (14)	166 (18)	100.25
26R2	2/4	50.68 (0.25)	2.09 (0.02)	13.56 (0.04)	13.83 (0.1)	0.23 (0.06)	6.02 (0.14)	10.86 (0.13)	2.32 (0.06)	0.23 (0.01)	0.13 (0.06)	343 (6)	200 (42)	99.44

[a] All given glass compositions are an average of five measurements and normalized to 100 wt% total, the standard deviations (1σ) are given in brackets. The given total refers to the original sum of the measured element oxide concentrations.

3.   METHODS

3.1.   Electron Microprobe

The major elements of the mineral phases and basaltic glasses were measured using an electron probe microanalysis (EPMA) at the Institute of Mineralogy in Hannover and at the Institute of Disposal Research in Clausthal. In both laboratories, a Cameca SX100 instrument was used at 15 kV acceleration potential. Mineral analyses were obtained with a 15nA beam current, using a focused beam and a peak counting time of 10s to determine the peaks and 5s background for each element (Si, Ti, Al, Fe, Mn, Mg, Ca, Na, K). Glasses were measured with a 10nA beam current using a defocused beam size of 10 μm with a peak counting time of 10s for all major elements. Cl and S were measured using a 40nA beam current with a peak counting time of 60s. For all elements, 5 spots on each glass sample were analyzed and the average values are reported in Tab. I.2.

The internal calibration standards were albite for Na, wollastonite for Si and Ca, Al_2O_3 for Al, Mn_2O_3 for Mn, TiO_2 for Ti, MgO for Mg, Fe_2O_3 for Fe, and orthoclase for K. During each session, sample measurements were verified by measuring external international standard materials: Basaltic Glass Juan de Fuca Ridge (USNM 111240/52 VG-2), Olivine (Fo_{90}) San Carlos (Gila Co., AZ, USNM 111312/444), and Plagioclase (Labradorite) Lake County (OR, USNM 115900) (Jarosewich et al., 1980). The analyses determined by microprobe were corrected using these external standard compositions. After the correction, the standard compositions were reproduced within the standard deviation of the EPMA analysis as shown in Fig. AI.1 and AI.2 in the Appendix. In order to address the potential problem of the sodium loss, the evolution of signal intensity with counting time was tested for one basaltic glass standard. Fig. AI.3 shows that no Na_2O

loss can be detected using a defocused beam (10µm) at 10 nA beam current, even for long counting times of 60 s. Thus, a correction for alkali loss is not necessary under the analytical conditions adopted in this study (10s counting time, 10 nA).

3.2. Infrared Spectroscopy

Glass H_2O concentrations were determined using a Fourier Transformation Infrared (FTIR) Bruker IFS88 spectrometer coupled with an IR Scope II microscope (Institute of Mineralogy, Leibniz University of Hannover). For IR measurements, glass fragments approximately 1mm² in size were mounted in ceramic rings and then doubly polished (thickness varied from 145-150 to 40-50 µm). The section thickness was measured for each individual sample using a digital micrometer (Mitutoyo, precision: ≤2µm). Before measuring, it was checked that no scratches, crystals, or pores were present in the measured glass volume. For all samples, spectra were collected in the mid-infrared (MIR) range using a spot size of 100 x 100 µm (every spectrum was the average of 50 scans). The operating conditions for MIR were: globar light source, KBr beam splitter, MCT (HgCdTe) detector, 4 cm^{-1} spectral resolution, spectral range from 13000 to 0 cm^{-1}. The H_2O concentration was measured at the peak that is attributed to the OH stretch vibration (3550 cm-1) using a molar absorption coefficient of 67 L•cm^{-1} • mol^{-1} (Stolper, 1982). The density was assumed to be a typical value for basaltic glasses, 2815 g/l. The H_2O concentration was calculated based on the Lambert-Beer law using the peak height, which was determined by reference to a straight tangential base line. Three measurements per sample were performed to account for possible variations in thickness due to polishing. The average values of such measurements were used to calculate the H_2O content of the glasses, with an uncertainty usually less than 0.02 wt%.

We also measured the absorption of CO_3^{2-} which can be detected in the same spectra at two peak positions, 1515 cm^{-1} and 1435 cm^{-1} (Fine and Stolper, 1986). However, only a few samples show weak CO_3^{2-}- peak doublets. In all other samples, CO_2, if present, was below the detection limit of the FTIR analysis (~20 ppm CO_2).

3.3. Geothermobarometry

Partial crystallization pressure and temperature were estimated for each individual composition by simulating the conditions of *Ol+Plag+Cpx* saturation in the basaltic melts (hereinafter referred to as multiple saturation after Sack et al., 1987). The COMAGMAT program (Ariskin and Barmina, 2004) was applied following the approach described in Almeev et al. (2008). In contrast to widely applied geobarometers (Yang et al., 1996; Herzberg, 2004; Villiger et al., 2007) or geothermometers (Ford et al., 1983; Beattie et al., 1991), the advantage of this method is that it provides both pressure and temperature estimations. In addition, the effect of small amounts of H_2O on crystallization temperatures (Michael & Chase, 1987; Danyushevsky, 2001) was accounted from recent experimental calibrations (Almeev et al., 2007, 2012; Médard et al., 2008).

We used two different approaches for the thermobarometry. First, fractional crystallization trends modeled with the COMAGMAT program (Ariskin and Barmina, 2004) were determined for one representative composition (U1350A 24R3 76-79cm) among the most MgO-rich samples with 8.5 wt% MgO (Tab. I.2), assumed to be parental for the whole volcanic Shatsky Rise series. All calculations were performed along the FMQ (fayalite-magnetite-quartz) oxygen buffer. In an attempt to produce the best match between calculated Liquid Lines of Descent (LLDs) and the chemical trends defined by the natural glass compositions pressure and initial H_2O content were systematically varied. We applied both isobaric and polybaric modes of fractional crystallization

calculations. The polybaric mode allows one to simulate the crystallization process during magma ascend.

In addition, *P-T* conditions of multiple saturation for every given basaltic glass composition were simulated by varying the pressure at given H_2O content in an attempt to observe simultaneous crystallization of the *Ol+Plag+Cpx* phase assemblage within the first few percentages of crystallization (the mode of equilibrium crystallization was used; see more details in Almeev et al.(2008)). In this approach, the H_2O content measured in the glasses was assumed to be representative for the amount of H_2O present during the differentiation of the corresponding liquid. The assumption of the magmatic H_2O origin was justified by the relatively constant H_2O/K_2O and relatively low Cl/K ratios (see below). The precision of this method is within the precision of the geothermobarometers used in the COMAGMAT model. Our calculations demonstrate that the stability curves of *Ol*, *Plag*, and *Cpx* intersect at a "point" of multiple saturation (when considered in *P-T* coordinates) within ± 5°C (within 1-2 % of crystallization) for 90% of the modeled Shatsky Rise compositions, allowing pressure to be determined within ± 50 MPa. For the other samples, pressure was modeled with precision better than ± 100 MPa, assuming minor temperature corrections to reach multiple saturation. These corrections did not, however, exceed 10°C and were always lower than the uncertainty of the mineral-melt geothermobarometers implemented in COMAGMAT (±10°C at 0.1 MPa and ±15-20°C at elevated pressure, Ariskin and Barmina (2004)).

The approach used in this study was also applied to experimental *Ol+Plag+Cpx*-saturated glasses produced on different Shatsky Rise starting compositions at *P* = 100, 200, 400, and 700 MPa under nearly anhydrous and slightly hydrous conditions (<0.2 and 0.4-1.1 wt% H_2O respectively, FTIR determinations), which represent the range of H_2O

contents found in the natural glasses from Tamu Massif. It has been found that the best

reproduction of multiple saturated conditions with an uncertainty of 15°C and 50 MPa is

observed when *Cpx* crystallization temperature is 10°C suppressed (temperature

correction -10°C for augite geothermometer described in Ariskin and Barmina, 2004).

Thus, with this correction, the COMAGMAT crystallization model was slightly

"adjusted" (Langmuir et al., 1992) to be used with the Shatsky Rise compositions.

4.   RESULTS

4.1.   Mineral Compositions of Hole U1347A

Tab. I.1 gives a summary of the phases which were recognized and analyzed along

the section of Hole U1347A. In general, the rock textures and mineral assemblages of

Hole U1347A do not change significantly along the profile. Depending on the position of

the sample within the lava flow, the groundmass texture varies from cryptocrystalline,

through microcrystalline, to very-fine-grained (and rarely to medium-grained) from

chilled margins to flow interiors respectively. *Ol* is altered and completely replaced by

clay minerals or calcite pseudomorphs (evidence for presence of *Ol* was observed in 37 of

77 thin sections). These pseudomorphs can be easily distinguished by the euhedral

habitus of former phenocrysts (Tab. I.1). All basalts contain phenocrysts of *Plag* and *Cpx*

within a matrix of intergranular texture. In a few thin sections *Ol* or *Cpx* (but not both)

were not observed. Based on mineral associations and textural characteristics, three

different groups can be recognized: (1) coarse-grained *Plag* phenocrysts/glomerocrysts

(up to 0.5 mm in size, discontinuously normal or multiply-zoned) with numerous

inclusions, (2) fine-grained *Plag* and *Cpx* subphenocrysts which show evidence for

undercooling, which caused extremely fast growth possibly not in equilibrium with the

surrounding melt (embayments, inclusions, skeletal growth) often building clots of

radiate intergrowth (skeletal, columnar, discontinuously normal, and/or sector zoned);

and (3) prismatic *Plag* and equigranular *Cpx* in crypto- to microcrystalline groundmass,

containing dendritic and skeletal magnetite (*Mag*).
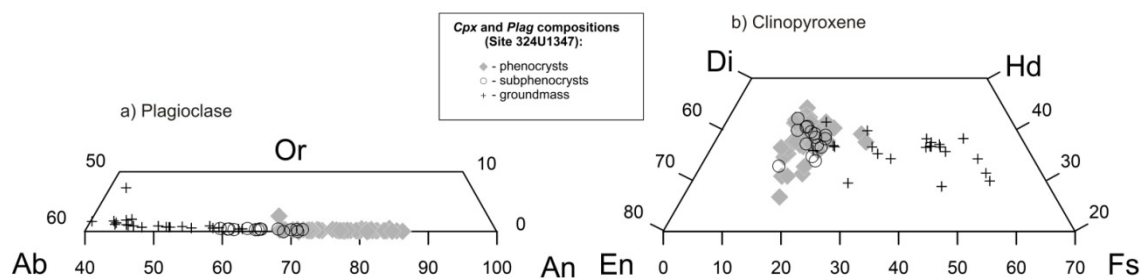
Figure I.3: Compositions of *Plag* (a) and *Cpx* (b) phenocrysts, subphenocrysts, and
microphenocrysts from the basaltic lavas cored at Site U1347, Shatsky Rise oceanic plateau. The data
points are individual measurements obtained for each crystal, plotted in the anorthite-albite-orthoclase (An-
Ab-Or) and the enstatite-ferrosilite-wollastonite (En-Fs-Wo) triangular diagrams. The data are available in
Husen et al. (2013) and via the PetDB database (http://www.earthchem.org/petdb).

Plag and *Cpx* (augite) exhibit mineral compositions typical for N-MORB. The

compositions gradually evolve from phenocrysts to subphenocrysts and to groundmass

microlithes, as indicated by decreasing An (molar proportions of Ca/(Ca+Na+K))

contents in *Plag* and decreasing Mg# (molar ratio of (Mg/(Mg+Fe))) in *Cpx* (Fig. I.3).

Plag phenocrysts range in composition from 90 to 65 mol% An, whereas *Plag*

subphenocrysts and *Plag* groundmass crystals are more albitic: 75- 65 mol% An and 55-

35 mol% An respectively (Fig. I.3). *Cpx* phenocryst and microphenocryst compositions

are similar (Fig. I.3); they display varying compositions in the field of Mg-rich augites

(60>En>40, in mol %; molar proportions of Mg/(Ca+Fe+Mg)). The groundmass *Cpx*

crystals are generally more evolved (45>En>20).

Plag and *Cpx* are the most abundant groundmass phases. Skeletal and dendritic

Mag also exists in some samples. Site U1347 basalts are vesicular, and all vesicles are

filled by secondary calcite. Some thin sections have veins of secondary calcite, zeolites, and chlorite.

4.2.   Major Element Compositions of Tamu Massif Glasses

The major element compositions of 41 basaltic glasses from Site U1347 are given in Tab. I.2 and shown in Fig. I.4. Our microprobe data confirm that the Tamu Massif magmas are evolved MORB-like tholeiitic basalts (6.6-5.0 wt% MgO). With an MgO decrease and a weak SiO_2 increase, those lavas show strong FeO enrichment and CaO and Al_2O_3 depletion. All minor elements (TiO_2, K_2O, and P_2O_5) exhibit a positive correlation with differentiation indices (e.g. MgO). Water concentrations from 0.18 to 0.6 wt% H_2O are within typical enriched MORB values (Jambon and Zimmermann, 1990; Danyushevsky et al., 2000), and are systematically higher in the most evolved compositions. The variations in glass compositions are complementary to the changes observed in subphenocryst mineral compositions. Thus, the highest An content in *Plag* (>75mol% An) and the most primitive *Cpx* (Mg#>80) were found in the basaltic melts with the highest MgO concentrations (6.2-6.7 wt% MgO). All these chemical characteristics indicate the importance of the crystal fractionation which occurred along *Ol+Plag+Cpx* mineral cotectics.

4.3.   Variations of Glass Composition along the Core

As mentioned above, Sano et al. (2012) demonstrated a large geochemical diversity in the basalts from sites U1349 and U1350, and emphasized the relatively homogeneous composition of rocks and glasses from Site U1347. Although our data also show the lack of large compositional variations in glasses from the *Upper Massive Basalt Flow* and *Upper* to *Lower pillow Lava Sections* units (Expedition 324 Scientists, 2010), minor compositional differences in the volcanic succession recovered at Tamu Massif can be

clearly detected (see Fig. I.2). We divided the chemical compositions of the fresh glasses into five groups based on their characteristic major (this study) and trace (Sano et al., 2012) element compositions which correlate with the lithologic units. To distinguish them from the stratigraphic Groups 1 to 3 from Expedition 324 Scientists (2010), Roman numbering has been given to the chemical groups proposed in this study: Group I to Group V.

Considered collectively, lavas from the *Middle* (stratigraphic Unit XII, Sager et al., 2010) and *Lower* (Unit XIV) *Pillow Lava Sections* (Fig I.2) exhibit a common compositional field with a weak increase of the degree of differentiation from the bottom to the top, as can be clearly observed for K_2O and TiO_2 (and all highly incompatible elements from Sano et al. (2012)), MgO, CaO, and Al_2O_3, and to a lesser extent for Na_2O and H_2O (Tab. I.2, Fig. I.2). These lavas are combined into one chemical group, **Group V**. The slightly lower MgO, Al_2O_3, and H_2O and slightly higher FeO concentrations found in two glass samples, 324-U1347A-26R1-135-137cm and 324-U1347A-26R2-2-4cm, recovered at the margin between the base of the *Lower Pillow Lava Section* (Unit XIV) and the top of the *Lower Massive Basalt Flow 5* (Unit XV, Stratigraphic Group 3), place them slightly off the trend defined by the Group V glasses. It should be noted that within the stratigraphic column these two samples are separated from the overlaying pillow basalts (Unit XIV) by a thin sedimentary horizon. Therefore, due to this small chemical variability we suggest that they may rather represent the quenched pillow rims of the *Lower Massive Basalt Flow 5*, which exhibits slightly but systematically lower Zr/Ti values (Sano et al., 2012). However, these are the only two samples of fresh glasses from the *Lower Massive Basalt Flow 5*; therefore we left them within Group V, keeping in mind that they may actually belong in a different group.

Part I: Geothermobarometry of Basaltic Glasses from the Tamu Massif, Shatsky Rise Oceanic Plateau

The next group, **Group VI**, consists of aphyric to sparsely *Plag* phyric basalt glasses from the lower *Upper Pillow Lava Section* (Units Xc and Xd, Fig. I.2 and Tab. I.1). In comparison to the Group V basalts, these rocks exhibit a higher H_2O/K_2O ratio (see Discussion below) and are notably more evolved and H_2O-rich (5.0-5.3 wt% MgO, 0.51-0.54 wt% H_2O). MgO and CaO contents in these samples are amongst the lowest found at Site U1347. In contrast to the differentiated basalts from Group IV, the glasses sampled at the top of this lava stack (the same *Upper Pillow Lava Section*, Unit Xa) again demonstrate more primitive compositions, which are somewhat similar to those from Group V (at the base of the pillow lava section). However, they are less hydrous (~0.2 wt% H_2O) and less differentiated with slightly different trace element ratios (H_2O/K_2O, H_2O/Ce, see Discussion below). In addition, according to the onboard observations (Sager et al., 2010), Units Xa and Xc are separated by a ~5 m thick sedimentary interval (Fig. I.2). The sedimentary layers in the stratigraphic column represent intervals without magmatic activity and interrupt the continuous record of eruptions, providing time for erosion processes. Based on the geochemical data, we grouped these pillow basalts from the *Upper Pillow Lava Section*, Unit Xa into an individual chemical group: **Group III**.

Chemical **Group II** consists of basalts from the *Upper Massive Flow 4* (stratigraphic Unit IX) which are very close in composition to the evolved Group IV basalts. However, Group II basalts are slightly richer in alkalis and other trace elements (Sano et al., 2012), and contain less CaO and FeO.

The final compositional **Group I** consists of samples from *Upper Massive Flow 1* and *Upper Massive Flow 2* (Stratigraphic Units IV and V respectively, Sager et al., 2010). Their compositions are intermediate between the "primitive" groups III and V and the "evolved" groups II and IV.

Part I: Geothermobarometry of Basaltic Glasses from the Tamu Massif, Shatsky Rise Oceanic Plateau
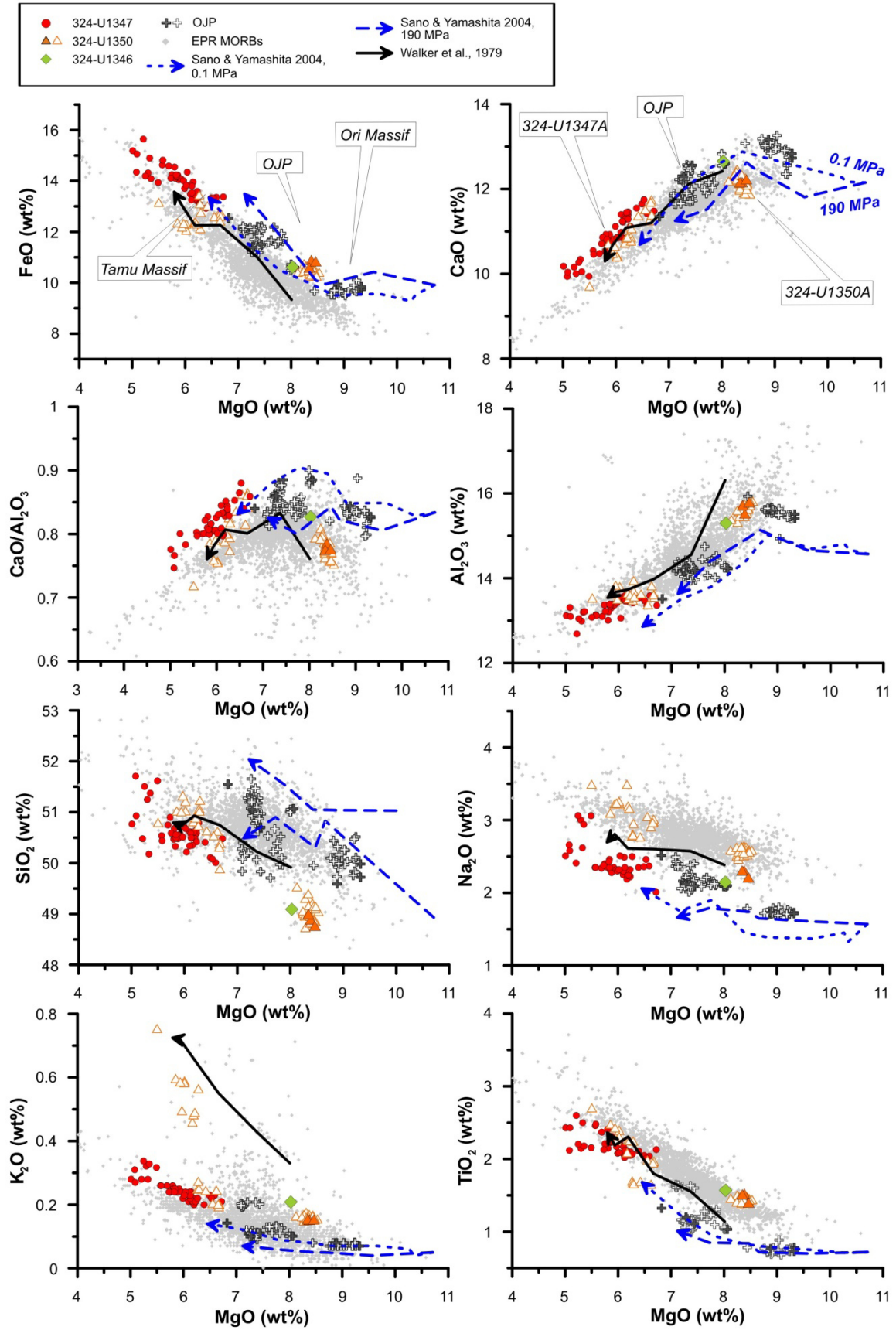
caption →

Figure I.4: Major element compositions of glasses from Sites U1347 (red circles, this study), U1350 (orange triangles; filled symbols refer to this study, open symbols are from Sano et al., 2012), and U1346 (green diamond, this study). The basalts from Ontong Java Plateau (OJP, open crosses (Michael, 2000; Roberge et al., 2004; Sano and Yamashita, 2004), dark gray crosses show compositions, which were used for thermobarometry, Tab. I.2) and the EPR MORB glass variations (gray diamonds) are shown for comparison. MORB data are from the PetDB petrological database (http://www.earthchem.org/petdb). See text for details.

Considered collectively, the microprobe measurements of basaltic glasses from the Tamu Massif revealed five compositional groups along the profile, which may represent magmas which attained different evolutionary stages within the magma chamber before eruption (see below). The different compositional groups are also distinguished by slightly different *Cpx* compositional ranges (see Fig. AI.4). The different groups denote different lithological units within the stratigraphic column, which were clearly identified by boundaries between pillow inflation units and massive flows or by the presence of a sedimentary layer. Below, we present results of the glass geothermobarometry and discuss the partial crystallization conditions of these different magma batches.

4.4. Water and Cl Content of Glasses

In this study, it is essential to clarify the origin of the water (magmatic or diffusion after quench) which was determined quantitatively by FTIR spectroscopy. The glasses in the chilled margins are well preserved and not or only slightly affected by alteration. The whole section U1347 provides mostly very fresh glasses, only few samples demonstrate zones of glass transformation to palagonite. The glasses without any evidence of palagonitization also do not show any evidence for the transport of mobile elements, such as depletion in Si, Al and alkalis (Staudigel and Hart, 1983).

Part I: Geothermobarometry of Basaltic Glasses from the Tamu Massif, Shatsky Rise Oceanic Plateau
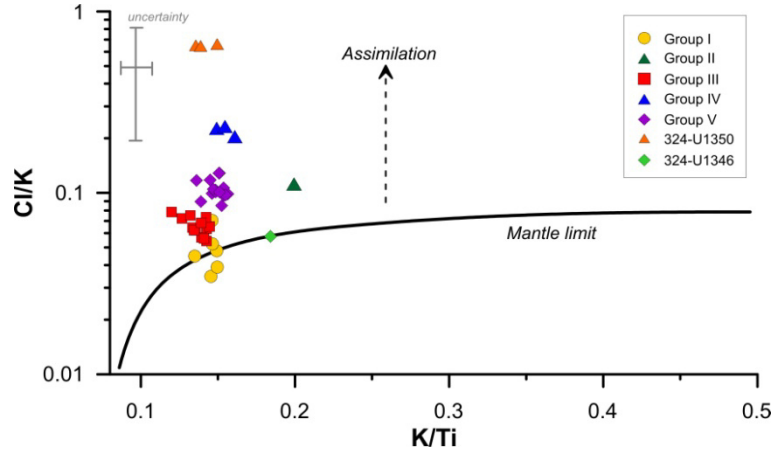
Figure I.5: The Cl/K ratios as a function of K/Ti are shown compared with ''mantle values'' (Michael and Cornell, 1998). The extent of potential assimilation of hydrothermally altered material or reaction with fluids (e.g., brine) is indicated by Cl/K ratios higher than that of in the mantle (mantle limit on the plot), since this ratio is unaffected by partial melting and fractional crystallization.

It has been shown that Cl/K is unaffected by partial melting and fractional crystallization and can indicate a signature of assimilation of hydrothermally altered material or of reaction with fluids (e.g. brine) if the values of Cl/K ratio are above 0.07 (Michael and Cornell, 1998). In the case of Shatsky Rise magmas (Fig. I.5), the basalt from Shirshov Massif and the basalts of the Group I from Tamu Massif have Cl/K ratios typical of mantle derived melts. Samples from Group III and V have higher Cl/K values but considering the large error of Cl determination by microprobe, they are still compatible with primary mantle signatures. The Cl/K ratios in glasses from Group IV are higher (~ 0.2) and may indicate reactions with seawater. The basalts from Ori Massif exhibit the highest Cl/K ratios (~0.7), suggesting that possible hydrothermal alteration was most intense in those glasses. However it is not clear if this process results from assimilation of hydrothermally altered material at high temperature or from a reaction with seawater after quench.

The infrared spectra did not show any evidence for significant incorporation of molecular H_2O in the glasses. To prove that their H_2O contents are primary and to exclude H_2O loss due to degassing or H_2O gain caused by low temperature alteration, we compared the H_2O concentrations in the glasses with the concentrations of other incompatible elements like K_2O and Ce. The positive correlation between these elements is an indication that most water is of primary origin (see further discussion below).

5. DISCUSSION

5.1. Chemical Variations in Basaltic Glasses from Shatsky Rise and Ontong Java Plateau

In this chapter we compare our data with lavas from OJP because it is also formed in the Pacific ocean (OJP: 122-90 Ma, Mahoney et al. (1994), Shatsky Rise: 146-127 Ma, Nakanishi et al. (1999)) and it has characteristics similar to Shatsky Rise, such as (1) deep levels of partial melting and high melt fractions (Sano et al., 2012; this study), (2) different types of magmas with depleted and slightly enriched source characteristics (Fitton and Godard, 2004; Mahoney et al., 1994; Sano et al., 2012), and (3) relatively low H_2O concentrations (Roberge et al., 2004; this study). Based on the investigation of progressive hot-spot tracks Clouard and Bonneville (2001) conclude that only four high volume pacific oceanic plateaus can be directly associated with the arrival of a plume head. Amongst them there are the Louisville hotspot which is attributed to the OJP and the Marquesas hotspot which could trigger the Hess Rise and Shatsky Rise volcanism (Clouard and Bonneville, 2001). However, in the case of Shatsky Rise, there is additional information on its tectonic history because its edifices were not modified by later tectonic processes, which is the case on OJP.

Part I: Geothermobarometry of Basaltic Glasses from the Tamu Massif, Shatsky
Rise Oceanic Plateau

In Fig. I.4, the naturally quenched glass compositions from the Tamu Massif (red dots) are plotted together with glasses from the Ori (orange filled and open triangles) and Shirshov (green diamond) massifs (Sites U1350 and U1346 respectively). The data shown by filled symbols are from this study and open symbols reflect data from Sano et al. (2012). For comparison we also reported MORBs from East Pacific Rise (light grey dots, obtained from the PetDB database), and basaltic glasses from the OJP (open crosses from Roberge et al. (2004) and Michael (2000); black crosses - samples used for thermobarometry in this study, Tab. I.3).

When compared to basalts from the Ori Massif, the compositions of the Tamu Massif (U1347A) glasses are similar to those of differentiated basaltic glasses sampled in the upper part of Hole U1350A (both normal- and high-Nb-type basalts with 5.5 to 6.7 wt% MgO, compare red dots and orange triangles in Fig. I.4). This similarity, however, is not perfect: Ori Massif glasses are not as rich in CaO and FeO as those from the Tamu Massif and they also have higher SiO_2 and Na_2O contents. The evolved Ori Massif glasses (with 5.5-7 wt% MgO) also do not display a trend of Al_2O_3 depletion with MgO decrease which would be expected for magmatic liquids evolving along a tholeiitic trend of differentiation. Most likely, in the case of the Ori Massif magmas, another mechanism (or mechanisms) in addition to crystal fractionation may have played a role (e.g. polybaric fractionation and internal magma mixing of magma batches produced in the course of magma ascend). The glass compositions of the pillow lavas from the base of U1350A (orange triangles in Fig. I.4) are the most primitive ones found on the Shatsky Rise (8.1-8.5 wt% MgO, Sager et al., 2010; Sano et al., 2012) and have no compositional counterparts in Site U1347. Only one glass analysis available from the whole core of the Shirshov massif has a composition which is close to the less evolved lavas from the Ori massif (8 wt% MgO, Tab. I.3, Fig. I.4). However, it is slightly more differentiated, and in

Continued **Table I.3:** Glass major element compositions [a] (EPMA) of selected glasses samples from Ori and Shirshov massifs and from the Ontong Java Plateau

Sample	H_2O (wt%)	P (MPa)	T (°C)	SiO_2 (wt% (stdev))	TiO_2 (wt% (stdev))	Al_2O_3 (wt% (stdev))	FeO (wt% (stdev))	MnO (wt% (stdev))	MgO (wt% (stdev))	CaO (wt% (stdev))	Na_2O (wt% (stdev))	K_2O (wt% (stdev))	P_2O_5 (wt% (stdev))	S (ppm (stdev))	Cl (ppm (stdev))	Total
Ori Massif (324-U1350A)																
22R3 80-82	0.29	650	1205	48.77	1.5	15.46	10.82	0.16	8.37	12.11	2.28	0.15	0.05	994	791	98.64
(IIc, 62)				(0.24)	(0.04)	(0.14)	(0.27)	(0.08)	(0.15)	(0.16)	(0.04)	(0.01)	(0.05)	(46)	(24)	
24R1 135,5-137	0.33	635	1203	48.88	1.4	15.66	10.53	0.16	8.33	12.11	2.28	0.15	0.06	980	796	98.58
(IIc, 86)				(0.34)	(0.01)	(0.22)	(0.25)	(0.03)	(0.09)	(0.25)	(0.09)	(0.01)	(0.05)	(58)	(19)	
24R3 76-79 *	0.31	665	1207	48.66	1.3	15.73	10.77	0.14	8.45	12.17	2.19	0.15	0.16	792	892	100.95
(III, 91)				(0.23)	(0.04)	(0.17)	(0.3)	(0.06)	(0.16)	(0.1)	(0.15)	(0.01)	(0.08)	(15)	(21)	
Schirshov Massif (324-U1346A)																
8R1 56-60	0.56	400	1174	49.04	1.5	15.29	10.62	0.18	8.02	12.65	2.15	0.21	0.14	99	795	100.58
				(0.07)	(0.03)	(0.14)	(0.35)	(0.03)	(0.13)	(0.05)	(0.06)	(0.01)	(0.07)	(18)	(8)	
Ontong Java Plateau																
192-1184-A-39R-7,95	0.19	480	1212	49.98	0.78	15.42	9.74	0.17	9.33	12.73	1.73	0.07	0.05	922	778	99.51
192-1185-B-5R-7,19	0.19	490	1213	49.72	0.73	15.51	9.85	0.16	9.33	12.83	1.71	0.07	0.08	818	936	99.73
192-1185-B-9R-1, 55	0.21	440	1208	49.59	0.77	15.60	9.95	0.16	8.88	13.17	1.73	0.08	0.07	957	929	99.19
192-1185-A	0.17	175	1178	51.07	1.03	14.23	10.61	0.19	8.06	12.60	2.10	0.10	0.00	705	1699	98.59
192-1186-A-32R-3,68	0.23	110	1164	50.71	1.11	14.18	11.50	0.20	7.44	12.56	2.10	0.11	0.09	1041	740	99.06
192-1183-A-57R-2,97	0.24	110	1161	51.05	1.20	14.28	11.37	0.21	7.28	12.28	2.12	0.10	0.09	1013	638	99.00
192-1185-A-9R-3,88	0.14	90	1152	51.55	1.32	13.51	12.54	0.23	6.82	11.35	2.52	0.14	0.00	692	3171	98.21

[a] All given glass compositions are an average of five measurements and normalized to 100 wt% total, the standard deviations (1σ) are given in brackets.

The given total refers to the original sum of the measured element oxide concentrations.

The stratigraphic and lithological units after Expedition Scientists 324 (2010) are given in brackets for samples from Ori Massif.

The glass compositions of Ontong Java Plateau basalts are presented in Roberge et al. (2004) and Michael (2000).

*The composition that was used as the starting composition for the modeling.

addition, it has higher K_2O and lower Na_2O concentrations, possibly indicating the source variability between the lavas from the two different massifs.

5.2. Melting Conditions: Assessment from Glass Na_2O and Ca/Al Corrected for Fractionation

In comparison to EPR N-MORBs, basaltic glasses from Site U1347 exhibit the highest FeO, CaO, and CaO/Al_2O_3, and the lowest SiO_2 and Na_2O values at any given MgO. The Tamu Massif lavas (together with the Ori and Shirshov Massif magmas) are, therefore, noticeably different from typical EPR MORBs. In this sense, they closely resemble (with the exception of SiO_2 and TiO_2) compositions of magmatic liquids from the OJP. It is important to note, that Na_2O and FeO contents in the Tamu Massif lavas are situated on the extension of the evolutionary trend defined by OJP basalts, probably indicating the existence of similar melting conditions for these two oceanic plateaus in the western Pacific.

It has been shown (Klein and Langmuir, 1987; Langmuir et al., 1992) that there is a correlation between the melt Fe_8 and Na_8 parameters with depth and degree of partial melting respectively (Fe_8 and Na_8 are values of these oxides calculated for a MgO content of 8 wt% to remove the effect of fractional crystallization). The average Fe_8 and Na_8 calculated for the OJP, and Tamu, Ori, and Shirshov massifs are: 2.1 and 10.5; 1.9 and 10.3; 2.4 and 11; and 2.2 and 10.7 respectively. In this study we used the parameterization proposed by Niu and Batiza (1991) taking Na_8 and Ca_8/Al_8 into account to estimate extents of partial melting. As illustrated in Fig. I.6 the low Na_8 and high Ca_8/Al_8, as well as high Fe_8 (and low Si_8) parameters obtained for Tamu Massif magmas suggest a high melt fraction in the source and the formation of melts at very high pressure. For comparison, EPR N-MORB indicate lower melt fractions (Fig.I.6; only glasses with 7.5-

Part I: Geothermobarometry of Basaltic Glasses from the Tamu Massif, Shatsky Rise Oceanic Plateau

8.5 wt% MgO are selected to minimize the error of fractionation correction). This observation is in agreement with the data of Sano et al. (2012) who demonstrated high $(Ce/Yb)_N$ and $(Sm/Yb)_N$ in normal-type basalts (from all major massifs of Shatsky Rise) and proposed that the melting beneath Shatsky Rise may have started in the garnet stability field, deeper than expected for N-MORB basalts, and stopped at the base of the lithosphere. However, the low Na_8 and high Ca_8/Al_8 obtained in this study is close to that found in OJP and suggest higher degrees of partial melting (20-23%) than those proposed in the previous publication (~15% , Sano et al., 2012).
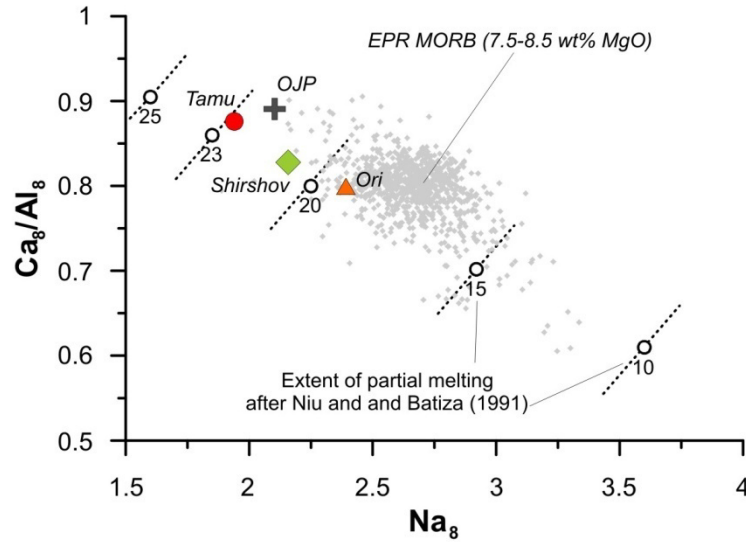
Figure I.6: Fractionation corrected average values of Ca_8/Al_8 versus Na_8 for the Tamu, Ori, and Shirshov Massifs of Shatsky Rise and OJP, in comparison to EPR MORBs with 7.5–8.5 wt% MgO. Ca_8/Al_8 versus Na_8 were calculated following the approach of Niu and Batiza (1991). See text for details.

5.3. Evidence for Low-Pressure Fractionation Processes: Comparison with Experiments

The Harker diagrams (Fig. I.4) show that the tholeiitic rocks collected during Expedition 324 (U147A, U1350A) follow an evolutionary trend controlled by a MORB fractionation path along the *Ol+Plag+Cpx* cotectics. Comparing natural geochemical trends with experimental LLDs enables a rough estimation of the conditions prevailing

during fractional crystallization. For comparison, the results of crystallization experiments obtained at 1 atm by Walker et al. (1979) are shown in Fig. I.4 (black arrow in Fig. I.4). The starting composition investigated by Walker et al. (1979) was a natural glass from the Mid-Atlantic Ridge (MAR, Oceanographer Fracture Zone), which has a composition similar to the most primitive composition of Shatsky Rise (e.g. from Site U1350). However, it is not exactly the same, because FeO is lower and Na_2O is highe). For most major elements, the observed experimental LLDs follow an evolutionary trend parallel to that defined by the natural Shatsky Rise basaltic glasses. Since the experiments of Walker et al. (1979) were performed at 1 atm along the FMQ oxygen buffer, the low pressures during differentiation of the Shatsky Rise magmas seem to be confirmed. Similar LLDs were observed for OJP initial composition at 1 atm and 190 MPa (also dry and FMQ redox conditions, blue arrows in Fig. I.4, Sano and Yamashita, 2004). However the pressure-sensitive CaO/Al_2O_3 ratios observed in the Shatsky Rise magmas exhibit values even higher than those produced at 1 atm. This would imply that the fractionation processes occurred at pressures lower than 1 atm, which is unrealistic and which emphasizes that the compositional differences in the parental melts need to be considered and that simple qualitative comparisons with experiments performed on materials of similar but slightly different compositions may not be conclusive.

5.4.   Evidence for Low-Pressure Fractionation Processes: LLDs for the Most Primitive Shatsky Rise Glass Composition

The evolution of CaO/Al_2O_3 as a function of MgO in the natural U1347 glasses is shown in Fig. I.7a and compared to LLDs calculated assuming ideal fractional crystallization of a less-differentiated Shatsky Rise glass composition (Sample 324-U1350-24R3-76-79 cm, Site U1350). By varying pressure and initial H_2O content, several isobaric LLDs have been simulated. The best fit between natural and modeled LLDs was

obtained at 100 and 200 MPa with 0.3 wt% H_2O in the parental composition (Fig. I.7a). If

the initial H_2O contents are higher, pressure must be lower to produce a better match

between the natural and calculated LLDs (see for example LLD at 200 MPa with 0.6 wt%

H_2O which is off the natural trend, Fig. I.7a). It should be noted that the evolved natural

compositions scatter around the modeled LLDs and form some clusters well correlating

with the groups I-V defined above. This can be attributed to independent evolutionary

histories with different initial crystallization conditions for each chemical group (Fig.

I.7a, see discussion below).

It is emphasized that the initial H_2O content of 0.3 wt% used for the calculations is

realistic, considering that these concentrations have been determined in the quenched

MgO-rich glasses of the Ori Massif (Tab. I.3). Thus, they represent maximum H_2O

concentrations present in the basaltic primary melts. The magmatic origin of the dissolved

H_2O determined in the quenched glasses is confirmed by the general positive correlation

between K_2O and H_2O concentrations in the glasses and the relatively constant H_2O/K_2O

ratio within the groups (see below).

5.5.   Magma Storage Conditions Prior to Eruption: Evidence for Successive

Magma Cycles

Using the inverse modeling approach (Almeev et al., 2008) the *P-T* conditions at

which basaltic melts are in equilibrium with *Ol+Plag+Cpx* were determined for the whole

dataset of glass compositions from Site U1347 (39 samples). H_2O contents determined in

the glasses by FTIR were assumed to be magmatic, thus affecting the mineral

crystallization temperature. The obtained temperatures and pressures range between 1100

and 1150°C and 0.1 and 240 MPa respectively, and are shown in Fig. I.8. On the basis of

the stratigraphic position and major element compositions, distinct *P-T* paths of magma

Part I: Geothermobarometry of Basaltic Glasses from the Tamu Massif, Shatsky Rise Oceanic Plateau
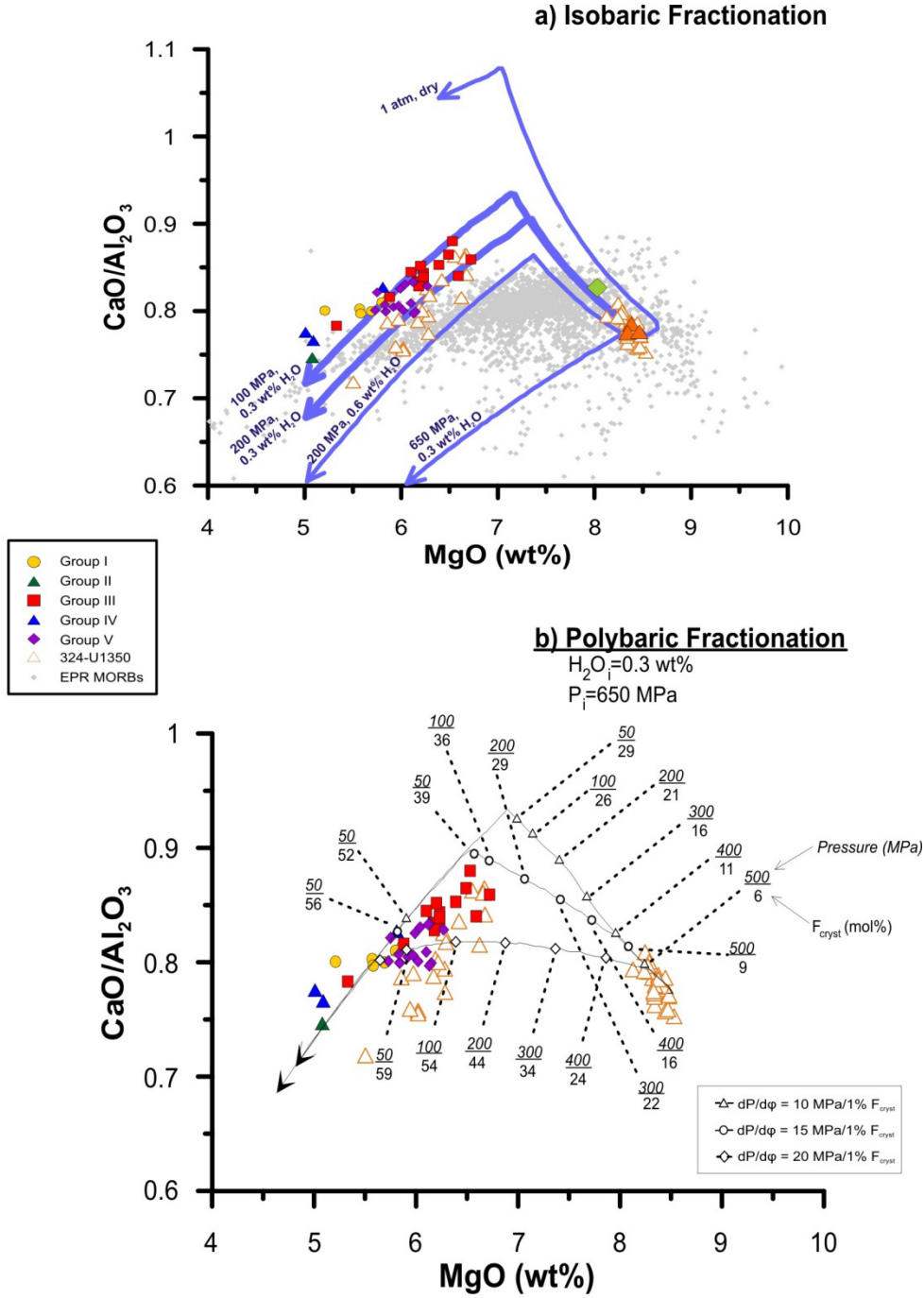
Figure I.7: (a) CaO/Al_2O_3 as a function of MgO content in the glasses from Sites U1347 and U1350. For comparison natural EPR MORB compositions (gray diamonds) are shown. The different symbols correspond to samples of the different Groups (I–V, see also Figure I.2 and text for details). Lines with arrows show the LLDs modeled under isobaric conditions with different initial H_2O contents (fractional crystallization along FMQ calculated using COMAGMAT model (Ariskin and Barmina, 2004)). (b) Symbols are similar to Figure I.7a, but the lines with arrows show the LLDs for polybaric crystallization simulating three different rates of ''magma ascend'': 10 MPa (open diamonds), 15 MPa (circles), and 20 MPa (open triangles) decrease of pressure per 1% crystallization. Numbers along the LLDs indicate the pressure decrease and the increase of degree of crystallization.

Part I: Geothermobarometry of Basaltic Glasses from the Tamu Massif, Shatsky Rise Oceanic Plateau

evolution can be observed for each group. In general, within each group, the estimated *P-T* conditions decrease with the MgO content of glasses (when a representative number of analyses is available) (Fig I.8):

Group I: 110-60 MPa, 1125-1115°C, ~0.3-0.6 wt% H_2O

Group II: ~25 MPa, ~1100°C, ~0.5 wt% H_2O

Group III: 210-90 MPa, 1150-1135°C, ~0.1-0.2 wt% H_2O

Group IV: 60 MPa - 1 atm, 1120-1100°C, ~0.5 wt% H_2O

Group V: 210-40 MPa, 1135-1115°C, ~0.2-0.5 wt% H_2O

Although the calculated temperatures and pressures vary within a relatively small range compared to the error of the method (±15°C, ±50 MPa), clear systematic changes of the thermodynamic conditions are observed within groups I to V (Fig. I.8). These differences in geochemistry and magma storage conditions between the groups along the profile most likely indicate individual crystallization histories for the magma batches which formed each unit. Keeping in mind that only a few glass samples were found in groups II and IV, and therefore *P-T* estimates need to be considered with caution, we can conclude that at least three different cycles can be clearly identified.

Each of those cycles is composed of an initial stage with eruption of less evolved MgO-rich high-*T* magmas stored at deeper levels, and a subsequent shift to more differentiated low-*T* conditions with magmas undergoing crystallization at shallower depths on their way towards the surface (Fig. I.2). For example, the Site U1347 stack of pillow basalts (*Upper to Lower Pillow Lava Section*, Units X, XII, and XIV) recorded two eruptive pulses (groups III and V) with evidence of prolonged polybaric crystallization. These pulses are interrupted by an interval representing a relatively long

period without magmatic activity (intercalated sedimentary layer with an estimated
thickness of ~ 6m). In addition, the second younger pulse is characterized by the eruption
of ~ 15-20°C hotter and slightly drier basaltic melts, indicating the arrival of a new, less-
differentiated magma batch.

The Group IV and Group II samples formed under lower *P-T* conditions and
exhibit major element compositions which indicate that the magmas could represent
evolved final products of the underlying magmatic pulses (Group V and Group III
magma, respectively). In any case, these final Group IV and Group II eruption events
might have been equilibrated at very shallow depths prior to eruption.
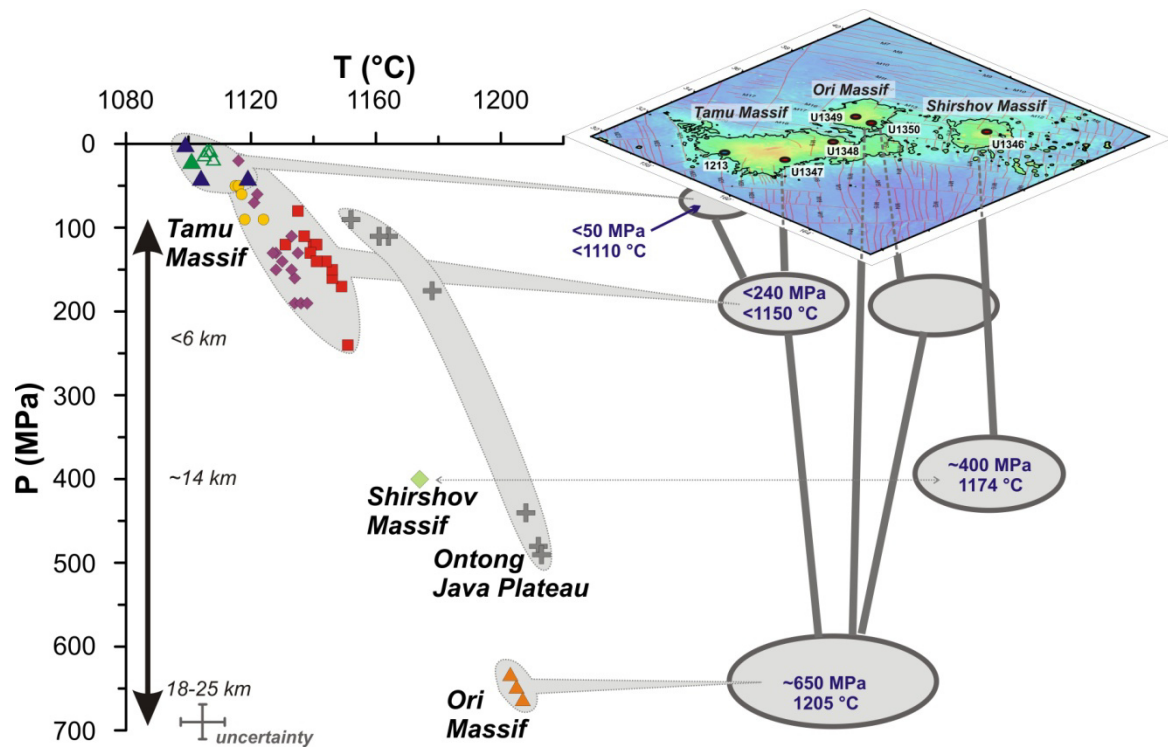
Figure I.8: Modeled *P-T* conditions of *Ol+Plag+Cpx* saturation for individual glass samples. The
different symbols correspond to the different groups from Tamu Massif (I–V, see also Figure I.2) and the
most MgO-rich glasses of Ori Massif (orange triangles), and Shirshov Massif (light green diamond), as well
as glass compositions from OJP (filled crosses, after Roberge et al., 2004). Open green triangles (Group II)
represent glasses determined in Sano et al. (2012). See text for details. On the right hand side, the
topographic map (Expedition 324 Scientists, 2010; Fig. I.1) is shown in a sketch of the potential magma
plumbing system beneath the Shatsky Rise.

Part I: Geothermobarometry of Basaltic Glasses from the Tamu Massif, Shatsky Rise Oceanic Plateau

The Group I magmas represent the third cycle of magmatic activity, when most of the *Upper Massive Basalt Flow 1* and *Upper Massive Basalt Flow 2* (Expedition 324 Scientists., 2010) were continuously erupting with nearly constant major and trace element compositions and minor changes in *P-T* conditions.

Our data are in good agreement with a recent study of (Sano et al., 2011), who presented a petrographic study of basalts from EPR (ODP Hole 1256D). They found cyclic variations in Mg# in bulk magma compositions along the drilled core. Oscillatory zoned *Plag* indicate several injections of magma pulses, followed by differentiation and possibly magma mixing. It was shown that fast-spreading ridges with high melt supply and well established melt lenses are usually characterized by a larger diversity in erupted magma compositions due to the longer retention time (Sinton and Detrick, 1992). This fast spreading systems are also characterized by effective magma mixing of ascending magma strains which cause buffering of differentiation.

In the case of Shatsky Rise, most erupted magmas are evolved with 5 to 6.7 wt% MgO (from both Tamu and Ori Massif), indicating that their parental melts already experienced intense fractionation until they reached the shallow levels where the main differentiation has proceeded. The eruption of primitive basalts (> 8.5 wt% MgO) beneath Tamu was not observed. However, primitive compositions were recorded in the lowest part of the core from Ori massif. Assuming that the Tamu Massif primitive melts are similar to those from Ori, one can see that there is a clear compositional gap between the evolved and less differentiated compositions in the interval of 6.7-8 wt% MgO (Fig. I.3). This indicates that the basaltic magmas from Tamu and Ori Massifs seem to reflect a steady state of the shallow level magma chamber, which is episodically refilled by magmas originated in a deeper magma reservoir. The accompanying mixing wipes out

primitive characteristics of the magmas. This steady state, however, can be interrupted by the eruption of more mafic magmas which is observed for example in the lowest (and hence oldest) part of the core at Ori Massif (Site U1350). Thus, the steady state conditions of the magma chamber(s) are recorded only for the late magmatic stages of the massif growth (Tamu and Ori).

5.6.   Polybaric Trend of Magma Evolution: the Genetic Link Between Tamu and Ori Massif Magmas

Using the inverse modeling approach described above we simulated the conditions of partial crystallization for four less differentiated Shatsky Rise compositions and determined pressures (depth) of a deep magma reservoir discussed above. As shown in Tab. I.3 and Fig. I.8, the most MgO-rich melts from Ori (with 0.3 wt% H_2O) and Shirshov (with 0.56 wt% H_2O) massifs are saturated with *Ol+Plag+Cpx* at ~650 MPa and 1205°C and at ~400 MPa and 1174°C respectively. Taking into account, that the most MgO-rich magmas from Ori Massif have the highest Cl/K ratios, which is indicative of assimilation, those magmas are possibly less hydrous, leading to even higher calculated pressures of partial crystallization (~800 MPa). This implies that, if primitive Shatsky Rise melts are saturated with *Cpx* and accumulated at depth under 600-800 MPa (~18-25 km), their subsequent evolution must have proceeded via polybaric crystallization during magma ascend. Isobaric crystallization of these melts at high pressures results in a strong depletion of CaO/Al_2O_3 in the residual melts which drives the compositions far away from the field of natural Shatsky Rise evolved compositions (note 650 MPa isobar in Fig. I.7a). In contrast, the modeled polybaric fractionation trends calculated for the Ori Massif primitive compositions drive the residual melts towards the differentiated Shatsky Rise glass compositions. These fractionation trends are shown in Fig. I.7b and were modeled applying an initial pressure of 650 MPa and 0.3 wt% H_2O in the melt and three different

Part I: Geothermobarometry of Basaltic Glasses from the Tamu Massif, Shatsky
Rise Oceanic Plateau

rates of pressure decrease per 1% of crystallization (dP/dΦ= 10, 15 and 20 MPa/1%, where P is pressure and Φ is crystallization degree, see also Almeev et al., 2013).

The two-level magma plumbing system proposed for the Shatsky Rise as a complex system of interconnected magma chamber(s) located at 18-25 km and <6 km (Fig. I.8), is similar to that assumed beneath OJP. Using the crystallization models of MELTS (Ghiorso and Sack (1995) and Weaver and Langmuir (1990)) respectively, Farnetani et al. (1996) and Michael (2000) demonstrated that crystallization beneath OJP took place in two stages, with crystallization of parental picritic magmas at Moho levels (800 MPa, Kroenke type Fitton and Godard, 2004, Roberge et al., 2004) followed by final crystallization in the uppermost crust (1atm-200 MPa, Kwaimbaita and Singgalo type, Fitton and Godard, 2004, Roberge et al., 2004, Kinman and Neal, 2006). But, in contrast to Shatsky Rise, the OJP magmas were probably slightly (~ 30°C) hotter (see our original calculations of P-T conditions for representative OJP glasses in Fig. I.8). It should be noted, however, that in both cases, about ~60-65% crystallization from the most primitive (~8-9 wt% MgO) melts is required to attain Shatsky Rise or OJP fractionated compositions with ~5-6 wt% MgO. Such large volumes of precipitated gabbro are responsible for the formation of the thick crust beneath Shatsky Rise and Ontong Java oceanic plateaus.

Part I: Geothermobarometry of Basaltic Glasses from the Tamu Massif, Shatsky
Rise Oceanic Plateau
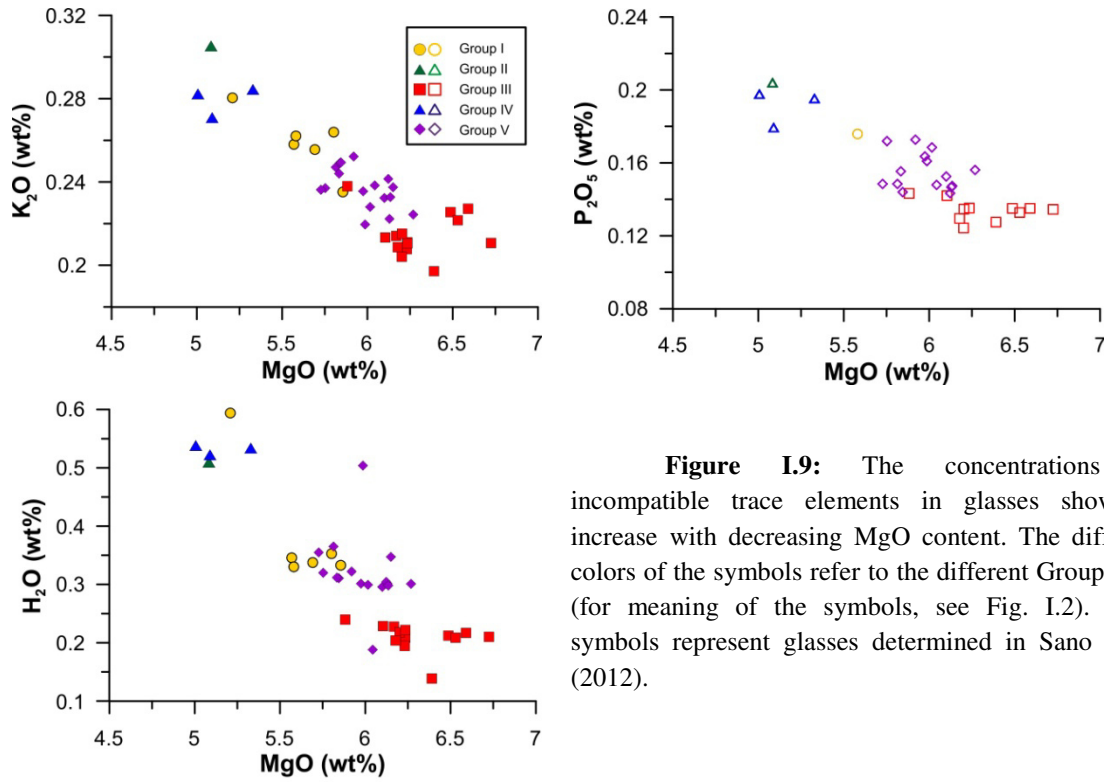
Figure I.9: The concentrations of incompatible trace elements in glasses show an increase with decreasing MgO content. The different colors of the symbols refer to the different Groups I–V (for meaning of the symbols, see Fig. I.2). Open symbols represent glasses determined in Sano et al. (2012).

5.7. Contribution from Trace Element Distribution along the Hole 1347A

We used incompatible trace elements to confirm the genetic relations between the different cycles and groups identified in the Tamu Massif basalts. As displayed in Fig. I.9, the incompatible elements (K_2O, H_2O, P_2O_5) are enriched during differentiation and show a negative correlation with MgO content. This leads to the assumption that all magmas recovered in U1347A are genetically related. However, a detailed analysis of the trace element ratios (Zr/Ti and H_2O/Ce) reveals slight differences between the different groups along the profile (Fig. I.10). Within each cycle the ratio of two incompatible elements such as Zr/Ti is nearly constant, suggesting that the evolution is controlled by crystal fractionation. The same observation is valid for H_2O/Ce (similar incompatibility; Michael, 1988; Hess, 1992). The different Zr/Ti observed for the different groups indicates that the primitive melts for each magma batch were generated under slightly

Part I: Geothermobarometry of Basaltic Glasses from the Tamu Massif, Shatsky Rise Oceanic Plateau

different melting conditions (melt fraction, *P-T* melting conditions) and that the primary melt H_2O content may have been different (different H_2O/Ce ratios; Fig. I.10). It is emphasized that the H_2O/Ce range determined in this study is in the same range as that observed in the Pacific region (between 155 and 213 ±40 for each region; Michael, 1995). Thus, if the differences seen in magmas from the different magmatic episodes along the Hole U1347A do not result from small-scale primitive magma variability (as a result of
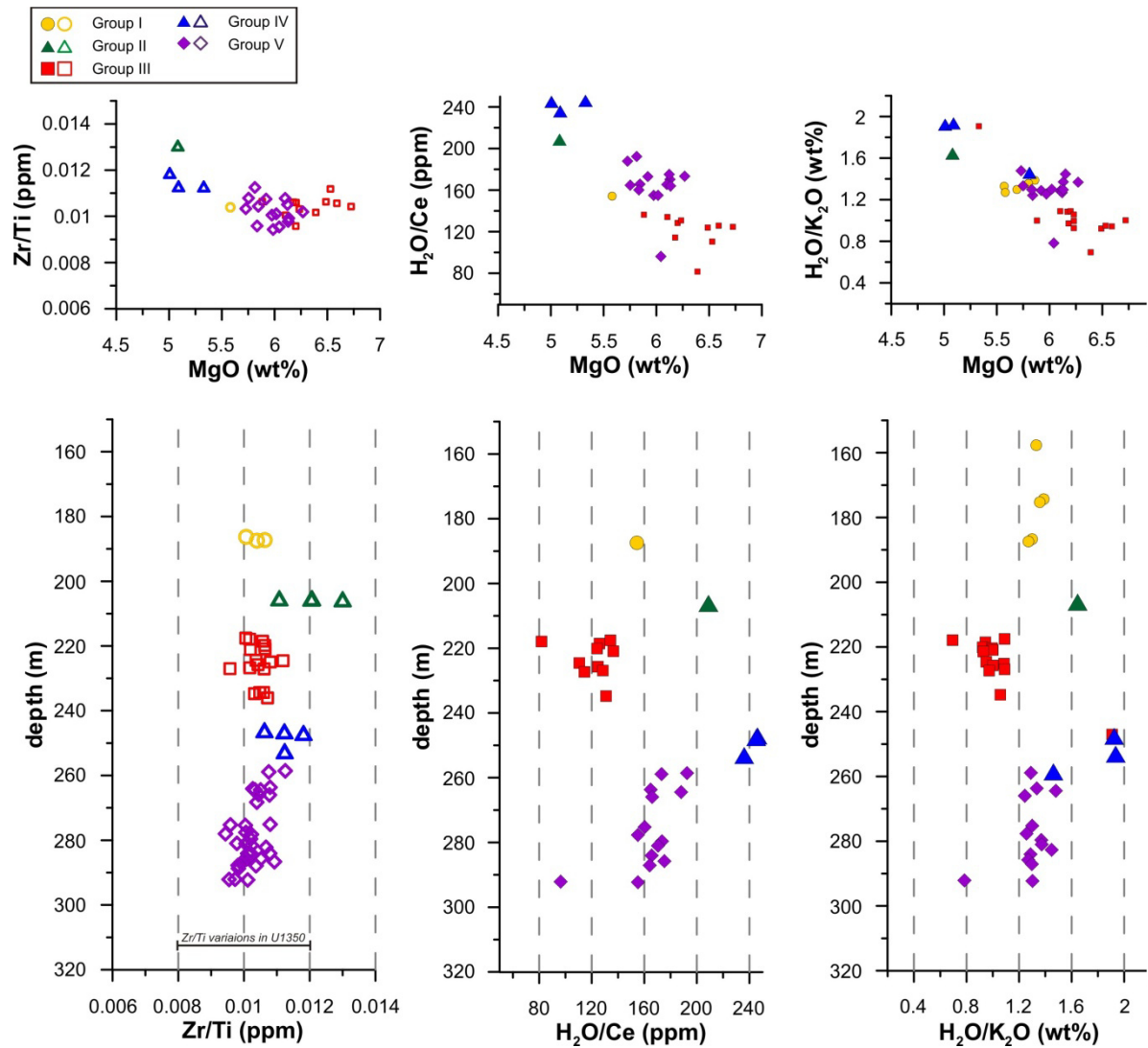
Figure I.10: Evolution of the Zr/Ti, H_2O/Ce, and H_2O/K_2O ratios along the U1347 profile. The Ti, Ce, and Zr concentrations in glasses analyzed by Sano et al. (2012) were used to calculate the ratios. The H_2O and K_2O concentrations are from glasses in this study. It is emphasized that the ratios were determined using samples collected at a very similar depth, but which were not identical (it is assumed that both samples represent the same lava flow). Symbols as in Fig I.2.

slightly different sources), these magmas should have originated in the same source reservoir, where the *P-T* conditions as well as parental melt H_2O content must have been different.

6. CONCLUSIONS

Our new dataset from Site 1347 complements previous data from Sano et al. (2012) and shows that the basaltic samples from Tamu Massif are located within the compositional range of global N-MORB. They are also located on the trend defined by basaltic magmas from other LIP, e.g. Ontong Java Plateau. Basaltic magmas from Site U1347, considered together with less-differentiated basalts from Site U1350, range within the EPR MORB field and follow a common tholeiitic trend of magma differentiation. Fractionation-corrected low Na_2O and high FeO contents in the Tamu Massif magma compositions can be attributed to higher melt fractions in the source (~20-23%) produced at depth within the garnet stability field. We have identified several compositional groups along the core of Site U1347, which may be related to small scale source variability and/or to differences in melting conditions. The Tamu Massif magmas were stored in magma chambers at pressures below 200 MPa and differentiated enroute to the surface. We identified at least two complete magmatic cycles comprised of (1) the arrival of less evolved magmas originating in magma reservoir(s) in the lower crust (18-24 km), (2) their subsequent polybaric crystallization in the course of the magma ascend, accumulation and further evolution within shallow magma chambers (<6 km) followed by eruption and (3) a time of inactivity. Occasionally, the primitive magmas could also reach the surface from depth without significant modification (at least for Ori and Shirshov Massifs these magmas have been recorded in cores). Within each magmatic pulse, in shallow magma chambers we also observed changes in magma storage conditions from ~

200 MPa to 1 atm and from ~ 1150 to ~ 1100°C, which is recorded in the chemistry of basaltic glasses. These very low pressures of partial crystallization (1 atm - 50 MPa) obtained for ~20% of the samples from Tamu massif together with their very low CO_2 contents indicate very shallow depths of Shatsky Rise magma eruption, which is in a good agreement with on-board studies of sedimentary layers which contain evidences of shallow submarine or even subaerial conditions. Although the absolute depth and temperatures of partial crystallization determined for the lavas of Shatsky Rise and Ontong Java plateaus are slightly different, both plateaus exhibit the presence of deep and shallow magma reservoirs with extensive crystallization, suggesting similarity in the construction mechanism of the ocean plateau lithosphere.

7.   ACKNOWLEDGMENTS

8.   REFERENCES

Almeev, R. R., Holtz, F., Koepke, J., Parat, F. & Botcharnikov, R. E. (2007), The effect of H_2O on olivine crystallization in MORB: Experimental calibration at 200 MPa. American Mineralogist, 92(4), 670-674, doi:10.2138/am.2007.2484

Almeev, R., Holtz, F., Koepke, J., Haase, K., and Devey, C. (2008), Depths of partial crystallization of H_2O-bearing MORB: Phase equilibria simulations of basalts at the MAR near Ascension Island (7-11 degrees S), Journal of Petrology, 49(1), 25-45, doi:10.1093/petrology/egm068.

Part I: Geothermobarometry of Basaltic Glasses from the Tamu Massif, Shatsky Rise Oceanic Plateau

Almeev, R. R., Holtz, F., Koepke, J. & Parat, F. (2012), Experimental calibration of the effect of H_2O on plagioclase crystallization in basaltic melt at 200 MPa, American Mineralogist, 97(7), 1234-1240, doi:10.2138/am.2012.4100

Almeev, R.R., Ariskin, A.A., Kimura, J.-I. and Barmina, G. (2013), The role of polybaric crystallization in genesis of andesitic magmas: phase equilibria simulations of the Bezymianny volcanic subseries, Journal of Volcanology and Geothermal Research, (in press), doi:10.1016/j.jvolgeores.2013.01.004

Ariskin, A.A., and Barmina, G.S. (2004), COMAGMAT: Development of a magma crystallization model and its petrological Applications, Geochemistry International, 42, 1-157.

Beattie, P., Ford, C., and Russell, D. (1991), Partition coefficients for olivine-melt and orthopyroxene-melt systems, Contributions to Mineralogy and Petrology, 109(2), 212-224, doi:10.1007/BF00306480

Clouard, V. r., and A. Bonneville (2001), How many Pacific hotspots are fed by deep-mantle plumes?, Geology, 29(8), 695-698, doi:10.1130/0091-7613(2001)029<0695:HMPHAF>2.0.CO;2

Coffin, M.F., and Eldholm, O. (1994), Large Igneous Provinces - crustal structure, dimensions, and external consequences. Reviews of Geophysics, 32(1), 1-36. doi:10.1029/93RG02508

Danyushevsky, L. V., Eggins, S. M., Falloon, T. J. & Christie, D. M. (2000), H_2O Abundance in Depleted to Moderately Enriched Mid-ocean Ridge Magmas; Part I: Incompatible Behaviour, Implications for Mantle Storage, and Origin of Regional Variations, Journal of Petrology, 41(8), 1329-1364, doi:10.1093/petrology/41.8.1329

Danyushevsky, L.V. (2001), The effect of small amounts of H_2O crystallisation of mid-ocean ridge and backarc basin magmas, Journal of Volcanology and Geothermal Research, 110(3-4), 265-280, doi:10.1016/S0377-0273(01)00213-X

Den, N., Ludwig, W.J., Murauchi, S., Ewing, J.I., Hotta, H., Edgar, N.T., Yoshii, T., Asanuma, T., Hagiwara, K., Sato, T. and Ando, S. (1969), Seismic-refraction measurements in the Northwest Pacific Basin, Journal of Geophysical Research, 74(6), 1421-1434, doi:10.1029/JB074i006p01421

Duncan, R.A., Richards, M.A. (1991), Hotspots, mantle plumes, flood basalts, and true polar wander, Reviews of Geophysics, 29, doi:10.1029/90RG02372

Expedition 324 Scientists. (2010), Testing plume and plate models of ocean plateau formation at Shatsky Rise, northwest Pacific Ocean, IODP Prel. Rept, 324, doi:10.2204/iodp.pr.324.2010

Farnetani, C.G., Richards, M.A. and Ghiorso, M.S., (1996), Petrological models of magma evolution and deep crustal structure beneath hotspots and flood basalt provinces, Earth and Planetary Science Letters, 143(1-4), 81-94. doi:10.1016/0012-821X(96)00138-0

Part I: Geothermobarometry of Basaltic Glasses from the Tamu Massif, Shatsky Rise Oceanic Plateau

Fine, G., and E. Stolper (1986), Dissolved carbon dioxide in basaltic glasses: concentrations and speciation,. Earth and Planetary Science Letters, 76(3-4), 263-278, doi:10.1016/0012-821X(86)90078-6

Fitton, J. G., and M. Godard (2004), Origin and evolution of magmas on the Ontong Java Plateau, Geological Society, London, Special Publications, 229(1), 151-178, doi: 10.1144/GSL.SP.2004.229.01.10

Ford, C.E., Russell, D.G., Craven, J.A., and Fisk, M.R. (1983), Olivine liquid equilibria - temperature, pressure and composition dependence of the crystal liquid cation partition-coefficients for Mg, Fe^{2+}, Ca and Mn, Journal of Petrology, 24(3), 256-265, doi:10.1093/petrology/24.3.256

Foulger, G.R. (2007), The "plate" model for the genesis of melting anomalies, The Geological Society of America, Special Paper, 430, doi:10.1130/2007.2430(01)

Ghiorso, M.S., and Sack, R.O. (1995), Chemical Mass Transfer in Magmatic Processes, IV. A Revised and Internally Consistent Thermodynamic Model for the Interpolation and Extrapolation of Liquid-Solid Equilibria in Magmatic Systems at Elevated Temperatures and Pressures, Contributions to Mineralogy and Petrology, 119, 197-212

Herzberg, C. (2004), Partial crystallization of mid-ocean ridge basalts in the crust and mantle, Journal of Petrology, 45(12), 2389-2405, doi:10.1093/petrology/egh040

Hess, P.C. (1992), Phase equilibria constraints on the origin of ocean floor basalts, In: J. Morgan, D. Blackman and J. Sinton (Editors), Mantle flow and melt generation at Mid-Ocean Ridges. Geophysical Monograph. American Geophysical Union, pp. 67-102, doi:10.1029/GM071p0067

Jambon, A., and J. L. Zimmermann (1990), Water in oceanic basalts – evidence for dehydration of recycled crust, Earth and Planetary Science Letters, 101(2-4), 323-331, doi:10.1016/0012-821X(90)90163-R

Jarosewich, E., Nelen, J.A., Norberg, J.A. (1980), Reference Samples for Electron Microprobe Analysis, Geostandards Newsletter, 4(1), 43-47, doi:10.1111/j.1751-908X.1980.tb00273.x

Kinman, W.S. and Neal, C.R. (2006), Magma evolution revealed by anorthite-rich plagioclase cumulate xenoliths from the Ontong Java Plateau: Insights into LIP magma dynamics and melt evolution, Journal of Volcanology and Geothermal Research, 154 (1–2), 131 - 157, doi:10.1016/j.jvolgeores.2005.09.024

Klein, E. M., and C. H. Langmuir (1987), Global correlations of ocean ride basalt chemistry with axial depth and crustal thickness, Journal of Geophysical Research-Solid Earth and Planets, 92(B8), 8089-8115, doi:10.1029/JB092iB08p08089

Korenaga, J. and Sager, W.W., (2012), Seismic tomography of Shatsky Rise by adaptive importance sampling, Journal of Geophysical Research: Solid Earth, 117(B8), B08102, doi:10.1029/2012JB009248

Langmuir, C. H., Klein, E. M. & Plank, T. (1992), Petrological systematics of midocean ridge basalts - constraints on melt generation beneath ocean ridges, in Mantle

Part I: Geothermobarometry of Basaltic Glasses from the Tamu Massif, Shatsky Rise Oceanic Plateau

Flow and Melt Generation at Mid-Ocean Ridges, edited by J. P. Morgan, et al., pp. 183-280, Amer Geophysical Union, Washington, doi:10.1029/GM071p0183

Mahoney, J. J., and K. J. Spencer (1991), Isotopic evidence for the origin of the Manihiki and Ontong Java oceanic plateaus, Earth and Planetary Science Letters, 104(2-4), 196-210, doi:10.1016/0012-821X(91)90204-U

Mahoney, J. J., Sinton, J. M., Kurz, M. D., Macdougall, J. D., Spencer, K. J. & Lugmair, G. W. (1994), Isotope and trace element characteristics of a super-fast spreading ridge: East Pacific rise, 13-23°S, Earth and Planetary Science Letters, 121(1-2), 173-193, doi:10.1016/0012-821X(94)90039-6

Mahoney, J.J., Duncan, R.A., Tejada, M.L.G., Sager, W.W., and Bralower, T.J. (2005), Jurassic-Cretaceous boundary age and mid-ocean-ridge-type mantle source for Shatsky Rise, Geology, 33(3), 185-188, doi:10.1130/G21378.1

Médard, E., and T. L. Grove (2008), The effect of H_2O on the olivine liquidus of basaltic melts: experiments and thermodynamic models, Contributions to Mineralogy and Petrology, 155(4), 417-432, doi:10.1007/s00410-007-0250-4

Michael, P. J., and R. L. Chase (1987), The influence of primary magma composition, H_2O and pressure on midocean ridge basalt differentiation, Contributions to Mineralogy and Petrology, 96(2), 245-263, doi:10.1007/BF00375237

Michael, P.J. and Cornell, W.C., (1998), Influence of spreading rate and magma supply on crystallization and assimilation beneath mid-ocean ridges: Evidence from chlorine and major element chemistry of mid-ocean ridge basalts, Journal of Geophysical Research, 103(B8), 18325-18356, doi:10.1029/98JB00791

Michael, P.J. (1988), Partition-Coefficients for Rare-Earth Elements in Mafic Minerals of High Silica Rhyolites - the Importance of Accessory Mineral Inclusions, Geochimica et Cosmochimica Acta, 52(2): 275-282, doi:10.1016/0016-7037(88)90083-X

Michael, P. (1995), Regionally distinctive sources of depleted MORB: Evidence from trace elements and H_2O, Earth and Planetary Science Letters, 131(3-4), 301-320, doi:10.1016/0012-821X(95)00023-6

Michael, P. J. (2000), Implications for magmatic processes at Ontong Java Plateau from volatile and major element contents of Cretaceous basalt glasses, Geochemistry, Geophysics, Geosystems, 1(12), doi:10.1029/1999GC000025

Morgan, W. J. (1972), Deep Mantle Convection Plumes and Plate Motions, AAPG Bulletin, 56(2), 203-213.

Nakanishi, M., Sager, W.W., and Klaus, A. (1999), Magnetic lineations within Shatsky Rise, northwest Pacific Ocean: Implications for hot spot-triple junction interaction and oceanic plateau formation, J. Geophys. Res., 104(B4), 7539-7556, doi:10.1029/1999JB900002

Niu, Y., Batiza, R. (1991), An empirical method for calculating melt compositions produced beneath mid-ocean ridges: Application for axis and off-axis (seamounts) melting, Journal of Geophysical Research: Solid Earth, 96 (B13), 2156-2202, doi:10.1029/91JB01933

Part I: Geothermobarometry of Basaltic Glasses from the Tamu Massif, Shatsky
Rise Oceanic Plateau

Richards, M. A., Jones D.L., Duncan R.A., Depaolo D.J., (1991), A Mantle Plume Initiation Model for the Wrangellia Flood Basalt and Other Oceanic Plateaus, Science, 254(5029), 263-267, doi:10.1126/science.254.5029.263

Roberge, J., White R.V., Wallace P.J., (2004), Volatiles in submarine basaltic glasses from the Ontong Java Plateau (ODP Leg 192): implications for magmatic processes and source region compositions, Geological Society, London, Special Publications, 229(1), 239-257, doi:10.1144/GSL.SP.2004.229.01.14

Sack, R.O., Walker, D. and Carmichael, I.S.E. (1987), Experimental petrology of alkalic lavas: constraints on cotectics of multiple saturation in natural basic liquids, Contributions to Mineralogy and Petrology, 96(1): 1-23, doi:10.1007/BF00375521

Sager, W.W., Kim, J., Klaus, A., Nakanishi, M., and Khankishieva, L.M. (1999), Bathymetry of Shatsky Rise, northwest Pacific Ocean: Implications for ocean plateau development at a triple junction, J. Geophys. Res., 104(B4), 7557-7576, doi:10.1029/1998JB900009

Sano, T., and Yamashita, S. (2004), Experimental petrology of basement lavas from Ocean Drilling Program Leg 192: implications for differentiation processes in Ontong Java Plateau magmas, Geological Society, London, Special Publications, 229(1), 185-218.

Sano, T., Sakuyama, T., Ingle, S., Rodriguez, S., Yamasaki, T. (2011), Petrological relationships among lavas, dikes, and gabbros from Integrated Ocean Drilling Program Hole 1256D: Insight into the magma plumbing system beneath the East Pacific Rise, Geochemistry Geophysics Geosystems, 12, 6, doi:10.1029/2011GC003548

Sano, T., Shimizu, K., Ishikawa, A., Senda, R., Chang, Q., Kimura, J.I., Widdowson, M., and Sager, W.W. (2012), Variety and origin of magmas on Shatsky Rise, northwest Pacific Ocean, Geochemistry Geophysics Geosystems, 13, 25, doi:10.1029/2012GC004235

Sinton, J. M., Detrick, R. S. (1992), Mid-ocean ridge magma chambers, Geophys. Res., 97 (B1), 156-202, doi:10.1029/91JB02508

Staudigel, H., and S. R. Hart (1983), Alteration of basaltic glass – mechanisms and significance for the oceanic-crust seawater budget, Geochimica Et Cosmochimica Acta, 47(3), 337-350. doi:10.1016/0016-7037(83)90257-0

Stolper, E. (1982), Water in silicate glasses: An infrared spectroscopic study, Contributions to Mineralogy and Petrology, 81(1), 1-17, doi:10.1007/BF00371154

Tatsumi, Y., Shinjoe, H., Ishizuka, H., Sager, W. W. & Klaus, A. (1998), Geochemical evidence for a mid-Cretaceous superplume, Geology, 26(2), 151-154, doi:10.1130/0091-7613(1998)026<0151:GEFAMC>2.3.CO;2

Villiger, S., Muentener, O., and Ulmer, P. (2007), Crystallization pressures of mid-ocean ridge basalts derived from major element variations of glasses from equilibrium and fractional crystallization experiments, Journal of Geophysical Research-Solid Earth, 112(B1), doi:10.1029/2006JB004342

Part I: Geothermobarometry of Basaltic Glasses from the Tamu Massif, Shatsky Rise Oceanic Plateau

Walker, D., Shibata, T., and Delong, S.E. (1979), Abyssal tholeiites from the ceanographer fracture-zone . 2. Phase-equilibria and mixing, Contributions to Mineralogy and Petrology, 70(2), 111-125, doi:10.1007/BF00374440

Weaver, J.S., Langmuir, C.H.(1990), Calculation of phase equilibrium in mineral-melt systems, Computers & Geosciences, 16 (1), 1-19, doi:10.1016/0098-3004(90)90074-4

Yang, H.J., Kinzler, R.J., and Grove, T.L. (1996), Experiments and models of anhydrous, basaltic olivine-plagioclase-augite saturated melts from 0.001 to 10 kbar, Contributions to Mineralogy and Petrology, 124(1), 1-18, doi:10.1007/s004100050169

Zhang, Y.-S., and Tanimoto, T. (1992), Ridges, hotspots and their interaction as observed in seismic velocity maps, Nature, 355(6355), 45-49, doi:10.1038/355045a0

Dissertation of Anika Husen

Part II: The Role of H$_2$O and Pressure on Multiple Saturation and Liquid Lines of
Descent in Basalts from the Shatsky Rise

Part II: The Role of H$_2$O and Pressure on Multiple Saturation and Liquid Lines of Descent in Basalts from the Shatsky Rise

A modified version of this part is submitted to the *Journal of Petrology*: The Role of H$_2$O and Pressure on Multiple Saturation and Liquid Lines of Descent in Basalts from the Shatsky Rise. Husen, A., Almeev, R. R., Holtz, F.

1.   ABSTRACT

Crystallization relations of three synthetic starting compositions (AH6: 8.6 wt% MgO, AH3: 8.0 wt% MgO, AH5: 6.4 wt% MgO) representing evolved and primitive tholeiitic basalts from the Shatsky Rise oceanic plateau, were experimentally determined in internally heated pressure vessels (IHPV) at 1075-1225°C and 100, 200, 400, and 700 MPa. We used graphite-platinum double capsules and Fe pre-saturated AuPd capsules in order to avoid Fe-loss. Graphite-platinum double capsules led to (1) redox conditions in IHPV buffered along the C-CO (carbon–carbon oxide) oxygen buffer and (2) nearly anhydrous conditions (<0.15 wt% H$_2$O). In Fe pre-saturated AuPd capsules, we attained fO$_2$ around the FMQ buffer and slightly higher H$_2$O contents (0.4-1.1 wt%).

Part II: The Role of H_2O and Pressure on Multiple Saturation and Liquid Lines of Descent in Basalts from the Shatsky Rise

At almost anhydrous conditions, the most MgO-rich basalt AH6 shows the crystallization sequence olivine, olivine+plagioclase, and olivine+plagioclase+ clinopyroxene (*Ol+Plag+Cpx*) at all investigated pressures. This was also observed in the intermediate composition AH3 at 100, 200 and 400 MPa. In contrast, at 700 MPa, this sequence was completely reversed in the basalt AH3 and the conditions of multiple saturation were assumed to be reached at 400 MPa at nearly dry conditions. In the evolved basalt AH5, *Cpx* crystallized first at all experimental conditions, followed by *Plag*. The subsequent *Ol* crystallization was observed only at pressures of 100, 200 and 400 MPa. The presence of small amounts of H_2O did not change the crystallization sequences but additionally magnetite (*Mag*) was observed in the latest stage of crystallization ($F_{cryst}>0.6$). The *Cpx* proportion is strongly increasing with increasing pressure and with the addition of H_2O, when phase assemblages of similar crystallization degree are compared.

Our experiments demonstrate that the presence of small amounts of H_2O (~ 0.4 – 1.1 wt% H_2O) affect significantly the crystallization of *Ol*, *Plag* and *Cpx* and with this the liquid lines of descent (LLDs). The significance of small amounts of melt H_2O is emphasized, because we show that the effect of the addition of 0.4 wt% H_2O on the LLDs is almost similar to what would be caused by a pressure increase of ~300 MPa. Furthermore, we demonstrate that H_2O contents in mid-ocean ridge basalt (MORB) melts cannot be neglected, because recent experimental studies under anhydrous conditions led to SiO_2 depletion during differentiation (e.g. Bender et al., 1978; Whitaker et al., 2007; Grove et al., 1992) and therefore could not reproduce the typical tholeiitic differentiation trend. The comparison of the experimental residual liquid compositions saturated with *Ol+Plag+Cpx* to natural Shatsky Rise basaltic glass compositions, implies that natural magmas were equilibrated at low pressures (<200 MPa). However, the LLDs produced

from different starting compositions but at similar pressures demonstrate that higher pressures are needed to reproduce the natural magmatic trends. This implies that the natural trends are most likely formed as a result of polybaric, rather than isobaric fractionation, and that the crystallization might have proceeded under slightly hydrous conditions.

2.   INTRODUCTION

Many experimental studies on MORB-like compositions were conducted in the last decades. Those provide a large dataset which helps understanding the differentiation mechanisms within the oceanic crust beneath mid-ocean ridges (MOR). Additionally they are used as a database for thermodynamic models, which provide a sufficient method for the estimation of differentiation temperatures and pressures (*P-T*). However, the available dataset is limited by two main factors: (1) pressure and (2) H$_2$O activity.

(1) Pressure: Considering that most fractionation at MOR occurs within the oceanic crust (1-6 km, 50-200 MPa, e.g. Purdy et al., 1992), this pressure range is barely represented by the experimental database. Most experiments were conducted at atmospheric pressure or at higher pressures using piston cylinders (>1 GPa). Mainly the 1 atm experiments were used for implications on MOR systems, assuming that the small pressure difference would have a minor effect on the results (Walker et al., 1979). In contrast to this, most geobarometers are calibrated in a much higher pressure range, which is not relevant for upper crustal levels. They are mainly based on piston cylinder experiments, like e.g. Herzberg (2004), Villiger et al. (2007), and Yang et al. (1996). The extrapolation of those barometers lead to valuable data, but with low accuracy (±100-200 MPa), because, as shown e.g. by Bender et al. (1978), pressure has a strong influence on

Part II: The Role of H_2O and Pressure on Multiple Saturation and Liquid Lines of
Descent in Basalts from the Shatsky Rise

Cpx stability, causing earlier crystallization (at higher temperatures) of *Cpx* at higher

pressures.

(2) H_2O: Most experiments were conducted without cosidering the role of H_2O

contents. Typically, H_2O concentrations in MORBs are low (<0.1-0.8), as presented e.g.

by Michael (1995), Danyushevsky (2001), and Sobolev & Chaussidon (1996). However,

already trace amounts of H_2O have a significant effect on the phase stabilities of mineral

phases (e.g. Michael & Chase, 1987; Danyushevsky et al., 1996; Almeev et al., 2007;

Almeev et al., 2012). This is not taken into account in 1 atm experiments, because

volatiles are almost not soluble in melts at such conditions. In contrast, small amounts of

H_2O are always generated during high pressure experiments using noble metal capsules

(also in nominally dry experiments; Holtz et al., 2001; Truckenbrodt & Johannes, 1999).

These are usually not determined and thus neglected (Sano & Yamashita, 2004).

With our new data, we complement the database for intermediate pressure

conditions. We provide data showing the influence of pressure and H_2O on phase

equilibria in a range, which is relevant to crustal processes. With our higher pressure

experiments (400 and 700 MPa), we simulate conditions for regions where the oceanic

crust is thickened, like at oceanic plateaus. We applied an experimental approach on

representative compositions of the Shatsky Rise oceanic plateau to contribute new data to

the characterization of the magma storage conditions beneath the plateau. Our

experiments simulate isobaric differentiation in the Shatsky Rise basaltic compositions at

different pressures while controlling the H_2O concentrations in a very low range (<1

wt%). The results were used (1) for the characterization of the effect of pressure and H_2O

on phase stabilities and LLDs, and (2) for comparison with natural MORBs, including a

Dissertation of Anika Husen

Part II: The Role of H₂O and Pressure on Multiple Saturation and Liquid Lines of
Descent in Basalts from the Shatsky Rise

more detailed discussion of the Shatsky Rise basaltic glasses, to gain information about their magma storage conditions.

3.   SHATSKY RISE

The Shatsky Rise has a volume of 4.3 x 106 km^3 (Sager et al., 1999) and consists of three different Massifs (Tamu, Ori and Shirshov Massifs). The emplacement of those large volumes of basaltic magmas result in massive volcanic complexes and locally thickened crust. Korenaga & Sager (2012) describe a crustal model with more than 30 km thickness of the oceanic crust at Shatsky Rise. After Sager et al. (2013) the Tamu Massif is formed rapidly in a short period, leading to the assumption that the whole Massif was formed by one single volcano, which is assumed to be the largest on earth.

The basaltic glass compositions recovered during Integrated Ocean Drilling Program (IODP) Expedition 324 on the Shatsky Rise oceanic plateau were described e.g. by Sano et al. (2012) and Husen et al. (2013) and their chemical compositions are illustrated in Fig. II.1. They are tholeiitic basalts ranging in the field of East Pacific Rise (EPR) MORBs, although they have distinctively high FeO concentrations and are low in Na₂O and SiO₂. Additionally, the more evolved Shatsky Rise lavas (MgO<6.5 wt%) have the highest CaO/Al₂O₃ ratios known for MORBs. Compared to other oceanic plateaus e.g. the Ontong Java Plateau (OJP) and Kerguelen, the Shatsky Rise basalts follow similar crystallization trends (e.g. Expedition 324 Scientists, 2010; Sano et al., 2012; Husen et al., 2013). In general, previous studies (Sano et al., 2012; Husen et al., 2013) showed that the magmas erupted on Shatsky Rise have differentiated in shallow depth at *Ol+Plag+Cpx* cotectics.

Part II: The Role of H$_2$O and Pressure on Multiple Saturation and Liquid Lines of Descent in Basalts from the Shatsky Rise

Figure 1.

Caption →

Dissertation of Anika Husen
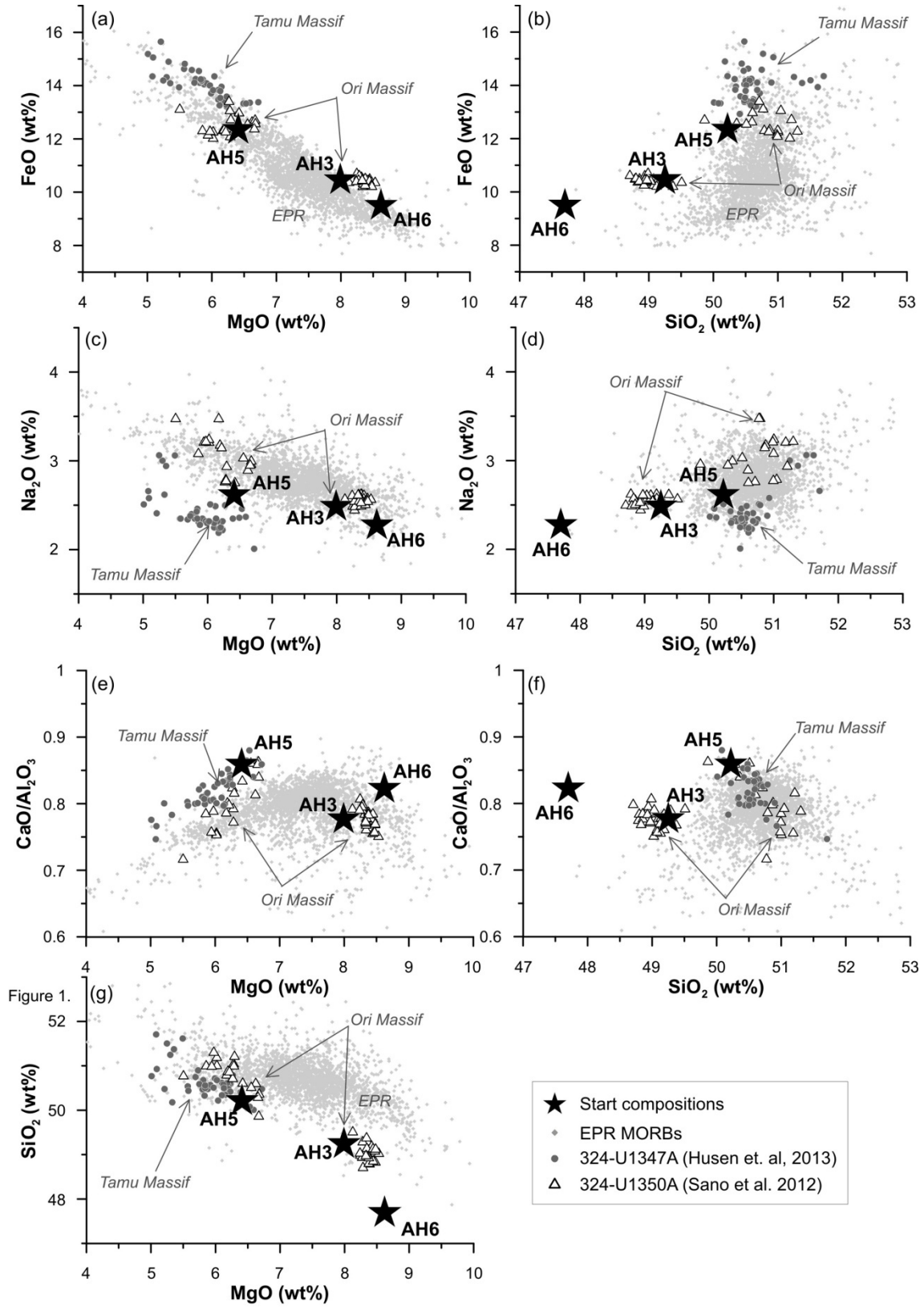
Part II: The Role of H$_2$O and Pressure on Multiple Saturation and Liquid Lines of
Descent in Basalts from the Shatsky Rise

Figure II.1: Displayed are the basaltic glass compositions from the Shatsky Rise and the whole range of natural EPR MORBs (grey points, PetDB, http://www.earthchem.org/petdb). Shatsky compositions from Tamu (Site U1347A – dark grey dots, Husen et al., 2013) and Ori Massif (Site U1350A – open triangles, Sano et al., 2012) are distinguished by symbols. For comparison also the synthetic starting compositions (AH3, AH5, AH6, black stars) used in this experimental study are displayed.

The water concentrations in the basaltic glasses, determined by (Husen et al., 2013), are low and range between 0.2 and 0.6 wt% H$_2$O (H$_2$O increases with progressive differentiation), which resembles typically low values compared to global MORBs (Danyushevsky et al., 2000; Sobolev & Chaussidon, 1996).

However, the Shatsky Rise oceanic crust is strongly thickened causing a long distance between the upper lithospheric mantle and the sea floor and thus, intense fractionation during ascent. Thermodynamic modeling using the COMAGMAT program (Almeev & Ariskin, 1996; Ariskin, 1999; Ariskin & Barmina, 2004), applying the approach of Almeev et al. (2008) indicated a multi level magma plumbing system, where fractionation occurred in different crustal levels (Husen et al., 2013), beneath Shatsky Rise.

4.   METHODS

4.1.   Starting Materials

The three starting materials used in our experiments are synthetic analogues of natural Shatsky Rise basaltic glasses recovered during IODP Expedition 324 (Expedition 324 Scientists, 2010). The most MgO-rich starting glass AH6 (8.6 wt% MgO), represents

an average composition of 15 *Ol*-hosted melt inclusions from moderately altered *Ol*-phyric basalts, cored at the Ori massif (sample 324U1349-12R4/37-39; Almeev et al., 2011). The original partly-crystallized inclusions were re-homogenized to a homogeneous glass by re-heating and quenching. Further, they were corrected to be in equilibrium with the host *Ol* using the Petrolog software (Danyushevsky and Plechov, 2011). The intermediate starting material AH3 (8.0 wt% MgO) is an analogue of the most MgO-rich natural glass recovered at the Ori Massif (sample 324U1350A-24R-3-44/47; Sano et al., 2012). The AH5 starting composition (6.4 wt% MgO) represents the most MgO-rich natural glass compositions cored at the Tamu Massif (sample 324U1347A-19R-1-78/85; Sano et al., 2012). At this massif, only evolved basaltic lavas were found (Sano et al., 2012; Husen et al., 2013).

Each starting glass was prepared from a mixture of pure element oxides (SiO$_2$, TiO$_2$, Al$_2$O$_3$, Fe$_2$O$_3$, MnO, P$_2$O$_5$, Cr$_2$O$_3$) and carbonates (CaCO$_3$, Na$_2$CO$_3$, K$_2$CO$_3$). The Cr$_2$O$_3$ was added only to the most MgO-rich starting material AH6, considering that in the evolved glasses its concentration is negligible. The powders were melted for 3 h in a Pt crucible at 1600°C and 1 atm in air. These melts were quenched to a glass by placing the crucible into a H$_2$O bath. Glasses were ground coarsely (<1mm) and re-melted for another 3 h to ensure the homogeneity of the starting materials. The compositions and homogeneity of the basaltic glasses were verified by electron microprobe (40-80 points). Finally, the glasses were crushed in a mortar and sieved to grain sizes of 75-125μm. The starting compositions are given in Tab. II.1 and are displayed in Fig. II.1 and the following figures as black stars.

Part II: The Role of H_2O and Pressure on Multiple Saturation and Liquid Lines of Descent in Basalts from the Shatsky Rise

Table II.1: compositions of the starting glasses

	AH6	AH3	AH5
SiO_2	47.70	49.25	50.22
TiO_2	0.89	1.45	1.99
Al_2O_3	16.76	15.64	13.74
FeO^T	9.51	10.47	12.36
MnO	0.19	0.17	0.41
MgO	8.62	7.99	6.41
CaO	13.80	12.16	11.81
Na_2O	2.28	2.49	2.62
K_2O	0.10	0.18	0.21
Cr_2O_3	0.09	-	-
P_2O_5	0.05	0.20	0.22
Total	100.0	100.0	100.0
MGN#	0.62	0.58	0.48
CaO/Al_2O_3	0.82	0.78	0.86

Glass measurements in wt%, normalized to
100 wt% total (given total refers original value)

4.2. Experimental Setups

To address the influence of small amounts of H_2O on phase relations, two sets of experiments with different capsule setups were utilized. In the first set, which is defined throughout the paper as "*dry*", the experimental charges were run in graphite-lined Pt double capsules. The top of the graphite capsule was closed with graphite powder to minimize the free volume. As an initial source of a COH-fluid, $Ag_2C_2O_4$ was added to the graphite capsule along with glass powder. The outer Pt-capsule was shut by point welding at both ends. The use of the inner graphite capsule protects the experimental material for Fe-loss to the noble metal capsule (Thompson & Kushiro, 1972) and also leads to almost anhydrous conditions during the experiment due to very low $f$$H_2O$ in the fluid in the presence of graphite (Holloway et al., 1992). Thus, the $f$$O_2$ in these experimental charges was buffered by the COH-fluid and estimated to be around FMQ-1 to FMQ-2 (e.g. Ulmer & Luth, 1991; Jakobsson & Oskarsson, 1994; French & Eugster, 1965). Determinations of Fe-speciation in our superliquidus runs using the colorimetric method described by Schuessler et al. (2008) showed that >90% of the total Fe was present as Fe^{2+} (Tab. II.2). This indicates redox conditions in the *dry* experimental set to be below or around FMQ-1.

Part II: The Role of H_2O and Pressure on Multiple Saturation and Liquid Lines of Descent in Basalts from the Shatsky Rise

In some (failed) experiments we observed pure iron droplets (Fe^0) precipitated from the basaltic melts indicating extremely reducing conditions. These charges were not properly shut by welding, which resulted in maintaining of an atmosphere of carbon and argon (pressure medium, see below) with negligible amounts of H_2 and O_2 in those experiments. The typical range of melt H_2O contents in *dry* experiments range from 0.04 to 0.14 wt%.

For the second set of experiments, which we defined throughout this paper as "*hydrous*", we used conventional $Au_{80}Pd_{20}$ capsules. To avoid the problem of Fe-loss from the experimental charge into the capsule material (Hall et al., 2004), the $Au_{80}Pd_{20}$ tubes were first pre-saturated with Fe, following the procedure from van der Laan & Koster van Groos (1991). The inner surface of the $Au_{80}Pd_{20}$ tubes was coated with Fe using an electroplating bath. The Fe-coated $Au_{80}Pd_{20}$ capsules were further annealed for 12-24 h under reducing Ar-H_2 atmosphere at 950°C and 1 atm. The amount of Fe in the capsule alloy was determined by the mass gain; it varied between 0.2 and 0.3 wt% metallic Fe. The Fe pre-saturated $Au_{80}Pd_{20}$ capsules were loaded with the starting material and $Ag_2C_2O_4$ as a source of a CO_2-rich fluid and shut by point welding.

Before the experiment, all capsules were pre-pressurized at ~50 MPa to check for possible leaks. H_2O was not added into the capsules, however it was generated in the experimental charges due to (1) the reaction of Fe reduction (starting glasses were produced in air logfO_2 = -0.68) and (2) the re-equilibration of small amounts of intrinsic H_2 with the CO_2-fluid. It should be noted that the behavior of H_2O in our experiments is not controlled by fractional crystallization. Similar to the *dry* set of experiments, the melt H_2O is buffered by the fluid phase (COH in *dry* and H_2O-CO_2 in *hydrous* experiments) under experimental conditions. Therefore, due to the positive dependence of H_2O and CO_2 solubilities on pressure, in experiments performed at higher pressures we always

Part II: The Role of H_2O and Pressure on Multiple Saturation and Liquid Lines of
Descent in Basalts from the Shatsky Rise

observed higher melt H_2O contents. The typical range of melt H_2O contents observed in

our *hydrous* experiments range from 0.4-1.1 wt%. The redox conditions in the *hydrous*

experiments were close or slightly above FMQ (based on evaluation of intrinsic redox

conditions in internally heated pressure vessel; Schuessler et al., 2008). Our colorimetric

measurements (Schuessler et al., 2008) of Fe^{2+}/Fe^{total} ratios in the experimental products,

which were run above or close to their liquidus (<15 $\%F_{crystal}$), show Fe^{2+} contents of 74-

83%. This corresponds to an fO_2 between FMQ-1 and FMQ+1.5.

4.3.   Experimental Facility and Conditions

The experiments were performed at pressures of 100, 200, 400, and 700 MPa and

at temperatures between 1050°C and 1225°C with 25°C steps (1125-1225°C for *dry*

experiments, 1050-1150°C for *hydrous* experiments). They were conducted in an

internally heated pressure vessel (IHPV) pressurized with Ar (IHPV without Shaw

membrane). A detailed description of the apparatus is given in Berndt et al. (2002). The

pressure was measured using a strain gauge manometer with an uncertainty of about 2

MPa. The pressure varied by ≤3 MPa during the experiments. The temperature was

measured with four unsheathed S-type ($Pt-Pt_{90}Rh_{10}$) thermocouples over a length of about

30 mm. In the most experimental runs the temperature varied by ±5°C. The temperature

was continuously recorded using the software iTools. In each experiment, the three

starting materials were run simultaneously. The capsules were first brought to the desired

pressure (e.g. 100 or 700 MPa) and then heated isobarically from room temperature to the

experimental run temperature with a ramp of 50°C/min. Thus, samples were taken

directly to the final experimental conditions without high-temperature annealing, and the

overheating did not exceed 10°C. The run duration varied from 46 to 108 hours (Tab.

II.2). After the experiment, all charges were rapidly quenched with a quench rate of about

150°C/s, which was sufficient to avoid quench effects.

Part II: The Role of H_2O and Pressure on Multiple Saturation and Liquid Lines of Descent in Basalts from the Shatsky Rise

4.4. Electron Probe Microanalysis

The major element compositions of the starting and experimental glasses and the mineral phases were obtained using a Cameca SX100 electron probe micro analyzer (EPMA) (University of Hannover) operated at an accelerating voltage of 15 kV. For mineral analyses, a focused beam with a 15nA current was used. The peak counting time was 10s for all elements (Si, Ti, Al, Fe, Mn, Mg, Ca, Na, K, Ni, Cr). Glasses were measured with 10nA, using defocused beam (5 or 10 μm). The peak counting time for glasses was 10 seconds for Si, Ti, Al, Fe, Mn, Mg, Ca and Cr, and 8 seconds for the alkalis. Matrix effects were corrected after the method of Pouchou & Pichoir (1991).

The following standards were used for the calibration: Fe_2O_3, MgO, TiO_2, Al_2O_3, Cr_2O_3, albite (Na), orthoclase (K), wollastonite (Si and Ca), apatite (P), and hausmannite (Mn). During each microprobe session, analytical precision and accuracy was verified by measuring the Smithsonian Institution's standard (Jarosewich et al., 1980): natural Juan de Fuca Ridge basaltic glass VG-2 (USNM 111240/52), San Carlos Olivine (USNM 111312/444), Lake County Plagioclase (USNM 115900) and internal *Cpx* standard. The accuracy of the EPMA measurements under the conditions described above is discussed in Husen et al. (2013) in more detail.

All glass analyses were normalized to 100 wt% to exclude the melt H_2O content. The compositions of the experimental minerals and glasses were used in a mass balance calculation to determine the phase proportions (Stormer and Nicholls, 1978). Calculated modes are given in Tab. II.2 (wt %), together with the residual sum of squares to the fit ($\sum R^2$). Most fits were satisfying with $\sum R^2 < 0.3$ (Tab. II.2).

Part II: The Role of H_2O and Pressure on Multiple Saturation and Liquid Lines of Descent in Basalts from the Shatsky Rise

Table II.2: Experimental conditions and phase assemblages for *dry* and *hydrous* experiments using three different starting materials.

Run	P, Mpa (±5MPa)	T, °C (±10)	duration (h)	H_2O (wt%)	error H_2O	CO_2 (ppm)	error CO_2	$\frac{Fe^{2+}}{Fe^{TOTAL}}$	Phases assemblage (phase proportions)	$\sum R^2$
DRY										
starting material: AH 6										
ShR603	102	1150	65						Ol (10), Plag (33), Cpx (15), Gl (42)	0.01
ShR616	103	1175	46	0.05	0.001	140	43		Ol (7), Plag (20), Cpx (4), Gl (68)	0.17
ShR609	102	1200	46	0.05	0.001	259	7		Ol (1), Plag (4), Gl (94)	0.08
ShR602	202	1150	108						Ol (11), Plag (40), Cpx (25), Gl (24)	*
ShR615	203	1175	73	0.08	0.002	486	42		Ol (5), Plag (18), Cpx (6), Gl (71)	0.05
ShR617	203	1225	65	0.09	0.003	873	25	0.88	Gl (100)	
ShR601	401	1150	66	0.05	0.006	196	9		Ol (18), Plag (50), Cpx (32)	*
ShR619	402	1175	91	0.06	0.001	1123	97		Ol (7), Plag (29), Cpx (21), Gl (43)	0.03
ShR605	402	1200	89	0.10	0.002	2102	243	0.97	Ol (4), Plag (15), Cpx (9), Gl (72)	0.03
ShR620	402	1225	63	0.04	0.052	2736	71		Gl (100)	
ShR604	698	1150	60						Ol (16), Plag (44), Cpx (40)	0.33
ShR606	700	1175	60						Ol (15), Plag (43), Cpx (41)	1.88
ShR611	700	1225	60						Ol (1), Plag (13), Cpx (18), Gl (67)	0.12
starting material: AH 3										
ShR322	101	1125	48						Ol (10), Plag (33), Cpx (17), Gl (40)	0.26
ShR318	106	1150	65					0.98	Ol (8), Plag (27), Cpx (11), Gl (53)	0.12
ShR316	105	1175	66	0.09	0.004	199	16		Ol (3), Plag (3), (0), Gl (94)	0.09
ShR315	102	1200	46					0.91	Gl (100)	
ShR324	203	1125	108	0.04	0.001	240	31		Ol (10), Plag (37), Cpx (19), Gl (33)	0.13
ShR323	202	1150	73	0.06	0.005	272	29		Ol (8), Plag (25), Cpx (14), Gl (53)	0.20
ShR305	202	1175	68						Ol (6), Plag (15), Cpx (4), Gl (75)	0.05
ShR313	202	1200	65					0.98	Gl (100)	
ShR326	402	1125	66						Ol (17), Plag (49), Cpx (33)	*
ShR307	401	1150	91						Ol (8), Plag (39), Cpx (22), Gl (31)	0.54
ShR304	402	1175	89	0.07	0.003	758	481		Ol (4), Plag (17), Cpx (12), Gl (67)	0.11
ShR311	402	1200	63						Ol (1), Gl (99)	-
ShR310	698	1150	60						Ol (10), Plag (48), Cpx (40)	
ShR312	700	1175	60						Ol (6), Plag (32), Cpx (33)	0.26
ShR314	700	1200	60	0.12	0.006	3615	272		Plag (14), Cpx (22), Gl (64)	0.23
ShR317	700	1225	60	0.11	0.008	5152	177		Cpx (5), Gl (94)	0.16
starting material: AH 5										
ShR520	101	1125	48	0.05	0.009	136	44		Cpx (2), Plag (17), Cpx (16), Gl (66)	0.09
ShR506	102	1150	65	0.05	0.003	209	15		Cpx (1), Gl (99)	*
ShR518	103	1175	46	0.08	0.005	184	30	0.88	Gl (100)	
ShR512	102	1200	46					0.98	Gl (100)	
ShR519	203	1125	108	0.09	0.005	517	66		Ol (2), Plag (19), Cpx (18), Gl (61)	0.01
ShR505	202	1150	73	0.08	0.004	775	61		Plag (3), Cpx (6), Gl (91)	0.10
ShR502	202	1175	68	0.07	0.002	781	28	0.88	Gl (100)	
ShR510	202	1200	65	0.08	0.005	712	38		Gl (100)	
ShR522	402	1125	66						Ol (tr), Plag (30), Cpx (33), Gl (36)	0.09
ShR504	401	1150	91	0.08	0.010	1347	94		Plag (17), Cpx (21), Gl (62)	0.30
ShR501	402	1175	89	0.10	0.003	745	18		Cpx (5), Gl (95)	0.03
ShR508	402	1200	63	0.12	0.008	1927	124	0.93	Gl (100)	
ShR507	698	1150	60						Plag (26), Cpx (38), Gl (36)	0.10
ShR509	700	1175	60	0.07	0.008	2320	81		Plag (22), Cpx (25), Gl (53)	0.14
ShR511	700	1200	60	0.14	0.011	4264	197		Cpx (9), Gl (91)	0.06
ShR514	700	1225	60	0.09	0.007	3873	404	0.94	Gl (100)	

Ol - olivine, Plag - plagioclase, Cpx - clinopyroxene, Gl - glass, Mag - magnetite
phase proportions were calculated via mass balance (Stormer & Nicholls, 1978)
 Fe^{2+}/Fe^{total} was determined by the colorimetric method published by Schuessler et al. (2008)
* phase proportions were determined by image analysis (not by mass balance)

Part II: The Role of H_2O and Pressure on Multiple Saturation and Liquid Lines of Descent in Basalts from the Shatsky Rise

Table II.2: continued

Run	P, Mpa (±5MPa)	T, °C (±10)	duration (h)	H_2O (wt%)	error H_2O	CO_2 (ppm)	error CO_2	$\frac{Fe^{2+}}{Fe^{TOTAL}}$	Phases assemblage (phase proportions)	$\sum R^2$
HYDROUS										
starting material: AH 6										
ShR660	102	1100	64						Ol (9), Plag (34), Cpx (25), Mag (tr), Gl (31)	0.01
ShR662	105	1125	65	0.37	0.01				Ol (8), Plag (30), Cpx (20), Gl (42)	0.07
ShR661	105	1135	89	0.54	0.02				Ol (6), Plag (21), Cpx (13), Gl (59)	0.15
ShR663	108	1155	64						Ol (6), Plag (23), Cpx (13), Gl (58)	0.004
ShR658	202	1075	64						Ol (11), Plag (49), Cpx (37), Mag (4)	*
ShR654[a)]	201	1103	70						Ol (9), Plag (49), Cpx (37)	*
ShR651[a)]	205	1125	65						Ol (6), Plag (25), Cpx (22), Gl (45)	0.18
ShR665	402	1098	67						Ol (8), Plag (48), Cpx (40)	0.14
ShR659	401	1100	70						Ol (9), Plag (48), Cpx (40), Mag (4)	0.50
ShR657	401	1125	62						Ol (7), Plag (36), Cpx (34), Mag (2), Gl (21)	0.01
ShR666	397	1150	63						Ol (5), Plag (35), Cpx (34), Mag (4), Gl (23)	0.02
starting material: AH 3										
ShR360	102	1100	64	0.43	0.02	110	19		Ol (7), Plag (26), Cpx (17), Gl (51)	0.27
ShR362	105	1125	65	0.48	0.02	273	46		Ol (6), Plag (20), Cpx (12), Gl (62)	0.11
ShR361	105	1135	89					0.82	Ol (4), Plag (3), Cpx (1), Gl (92)	0.28
ShR363	108	1155	64	0.51	0.02	749	39		Ol (2), Plag (3), Cpx (2), Gl (93)	*
ShR358	202	1075	64	0.48	0.02	359	89		Ol (8), Plag (32), Cpx (24), Gl (35)	0.09
ShR354[a)]	201	1100	70	0.26	0.04				Ol (6), Plag (31), Cpx (25), Gl (37)	0.02
ShR350[a)]	205	1125	65	0.75	0.04	104	23	0.79	Ol (5), Plag (13), Cpx (12), Gl (70)	0.30
ShR351[a)]	204	1150	65	0.90	0.03	269	24	0.82	Gl (100)	
ShR359	401	1100	70	0.00	0.00				Ol (5), Plag (31), Cpx (30), Mag(1), Gl (33)	0.02
ShR357	401	1125	62	0.00	0.00				Ol (4), Plag (26), Cpx (28), Gl (41)	0.04
ShR366	397	1150	63	0.37	0.02	1583	60		Ol (4), Plag (25), Cpx (26), Gl (45)	0.57
starting material: AH 5										
ShR560	102	1100	64	0.63	0.03	230	152		Plag (9), Cpx (15), Gl (76)	0.26
ShR562	105	1125	65	0.73	0.02	436	33	0.81	Cpx (7), Gl (93)	0.12
ShR561	105	1135	89	0.82	0.03	526	27	0.83	Cpx (1), Gl (99)	*
ShR563	108	1155	64	0.57	0.02	577	43	0.74	Gl (100)	
ShR558	202	1075	64	0.79	0.03	526	324		Ol (1), Plag (14), Cpx (24), Gl (63)	0.06
ShR554[a)]	201	1100	70	0.63	0.03	47	18		Ol (1), Plag (15), Cpx (23), Gl (62)	0.00
ShR550[a)]	205	1125	65	0.94	0.04	98	23	0.80	Cpx (11), Gl (88)	0.15
ShR551[a)]	204	1150	65	1.12	0.03	82	25	0.82	Gl (100)	
ShR565	402	1098	67	0.56	0.01	342	9		Plag (25), Cpx (33), Gl (40)	0.10
ShR559	401	1100	70	0.69	0.03	1512	77		Plag (19), Cpx (30), Gl (50)	0.31
ShR557	401	1125	62	0.77	0.03	2441	143		Plag (10), Cpx (20), Gl (70)	*
ShR566	397	1150	63						Plag (9), Cpx (18), Gl (73)	0.17

Ol - olivine, Plag - plagioclase, Cpx - clinopyroxene, Gl - glass, Mag - magnetite

phase proportions were calculated via mass balance (Stormer & Nicholls, 1978)

Fe^{2+}/Fe^{total} was determined by the colorimetric method published by Schuessler et al. (2008)

[a)] experiments were performed without initial source of CO_2-fluid ($Ag_2C_2O_4$)

* phase proportions were determined by image analysis (not by mass balance)

4.5. Fourier Transformation Infrared Spectroscopy (FTIR)

Glass H_2O and CO_2 concentrations were determined using FTIR spectroscopy (Bruker IFS88 FTIR, University of Hannover; operation conditions: MCT narrow range detector, globar light source and KBr beamsplitter). For these measurements glass fragments from the experimental products with a size of approximately 1mm² were used.

Part II: The Role of H_2O and Pressure on Multiple Saturation and Liquid Lines of Descent in Basalts from the Shatsky Rise

The glass fragments were mounted in epoxy mixed with Al_2O_3 granules and polished from both sides to a thickness of approximately 100 µm. The thickness was measured with a digital micrometer (Mitutoyo, precision: ≤2 µm). The spectrometer was coupled with an IR-Scope II optical microscope. Before the measurements, the quality of the glass volume was controlled for the presence of scratches, crystals, or other impurities (pores, bubbles etc.). The spectra obtained from glass volumes containing crystals were used only in the case if the targeted absorption peak could be clearly identified without evidences of interference with the absorption peak of molecular H_2O at 1630cm^{-1} .The H_2O concentration was determined at the peak which is attributed to the OH stretch vibration (3550 cm^{-1}) (Stolper, 1982) using a molar absorption coefficient of 68 L•cm^{-1}•mol^{-1} (Shishkina et al., 2010). On each sample, three spectra were taken with a spot size of 100 x 100 µm (every spectrum was the average of 50 scans). The density was assumed to be a typical value for dry basaltic glasses, 2815 g/l. The H_2O concentration was calculated from the peak height, which was determined by referring a straight tangential base line.

Because the CO_2 is dissolved mainly as CO_3^{2-} in basaltic glasses, we measured the absorption of CO_3^{2-} which can be detected after Fine & Stolper (1986) at two peak positions at 1515 cm^{-1} and 1435 cm^{-1}. We used a typical absorption coefficient of 607 L•cm^{-1}•mol^{-1} (Shishkina et al., 2010) for the calculation of the concentration of CO_2 in the glasses based on the peak height at each position. The average of both calculated concentration values was used for further discussion of the *dry* experiments. In the case of our *hydrous* experiments, our calculation is based on the absorption at 1435 cm^{-1}, because at higher H_2O concentrations, the 1515 cm^{-1} peak led to systematically overestimated CO_3^{2-} concentrations, due to the overlapping absorption band of molecular H_2O at 1630 cm^{-1} (e.g., Behrens et al., 2009; Botcharnikov et al., 2006; Shishkina et al., 2010).

5.   RESULTS

Experimental run conditions, phase assemblages, and their calculated proportions, and the glass H_2O and CO_2 contents are reported in Tab. II.2. Average glass compositions with standard deviations and the number of points averaged are reported Tab. II.3 and II.4 for *dry* and *hydrous* experiments respectively. Phase compositions and mineral–liquid exchange coefficients (K_{DS}) are summarized in Tab. II.5 and II.6 (details can be found in the Appendix in Tabs. AII.1-AII.7).

5.1.   Experimental Products

The applied temperature range allowed us to bracket the liquidus at *dry* conditions at nearly all pressures for all three starting compositions. In *hydrous* experiments, the liquidus was bracketed only at 100 and 200 MPa in AH5, and in AH3 at 200 MPa. All experiments contain a different proportion of liquid associated with idiomorphic crystals with varying sizes between 2 and 20 μm (Fig. II.2). The mineral phases found in the experimental products of all three starting compositions are *Ol*, *Plag* and *Cpx*, which reproduce well the natural phase assemblage of the natural basalts. In the primitive AH6 and in the intermediate AH3 compositions, oxide phases were also observed (*Mag*). In both, *dry* and *hydrous* sets of experiments, bubbles were observed in all runs (black areas in Fig. II.2), indicating the presence of the fluid phase; thus all experiments are considered to represent fluid-saturated conditions with extremely low (*dry*) and low (*hydrous*) aH_2O in the system. The high crystal fractions at lower temperatures impede the measurements of dissolved volatiles, thus it was only possible to determine H_2O and CO_2 concentrations in 60% of the samples (Tab. II.2). Also, it should be noted that those data which were obtained for samples with relatively high crystallinities (>30%) represent only minimum values, as the presence of crystals may change the absorption coefficient for IR waves and also decreases the targeted volume. Although the investigated range of

Part II: The Role of H$_2$O and Pressure on Multiple Saturation and Liquid Lines of
Descent in Basalts from the Shatsky Rise

melt H$_2$O concentrations (<1.2 wt% H$_2$O) is generally low, the experimental setups used

in our study allowed us to investigate the effect of H$_2$O on phase equilibria in a scale of

nearly one order of magnitude difference of the melt H$_2$O: ~0.04-0.14 wt% H$_2$O in *dry*

and ~0.4-1.11 wt% H$_2$O in *hydrous* experiments.

5.2. Attainment of Equilibrium

The experiments presented in this work are crystallization experiments with run

durations between 46 and 108 h. According to the kinetic test of Freise et al. (2009) we

expect, that equilibrium conditions were reached in our experiments. Freise et al. (2009)

demonstrated near equilibrium conditions in an alkali basalt at 1100°C and 400 MPa

under "nominally *dry*" conditions after less than three hours. However, the following

observations indicate that our experiments were close to equilibrium conditions:

(1) The crystallization experiments were conducted using glassy starting powder.

All precipitated crystals are euhedral and evenly distributed within the experimental

charges (Fig. II.2), and are homogenous in composition (see e.g. standard deviations in

Tab. II.5 and II.6, and Tabs. AII.1-AII.7). All experiments were successfully mass

balanced and the residual sum of squares ($\sum$R²) are low (0.01 - 0.3, Tab. II.2) for the most

of our experiments, indicating small differences between the calculated silicate

compositions and the starting material. No quench, resorbed, zoned or sector-zoned

crystals were observed amongst the experimental products.

(2) Crystal-liquid exchange coefficients (K$_D$; Tabs. II.5 and II.6, and discussion

below) are in general agreement with other high-pressure high-temperature phase

equilibrium studies (Grove et al., 1992; Sano & Yamashita, 2004; Whitaker et al., 2007).

The average Fe-Mg exchange distribution coefficients (K$_{DFe-Mg}$=(X$_{Fe}^{xtl}$ • X$_{Mg}^{liq}$)/ (X$_{Mg}^{xtl}$ •

X$_{Fe}^{liq}$) for *Ol*-liquid and *Cpx*-liquid equilibria are 0.28±0.02 and 0.22±0.03 for *dry* and

Part II: The Role of H₂O and Pressure on Multiple Saturation and Liquid Lines of Descent in Basalts from the Shatsky Rise

200 MPa, 1130°C, AH3
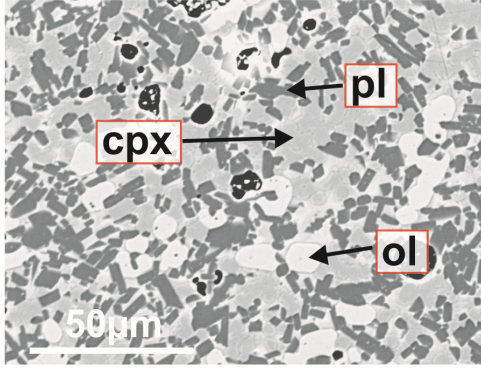
a) F_{cryst}=66%, 0.04 wt%H₂O

b) F_{cryst}=30%, 0.75 wt%H₂O

400 MPa, 1175 °C, 0.07-0.1 wt%H₂O
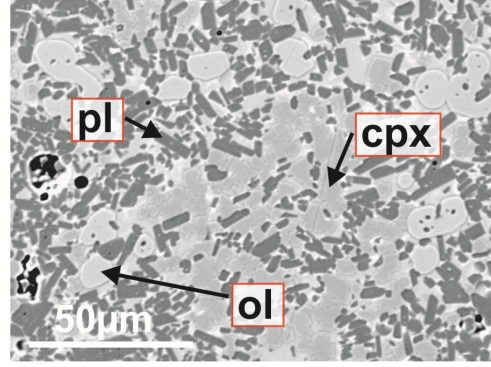
c) AH6 - 8.6 wt%MgO
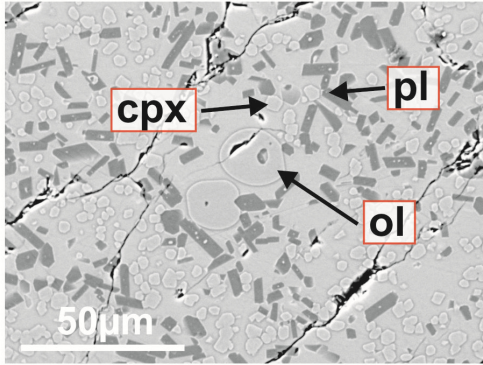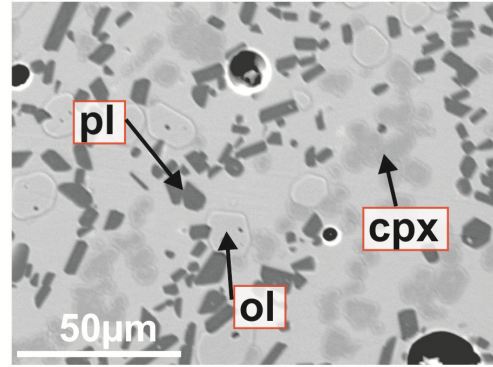
d) AH3 - 8.0 wt%MgO

e) AH5 - 6.4 wt%MgO

Figure II.2: BSE images of selected samples illustrate the texture of the experimental run products: a) ShR324, b) ShR350, c) ShR619, d) ShR304, d) ShR501. Comparison of a and b (left column) shows the effect of H₂O on the crystallinity at similar *P-T* conditions. The right column displays experiments at similar *P-T*-H₂O conditions using different starting materials.
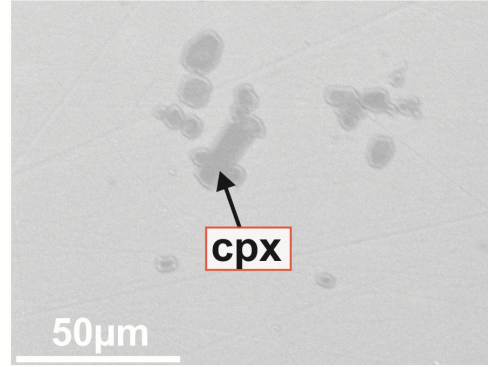
0.27±0.01 and 0.30±0.03 for *hydrous* experiments, respectively. Similarly, the average *Plag*-liquid Ca-Na exchange distribution coefficients (K_{DCa-Na}=(X_{Ca}^{xtl} • X_{Na}^{liq})/(X_{Na}^{xtl} • X_{Ca}^{liq}) are 1.0±0.2 and 1.17±0.3 for *dry* and *hydrous* experiments respectively.

(3) As reported above, to avoid the problem of Fe-loss to the capsule material (e.g. Berndt et al., 2005; Sisson & Grove, 1993), all capsules for our *hydrous* experiments

Dissertation of Anika Husen

Part II: The Role of H$_2$O and Pressure on Multiple Saturation and Liquid Lines of
Descent in Basalts from the Shatsky Rise

were Fe pre-saturated. To prove that the Fe pre-saturation was successful and the pre-saturated amount was correct, we conducted several super-liquidus experiments with various amounts of Fe pre-saturation. The glass compositions were checked for Fe-loss or gain afterwards. These test experiments showed that there was no significant change in the melt FeO content in the range of the applied pre-saturated Fe contents (0.2-0.3 wt% Fe in alloy). Measurements of the capsule materials after these experiments demonstrated that the incorporated Fe gradually decreased from the interface with the glass towards the outer rim of the capsule wall, which is an artifact of the Fe-coating via electroplating. However, as mentioned above, our mass balance calculations, revealed appropriate $\sum R^2$ values, showing little evidences of the melt Fe-loss (or gain back from the capsule) and proving that no significant interaction with the capsule material has occurred during the experimental treatment.

Regarding the H$_2$O contents, we also assume the attainment of equilibrium in our experiments. After Berndt et al. (2002) the osmotic equilibrium between the interior of a Au or Pd capsule (similar dimensions like in our experiments) and the surrounding pressure medium is reached after 1.5 h at 200 MPa. Furthermore, Berndt et al. (2002) state that, according to Chekhmir et al. (1985), the H$_2$ diffusion through the noble metal rather than through the basaltic liquid is the limiting factor for fast equilibration. Thus, we expect that the final fH$_2$O is reached after 1.5 h, which is clearly shorter than our experimental run durations. In the case of Berndt et al. (2002) non-equilibrium conditions were observed in chemical zoning in *Ol* due to short run durations (5h). Considering our (compared to Berndt et al., 2002) long run durations (<46h) and the absence of chemical zoning (short diffusion distances), we assume that our experimental phase assemblage is in equilibrium with the determined H$_2$O concentrations.

Part II: The Role of H$_2$O and Pressure on Multiple Saturation and Liquid Lines of Descent in Basalts from the Shatsky Rise

caption →

Dissertation of Anika Husen
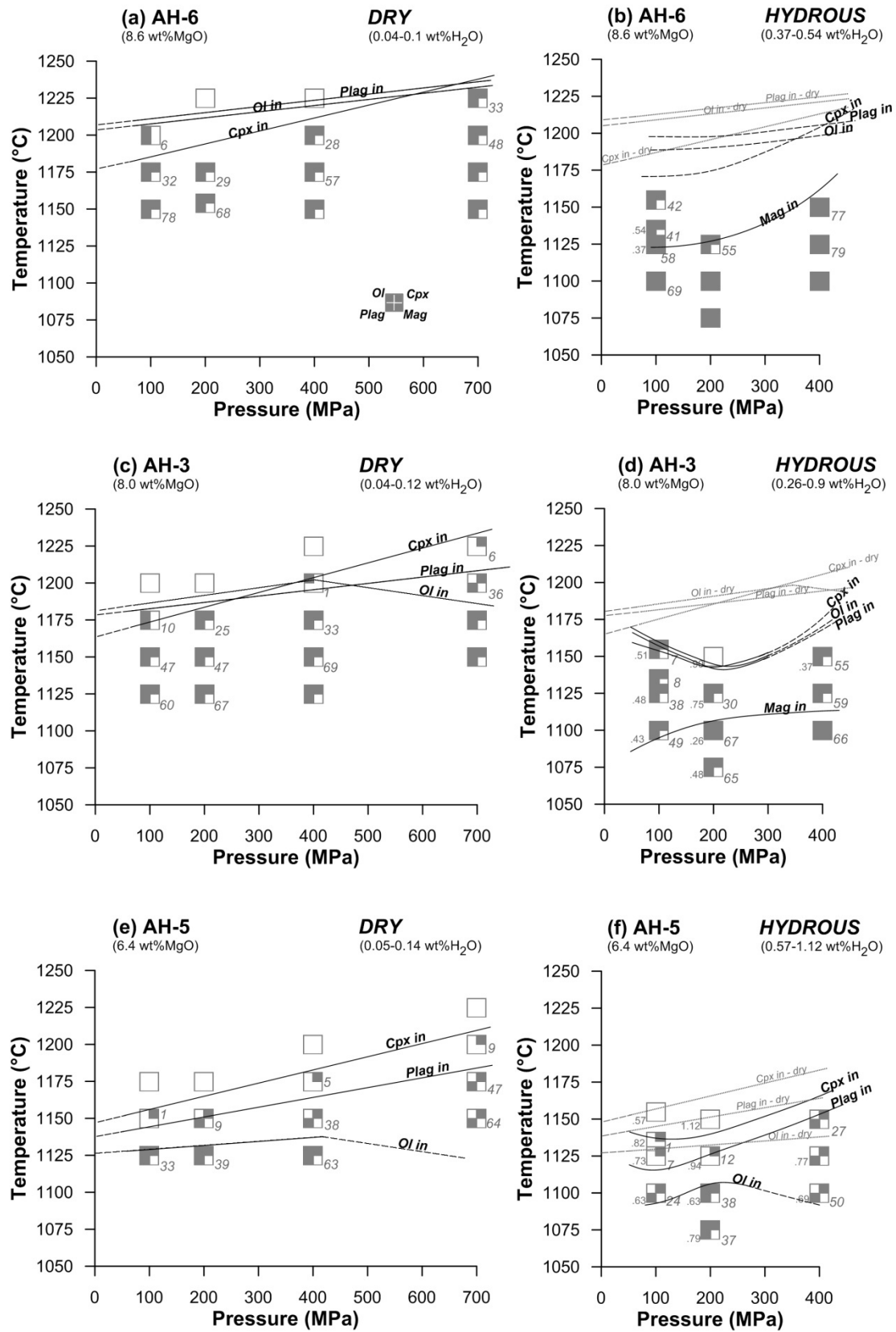
Part II: The Role of H$_2$O and Pressure on Multiple Saturation and Liquid Lines of
Descent in Basalts from the Shatsky Rise

Figure II.3: The phase diagrams show the stability of different mineral phases dependent on pressure and temperature in the three different starting materials (initial MgO content increases from top to bottom: AH6 - AH3 - AH5) and for experiments conducted at *dry* conditions (left column) and *hydrous* conditions (right column). The filled corners in each square mark the presence of the mineral in the experimental product for given conditions. Stability fields are marked by solid lines (partly dashed if estimated) (*Ol* in/*Plag* in/*Cpx* in/*Mag* in). In the diagrams for *hydrous* conditions, also results of *dry* experiments are displayed for comparison (light grey dashed lines). Additionally, small grey numbers at the right of each symbol indicate the crystallization degree and those at the left (only for *hydrous* experiments) the H$_2$O content measured in the experimental liquid.

5.3.   Crystallization Sequence and Phase Relations

The experimental crystallization sequences and the determined stability fields of

the minerals for all three starting compositions and the two experimental setups are

shown in *P-T* diagrams in Fig. II.3. From the top to the bottom of Fig. II.3, one can see

the change of mineral stabilities with the change of initial melt composition. The effect of

H$_2$O on phase relations can be evaluated for each starting composition by comparison of

the left (*dry* experimental setup) and the right (*hydrous* experimental setup) *P-T* diagrams

in Fig. II.3. It should be noted, that the "*hydrous*" *P-T* diagrams also represent more

oxidizing conditions (FMQ-1 to FMQ+1), than the "*dry*" *P-T* diagrams (FMQ-2 to FMQ-

1) (see experimental setups above). Below, we discuss phase relations for each starting

composition, both for *dry* and *hydrous* experimental setups.

5.3.1   *AH6, 8.6% MgO*

Under *dry* conditions the liquidus of the AH6 basalt is observed between 1200 and

1225°C at 100 MPa and at above 1225°C at 700 MPa (Fig. II.3a). *Ol* and *Plag* are

liquidus phases at 100, 200 and 400 MPa, whereas at 700 MPa and 1225°C all three

phases (*Ol*+*Plag*+*Cpx*) crystallize simultaneously. At 100 and 200 MPa experiments, the

appearance of *Cpx* and the transition from *Ol*+*Plag* to *Ol*+*Plag*+*Cpx* cotectics was

bracketed between 1200 and 1175°C. In contrast, at 700 MPa, the order of crystallization

Dissertation of Anika Husen

Part II: The Role of H₂O and Pressure on Multiple Saturation and Liquid Lines of
Descent in Basalts from the Shatsky Rise

cannot be directly observed from the phase diagram (Fig. II.3a). However, we believe that *Cpx* should be the liquidus phase at 700 MPa, because it is prevailing in the solid phase after about 30% of crystallization at 1225°C (run ShR11, Tab. II.2) (proportions of *Ol+Plag+Cpx* cotectic crystallization are ~7-10 %*Ol* : 40-50 %*Cpx* : 60-50 % *Plag*, see discussion below). Similar to previous works (e.g. Bender et al., 1978), our experiments demonstrate, that pressure has a similar positive effect on *Plag* and *Ol* liquidus (about 4-5°C per 100 MPa), whereas the liquidus of *Cpx* is steeper (dT/dP~9°C/100 MPa).

Under *hydrous* conditions (Fig. II.3b), the liquidus of AH6 was not bracketed at any investigated pressure. All experiments show the saturation with *Ol+Plag+Cpx* below 1170°C and with *Ol+Plag+Cpx+Mag* below 1125°C at 100 MPa and below 1150°C at 400 MPa (after ~60% and ~80 % crystallization, respectively).

5.3.2   *AH3, 8.0% MgO*

Under *dry* conditions, the liquidus of the intermediate starting composition AH3 with 8% MgO is ~25-30°C lower (Fig. II.3c), compared to the previous more MgO-rich basalt AH6 (8.6% MgO). At 100 and 200 MPa, the liquidus in AH3 is bracketed between 1200 and 1175°C. At 400 MPa it is located between 1225 and 1200°C. Although the liquidus was not bracketed by our experiments at 700 MPa, it can be located slightly above 1225°C at this pressure, considering the change of phase relations with pressure (Fig. II.3c) and the low crystal proportion (6%) in the run SHR-317 at 1225°C and 700 MPa. At 100, 200 and 400 MPa *Ol* or *Ol+Plag* are the liquidus phases, whereas at higher pressures (500-700 MPa), *Cpx* crystallizes first, and the crystallization sequence is: *Cpx*, *Cpx+Plag* and *Cpx+Plag+Ol*. At 700 MPa, the crystallization of *Ol* is strongly subordinate - it is observed only after more than 40% crystallization of *Cpx* and *Plag*. Similar to AH6, the stability line of *Cpx* is steeper than that of *Ol* and *Plag*.

Part II: The Role of H_2O and Pressure on Multiple Saturation and Liquid Lines of
Descent in Basalts from the Shatsky Rise

The *hydrous* liquidus in AH3 is bracketed only at 200 MPa and it is located between 1150 and 1125°C (Fig. II.3d). An increased H_2O content leads to a liquidus depression of ~ 25°C at 100 MPa to ~50°C at 200 MPa. All three main silicate phases are crystallizing in a narrow range in AH3 under *hydrous* conditions. Thus, the order of crystallization cannot be resolved. The slightly higher H_2O content facilitated the appearance of *Mag* in runs with crystallization degrees above 55%.

5.3.3 AH5, 6.4% MgO

Under *dry* conditions, the liquidus of the most evolved AH5 basalt is defined by *Cpx* crystallization at all investigated pressures (from ~1155°C at 100 MPa to ~1200°C at 700 MPa, Fig. II.3e). *Plag* is the second, and *Ol* is the third crystallizing mineral. The stability of *Ol* is strongly subordinate - it appears after ~30% and 40% of *Cpx+Plag* crystallization at 100 MPa and 400 MPa respectively. It was not observed at 700 MPa after ~65% of crystallization. The liquidus of AH5 under *dry* conditions is well bracketed at all pressures, which allows us to estimate *dT/dP* of *Cpx* crystallization to be ~9°C per 100 MPa.

The addition of H_2O does not change the crystallization sequence in the AH5 composition, but similar to the other basalts, it results in a liquidus depression up to 10-20°C at 100-200 MPa (Fig. II.3f). In general, the liquidus depression in the system where *Cpx* is the liquidus phase seems to be slightly lower, compared to the more primitive system where *Ol* or *Ol+Plag* are liquidus phases. Similar to *dry* conditions, under *hydrous* conditions, *Ol* is not observed at the higher pressure. In the presence of small amounts of H_2O, *Ol* crystallization was absent even at lower pressures compared to *dry* runs (at 400 MPa up to 50% crystallization).

Part II: The Role of H$_2$O and Pressure on Multiple Saturation and Liquid Lines of Descent in Basalts from the Shatsky Rise

---

5.4.   Phase Proportions

The calculated modes of melt and solid phases are given in Tab. II.2 and plotted for each pressure and for *dry* (left) and *hydrous* (right) conditions in Fig. II.4 for the AH3 basalt (and in the Appendix: Fig. AII.1 and A II.2 for AH6 and AH5).

As shown above, the crystallization near the liquidus of the MgO-rich basalts AH6 and AH3 under *dry* conditions at 100 and 200 MPa is controlled by *Ol+Plag* followed by *Ol+Plag+Cpx* precipitation. At higher pressures (400 and 700 MPa), near the liquidus, the crystallization of AH6 and AH3 is already dominated by *Ol+Plag+Cpx*, and *Plag+Cpx* at 700 MPa. In Fig. II.4 it is clearly seen that with pressure increase, the stability and the proportion of crystallizing *Cpx* in the solid phase is gradually increasing. For example, in the AH3 basalt, the mineral proportions (*Ol*:*Plag*:*Cpx*) at 1150°C change from 18:58:24 at 100 MPa to 10:49:41 at 700 MPa (Fig. II.4a and d). Similar to *dry* conditions, higher *Cpx* proportion is observed with pressure increase in *hydrous* experiments.

The crystallization of *Ol* in the most evolved basalt AH5 is strongly suppressed. It is less than 5% in the solid phase in runs at 100, 200 and 400 MPa under *dry* conditions (1125°C) and less than 3 % at 200 MPa in the presence of 0.6-0.8 wt% H$_2$O. The proportion of *Cpx* along *Plag-Cpx* cotectics in AH5 also tends to slightly increase with pressure, e.g. from 45:55 (*Plag*:*Cpx*) at 400 MPa to 41:59 at 700 MPa (Fig. AII.2 c and d) and 1150°C.

Our experiments also demonstrate that at any given pressure at similar crystallinity, the abundance of *Cpx* in *Ol+Plag+Cpx* (AH6 and AH3, Fig. II.4) or *Plag-Cpx* (AH5) mineral assemblages is systematically higher in *hydrous* glasses in comparison to their *dry* counterparts (compare left and right plots in Fig. II.4). For example, considering 200 MPa *dry* and *hydrous* experiments at similar degree of

crystallization (30 %) (e.g. *dry*: interpolation between runs ShR305 and ShR323, and

hydrous: ShR350, Fig. II.4 c and f), the *Cpx* has a relatively higher mode in *hydrous*

experiments. In *dry* experiments, *Cpx* makes up ~20 % of the solid phase (23:57:20),

whereas at *hydrous* conditions, the *Cpx* proportion is ~40 % in the solid phase (17:43:40).

Figure II.4: Phase proportions in experiments with AH3 calculated via mass balance (accuracy: total residuals <1 and $\sum r^2$<0.3) are shown dependent on temperature at different H$_2$O conditions (right and left columns) and different pressures (increasing from top to bottom). H$_2$O contents for *hydrous* experiments are given by grey labels when measured. In (b) and (f) phase proportions at similar crystallization degrees are marked for comparison of *dry* and *hydrous* conditions: small grey numbers at the y-axis indicate phase proportions referring to the whole phase assemblage, whereas grey numbers at the right hand side indicate the phase proportions referring to the solid phase only.

Lq – liquid, Ol – olivine, Pl – plagioclase, Cpx – clinopyroxene, Mag – magnetite

Part II: The Role of H$_2$O and Pressure on Multiple Saturation and Liquid Lines of Descent in Basalts from the Shatsky Rise
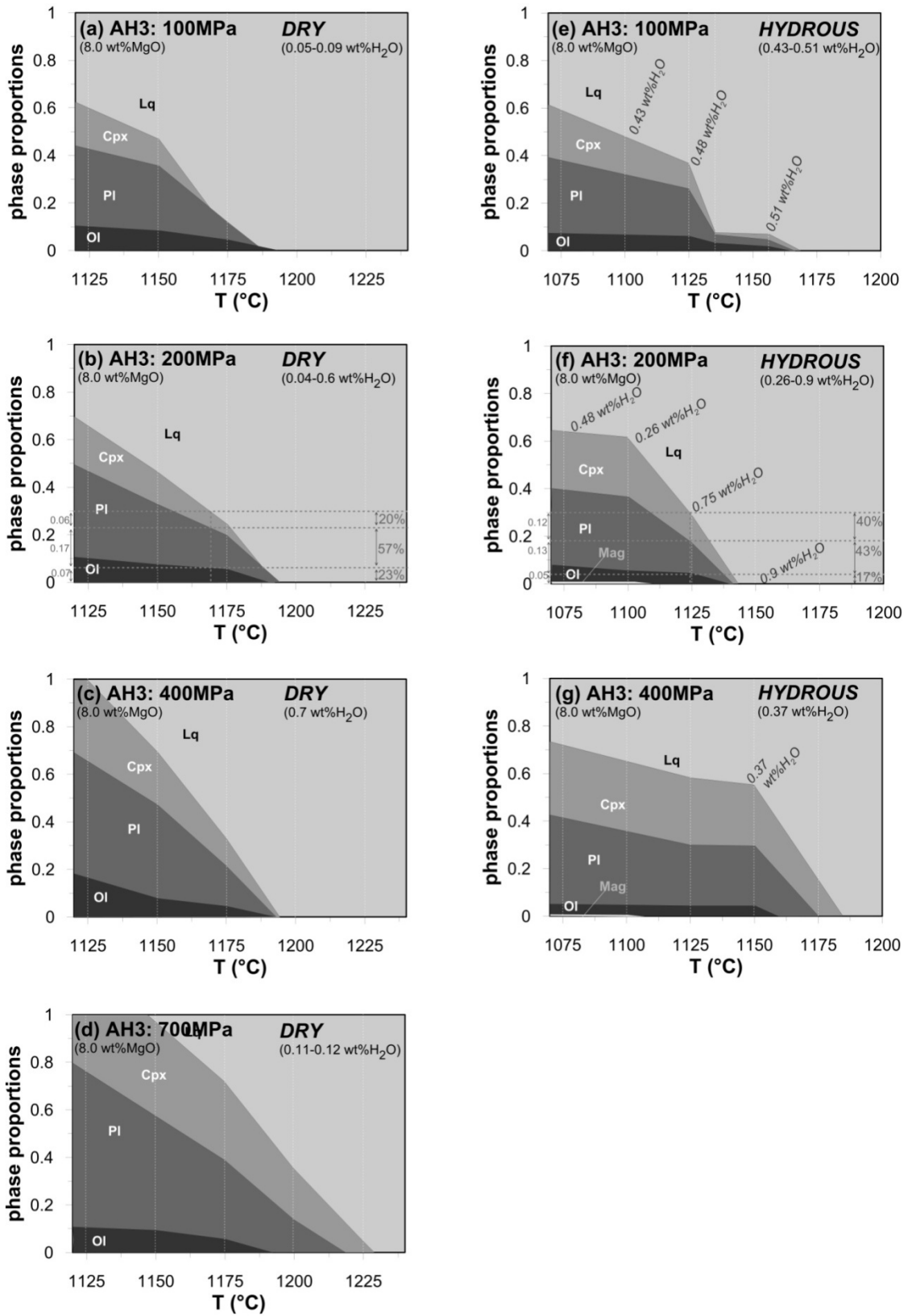
← *caption*

Table II.3: Compositions of experimental glasses from *dry* experiments

Run	P (MPa)	T (°C)	Total	n	SiO$_2$	TiO$_2$	Al$_2$O$_3$	FeOtot	MnO	MgO	CaO	Na$_2$O	K$_2$O	P$_2$O$_5$	CaO/Al$_2$O$_3$	Mg#
starting material: AH 6																
ShR603	102	1150	101.55	3	47.43 (.12)	1.67 (.01)	14.21 (.18)	14.29 (.29)	0.28 (.02)	5.6 (.06)	13.25 (.51)	3.01 (.13)	0.26 (.01)	b.d.	0.93	42.35
ShR616	103	1175	100.81	6	48.23 (.22)	1.16 (.03)	15.29 (.29)	11.44 (.15)	0.2 (.03)	7.15 (.06)	13.91 (.19)	2.44 (.1)	0.18 (.01)	b.d.	0.91	53.96
ShR609	102	1200	101.30	11	47.95 (.6)	0.93 (.04)	16.42 (.2)	9.99 (.16)	0.21 (.01)	8.43 (.12)	13.73 (.18)	2.22 (.08)	0.11 (.01)	b.d.	0.84	61.29
ShR602	202	1150	101.63	4	45.73 (.44)	1.87 (.05)	13.21 (.36)	16.66 (.91)	0.33 (.09)	6.17 (.17)	12.33 (.32)	3.34 (0.2)	0.35 (.01)	b.d.	0.93	41.01
ShR615	203	1175	100.52	5	48.33 (.18)	1.22 (.03)	15.21 (.19)	11.4 (.25)	0.18 (.06)	7.49 (.11)	13.54 (.09)	2.5 (.07)	0.14 (.02)	b.d.	0.89	55.20
ShR617	203	1225	101.65	5	47.79 (.33)	0.84 (.02)	16.93 (.08)	9.37 (.22)	b.d.	8.66 (.07)	13.74 (.1)	2.38 (.05)	0.11 (.01)	b.d.	0.81	63.44
ShR619	402	1175	100.74	9	46.18 (.24)	1.63 (.04)	15.42 (.31)	14.34 (.21)	0.25 (.05)	6.32 (.15)	12.25 (.13)	3.38 (.09)	0.22 (.02)	b.d.	0.79	45.25
ShR605	402	1200	100.10	6	47.63 (.35)	1.07 (.02)	15.99 (.44)	11.5 (.15)	0.23 (.02)	7.74 (.11)	13.31 (.17)	2.4 (.09)	0.14 (.02)	b.d.	0.83	55.81
ShR620	402	1225	101.45	20	47.88 (.23)	0.83 (.03)	16.88 (.14)	9.46 (.18)	0.2 (.03)	8.46 (0.1)	13.85 (.25)	2.35 (.08)	0.11 (.01)	b.d.	0.82	62.66
ShR611	700	1225	101.01	7	47.32 (.21)	1.15 (.04)	16.81 (.21)	12.01 (.27)	0.22 (.05)	7.68 (.04)	12.13 (.05)	2.53 (.12)	0.15 (.01)	b.d.	0.72	54.52
starting material: AH 3																
ShR322	101	1125	101.51	7	47.60 (.37)	2.79 (.12)	13.60 (.69)	15.23 (.44)	0.37 (.06)	4.94 (.29)	11.11 (.14)	3.53 (.16)	0.38 (.04)	0.44 (.03)	0.82	37.85
ShR318	106	1150	101.10	8	48.82 (.18)	2.18 (.04)	13.84 (.26)	14.15 (.23)	0.30 (.07)	5.61 (.48)	11.74 (.23)	3.01 (.09)	0.35 (.02)	b.d.	0.85	42.67
ShR315	102	1200	101.75	8	49.35 (.2)	1.38 (.05)	15.70 (.15)	10.43 (.2)	0.24 (.04)	7.78 (.09)	12.36 (.21)	2.59 (.1)	0.17 (.02)	b.d.	0.79	58.33
ShR324	203	1125	100.95	5	47.37 (.2)	3.12 (.08)	13.11 (.25)	16.37 (.77)	0.29 (.08)	5.10 (.5)	10.66 (.37)	3.55 (.15)	0.42 (.02)	b.d.	0.81	36.88
ShR323	202	1150	101.13	6	48.48 (.34)	2.26 (.13)	14.38 (.99)	14.08 (.82)	0.33 (.07)	5.54 (.31)	11.51 (.23)	3.14 (.17)	0.30 (.03)	b.d.	0.80	42.46
ShR305	202	1175	101.86	6	49.39 (.18)	1.74 (.03)	14.71 (.22)	11.99 (.19)	0.25 (.06)	6.60 (.08)	12.28 (.28)	2.82 (.11)	0.21 (.01)	b.d.	0.83	50.81
ShR313	202	1200	101.54	6	49.48 (.33)	1.38 (.02)	15.61 (.08)	10.47 (.19)	0.21 (.01)	7.84 (.1)	12.27 (.12)	2.56 (.09)	0.17 (.02)	b.d.	0.79	58.43
ShR307	401	1150	99.69	2	46.16 (.38)	3.50 (.1)	11.61 (.5)	18.56 (.71)	0.30 (.09)	6.04 (0.3)	10.62 (.02)	2.77 (.32)	0.44 (.05)	b.d.	0.92	37.90
ShR304	402	1175	101.17	8	48.48 (.25)	1.99 (.05)	14.89 (.27)	12.97 (.34)	0.28 (.03)	6.52 (.13)	11.48 (.09)	2.85 (.07)	0.26 (.02)	0.28 (.07)	0.77	48.53
ShR311	402	1200	100.49	8	49.03 (.17)	1.41 (.04)	15.55 (.15)	10.41 (.11)	0.23 (.02)	7.78 (.12)	12.59 (.09)	2.64 (.12)	0.17 (.02)	0.18 (.02)	0.81	58.37
ShR312	700	1175	100.66	7	45.61 (.52)	3.20 (.07)	14.45 (.68)	17.62 (.55)	0.32 (.09)	5.00 (.25)	9.69 (.39)	3.29 (.33)	0.41 (.04)	b.d.	0.67	34.73
ShR314	700	1200	100.21	5	47.64 (.15)	1.92 (.05)	15.75 (.2)	13.60 (.27)	0.29 (.08)	6.75 (.17)	10.50 (.13)	3.07 (.11)	0.27 (.01)	0.21 (.03)	0.67	48.23
ShR317	700	1225	99.93	9	49.49 (.23)	1.44 (.03)	16.22 (.26)	10.58 (.27)	0.19 (.03)	7.24 (.11)	11.82 (.14)	2.76 (.1)	0.19 (.02)	0.08 (.04)	0.73	56.20
starting material: AH 5																
ShR520	101	1125	101.17	6	49.38 (.38)	2.58 (.07)	12.96 (.42)	15.53 (.27)	0.47 (.07)	5.00 (.31)	10.51 (.29)	3.26 (.12)	0.31 (.01)	b.d.	0.81	37.67
ShR506	102	1150	99.80	6	50.55 (.3)	1.90 (.06)	13.70 (.18)	12.26 (.17)	0.45 (.08)	6.37 (.07)	11.82 (.07)	2.72 (.04)	0.23 (.01)	b.d.	0.86	49.37
ShR518	103	1175	100.85	10	50.36 (.21)	1.91 (.05)	13.81 (.12)	12.46 (.19)	0.39 (.05)	6.38 (.08)	11.84 (.16)	2.63 (.14)	0.22 (.02)	b.d.	0.86	48.99
ShR512	102	1200	100.86	8	50.40 (.53)	1.93 (.01)	13.74 (.19)	12.64 (.26)	0.37 (.04)	6.48 (.17)	11.59 (.13)	2.64 (.11)	0.22 (.02)	b.d.	0.84	49.02
ShR519	203	1125	101.28	13	49.06 (.24)	2.86 (.05)	12.65 (.12)	16.22 (.28)	0.49 (.08)	4.79 (.06)	10.05 (.13)	3.02 (.11)	0.34 (.02)	0.52 (.17)	0.79	35.65
ShR505	202	1150	99.33	5	50.12 (.26)	1.98 (.04)	14.02 (.11)	13.00 (.21)	0.40 (.06)	6.07 (.1)	11.26 (.05)	2.90 (.05)	0.25 (.01)	b.d.	0.80	46.69
ShR502	202	1175	101.72	20	50.19 (.26)	1.90 (.04)	13.65 (.13)	12.56 (.19)	0.38 (.06)	6.48 (.11)	11.72 (.14)	2.62 (.08)	0.20 (.01)	0.30 (.08)	0.86	49.18
ShR510	202	1200	100.84	9	50.51 (.35)	1.91 (.04)	13.71 (.09)	12.63 (.14)	0.36 (.04)	6.45 (.13)	11.57 (.14)	2.64 (.08)	0.22 (.01)	b.d.	0.84	48.94
ShR522	402	1125	100.42	5	46.26 (.17)	4.10 (.06)	11.93 (0.4)	20.07 (.62)	0.59 (.06)	4.04 (.23)	9.16 (.21)	2.93 (.07)	0.41 (.03)	0.51 (.06)	0.77	27.40
ShR504	401	1150	100.94	5	48.69 (.29)	2.58 (.06)	13.51 (.37)	16.22 (.47)	0.47 (.07)	5.34 (.23)	9.90 (.26)	2.99 (.15)	0.31 (.02)	b.d.	0.73	38.21
ShR501	402	1175	101.29	10	50.09 (.21)	1.98 (.04)	14.34 (.14)	12.61 (.2)	0.40 (.07)	6.00 (.09)	11.4 (.15)	2.69 (.1)	0.22 (.01)	0.29 (.09)	0.80	47.14
ShR508	402	1200	99.73	5	50.04 (.36)	1.94 (.05)	13.70 (.12)	12.45 (.37)	0.39 (.03)	6.57 (.03)	11.81 (.12)	2.64 (.13)	0.22 (.02)	0.23 (.02)	0.86	49.75
ShR507	698	1150	100.35	3	46.20 (.76)	3.80 (.69)	14.30 (.97)	18.84 (.11)	0.47 (0.1)	3.26 (.82)	9.04 (.54)	3.05 (.34)	0.42 (.09)	0.63 (.11)	0.63	24.51
ShR509	700	1175	100.49	11	47.92 (.23)	3.00 (.07)	13.14 (.24)	17.26 (.43)	0.45 (.05)	4.87 (.28)	9.66 (.35)	2.95 (.14)	0.33 (.02)	0.42 (.03)	0.73	34.59
ShR511	700	1200	99.70	6	49.88 (.46)	2.11 (.02)	14.67 (.25)	12.83 (.12)	0.41 (.08)	5.64 (.06)	10.99 (.06)	2.99 (.12)	0.24 (.02)	0.24 (.05)	0.75	45.19
ShR514	700	1225	100.86	14	50.63 (.35)	1.92 (.05)	13.70 (.16)	12.67 (.28)	0.39 (.05)	6.19 (.15)	11.61 (.17)	2.66 (.09)	0.23 (.01)	b.d.	0.85	47.84

Glass measurements in wt%, normalized to 100wt%. The the standard deviations (1σ) are given in brackets. The given total shows the not normalized value.

b.d. – below detection limit, *n* – number of analysis

Part II: The Role of H₂O and Pressure on Multiple Saturation and Liquid Lines of Descent in Basalts from the Shatsky Rise

Dissertation of Anika Husen

Table II.4: Compositions of experimental glasses from *hydrous* experiments

Run	P (MPa)	T (°C)	Total	n	SiO_2	TiO_2	Al_2O_3	FeOtot	MnO	MgO	CaO	Na_2O	K_2O	P_2O_5	CaO/ Al_2O_3	Mg#
starting material: AH 6																
ShR660	102	1100	101.51	4	47.10 (.94)	1.83 (.26)	15.53 (.06)	15.22 (1.3)	0.21 (.02)	5.00 (.31)	11.31 (.67)	3.51 (.29)	0.29 (.05)	b.d.	0.73	41.64
ShR662	105	1125	100.16	6	47.81 (.29)	1.60 (.03)	15.06 (.33)	13.85 (0.2)	0.25 (.05)	6.04 (.22)	11.74 (.11)	3.40 (.11)	0.25 (.01)	b.d.	0.78	48.66
ShR661	105	1135	99.72	5	48.39 (.29)	1.33 (.04)	15.33 (.32)	12.23 (.58)	0.23 (.08)	6.94 (.09)	12.14 (.32)	3.22 (.1)	0.18 (.01)	b.d.	0.79	55.21
ShR663	108	1155	101.16	5	48.22 (.27)	1.35 (.03)	14.90 (.24)	12.76 (.28)	0.23 (.07)	6.78 (.18)	12.50 (.2)	2.99 (.08)	0.18 (.02)	0.10 (.07)	0.84	53.60
ShR650	205	1125	99.81	13	48.88 (.38)	1.47 (.08)	16.01 (.78)	13.02 (.38)	0.24 (.05)	6.24 (.44)	10.91 (.65)	3.03 (.15)	0.21 (.02)	b.d.	0.68	51.01
ShR657	401	1125	99.93	9	47.39 (.46)	1.94 (.05)	16.32 (.46)	15.11 (.59)	0.30 (.05)	5.32 (.38)	9.77 (.71)	3.51 (.2)	0.34 (.04)	b.d.	0.60	43.34
ShR666	397	1150	99.27	5	47.54 (.26)	2.15 (.05)	15.41 (.29)	14.81 (0.3)	0.29 (.02)	5.99 (.19)	10.05 (.52)	3.16 (.09)	0.39 (.03)	0.19 (.06)	0.65	46.79
starting material: AH 3																
ShR360	102	1100	100.43	6	48.63 (.24)	2.25 (.05)	14.43 (.14)	14.31 (.25)	0.24 (.02)	5.63 (.21)	10.84 (.18)	3.36 (.17)	0.31 (.02)	b.d.	0.75	46.08
ShR362	105	1125	100.42	7	49.30 (.24)	2.00 (.02)	14.82 (.22)	12.89 (.37)	0.24 (.02)	5.89 (.07)	11.37 (.07)	3.20 (.15)	0.27 (.01)	b.d.	0.77	49.84
ShR361	105	1135	100.23	13	49.80 (.29)	1.57 (.02)	15.79 (.14)	10.33 (.21)	0.22 (.05)	6.68 (.12)	12.38 (.19)	3.03 (.15)	0.21 (.01)	b.d.	0.78	58.42
ShR363	108	1155	99.80	12	49.61 (.34)	1.56 (.03)	15.17 (.19)	10.62 (.25)	0.18 (.05)	7.24 (.14)	12.61 (.18)	2.67 (.07)	0.20 (.01)	0.14 (.06)	0.83	59.73
ShR358	202	1075	99.55	7	48.40 (.23)	2.90 (.03)	14.65 (.18)	15.37 (.28)	0.30 (.07)	4.73 (.08)	9.84 (.1)	3.39 (.1)	0.42 (.02)	b.d.	0.67	40.11
ShR354	201	1100	100.33	8	48.56 (.24)	2.64 (.04)	14.70 (.14)	15.29 (.29)	0.26 (.06)	5.04 (.14)	9.53 (.31)	3.20 (.1)	0.37 (.02)	0.42 (.01)	0.65	41.72
ShR350	205	1125	100.12	9	49.57 (.18)	1.93 (.03)	15.66 (.17)	12.46 (.3)	0.24 (.05)	5.88 (.12)	10.86 (.3)	3.12 (.08)	0.28 (.02)	b.d.	0.69	50.62
ShR351	204	1150	100.00	20	49.66 (.26)	1.43 (.04)	15.65 (.11)	9.95 (.24)	0.23 (.04)	7.78 (.14)	12.55 (.13)	2.54 (.12)	0.19 (.02)	b.d.	0.80	62.96
ShR359	401	1100	100.43	6	47.97 (.68)	2.84 (.07)	15.29 (.31)	15.42 (.22)	0.29 (.02)	4.93 (.17)	9.19 (.23)	3.24 (.11)	0.45 (.04)	0.39 (.01)	0.60	40.98
ShR357	401	1125	99.83	7	48.21 (.31)	2.39 (.08)	15.31 (.44)	15.27 (.35)	0.27 (.07)	5.43 (.32)	9.41 (.39)	3.33 (.18)	0.38 (.03)	b.d.	0.61	43.61
ShR366	397	1150	98.73	7	47.70 (.31)	2.35 (.04)	14.95 (.23)	15.34 (.22)	0.21 (.06)	5.87 (.2)	9.89 (.18)	3.13 (.11)	0.32 (.01)	0.20 (.08)	0.66	45.43
starting material: AH 5																
ShR560	102	1100	101.08	11	49.74 (.24)	2.24 (.03)	14.26 (.16)	14.18 (.32)	0.37 (.06)	5.58 (.13)	10.31 (.13)	3.06 (.11)	0.25 (.02)	b.d.	0.72	46.09
ShR562	105	1125	100.28	13	50.14 (.39)	1.97 (.04)	14.44 (.23)	12.72 (.33)	0.41 (.08)	5.90 (.12)	11.13 (.14)	3.07 (.12)	0.23 (.02)	b.d.	0.77	50.21
ShR561	105	1135	100.10	12	50.61 (.28)	1.95 (.03)	13.91 (.17)	11.84 (.23)	0.38 (.08)	6.44 (.06)	11.84 (.16)	2.80 (.09)	0.22 (.01)	b.d.	0.85	54.19
ShR563	108	1155	99.59	15	50.24 (.19)	1.95 (.03)	13.66 (.14)	12.42 (.31)	0.37 (.07)	6.63 (.11)	11.68 (.19)	2.62 (.12)	0.21 (.02)	0.19 (.1)	0.86	53.70
ShR558	202	1075	99.32	7	49.88 (.27)	2.68 (.05)	14.22 (.15)	15.46 (.28)	0.47 (.07)	4.52 (.09)	9.22 (.2)	3.22 (.17)	0.33 (.01)	b.d.	0.65	38.83
ShR554	201	1100	100.58	9	49.06 (.18)	2.56 (.03)	13.67 (.14)	15.79 (.3)	0.46 (.07)	5.09 (.15)	9.59 (.2)	3.08 (.07)	0.28 (.02)	0.42 (.02)	0.70	41.19
ShR550	205	1125	100.06	10	50.66 (.24)	2.04 (.02)	15.05 (.17)	12.58 (.19)	0.38 (.07)	5.32 (.11)	10.75 (0.1)	2.97 (.08)	0.25 (.02)	b.d.	0.71	47.89
ShR551	204	1150	99.78	40	51.28 (.26)	2.00 (.04)	13.89 (.16)	11.16 (.23)	0.40 (.05)	6.55 (.13)	11.85 (.15)	2.64 (.09)	0.23 (.02)	b.d.	0.85	56.08
ShR559	401	1100	99.48	4	49.25 (.35)	2.98 (.06)	14.36 (.34)	16.37 (.2)	0.46 (.04)	4.67 (.31)	8.46 (.54)	3.06 (.11)	0.37 (.02)	b.d.	0.59	38.28
ShR566	397	1150	99.20	8	49.44 (.29)	2.31 (.04)	14.31 (.17)	14.46 (.28)	0.43 (.08)	5.41 (.06)	10.08 (.18)	3.04 (.11)	0.25 (.01)	0.25 (.08)	0.70	44.83

Glass measurements in wt%, normalized to 100wt%. The the standard deviations (1σ) are given in brackets. The given total shows the not normalized value.

b.d. – below detection limit, *n* – number of analysis

Part II: The Role of H₂O and Pressure on Multiple Saturation and Liquid Lines of Descent in Basalts from the Shatsky Rise

5.5. Liquid Composition

Residual glass compositions for each starting material for *dry* and *hydrous* sets of experiments are shown on the left and right plots respectively in Figs. II.5-II.8 for CaO, Al_2O_3, CaO/Al_2O_3, and SiO_2 and in the supplementary material in the Appendix II for FeO, Na_2O, CaO, and Al_2O_3 (Fig. AII.3 - AII.6). Similar to previous studies conducted on basalts under anhydrous conditions (Grove and Bryan, 1983; Tormey et al., 1987; Kinzler and Grove, 1992; Yang et al., 1996; Grove et al., 1992, Whitaker et al., 2007), the evolution of the liquid phase in our experiments proceeds along *Ol+Plag*, *Cpx+Plag* and *Ol+Plag+Cpx* mineral cotectics and thus, follows a typical tholeiitic differentiation trend of FeO enrichment.

Figure II.5: The experimentally produced LLDs (dark grey solid lines) for CaO (wt%) for the intermediate one of the three starting materials (black stars), AH3, are shown in comparison to the range of natural EPR MORBs (grey points, PetDB). A) shows *dry* LLDs, b) shows *hydrous* LLDs. Different pressures are indicated by different symbols (see legend). In the diagram displaying hydrous conditions, also dry LLDs are shown for comparison (light grey dashed lines).

Part II: The Role of H_2O and Pressure on Multiple Saturation and Liquid Lines of Descent in Basalts from the Shatsky Rise

Under *dry* conditions (< 0.15 wt% H_2O), FeO, K_2O, TiO_2, and Na_2O abundances in the residual glasses continuously increase during crystallization. Behaviors of CaO and Al_2O_3 are controlled by the presence of *Cpx* or *Plag* amongst the crystallizing minerals, respectively. CaO (Fig. II.5a) slightly increases during *Ol+Plag* crystallization (e.g. at 100 MPa in AH3, Fig. II.5a) and strongly decreases in all *Cpx*-bearing runs. As discussed above, the proportion of *Cpx* in the solid phase is gradually increasing with pressure (Fig. II.4). This leads to a stronger decrease in the melt CaO contents and also in a sharper drop of the melt CaO/Al_2O_3 ratio (Fig. II.6) in the high pressure runs. Al_2O_3 (Fig. II.7a) is progressively decreasing in *Ol+Plag* or *Ol+Plag+Cpx* saturated experiments, and increasing in *Plag+Cpx* saturated and *Plag*-free runs (e.g. in runs at 700 MPa: AH3, Fig. II.7a). Low pressures drive the liquids to more Al_2O_3-depleted compositions; these are usually experiments where *Plag* is the dominant phase.

The most interesting observation in our experiments is the strong SiO_2 depletion with progression of crystallization, which results in a deviation of the evolutionary path away from the field of natural tholeiitic MORB glasses (Fig. II.8, see also discussion below). The degree of SiO_2 depletion correlates positively with pressure, especially in the two most primitive starting materials AH3 and AH6 (Fig. II.8a and b) - stronger depletion is observed in runs conducted at higher pressures. SiO_2 enrichment is recognized in *Plag*-free runs with only *Ol* or *Cpx* crystallization, and in the early stage of crystallization, where *Ol* dominates the solid phase (e.g. AH6 at low pressures or AH5 at 700 MPa).

Part II: The Role of H$_2$O and Pressure on Multiple Saturation and Liquid Lines of Descent in Basalts from the Shatsky Rise
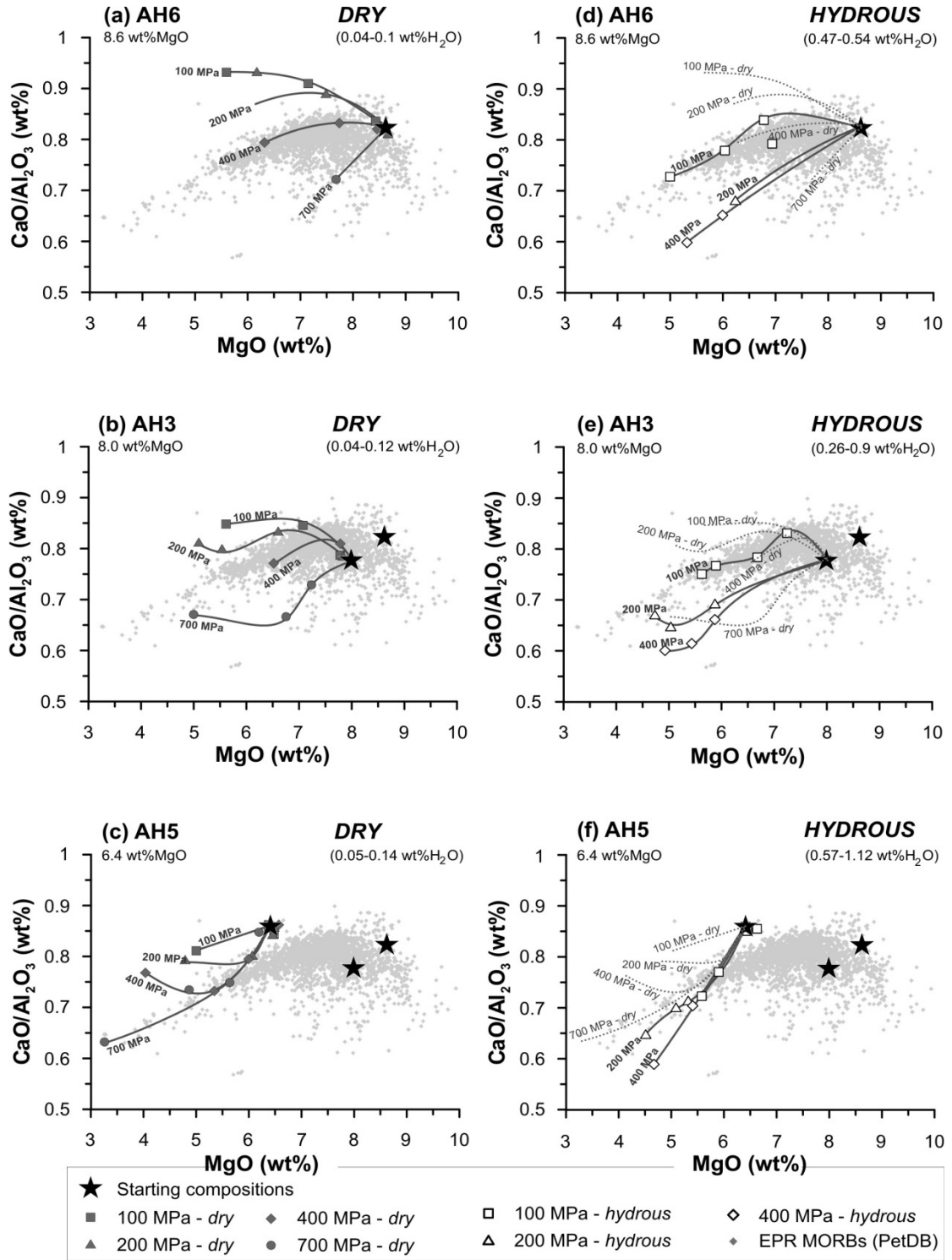
Figure II.6: The experimentally produced LLDs (dark grey solid lines) for CaO/Al$_2$O$_3$ (wt%) for three different starting materials (black stars) are shown in comparison to the range of natural EPR MORBs (grey points, PetDB). Different columns show different H$_2$O contents (left: *dry*, right: *hydrous*) and starting compositions vary from top to bottom (AH6 - AH3 - AH5). Different pressures are indicated by different symbols (see legend). In diagrams displaying hydrous conditions also dry LLDs are shown for comparison (light grey dashed lines).

Part II: The Role of H$_2$O and Pressure on Multiple Saturation and Liquid Lines of Descent in Basalts from the Shatsky Rise
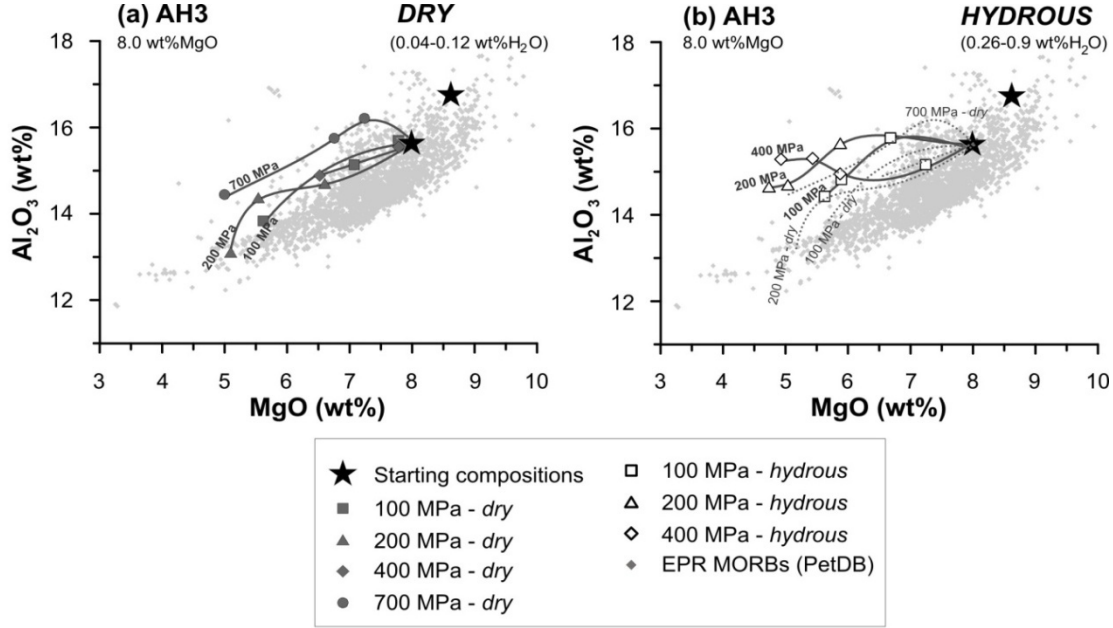
Figure II.7: The experimentally produced LLDs (dark grey solid lines) for Al$_2$O$_3$ (wt%) for the intermediate one ot the three starting materials (black stars), AH3, are shown in comparison to the range of natural EPR MORBs (grey points, PetDB). A) shows *dry* LLDs, b) shows *hydrous* LLDs. Different pressures are indicated by different symbols (see legend). In the diagram displaying *hydrous* conditions also *dry* LLDs are shown for comparison (light grey dashed lines).

Elevated melt H$_2$O concentrations in our *hydrous* experiments (0.4-1.1 wt% H$_2$O) principally did not change the trends observed for FeO, K$_2$O, TiO$_2$, and Na$_2$O in the residual liquids. However, compared to *dry* conditions, Al$_2$O$_3$ is less efficiently extracted from the *hydrous* melts due to the relatively late crystallization of *Plag* compared to the other minerals, especially *Cpx* (Fig. II.7). This results in slightly higher Al$_2$O$_3$ contents in the *hydrous* melts compared to *dry* melts produced at similar pressures. In contrast, CaO in *hydrous* residual melts is more depleted than in *dry* liquids (Fig. II.5); this extent of CaO depletion (*hydrous* LLD versus *dry* LLD) is most pronounced in the most MgO-rich basalt AH6 and is decreasing in transition to the evolved AH3 composition (e.g. compare isobar under *dry* and *hydrous* conditions in Fig. AII.5 a-d for AH6 and AH3). Similar to our *dry* experiments, the CaO/Al$_2$O$_3$ ratio in *hydrous* residual melts decreases in *Cpx*-

Dissertation of Anika Husen

Part II: The Role of H$_2$O and Pressure on Multiple Saturation and Liquid Lines of
Descent in Basalts from the Shatsky Rise

bearing runs and the extent of this depletion is pressure dependent (Fig. II.6). In addition,
our new experiments demonstrate how the CaO/Al$_2$O$_3$ ratio decreases in the presence of
small amounts of H$_2$O. This effect is even more pronounced compared to the CaO/Al$_2$O$_3$
drop induced by pressure (compare left and right column in Fig. II.6; see also discussion
below). In contrast to *dry* conditions, SiO$_2$ in *hydrous* residual melts decreases only
slightly (AH3 and AH5) or even behaves constantly (AH6) with progression of
crystallization (Fig. II.8).

Progressive crystallization and decrease of the melt fraction (F$_{melt}$) reasonably
correlates with the decrease of the melt Mg# (Fig. II.9). In all three basalts with different
initial Mg#, there is a linear dependence of the F$_{melt}$ and melt Mg#, clearly illustrating that
melt Mg# can be utilized as an index of differentiation. The residual liquids produced
under *dry* and *hydrous* conditions at different pressures follow the same trends (Fig. II.9)
defined by the Mg# of the given basaltic composition. It should be emphasized, that for
each basalt, the *hydrous* liquids are slightly, but systematically more MgO-rich (higher
Mg#) than the *dry* melts. This is a direct result of more oxidized conditions prevailing in
the *hydrous* set of experiments (Tab II.2) which results in lower proportions of the Fe^{2+} in
the melt, and thus higher values of the Mg#.

Part II: The Role of H₂O and Pressure on Multiple Saturation and Liquid Lines of Descent in Basalts from the Shatsky Rise
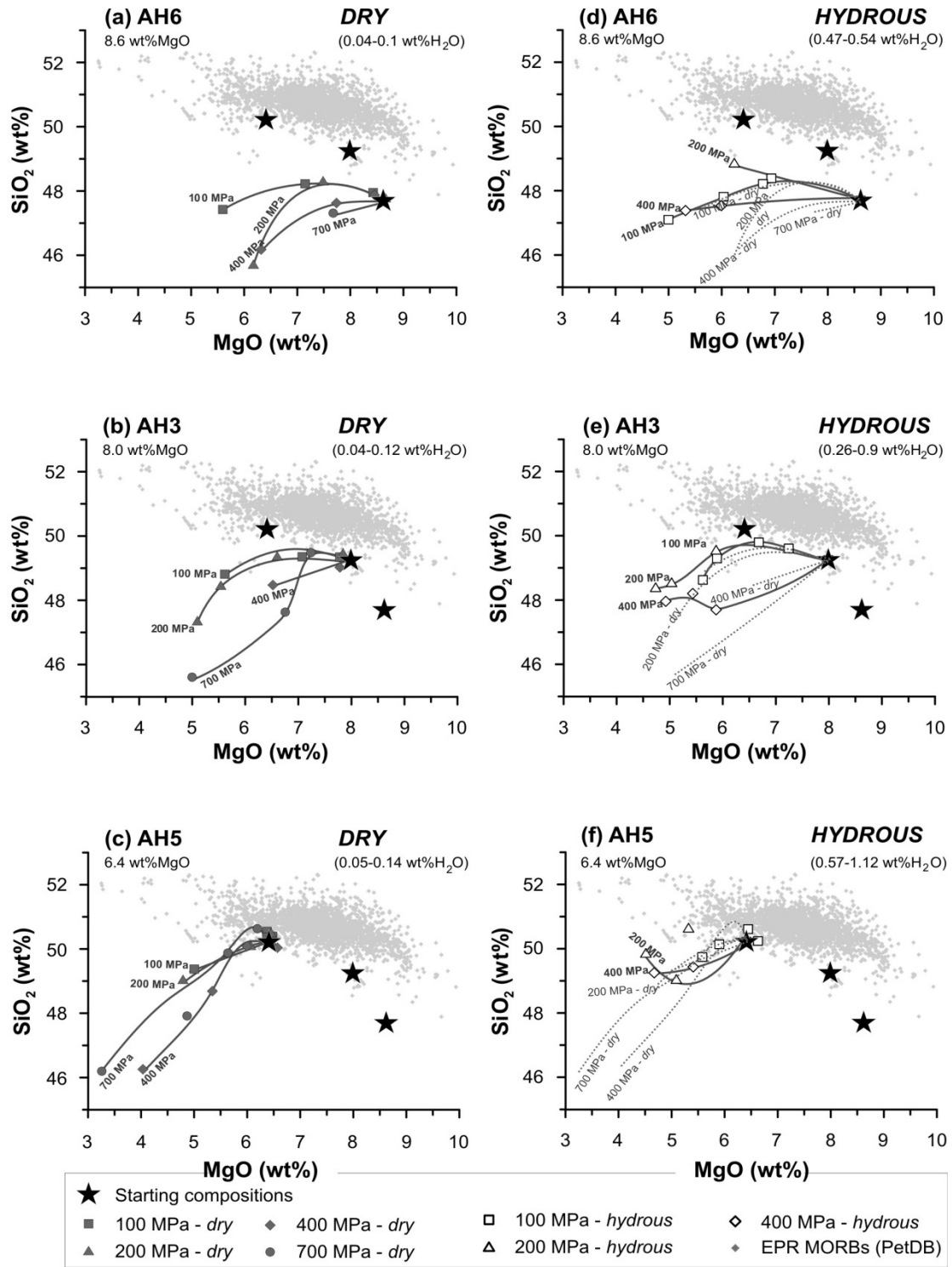
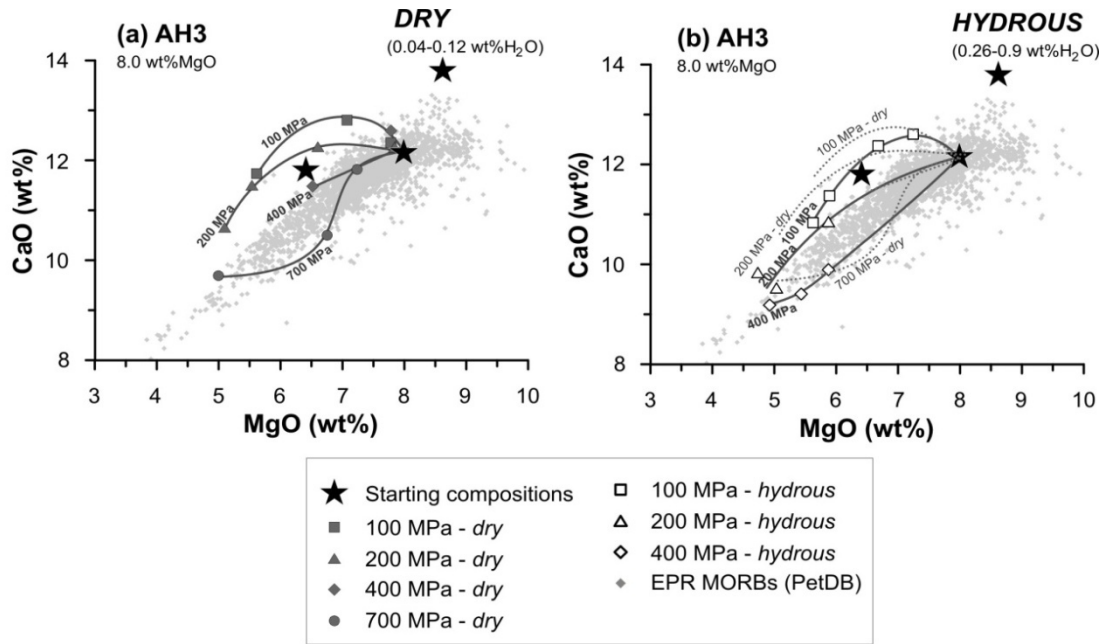**Figure II.8:** The experimentally produced LLDs (dark grey solid lines) for SiO_2 (wt%) for three different starting materials (black stars) compared to the range of natural EPR MORBs (grey points, PetDB). *Dry* and *hydrous* H_2O contents are shown in left and right column respectively; the starting compositions vary from top to bottom (AH6 - AH3 - AH5). In diagrams displaying *hydrous* conditions also *dry* LLDs are shown for comparison (light grey dashed lines).

Part II: The Role of H₂O and Pressure on Multiple Saturation and Liquid Lines of
Descent in Basalts from the Shatsky Rise
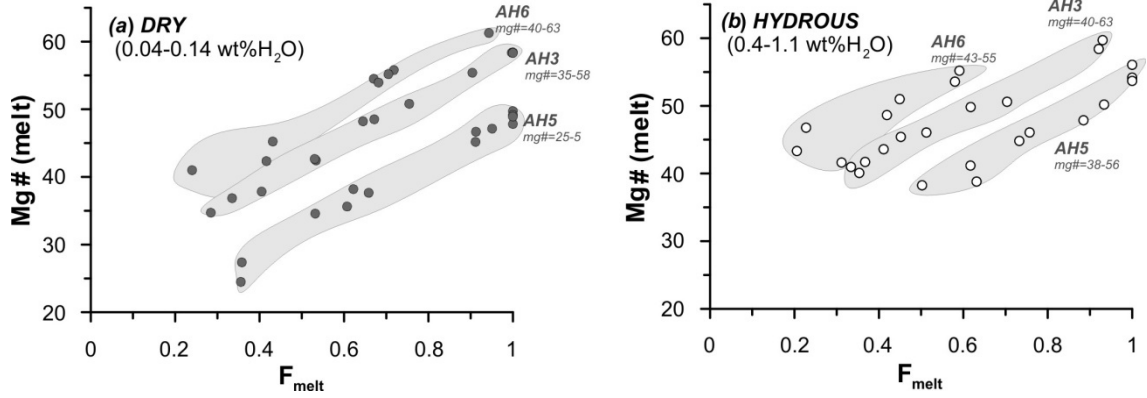
Figure II.9: The melt evolution (represented by the melt Mg#) with increasing crystallization
degree (decreasing melt fraction) is shown for *dry* (a) and *hydrous* conditions (b). Note that due to higher
fO_2 in *hydrous* experiments, the Fe^{2+} in melts is relatively lower causing a relatively higher Mg#.
Experimental melts produced by the different starting materials are marked by grey fields as indicated by
labels.
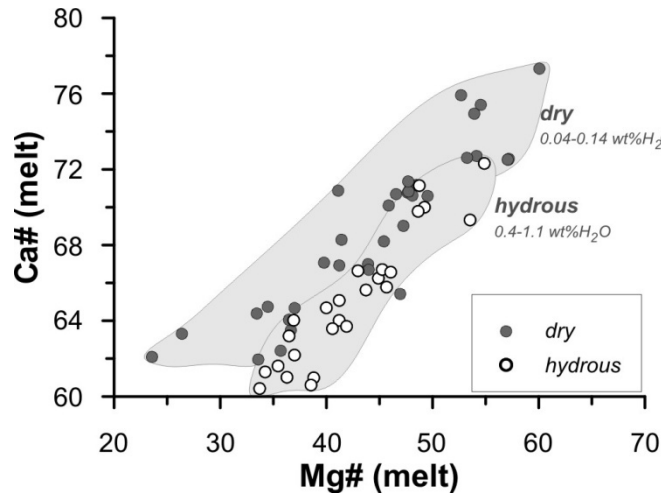
Figure II.10: The evolution of Ca# of the melt [Ca#= Ca/(Ca+Na)] is shown dependent on the
Mg# (representative of crystallization degree). Different H₂O conditions are represented by different colors
(*dry*: dark grey, *hydrous*: white) and are additionally highlighted by grey fields. Although, higher Mg# in
hydrous experiments are related to higher fO_2 in *hydrous* experiments, and thus relatively lower Fe^{2+} in
melts, *hydrous* experiments revealed to systematically lower Ca# compared to *dry* experiments.

Part II: The Role of H₂O and Pressure on Multiple Saturation and Liquid Lines of Descent in Basalts from the Shatsky Rise
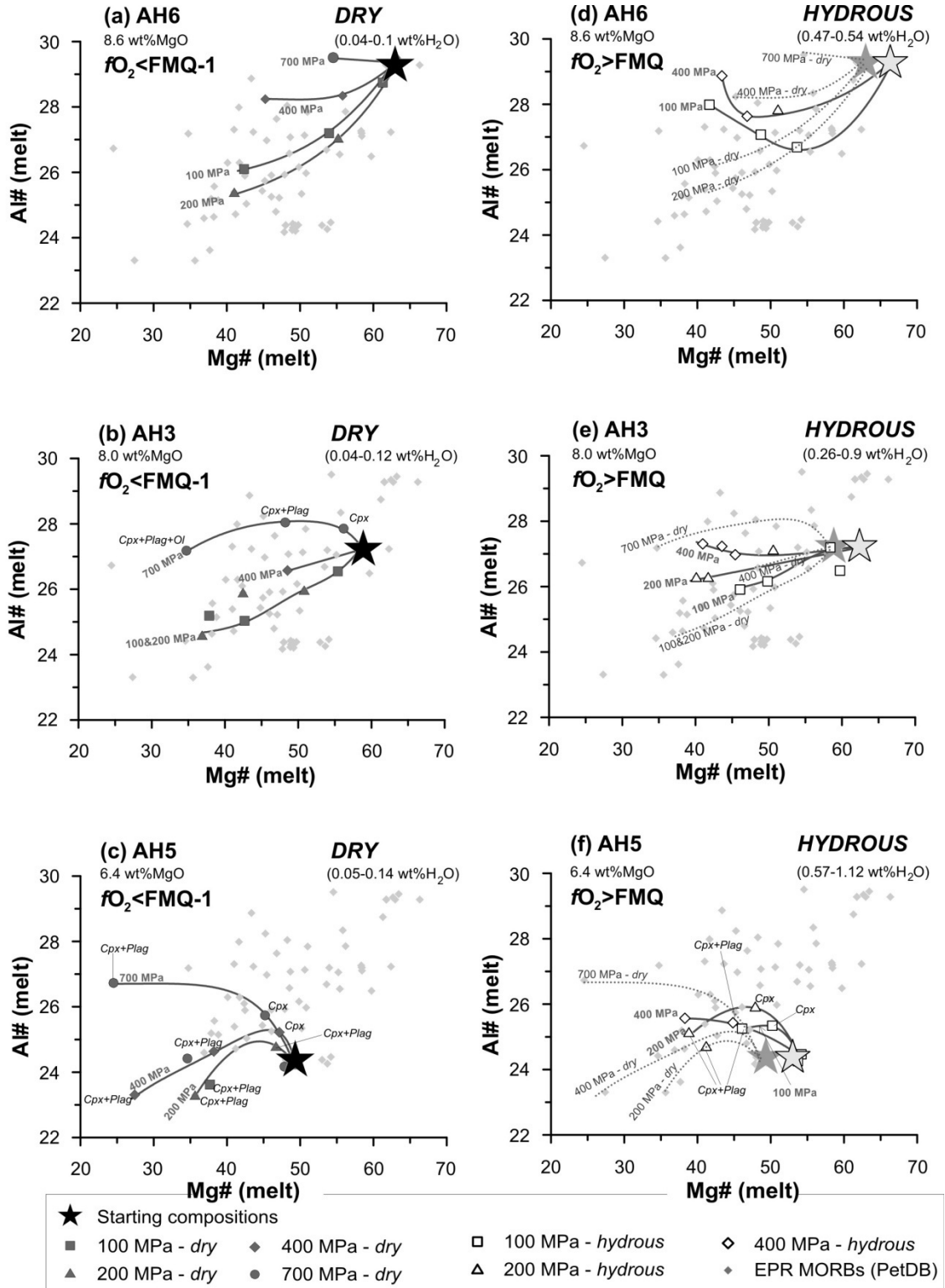

**Figure II.11:** Evolution of Al# of the melt [Al#=Al/(Si+Al)] is shown dependent on Mg# (representative of crystallization degree). Isobaric experiments are connected by solid lines. Left and right column show diagrams for *dry* and *hydrous* conditions respectively. From top to bottom LLDs from different starting compositions (stars) are displayed (AH6 - AH3 - AH5). In diagrams for *hydrous* experiments also results of *dry* experiments are shown for comparison (light dashed lines, darker grey star). The mineral assemblage is given by labels for AH3 (b) and AH5 (c and f).

The effect of small amounts of H_2O and pressure on liquid composition can also be resolved when other compositional characteristics are used. For example, *hydrous* glasses (0.4-1.1 wt% H_2O) tend to have slightly but systematically lower Ca# [Ca#=Ca/(Ca+Na)] than *dry* melts (<0.1 wt% H_2O) at similar degrees of crystallization (Fig. II.10) (when Mg# is used as indices of differentiation). In addition to CaO/Al_2O_3 ratio, the melt Al# [Al#=Al/(Si+Al)] strongly varies with pressure. In general, in both, *dry* and *hydrous* experiments, melt Al#s are higher in experiments conducted at higher pressures (Fig. II.11). When compared to the starting compositions, the Al# decreases in melts saturated with *Ol+Plag* and increases in liquids which are in equilibrium with *Cpx* (e.g. melt Al# is increasing during single *Cpx* crystallization in *dry* experiments in AH6 and AH3 at 700 MPa as well as in AH5 at all investigated pressures (#ShR317 and #ShR501, Fig. II.11b and c, Tab. II.2)). When compared to *dry* conditions, the experimental liquids produced in the presence of small amounts of H_2O tend to have systematically higher values of the melt Al# due to the relatively higher *Cpx* proportion in the presence of higher melt H_2O (see e.g. *dry* and *hydrous* isobaric trends for AH3 starting composition in Fig. II.11b and d).

5.6. Mineral Composition

The effects of experimental temperatures, pressures and different H_2O contents on the mineral compositions are shown in Figs. II.12-II.15 and in the Appendix II (Figs. AII.7-AII.9). In general, temperature decrease leads to the crystallization of Fe-rich *Ol* and *Cpx*, and albite-rich *Plag*. Pressure increases the stabilities of the minerals with the following consequences: at similar temperatures, the experimental charges produced at higher pressures are more crystallized, residual glass compositions are more evolved, and the Fe-Mg silicates are less MgO-rich, as well as *Plag* is more albitic. In contrast to *dry*

conditions, H_2O depresses the liquidus of the investigated basalts, resulting in the crystallization of minerals with more primitive compositions (more MgO-rich *Ol* and *Cpx* and more anorthitic *Plag*) at lower temperatures (Figs. AII.7-AII.9).
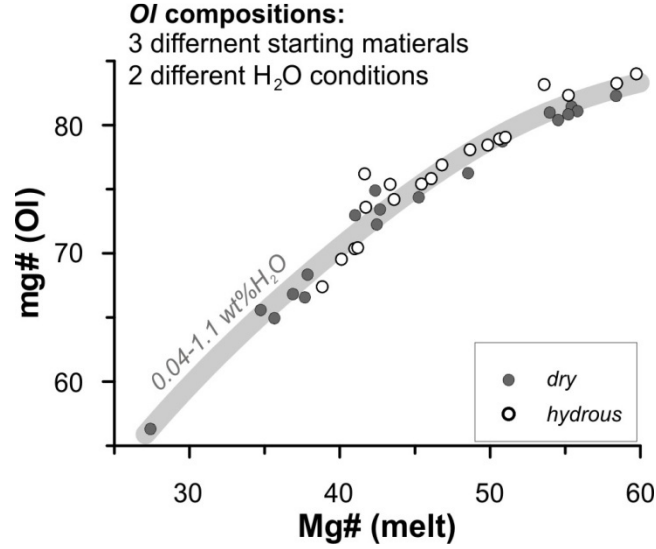
Figure II.12: Correlation of *Ol* compositions represented by their Mg# (averages of 3-16 analyses) is shown. Grey and white dots represent experiments at *dry* and *hydrous* conditions respectively.

5.6.1 *Olivine*

The compositions of the experimentally produced *Ol* range between 55 and 88 mol% Fo. In general, Fo-rich *Ol* are found in the more MgO-rich starting materials (Tabs. II.5 and II.6, and Fig. AII.7). For example, under similar *P-T* conditions (all are at 100 MPa and 1150°C) *Ol* from the AH6 basalt has Fo_{74} under *dry* and Fo_{82} under *hydrous* conditions, whereas the *Ol* from AH3 are Fo_{72} and Fo_{83}. *Ol* in the most evolved AH5 is the latest phase appearing after >30% of onset *Plag+Cpx* crystallization in both *dry* and *hydrous* experiments. It has maximum Fo_{65} under *dry* and Fo_{70} under *hydrous* conditions. In experiments where *Ol* is the liquidus phase (AH6, AH3 100-400 MPa, Fig. AII.7a and b) it is clearly seen that with pressure increase, the Fo content in *Ol* systematically

Part II: The Role of H$_2$O and Pressure on Multiple Saturation and Liquid Lines of Descent in Basalts from the Shatsky Rise

**Table II.5:** Summary of compositions of experimental minerals in *dry* experiments

| Run	P (MPa)	T (°C)	Dur (h)	*Ol*	Fo (mol%)	Mg # (Ol)	K$_{DFe-Mg}$ (Ol)	*Plag*	An (mol%)	K$_{DCa-Na}$ (Plag)	*Cpx*	MGN# (Cpx)	K$_{DFe-Mg}$ (Cpx)
starting material: AH6													
ShR603	102	1150	60		73.85	74.91	0.25		74.04	1.19		81.25	0.17
ShR616	103	1175	46		80.04	80.99	0.28		74.39	0.92		83.40	0.23
ShR609	102	1200	46		84.22	85.03	0.28		81.18	1.26			
ShR602	202	1150	73		71.92	72.98	0.26		73.30	1.38		79.20	0.18
ShR615	203	1175	71		79.95	80.85	0.29		78.22	1.20		85.03	0.22
ShR601	401	1150	91		66.33	67.40			71.70			74.57	
ShR619	402	1175	64		73.40	74.38	0.28		72.18	1.31		79.19	0.22
ShR605	402	1200	63		80.24	81.10	0.29		76.51	1.06		82.91	0.26
ShR604	698	1150	60		58.74	60.26			63.01			68.27	
ShR606	700	1175	60		63.50	64.46			67.89			68.42	
ShR611	700	1225	60		79.73	80.41	0.29		73.42	1.05		82.77	0.25
starting material: AH3													
ShR322	101	1125	48		67.27	68.35	0.28		64.28	1.05		76.64	0.19
ShR318	106	1150	65		72.45	73.43	0.27		64.98	0.87		79.79	0.19
ShR321	103	1175	46		80.60	81.45	0.28		73.39	1.05		0.00	
ShR324	203	1125	108		65.79	66.83	0.29		62.65	1.03		75.95	0.19
ShR323	202	1150	73		71.31	72.27	0.28		67.49	1.04		79.66	0.19
ShR305	202	1175	68		77.83	78.74	0.28		69.85	0.98		82.44	0.22
ShR326	402	1125	66		59.73	60.66			59.49			68.03	
ShR307	401	1150	91		67.51	68.43	0.28		63.03	0.82		74.61	0.21
ShR304	400	1175	89		75.41	76.27	0.29		67.86	0.97		80.43	0.23
ShR311	402	1200	63		81.57	82.29	0.30						
ShR310	698	1150	60		58.35	59.19			57.39			62.71	
ShR312	700	1175	60		64.46	65.60	0.28		60.99	0.98		70.15	0.23
ShR314	700	1200	60						65.79	1.03		78.01	0.26
ShR317	700	1225	60									83.70	0.25
starting material: AH5													
ShR520	101	1125	48		65.36	66.58	0.30		61.45	0.91		74.86	0.20
ShR506	102	1150	60									79.32	0.25
ShR519	203	1125	108		63.90	64.96	0.30		61.20	0.87		73.61	0.20
ShR505	202	1150	73						65.61	0.90		78.05	0.25
ShR522	402	1125	66		55.19	56.32	0.29		53.27	0.68		63.87	0.21
ShR504	401	1150	91						60.57	0.85		72.87	0.23
ShR501	400	1175	89									78.37	0.25
ShR507	698	1150	60						52.55	0.70		62.75	0.19
ShR509	700	1175	60						56.02	0.72		68.47	0.24
ShR511	700	1200	60									76.66	0.25

Ol – olivine, Plag – plagioclase, Cpx – clinopyroxene, Dur – duration
Fo – Forsterite content, An – Anorthite content
$K_{DFe-Mg}=(X_{Fe}^{xtl} \cdot X_{Mg}^{liq})/ (X_{Mg}^{xtl} \cdot X_{Fe}^{liq})$
$K_{DCa-Mg}=(X_{Ca}^{xtl} \cdot X_{Na}^{liq})/(X_{Na}^{xtl} \cdot X_{Ca}^{liq})$
Detailed data on mineral compositions is given in Tabs. AII.1-AII.7, all presented values represent averages of 2-10 measurements

decreases for given temperature. However, it should be emphasized, that runs produced at similar temperatures, but at different pressures, have significantly different stages of fractionation (e.g. in AH6 at 1200°C, crystallinities and glass Mg# numbers are 0.06 and 60 at 100 MPa, and 0.48 and 46 at 700 MPa). When compositions of experimental *Ol* are compared to their corresponding melt Mg# (which strongly correlates with crystallization degree and is independent on pressure and melt H$_2$O), no effect of pressure or H$_2$O on the Fo content (Mg#) in *Ol* can be recognized (Fig. II.12).

Part II: The Role of H$_2$O and Pressure on Multiple Saturation and Liquid Lines of Descent in Basalts from the Shatsky Rise

Table II.6: Summary of compositions of experimental minerals in *hydrous* experiments

Run	P (MPa)	T (°C)	Dur (h)	*Ol*	Fo (mol%)	Mg # (Ol)	K$_{DFe-Mg}$ (Ol)	*Plag*	An (mol%)	K$_{DCa-Na}$ (Plag)	*Cpx*	MGN# (Cpx)	K$_{DFe-Mg}$ (Cpx)
starting material: AH6													
ShR660	102	1100	64		75.20	76.21	0.22		71.74	1.44		73.57	0.26
ShR662	105	1125	65		77.22	78.09	0.27		72.97	1.43		75.36	0.31
ShR661	105	1135	89		81.53	82.34	0.26		79.65	1.88		79.32	0.32
ShR663	108	1155	64		82.26	83.18	0.23		81.18	1.88		78.49	0.32
ShR658	202	1075	64		71.01	72.01			65.55			71.63	
ShR654	201	1100	70		73.63	74.65			68.53			73.91	
ShR650	205	1125	65		78.25	79.06	0.28		75.89	1.58		74.85	0.35
ShR659	401	1100	70		71.02	71.92			65.29			70.68	
ShR665	402	1100	67		71.62	72.97			63.70			71.58	
ShR657	401	1125	62		74.53	75.39	0.25		66.83	1.33		71.97	0.30
ShR666	397	1150	63		76.14	76.91	0.26		67.89	1.23		72.76	0.33
starting material: AH3													
ShR360	102	1100	64		74.98	75.84	0.27		67.08	1.16		74.58	0.29
ShR362	105	1125	65		77.62	78.46	0.27		65.00	0.96		76.73	0.30
ShR361	105	1135	89		82.49	83.27	0.28		73.88	1.27		81.48	0.32
ShR363	108	1155	64		83.19	84.01	0.28		73.31	1.06		79.14	0.39
ShR358	202	1075	64		68.72	69.55	0.29		59.76	0.94		71.34	0.27
ShR354	201	1100	70		72.83	73.61	0.26		62.46	1.03		74.17	0.25
ShR350	205	1125	65		78.17	78.94	0.27		67.72	1.10		76.79	0.31
ShR359	401	1100	70		69.41	70.37	0.29		59.66	0.96		70.52	0.29
ShR357	401	1125	62		73.46	74.21	0.27		63.65	1.14		71.21	0.31
ShR366	397	1150	63		74.67	75.42	0.27		65.36	1.10		71.78	0.33
starting material: AH5													
ShR560	102	1100	64						66.00	1.05		73.25	0.31
ShR562	105	1125	65									76.88	0.30
ShR561	105	1135	89									79.74	0.30
ShR558	202	1075	64		66.47	67.41	0.31		59.80	0.95		71.02	0.26
ShR554	201	1100	70		69.51	70.45	0.29		63.38	1.02		71.11	0.28
ShR550	205	1125	65									75.07	0.31
ShR559	401	1100	70						55.32	0.82		66.73	0.31
ShR566	397	1150	63						61.69	0.89		73.04	0.30

Ol – olivine, Plag – plagioclase, Cpx – clinopyroxene, Dur – duration
Fo – Forsterite content, An – Anorthite content
$K_{DFe-Mg} = (X_{Fe}^{xtl} \cdot X_{Mg}^{liq}) / (X_{Mg}^{xtl} \cdot X_{Fe}^{liq})$
$K_{DCa-Mg} = (X_{Ca}^{xtl} \cdot X_{Na}^{liq}) / (X_{Na}^{xtl} \cdot X_{Ca}^{liq})$
Detailed data on mineral compositions is given in Tabs. AII.1-AII.7, all presented values represent averages of 2-16 measurements

For most of the experiments, the K$_D$s for Fe-Mg exchange are in the range of 0.26-0.31 (calculated using known Fe^{2+} in the melt, Tab. II.5 and II.6). Only runs with high degrees of crystallization have K$_D$s below 0.26, probably indicating analytical problems (small melt pools) or problems with the achievement of equilibrium conditions in these runs with very low proportion of the liquid phase. Our experimental data do not demonstrate any systematic effects of H$_2$O or pressure on *Ol*-melt exchange equilibria.

5.6.2 *Plagioclase*

It has been previously demonstrated in many experimental studies, that *Plag* shows systematic compositional changes with temperature, pressure, and melt H$_2$O. For

example, under *dry* conditions, within the temperature interval of about 50°C, the *Plag* composition is becoming ~10 mol% lower in An content in all studied basalts. Higher pressures seem to favor the crystallization of more albitic *Plag* (see e.g. runs #ShR603 (74 mol%An in *Plag*) and #ShR604 (63 mol%An in *Plag*) at 1150°C and 200 and 700 MPa, Tab. II.5 and II.6, and Fig. AII.8a). However, similar to the effect of pressure on *Ol* composition discussed above, the runs conducted at similar temperatures but various pressures strongly differ in the degrees of crystallization (in the case of #ShR603 and #ShR604, melt proportions are 42wt% in #ShR603, whereas #ShR604 is completely crystallized). When *Plag* composition is plotted versus melt Mg# (Fig. II.13a), it can be noticed that the pressure has no significant effect on the An content in the experimental *Plag* (*Plag* at 700 MPa is only ~ 2-3 mol% An poorer than *Plag* at 100 MPa). In comparison to *dry* conditions, the *Plag* produced at similar degree of crystallization (Mg# or F$_{liq}$) but under *hydrous* conditions has similar composition. Note, however, the temperatures between *dry* and *hydrous* counterparts are different. Both, pressure and melt H$_2$O content, affect the stability of the *Plag* by increasing (pressure) or decreasing (H$_2$O) the temperature of the *Plag*-melt equilibria. Additionally, the solid assemblage plays a major role as shown in Fig. II.13a (melt Mg# vs. An), where *Plag* compositions can be easily distinguished between *Ol*+*Plag* (high-An *Plag*) and *Ol*+*Plag*+*Cpx* (low-An *Plag*) cotectic assemblages.

In contrast to pressure and melt H$_2$O, the effect of the melt composition on *Plag* seems to be more evident. As displayed in Tab. II.5 and II.6, *Plag* crystallizing from AH6, AH3 and AH5 starting compositions have 63-81, 57-75 and 52-66 mol% An respectively. The most primitive AH6 basalt crystallizes An-rich *Plag* at higher temperature, whereas the evolved basalt AH5 is crystallizing *Plag* with more albitic composition at lower temperatures.

Part II: The Role of H$_2$O and Pressure on Multiple Saturation and Liquid Lines of Descent in Basalts from the Shatsky Rise
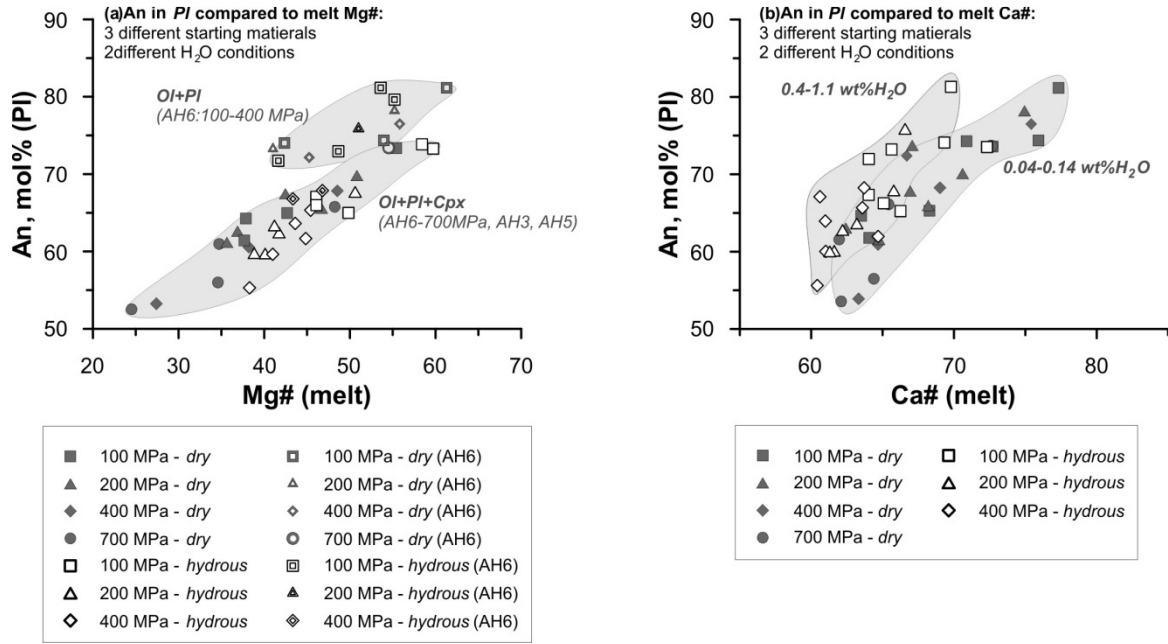
Figure II.13: Correlation of *Plag* composition represented by the An content (mol%) (averages of 2-10 analyses) with melt Mg# (a) and melt Ca# (b) is shown. Different symbols represent different experimental pressures, grey and white symbols indicate *dry* and *hydrous* conditions respectively. In a, experiments using AH6 are represented by open symbols. Grey fields mark experiments with similar characteristics (a: liquidus mineral assemblage, b: H$_2$O conditions).

Panjasawatwong et al. (1995) have demonstrated that *Plag* compositions depend on melt Ca# and Al#. Fig. II.13b also shows a strong positive correlation between the An in *Plag* and the melt Ca# in our experiments. As the Ca# of the melt is correlated to the melt Mg# (Fig. II.10), AH6 has the highest melt Ca# and thus the highest An contents in *Plag*, whereas the melt Ca# and the corresponding An in *Plag* are the lowest in AH5. Under *hydrous* conditions, melts with similar Ca# crystallize more anorthitic *Plag* (see field of "*hydrous Plag*" in Fig. II.13b slightly displaced to more An-enriched compositions).

An in *Plag* is also positively correlated with the melt Al# (Fig. II.14). However, as discussed above, the melt Al# is influenced by pressure, and H$_2$O content due to different proportions of Mg-Fe silicates and *Plag* in the solid phase (see phase proportions and

Part II: The Role of H₂O and Pressure on Multiple Saturation and Liquid Lines of
Descent in Basalts from the Shatsky Rise

liquid composition and Figs. II.4 and II.11 respectively). In low pressure runs, where *Plag*

is the liquidus phase (besides *Ol*), highest An contents in *Plag* were observed for certain

Al# of the melt. In contrast, at higher pressure, the melt Al# is controlled by

Ol+Plag+Cpx cotectic crystallization leading to lower melt Al# for given degree of

crystallization (melt Mg#) (increasing *Cpx* proportion in solid phase). This results in

systematically lower anorthitic *Plag* at similar melt Al#, meaning certain An content

crystallizes in a melt with higher Al# at higher pressure. Thus, the highest pressures (700

MPa) led to highest melt Al# in equilibrium with given An in *Plag*. Similarly to pressure,

the presence of small amounts of H₂O decreases the An contents in *Plag* at given melt

Al#, because the *Cpx* stability is enhanced relative to *Plag* in *hydrous* runs, which in turn

results in relatively higher Al# of the melt in equilibrium with the *Plag*.
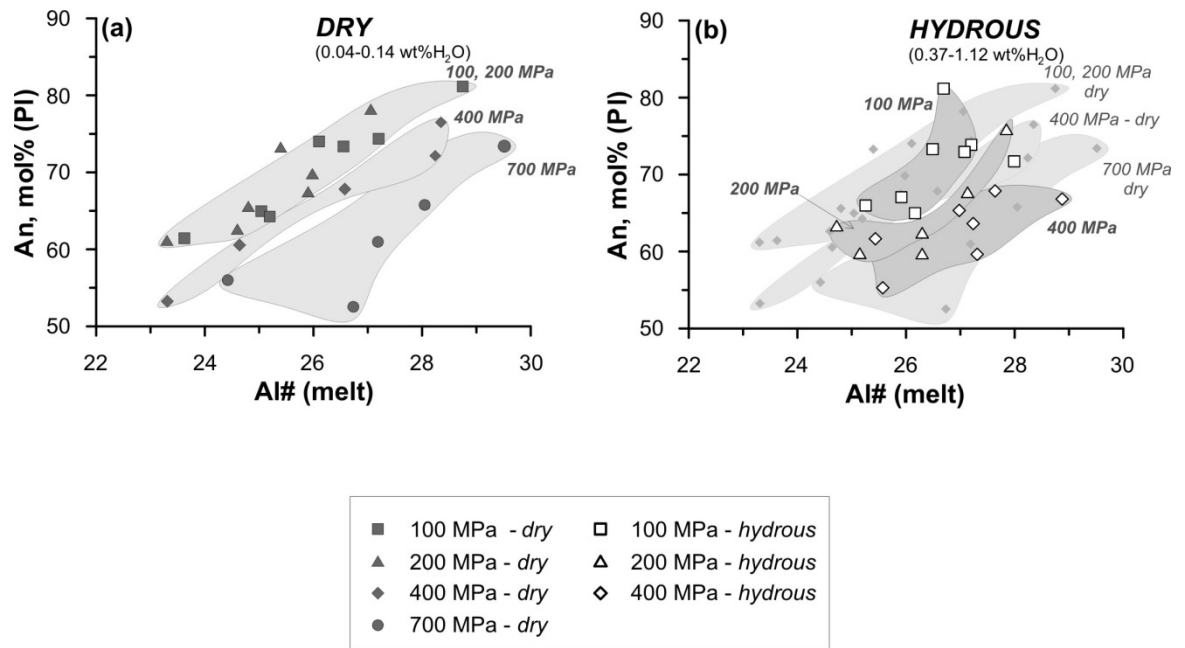
Figure II.14: Correlation of *Plag* composition represented by the An content (mol%) (averages of 2-10 analyses) with melt Al# is shown. Different symbols represent different experimental pressures. (A) and (b) display *dry* and *hydrous* conditions respectively. Grey fields mark experiments conducted at similar pressures. In (b), the fields representing *dry* experiments are shown for comparison.

Part II: The Role of H_2O and Pressure on Multiple Saturation and Liquid Lines of Descent in Basalts from the Shatsky Rise

The role of H_2O on *Plag*-melt equilibria can also be recognized from slightly higher K_{DCa-Na} observed in *hydrous* experiments (Tab. II.5 and II.6). It has been previously demonstrated by many experimental studies that the K_{DCa-Na} is gradually increasing with increasing melt H_2O (Sisson and Grove, 1993; Hamada, 2008; Honma, 2012; Takagi, 2005; Almeev, 2012). Although the distribution coefficients in some of our experiments tend to be slightly higher in the *hydrous* runs (e.g. in AH6), in general, they are in the range of 0.8 - 1.5 as previously reported for anhydrous (or with low aH_2O, Almeev, 2012) conditions. Superimposed is also the influence of different melt compositions: the K_DS are generally higher in experiments with the basalt AH6, which has the highest Mg#, Ca#, and Al#. In contrast, the most evolved AH5 basalt with the lowest melt Ca# and Al# also show the lowest K_DS (Tab. II.5 and II.6).

5.6.3   *Clinopyroxene*

In general, the experimentally produced *Cpx* demonstrate compositional systematics similar to the behavior of *Ol* (see above). With progression of crystallization (temperature decrease) the Mg# of *Cpx* drops down (e.g. from 83 to 68 in AH6 under *dry* conditions and 700 MPa, Fig. AII.9a). For all starting compositions, at constant temperatures, low-pressure *Cpx* are more MgO-rich than high-pressure *Cpx*, because they are crystallizing from the more evolved and thus less MgO-rich liquid (e.g. in *Cpx* crystallized in AH3 at 1150°C and *dry* conditions have Mg#=80 at 100 and 200 MPa, Mg#=75 at 400 MPa and Mg#=63 at 700 MPa, Fig. AII.9b). The comparison of *Cpx* crystallized in the three different starting compositions shows that *Cpx* from the primitive AH6 and AH3 basalts crystallize at higher temperatures and are more MgO-rich than those from the evolved AH5 starting composition. First *Cpx* in AH6 exhibit Mg# between 79 and 85, and in AH3 Mg# between 80 and 84, whereas the first *Cpx* in AH5 show Mg#

Part II: The Role of H$_2$O and Pressure on Multiple Saturation and Liquid Lines of
Descent in Basalts from the Shatsky Rise

of ~78 (Tab. II.5 and II.6).

At lower pressures in the AH6 and AH3 basalts, *Cpx* crystallization is subordinate

with respect to earlier *Ol+Plag* crystallization (see phase diagrams in Fig. II.3). In

contrast to systematics between Mg# and temperature observed in *Ol*, the Mg# of *Cpx* at

similar temperature are not significantly different in *hydrous* and *dry* experiments. In the

AH5 starting composition, *Cpx* is the liquidus phase at all investigated pressures. In this

case, the Mg# of the *Cpx* from *hydrous* charges is slightly higher than that of *Cpx* from

dry runs at similar temperature. For example, *Cpx* crystallizing in AH5 at 400 MPa and

1125°C (as the only liquidus phase) has a Mg# of 64 under *dry* conditions and a Mg# of

~69 under *hydrous* conditions. In contrast, in the AH6 basalt at 400 MPa and 1150°C,

Ol+Plag+Cpx is observed after initial *Ol+Plag* crystallization, and the *Cpx* have Mg#s of

75 and 73 under *dry* and *hydrous* conditions respectively (Tabs. II.5 and II.6, Fig. AII.9f).
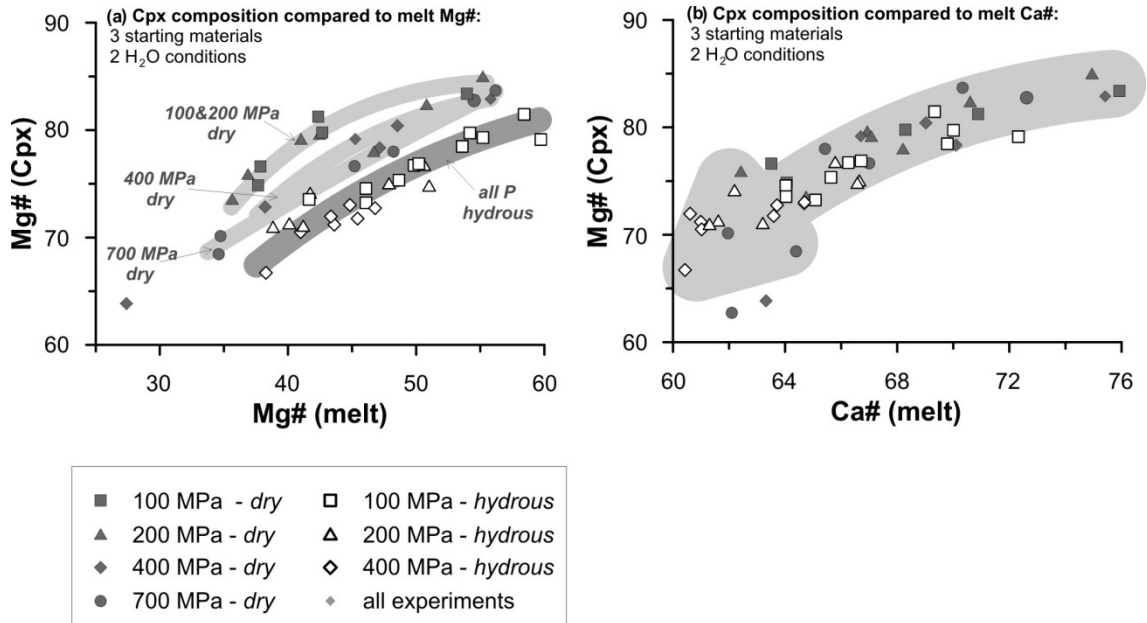
Figure II.15: Correlation of *Cpx* composition represented by their Mg# (averages of 2-11
analyses) with melt Mg# (a) and melt Ca# (b) is shown. Different symbols represent different experimental
pressures, grey and white symbols indicate *dry* and *hydrous* conditions respectively. In (a), grey fields mark
experiments conducted at similar conditions (pressure and H$_2$O content).

Part II: The Role of H_2O and Pressure on Multiple Saturation and Liquid Lines of Descent in Basalts from the Shatsky Rise
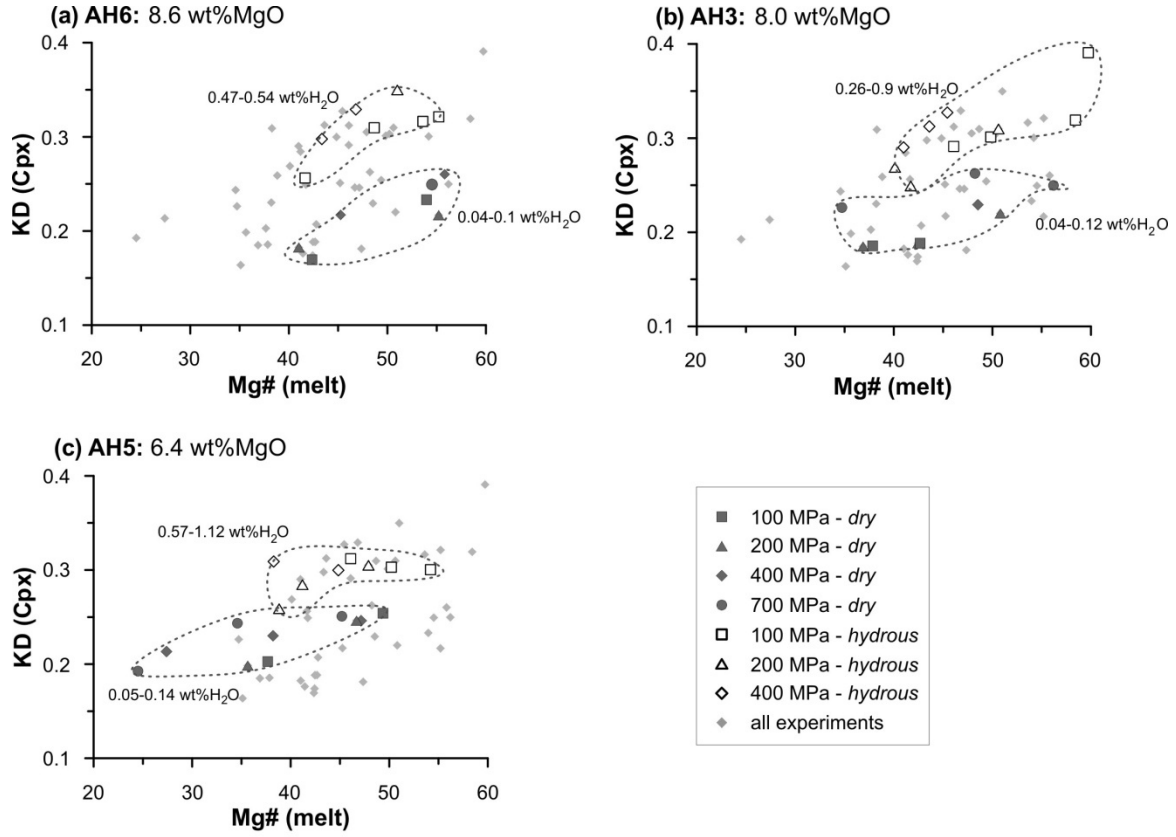
Figure II.16: Exchange distribution coefficients of Fe and Mg for melt and *Cpx* ($K_D=(X_{Fe}^{xtl} \cdot X_{Mg}^{liq})/(X_{Mg}^{xtl} \cdot X_{Fe}^{liq})$) are shown for given melt Mg#. A), b), and c) display K_DS obtained in different starting compositions AH6, AH3, and AH5 respectively. Different symbols represent different experimental pressures, grey and white symbols indicate *dry* and *hydrous* conditions, respectively. Dashed lines enclose values obtained for experiments conducted at similar H_2O conditions. The range of K_Ds in all experiments is shown for comparison (light grey diamonds).

The comparison of *Cpx* compositions (Mg#) with the melt Mg# shows the effects of pressure and H_2O on Fe-Mg exchange equlibria between high-Ca pyroxene and liquid. Under *dry* conditions, high pressure liquids tend to crystallize *Cpx* which are slightly lower in Mg# compared to *Cpx* produced from melts with similar Mg# but at lower pressures. For example in a *dry* melt with Mg# of ~43 (Fig. II.15a), the Mg# in *Cpx* changes with pressure from ~77 at 700 MPa (ShR511, 1200°C) through ~79 at 400 MPa (ShR619, 1175°C), to ~81 at 200 MPa (ShR603, 1150°C). Remarkably, the correlation between Mg#s of the coexisting *Cpx* and liquids is linear in high pressure (700 MPa) runs

Dissertation of Anika Husen

Part II: The Role of H$_2$O and Pressure on Multiple Saturation and Liquid Lines of
Descent in Basalts from the Shatsky Rise

where *Cpx* is usually the liquidus phase. Under *hydrous* conditions, the effect of different

pressures cannot be resolved (Fig. II.15a). However, in the presence of small amounts of

H$_2$O, the *Cpx*-melt pairs are systematically shifted towards higher Mg# in the melt and

lower Mg# in the *Cpx*. The high Mg# in experimental liquids produced under *hydrous*

conditions are also caused by the more oxidized conditions (see Tab. II.2). However,

lower Mg# in *Cpx* can be only linked to the effect of H$_2$O which possibly affected the Fe-

Mg exchange equilibria between *Cpx* and melt. In a more oxidized (proportion of Fe^{2+} is

lower) and thus more Mg-rich liquid, one should expect the crystallization of slightly

more MgO-rich *Cpx*, which is not the case in our experiments. Fig. II.16 clearly

demonstrates that Fe-Mg exchange distribution coefficients between *Cpx* and liquid

(K$_{DFe-Mg}$) are systematically higher in our *hydrous* experiments for all observed starting

compositions (Tab. II.5 and II.6, and Fig. II.16).

Finally, although it correlates positively with the melt Ca# (Fig. II.15b), the Mg#

of *Cpx* does not exhibit any systematics regarding the effects of pressure or H$_2$O on the

relation to the melt Ca#, which was reported above in the case of *Plag*.

5.6.4   Magnetite

Mag was observed in experiments conducted with the AH6 and AH3 basaltic

compositions in the presence of small amounts of H$_2$O (Fig. II.3). In contrast to our *dry*

experiments conducted in the presence of graphite (CCO oxygen buffer, FMQ-1 to FMQ-

2 (e.g. Ulmer & Luth, 1991; Jakobsson & Oskarsson, 1994; French & Eugster, 1965)), the

redox conditions in our *hydrous* experiments were most likely maintained along the

FMQ+0.5 oxygen buffer. The presence of higher melt H$_2$O concentrations (which

suppress crystallization of silicate phases) and higher *f*O$_2$ favored stabilization of *Mag*

after >60% of crystallization of *Ol*+*Plag*+*Cpx*. The experimental *Mag* display a narrow

Dissertation of Anika Husen

Part II: The Role of H₂O and Pressure on Multiple Saturation and Liquid Lines of
Descent in Basalts from the Shatsky Rise

compositional range: X^{USP} (calculated after Stormer et al., 1983) varies between 0.2 and 0.4. The *Mag* in AH6 shows slightly higher X^{USP} with decreasing temperature. For example, *Mag* in run ShR666 (1150°C and 400 MPa) has X^{USP}=0.2, whereas *Mag* in run ShR658 (1075°C and 200 MPa) contains X^{USP}=0.3 (Tab. AII.7).

6. DISCUSSION

Despite the generally low total range of melt H_2O concentrations investigated in our study (<1.2 wt% H_2O), the use of two experimental setups allowed us to investigate the effect of H_2O on phase equilibria in a scale of nearly one order of magnitude difference of melt H_2O concentrations: ~0.04-0.14 wt% H_2O in *dry* and ~0.4-1.11 wt% H_2O in *hydrous* experiments. Below, we discuss the effects of these small amounts of H_2O (referred as *hydrous* conditions) on different aspects of basaltic magma crystallization, followed by general implications of our experimental data to magma crystallization processes beneath the Shatsky Rise ocean plateau.

6.1. Effect of H₂O on Cotectic Crystallization

Similar to many other studies, under *dry* conditions (H_2O<0.14 wt%), the most MgO-rich basalt AH6 in our work has the highest liquidus. With pressure, the *dry* liquidus temperatures of all 3 investigated basalts are increasing. In addition, due to an earlier precipitation of the *Cpx* at higher pressures, the order of crystallization changes (e.g. AH3, Fig. II.3c) from *Ol+Plag* -> *Ol+Plag+Cpx* (at 100-400 MPa) to *Cpx->* *Cpx+Plag* -> *Ol+Plag+Cpx* (at 700 MPa). A similar change in the crystallization sequence was observed with the change of the starting composition: in the most evolved basalt AH5 the sequence *Cpx-> Cpx+Plag* -> *Ol+Plag+Cpx* was observed at all investigated pressures.

Part II: The Role of H_2O and Pressure on Multiple Saturation and Liquid Lines of Descent in Basalts from the Shatsky Rise

The addition of ~ 0.4 – 1.1 wt% H_2O results in a depression of the liquidus by ~20°C (e.g. AH3 at 100 MPa, ~0.5 wt% H_2O) to ~40°C (e.g. AH3 at 200 MPa, ~0.9 wt% H_2O). However, for experiments performed at 100 MPa, the liquidus depression is less pronounced than at high pressures (e.g. compare 100 MPa and 200 MPa *dry* and *hydrous* runs for all starting materials). Thus, the shape of the H_2O-bearing liquidus on the *P-T* diagram is characterized by a minimum (Fig. II.3), which is located at 100 MPa in the most evolved basalt AH5 and at slightly higher pressures (~200 MPa) in the less differentiated basalts. Note, that our *hydrous* phase diagrams reflect phase relations for a range of H_2O contents (0.3-1.1 wt% H_2O, small numbers in Fig. II.3). It can be seen in Fig II.3d, that the H_2O contents in the 200 MPa crystal-free experiment at 1150°C (ShR351, 0.9 wt% H_2O) and the first crystal-bearing experiment at 1125°C (ShR 350, 0.75 wt% H_2O) are slightly higher compared to their 100 MPa counterparts (ShR363: 0.51 wt% H_2O, ShR362: 0.48 wt% H_2O). As higher melt H_2O concentrations depress more strongly the liquidus, these differences might already be responsible for the minimum in the liquidus temperature.

It has been emphasized by previous studies that the the depression of *Ol*, *Plag* and *Cpx* stability is the major effect of H_2O on MORB phase equilibria and that this has different intensity for the different mineral phases (Michael and Cornell, 1998; Danyushevsky, 2001; Almeev et al., 2007, 2012; Médard and Grove, 2008). For example, Danyushevsky (2001) and Almeev et al. (2012) demonstrated that *Plag* is the phase, which is the most affected by H_2O (in comparison to *Ol*). The change of the precipitating mineral assemblages induced by the presence of H_2O in the melt should result in systematic changes of LLDs for CaO, Al_2O_3, SiO_2 and the CaO/Al_2O_3. For example in the studied basalts, differences between *dry* and *hydrous* LLD are observed for FeO, Al_2O_3, SiO_2 and the CaO/Al_2O_3 (see above). However, the phase diagrams constructed for

Part II: The Role of H$_2$O and Pressure on Multiple Saturation and Liquid Lines of
Descent in Basalts from the Shatsky Rise

Table II.7: Cotectic crystallization proportions for AH3 and AH6

Run	P (MPa)	T (°C)	Ol	Plag	Cpx	ΔT (°C)
starting material: AH3						
DRY						
ShR322	101	1125	11	43	46	25
ShR323	202	1150	9	47	43	25
ShR307	401	1150	10	61	29	25
ShR310	698	1150	13	61	27	25
HYDROUS						
ShR360	102	1100	11	54	35	55
ShR358	202	1075	9	55	36	50
ShR359	401	1100	8	50	43	50
starting material: AH6						
DRY						
ShR603	102	1150	12	47	42	25
ShR602	202	1150	12	48	41	25
ShR619	402	1175	13	47	40	25
ShR608	700	1200	20	53	27	25
HYDROUS						
ShR662	105	1125	11	42	47	25
ShR654	201	1100	6	58	36	25
ShR665	402	1100	6	61	33	25

Ol – olivine, Plag – plagioclase, Cpx – clinopyroxene
Crystallization proportions are calculated referring to the nearest experiment at higher
temperature respectively. They resemble the increase of each phase proportion normalized
to the decrease in melt fraction.

hydrous conditions (right plots in Fig. II.3) do not demonstrate significant changes in the
order of crystallization sequence for all basalts and all pressures. Thus, the differences
observed in our *hydrous* and *dry* LLDs for some major oxides cannot be directly
explained by the changes of crystallization orders. Our data show that the major factor
controlling the evolution of the liquid are the crystallization proportions of the minerals in
the solid phase.

6.2.   Effect of H$_2$O on Cotectic Crystallization Proportions

Our data show that the mineral proportions are slightly different in the presence of
small amounts of H$_2$O, when compared to the anhydrous system. For a dry basalt, Grove
et al. (1992) reported the following proportions of *Ol+Plag* and *Ol+Plag+Cpx* cotectic
crystallization (in weight %): 30:70 (*Ol*:*Plag*) at 0.1 MPa, 8:55:37 (*Ol*:*Plag*:*Cpx*) at 0.1
MPa, 11:59:30 (*Ol*:*Plag*:*Cpx*) at 200 MPa, and 16: 57:27 (*Ol*:*Plag*:*Cpx*) at 800 MPa.
Thus, in a *dry* system, with increasing pressure, the cotectic proportion of *Cpx* is
decreasing, whereas the proportion of *Ol* is increasing and the proportion of *Plag* stays

Dissertation of Anika Husen

Part II: The Role of H$_2$O and Pressure on Multiple Saturation and Liquid Lines of
Descent in Basalts from the Shatsky Rise

relatively constant. Similar relationships are also observed in our experiments with the

AH6 and AH3 basalts conducted under *dry* conditions (Tab. II.7 and Fig. II.17). Although

the absolute values are slightly different from those of Grove et al. (1992), the

crystallization proportion of *Cpx* is also decreasing and the proportion of *Ol* tend to

increase with pressure. In our *dry* experiments, the *Plag* proportion is increasing in AH3

and decreasing in AH6, reflecting the fact that in the course of the magmatic evolution

and thus the change of the solid solution compositions, the cotectic proportions may also

change. It has to be noted that the cotectic proportions at ShR310 (1150°C, 700 MPa)

were obtained from experiments with very high crystallinities, where an accurate

determination of the phase compositions (in particular for glasses) and thus the phase

proportions is problematic. In contrast to *dry* conditions, in our *hydrous* experiments, the

proportions of *Cpx* and *Ol* are opposite: an increase of *Cpx* and a decrease of *Ol* with

increasing pressure (Tab. II.7 and Fig II.17). In addition, the proportion of *Plag* also

decreases in *hydrous* runs (note that in the case of *hydrous* runs values from ShR654 and

ShR665 (1100°C, 200 MPa and 400 MPa) were obtained at very high crystallinities).

Part II: The Role of H$_2$O and Pressure on Multiple Saturation and Liquid Lines of Descent in Basalts from the Shatsky Rise
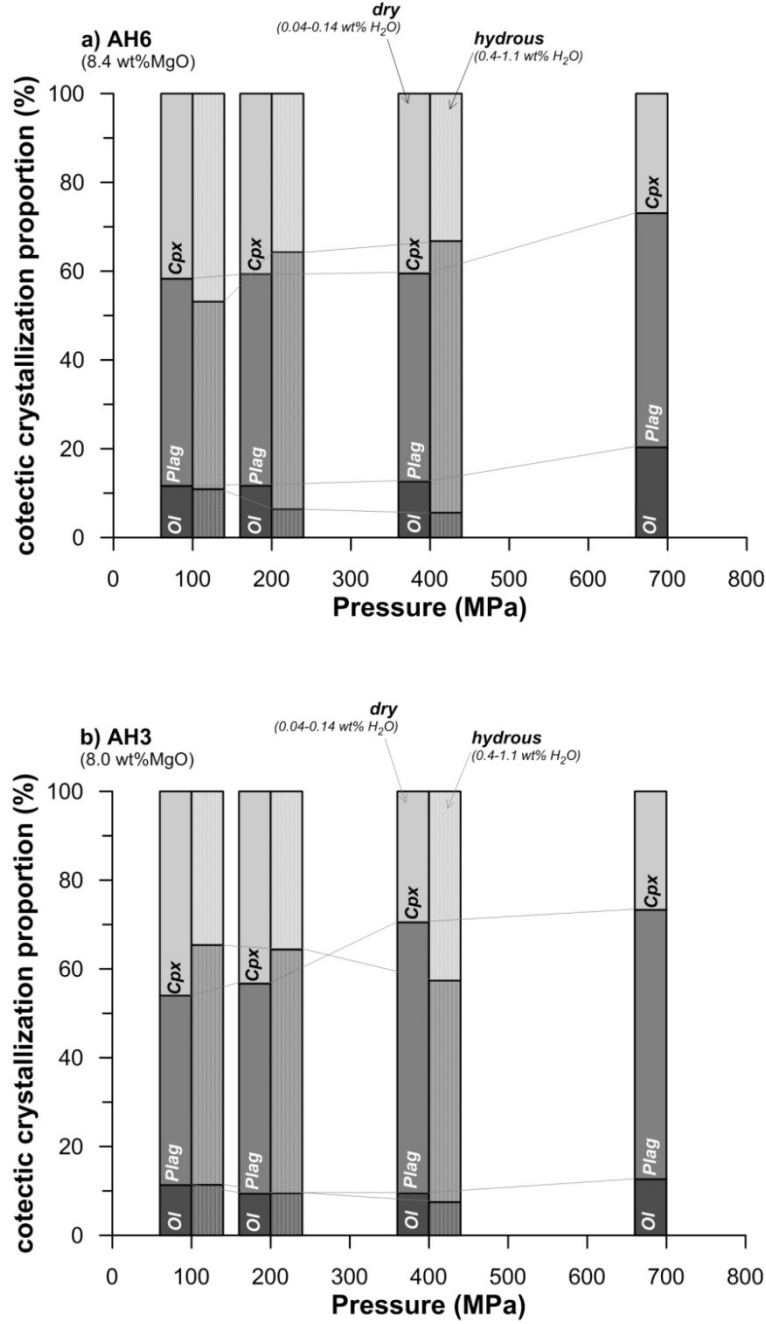
Figure II.17: Cotectic crystallization proportions at given pressures are given for (a) AH6 and (b) AH3. Solid and shaded bars show *dry* and *hydrous* conditions respectively. Crystallization proportions are calculated by normalization of the change in mineral proportion to 1% of crystallization, e.g. $\Delta F_{Plag}/\Delta F_{liq}$.

Dissertation of Anika Husen

Part II: The Role of H$_2$O and Pressure on Multiple Saturation and Liquid Lines of Descent in Basalts from the Shatsky Rise

6.3. Effect of Pressure and H$_2$O Contents on Multiple Saturation – Implications to MORBs

It has been shown by many previous experimental studies, that basaltic magmas beneath MORs mainly evolve along low pressure *Ol+Plag* and *Ol+Plag+Cpx* cotectics (Grove et al., 1992). Danyushevsky (2001) and Michael (1995), also emphasized the importance of small amounts of H$_2$O on the LLDs in basaltic systems (particularly on FeO and Al$_2$O$_3$ contents). However, in barometric calculations, the effect of small amounts of H$_2$O is generally ignored (Herzberg, 2004; Villiger et al., 2007; Yang et al., 1996). Only the models of Danyushevsky et al. (1996) and Danyushevsky (2001) are taking the effect of melt H$_2$O content into account. However, the effect of H$_2$O on *Cpx* stability and thus the interplay between the effects of pressure and of H$_2$O on the LLDs was not yet addressed in theoretical and experimental literature. Although the approach of Almeev et al. (2008) accounts for the effects of H$_2$O on *Ol*, *Plag* and *Cpx* temperatures, the accuracy of this method was not confirmed experimentally.

In Fig II.18, we compare experimental LLDs obtained in our *dry* (100-700, <0.14wt% H$_2$O) and *hydrous* (100 and 400 MPa, ~0.5 wt% H$_2$O) experiments. The diagram illustrates that with progression of melt evolution (decrease of MgO), the CaO/Al$_2$O$_3$ ratio increases in the course of *Ol+Plag* crystallization and decreases iduring *Ol+Plag+Cpx* crystallization. In this diagram the effect of pressure and the effect of H$_2$O on multiple saturated liquids can be distinguished. Our new data clearly demonstrate the significant effect of small amounts of H$_2$O on the LLDs, when our *dry* and *hydrous* LLDs produced at similar pressures are compared. Thus, the addition of only 0.4 wt% of H$_2$O leads to the same decrease of the CaO/Al$_2$O$_3$ ratio which would be caused by a pressure increase from 100 MPa to ~300 MPa at *dry* conditions (e.g. corresponding to ~6 km difference in depth in the crust). Thus, the effect of small amounts of H$_2$O needs to be

Dissertation of Anika Husen

Part II: The Role of H₂O and Pressure on Multiple Saturation and Liquid Lines of
Descent in Basalts from the Shatsky Rise

considered in geobarometric calculations of the nominally "dry" MORB magmas. According to our experimental data, the presence of only 0.4 wt% H_2O may affect pressure estimates up to 300 MPa (Fig. II.18). Furthermore, the whole range of natural EPR MORB glasses (shown in Fig. II.18 for comparison by light grey symbols) could be explained only by the variation of H_2O below 0.4 wt% at isobaric conditions.
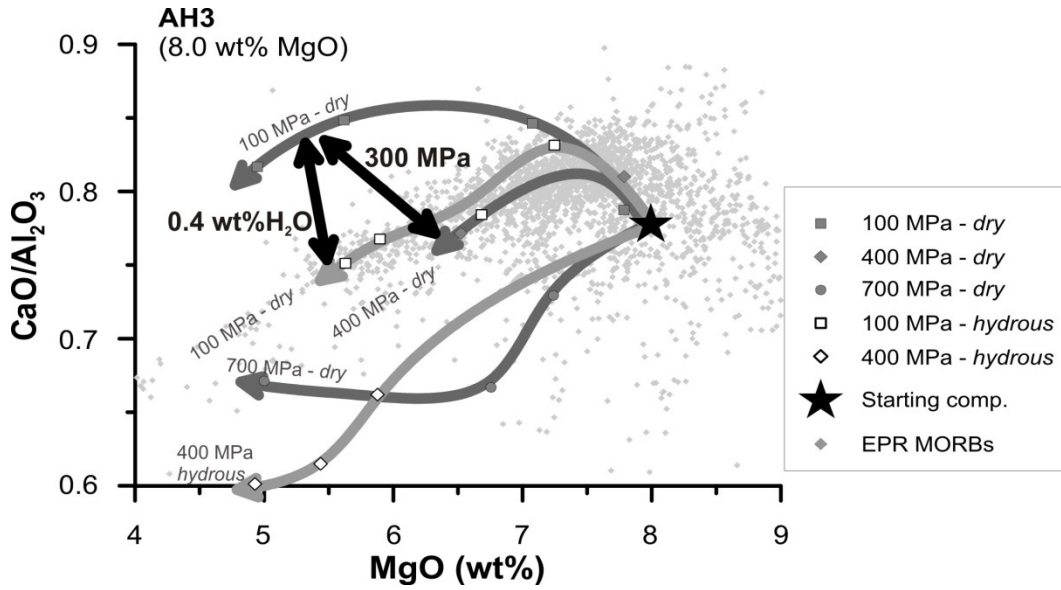
Figure II.18: Experimental LLDs for the intermediate starting material AH3 (8 wt% MgO, black star) obtained for different pressures and H_2O conditions. Increasing CaO/Al_2O_3 resembles *Ol+Plag* crystallization, whereas decreasing CaO/Al_2O_3 implies *(Ol+)Pl+Cpx* crystallization. Different symbols represent experimental liquid compositions obtained at different experimental pressures, grey and white symbols indicate *dry* and *hydrous* conditions respectively. Isobaric LLDs are drawn by grey arrows, darker and lighter colors indicate *dry* and *hydrous* conditions respectively. EPR MORBs (PetDB) are shown for comparison (light grey dots).

6.4.   Effect of H₂O and Pressure on Liquid Evolution within Mineral Component Space

As discussed above, the crystallization sequences, phase proportions, and LLDs are strongly affected by the initial starting compositions, pressure, and the melt H_2O content. Using glass compositions recalculated following the scheme of Grove (1993) into mineral end member components, we can further discuss the role of pressure and

Part II: The Role of H₂O and Pressure on Multiple Saturation and Liquid Lines of
Descent in Basalts from the Shatsky Rise

H_2O on *Ol+Plag+Cpx* cotectic crystallization within the *Ol-Cpx*-quartz (*Qz*) pseudoternary plot (projection of the basalt tetrahedron from the *Plag* apex, Fig. II.19). It has been previously demonstrated that the position of *dry Ol+Plag+Cpx* cotectics is pressure-sensitive and that with a pressure increase it is shifting towards the *Ol-Qz* sideline with an expansion of the *Cpx* primary volume (e.g. Walker et al., 1979; Yang et al., 1996). The effect of pressure on *Ol+Plag+Cpx* cotectic crystallization in the *dry* basaltic system has been calibrated in many studies, (e.g. Yang et al., 1996; Herzberg, 2004). However, as already mentioned above, the effect of small amounts of H_2O on *Ol+Plag+Cpx* cotectics was not addressed by experimental studies and assumed to be negligible (e.g. Herzberg, 2004).

In Fig. II.19, the recalculated experimental glass compositions obtained in our study are projected for each starting material (rows) for *dry* (left column) and *hydrous* (right column) conditions. Note that all projections shown in Fig. II.19 are only a part of the whole pseudoternary diagram (0.6-0.4-0.8, *Ol-Qz-Cpx*) as shown on the small plot right to the legend. Natural MORB glasses are shown for comparison as small grey dots. The starting composition AH6 has a nepheline normative character (negative value of the *Qz* component) and its projection is outside of the pseudoternary plot (to the left side of the *Ol-Cpx* sideline).

In general and similar to the previous studies, the pressure increase in our experiments drives the multiple saturated liquids away from the *Cpx* apex (e.g. compare 100, 400 and 700 MPa LLDs for AH6) (Fig. II.19a).

Dry conditions

Crystallization along *Ol+Plag* cotectics (e.g. at 100, 200, 400 in AH6 and AH3) drives the melt compositions away from the *Ol* apex and towards the *Cpx* apex (e.g. at

Dissertation of Anika Husen

Part II: The Role of H$_2$O and Pressure on Multiple Saturation and Liquid Lines of
Descent in Basalts from the Shatsky Rise

100 and 200 MPa). When *Cpx* starts to crystallize, the residual liquids start to evolve along the *Ol+Plag+Cpx* cotectics. However, in our runs all multiple saturated liquids are following a trend away from the *Qz* apex towards SiO$_2$-poor compositions (see also discussion below about SiO$_2$ depletion). Experiments at 700 MPa using AH6 and AH3, and runs at all pressures using AH5 have *Cpx* as the first crystallizing phase (see phase diagrams), which results in LLDs trending away from the *Cpx* apex towards *Ol*. When *Ol+Plag+Cpx* cotectics are reached, the LLDs also start to follow the *Qz* depletion trend (ShR314 at 700 MPa and 1200°C with AH3). In some cases, experimental liquids are close to be multiple saturated and are appearing on the plot exactly in the projection of the starting composition (e.g. ShR605 at 400 MPa and 1200°C in AH6).

Hydrous conditions

In our *hydrous* experiments (right plots in Fig. II.19), similar systematics can be observed when different isobaric *Ol+Plag+Cpx* cotectics are considered. However, all 3 mineral cotectic compositions are shifted towards the *Ol* apex parallel to the *Cpx-Ol* sideline towards compositions which are lower in the *Cpx* component. This is in a good agreement with the relatively high proportion of *Cpx* in the solid phase under *hydrous* conditions (see phase proportions). Interestingly, the appearance of *Mag* in AH3 at 200 and 400 MPa (ShR354 and ShR359) leads also to a drop in *Cpx* component and a slight shift towards the *Qz* apex (Fig. II.19). In contrast, in AH6, no significant influence of *Mag* on the LLDs can be observed (Fig. II.19).

Figure II.19: Experimental starting compositions (black stars) and liquid compositions recalculated into mineral end member components after Grove (1993) displayed in the projection of the basalt tetrahedron from the *Plag* apex on the *Ol-Cpx-Qz* plain (0.6-0.4-0.8, *Ol-Qz-Cpx*). Left and right column show diagrams for *dry* and *hydrous* conditions respectively. From top to bottom LLDs from different starting compositions (stars) are displayed (AH6 - AH3 - AH5). Isobaric experiments are connected by solid lines (LLDs). Different symbols represent experimental liquid compositions obtained at different experimental pressures; grey and white symbols indicate *dry* and *hydrous* conditions respectively.

Part II: The Role of H₂O and Pressure on Multiple Saturation and Liquid Lines of Descent in Basalts from the Shatsky Rise
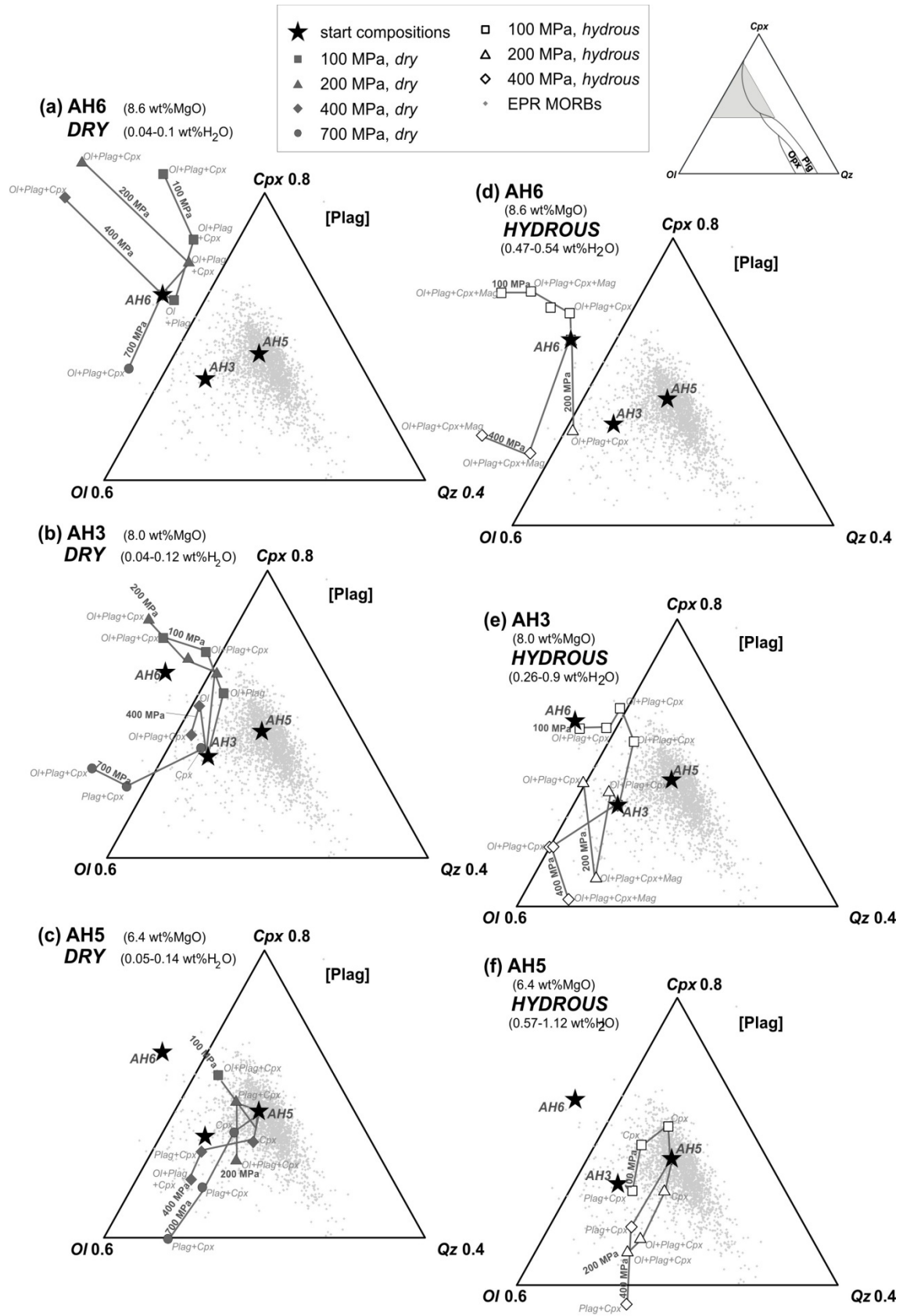
← *caption*

Part II: The Role of H$_2$O and Pressure on Multiple Saturation and Liquid Lines of Descent in Basalts from the Shatsky Rise

---

In Fig. II.20, the multiple saturated liquids (*Ol+Plag+Cpx* cotectics) produced from all three starting compositions are shown for each investigated pressure (100, 200, 400 and 700 MPa) for both, *dry* and *hydrous* conditions. Previous experimental data conducted at 200 and 800 MPa (Grove et al., 1992), 190 MPa (Sano & Yamashita, 2004), and 280, 430, and 680 MPa (Whitaker et al., 2007) are shown for comparison.

According to our experiments, our *dry* and *hydrous* 100 MPa cotectics intersect at the *Ol-Cpx* sideline (Fig. II.20). For all other pressures, *hydrous* cotectics are always shifted towards the *Ol* apex. Our 200 MPa cotectic line is in agreement with the experiments presented by Sano & Yamashita (2004) and Grove et al. (1992): their 190 MPa and 200 MPa multiple saturated liquids are located on the prolongation of our cotectic line towards the more *Qz* enriched compositions. Similarly, the experimental *Ol+Plag+Cpx* saturated liquids of Whitaker et al. (2007) conducted at 430 and 690 MPa are projected along our 400 and 700 MPa *dry* cotectics, whereas those of 280 MPa are projected between our 200 and 400 MPa cotectic lines.

Figure II.20: *Ol+Plag+Cpx* saturated experimental liquid compositions recalculated into mineral end member components after Grove (1993) displayed in the projection of the basalt tetrahedron from the *Plag* apex on the *Ol-Cpx-Qz* plain (0.6-0.4-0.8, *Ol-Qz-Cpx*). *Dry* (grey symbols) and *hydrous* (white symbols) runs are compared for each pressure (a-d). Additionally literature data from Sano & Yamashita (2004), Whitaker et al. (2007) and Grove et al. (1992) and 1 atm cotectics (Walker et al., 1979) are shown. Estimated cotectic lines are drawn by dashed lines. A summary of all cotetcic lines (100-700 MPa and *dry* and *hydrous* conditions) in the whole *Ol-Cpx-Qz* plain is displayed in (e). In a) also natural glasses from Tamu (grey dots) and Ori (open triangles) massifs are shown.

Note that the melt analysis for highly crystalline samples (>80%) like e.g. ShR312 (*Ol+Plag+Cpx*, 700 MPa) have a relatively high uncertainty in melt composition analysis.

Part II: The Role of H$_2$O and Pressure on Multiple Saturation and Liquid Lines of Descent in Basalts from the Shatsky Rise

← *caption*

Part II: The Role of H_2O and Pressure on Multiple Saturation and Liquid Lines of
Descent in Basalts from the Shatsky Rise

Considered collectively, the cotectic line of *Ol+Plag+Cpx* is shifted towards higher normative *Ol* contents with increasing pressure. The presence of 0.4-1.1 wt% H_2O also results in a shift of the *Ol+Plag+Cpx* cotectics with an expansion of the primary volume of *Cpx*. Thus, the increase in pressure and the addition of H_2O have similar effects on the location of the cotectic lines (Fig. II.20). As a consequence, the *hydrous* 200 MPa cotectic line (0.3-0.8 wt% H_2O) is located between the *dry* 400 and 700 MPa cotectics, which clearly illustrates the importance of the consideration of the small amounts of H_2O in barometric simulations. This is in agreement with our previous discussion of the LLDs on the CaO/Al_2O_3 vs. MgO plot (Fig. II.18).

It has been shown that when compared to the 1 atm cotectics (Walker et al., 1979), the natural MORB glasses (e.g. EPR glasses, Fig. II.20) are projected slightly to more *Ol*-enriched compositions, or in other words, they are shifted in the direction of slightly higher pressure cotectics. Our new data suggest that in addition to pressure, the presence of small amounts of H_2O can also be responsible. Moreover, since MORBs have typically very low H_2O (<0.6 wt%) contents, it was generally assumed that pressure is the main factor controlling the direction of the LLDs in the course of crystallization. Our experimental liquids projected on the pseudoternary diagram show, that the presence of ~0.6 wt% H_2O has an effect on the position of the *Ol+Plag+Cpx* cotectics which is comparable with a pressure increase of ~ 300 MPa at *dry* conditions. This, again, leads to the conclusion that the presence of H_2O is crucial to be considered in pressure estimations. Additionally, all pressures estimated without taking the H_2O into account, reflect only maximum values and might be significantly lower, because similar cotectic compositions and melt CaO/Al_2O_3 can be produced at much lower pressures when small amounts of H_2O are present (Fig. II.18 and II.20).

The Shatsky Rise glasses (Husen et al., 2013; Sano et al., 2012) have 0.2-0.6 wt% H_2O (Tamu Massif, Husen et al., 2013) and are projected on continuation of the *dry* 200 MPa or *hydrous* 100 MPa cotectics. This is in a good agreement with previous pressure estimates (Husen et al., 2013).

6.5. SiO₂ Depletion in Experimental Basalts

Generally, the Harker type diagrams show that our experiments reproduce well the natural array of MORB compositions for all major oxides, except that one for SiO_2 (Fig. II.8). In contrast to the natural EPR MORBs and the Shatsky Rise basalts, our experimental LLDs show a SiO_2 depletion trend for experimental equilibrium crystallization. This also leads to the trend away from the *Qz*-rich compositions when the glass compositions are re-calculated into mineral components and projected from the *Plag* apex onto the *Ol-Cpx-Qz* pseudoternary plane (Fig. II.19). The SiO_2 depletion in the most MgO-rich starting material AH6 can be explained by its nepheline normative (e.g. CIPW norm calculated after Cross et al., 1902) character (visible in Fig. II.19a: AH6 with a negative value of the *Qz* content is projected outside of the pseudoternary plot). However, the two more evolved starting compositions AH3 and AH5 are both *Ol* normative, but show also SiO_2 depletion during the crystallization. Only experiments with more than 20% *Ol* in the solid phase lead to increasing SiO_2 concentrations in the remaining glass (these experiments are not multiple saturated). In contrast, the natural MORB glasses are generally following the trend of SiO_2 enrichment (see also ternary plots).

The comparison of our starting materials with the natural basalts (Fig. II.1) shows that the SiO_2 contents in our starting materials are significantly lower than in the EPR MORBs (and in most of the other experimental studies), reflecting the SiO_2-poor

Part II: The Role of H_2O and Pressure on Multiple Saturation and Liquid Lines of
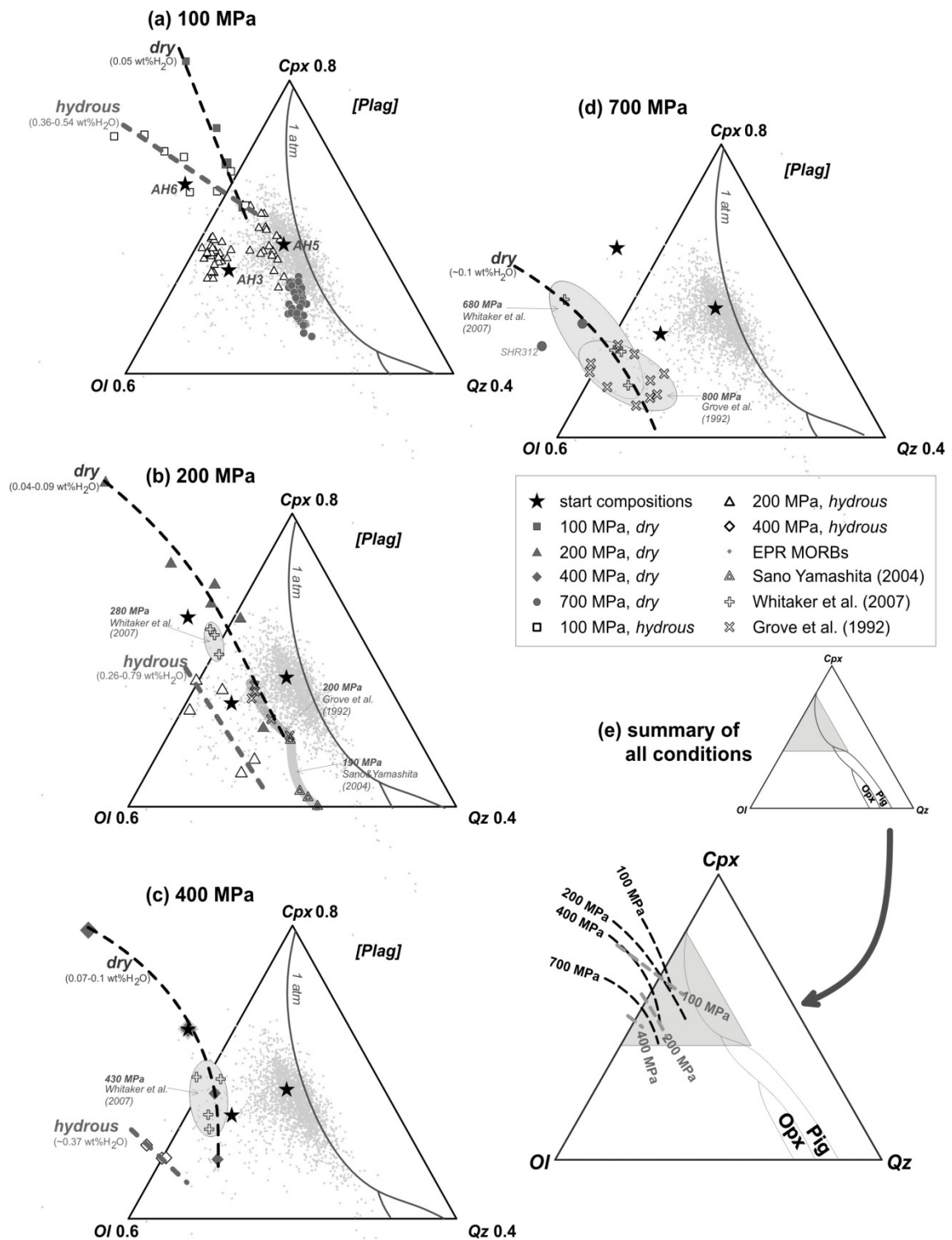Descent in Basalts from the Shatsky Rise

character of the Shatsky Rise magmas. Compared to the EPR MORB array, the most

MgO-rich starting material AH6 is 1 wt% lower (leading to nepheline normative

character) and the intermediate composition AH3 is 0.5 wt% lower in SiO_2. The most

evolved starting material AH5 resembles the lowest SiO_2 contents known for EPR

MORBs. Although our initial synthetic compositions are good representatives of the

Shatsky Rise magmas (of different evolutionary stages), our experimental residual liquids

remain in conflict with the SiO_2 enrichment observed in natural Shatsky Rise lavas.

The SiO_2 depletion in the MORB system has already been observed in a number

of experimental studies (Bender et al., 1978; Whitaker et al., 2007; Grove et al., 1992;

Villiger et al., 2004 (in equilibrium crystallization runs)). They found SiO_2 depletion in

all experiments conducted at elevated pressures (200 MPa - 1 GPa) in graphite-lined

double capsules, and only at 1 atm, SiO_2 enrichment was observed for the same

composition (Whitaker et al., 2007). Considering that SiO_2 enrichment in other studies

was only achieved in the presence of small amounts of H_2O (without being always

determined) in experiments in noble metal containers, as e.g. in Sano & Yamashita

(2004), Berndt et al. (2005), and Feig et al. (2006), our experiments again prove that the

H_2O content in natural MORBs is a crucial factor for the tholeiitic evolution and that the

assumption of dry MORBs is not applicable in thermodynamic models. Since no SiO_2

depletion trends in natural MORB systems are known, we conclude that all MORBs

evolve in the presence of a small amount of H_2O which is sufficient for *Plag* liquidus

depression.

It should be noted, that our *hydrous* experiments demonstrate less SiO_2 depletion

because the presence of H_2O increases the An content in the *Plag* at given *P-T* conditions.

In addition, the H_2O lowers the relative proportion of the crystallizing *Plag* which is a

Part II: The Role of H$_2$O and Pressure on Multiple Saturation and Liquid Lines of Descent in Basalts from the Shatsky Rise

---

phase with high SiO$_2$ content. However, using our experimental starting materials, SiO$_2$ enrichment could not be reproduced, although our *hydrous* runs evolved in the presence of 0.4-1.14 wt% H$_2$O. Below, we compare our experimental data to those presented by Sano & Yamashita (2004), who conducted an experimental study on an OJP basalt. The OJP basalts have many similarities to the Shatsky Rise lavas (Husen et al., 2013): e.g. low Na$_2$O, TiO$_2$, and high FeO contents in the basaltic glasses. However, the basalts from these two plateaus differ in SiO$_2$: OJP basalts have higher SiO$_2$ contents varying within the field of EPR MORBs. The study of Sano & Yamashita (2004) is a good example for the experimental reproduction of the SiO$_2$ enrichment trend found in natural MORBs (see Part I Fig. I.4).

The SiO$_2$ contents of the solid phase in the experiments of Sano & Yamashita (2004), never exceeds the initial SiO$_2$ content of the starting material. In contrast, our experimental runs show solid phase compositions with SiO$_2$ contents, which are usually higher than in the starting materials. Compared to experiments from Sano & Yamashita (2004), we produced *Plag* which are higher in SiO$_2$ contents. As displayed in Fig. II.21a (and II.13a), our experimental *Plag* produced in the AH3 and AH5 basalts are systematically more albitic for the given melt Mg#, when compared to those presented in Sano & Yamashita (2004). The An contents in the experimental *Plag* of Sano & Yamashita (2004) are all in the range of 75-82 mol% An (48-51 wt% SiO$_2$), whereas our experimental *Plag* in AH3 and AH5 are below 75 mol% An (49-56 wt% SiO$_2$).

Part II: The Role of H_2O and Pressure on Multiple Saturation and Liquid Lines of
Descent in Basalts from the Shatsky Rise
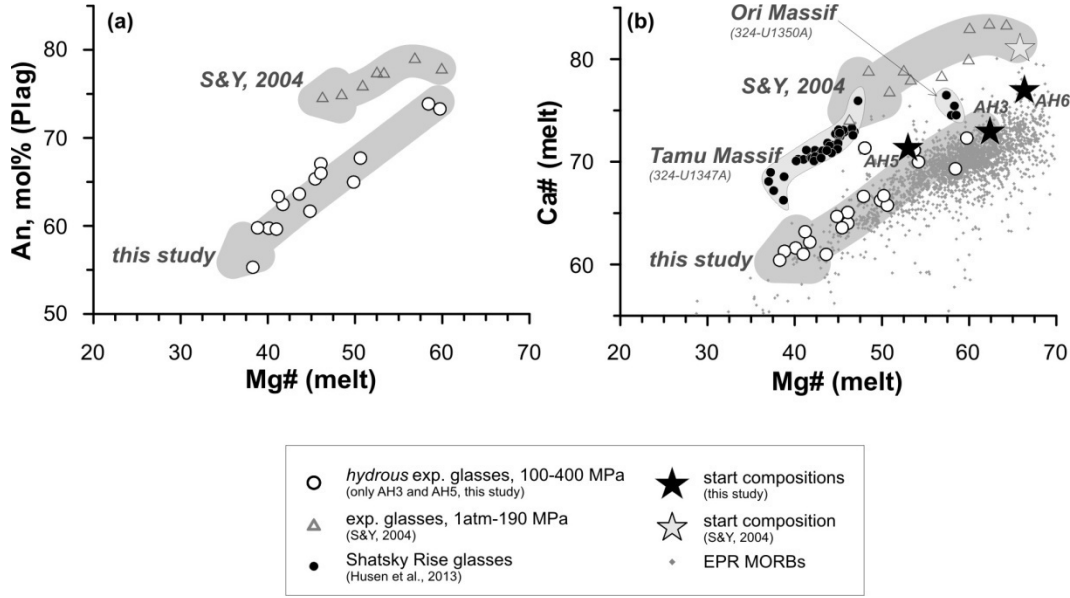
Figure II.21: (a) Compositions of experimentally produced *Plag* at given melt Mg#. Grey triangles display 190 MPa experiments from Sano & Yamashita (2004) using a basaltic starting composition from Ontong Java Plateau. (b) Basaltic glass compositions from this study (black stars and white dots), the experimental study of Sano & Yamashita (2004) (grey star and grey triangles), Shatsky Rise natural basalts (black dots), and EPR MORBs (PetDB, grey points) are shown. Natural Shatsky glass compositions are presented in Husen et al. (2013), we indicate fields of Tamu and Ori Massifs.

Note, that (1) only experiments using AH3 and AH5 are shown, because AH6 is nepheline normative and not further discussed regarding SiO_2 depletion trend; (2) we display only *hydrous* experiments (100-400 MPa, white dots) in order to compare experiments conducted at similar H_2O conditions, because Sano & Yamashita (2004) also applied AuPd capsules); and (3) Mg# of *hydrous* liquid compositions were calculated referring Fe^{2+}/Fe^{total}=0.82.

As the *Plag* composition is mainly a function of the liquid composition and the temperature, we assume that the comparison of the liquid compositions at given Mg# can be used to visualize the differences between the systems with high and low anorthitic *Plag* and thus SiO_2 enrichment or depletion during differentiation. In the chapter above (Mineral Compositions and Fig. II.13), we showed that the composition of experimental *Plag* is strongly correlated to the melt Mg# and Ca# with a little influence of the H_2O content (in the investigated range of melt H_2O).

Part II: The Role of H$_2$O and Pressure on Multiple Saturation and Liquid Lines of Descent in Basalts from the Shatsky Rise

In Fig. II.21b, we demonstrate that the starting material and the residual liquid compositions of Sano & Yamashita (2004) have higher melt Ca# at given melt Mg#. Compared to the OJP basalt from Sano & Yamashita (2004), our experimental glasses have lower melt Ca# which is directly related to crystallization of the more albitic *Plag* (see Fig. II.21a). Also in the natural Shatsky Rise glasses, higher Ca# compared to our experimental glasses were found (Fig. II.21b), this explains the observed difference between natural (presented in Husen et al., 2013) and experimental An contents in *Plag*. We assume that these differences result in the opposite trends regarding the SiO$_2$ in residual liquids.

When further compared to MORBs, it can be seen that the experimental OJP and the natural Shatsky Rise glasses, as well as our experimental melts are higher in the Ca# for given Mg# (Fig. II.21b). Additionally, EPR MORBs evolve from parental liquids which are generally higher in SiO$_2$ contents (Fig. II.8). Therefore, the crystallization of even more albitic *Plag* from any EPR melt is resulting in constant or slight enrichment of SiO$_2$ (the precipitating solid phase is still lower in SiO$_2$ than the parental composition). In contrast, if SiO$_2$ in the initial melt composition is already low (the case of Shatsky Rise), the crystallization of high anorthitic *Plag* (which depends on Ca# of coexisting melt) is required to produce lower SiO$_2$ in the solid phase.

To prove our assumption that the high An contents are the main reason for the SiO$_2$ depletion, we used the COMAGMAT program (Ariskin & Barmina, 2004) to calculate LLDs for equilibrium crystallization using our intermediate starting material AH3. The simulated LLDs show that the equilibrium crystallization (200 MPa, 0.1 and 0.6 wt% H$_2$O, solid grey lines) reproduce well our experimental glass compositions regarding the SiO$_2$ content (Fig. II.22). Thus, we assume that it is reasonable to apply the

Part II: The Role of H$_2$O and Pressure on Multiple Saturation and Liquid Lines of Descent in Basalts from the Shatsky Rise

COMAGMAT model to test the effect of starting compositions with different Ca# on the LLDs. We modified the Ca# by varying the initial Na$_2$O contents, because those are significantly higher in our starting compositions compared to the natural Shatsky Rise basalts (Fig. II.1). First, we calculated the Na$_2$O content, which would lead to Ca# in the starting material AH3 similar to that of the natural samples with similar MgO content (Na$_2$O$_{Ca\#78}$=1.9). Then we used the "new" composition of AH3 to simulate equilibrium crystallization, in order to find out, if lower Na$_2$O in the starting composition would support the SiO$_2$ enrichment. In the case of AH3, lower initial Na$_2$O drives the LLDs to SiO$_2$ enrichment (thick black line in Fig. II.22), which supports our assumption, that the Ca# and An content of the *Plag* are the most important factors controlling the SiO$_2$ depletion or enrichment in the residual liquids. With our experiments we show the strong effect of the relative abundances of CaO and Na$_2$O (expressed as Ca#) on the LLDs.

In addition, the lack of Fe-Ti-Oxides in the crystallization sequence contributes also to the high SiO$_2$ in the solid phase. In the study of Walker et al. (1979), a compositionally similar starting material from the Mid-Atlantic Ridge (MAR) was used. The Ca# is in the same range and the Al# is slightly higher, although both SiO$_2$ and Al$_2$O$_3$ are higher in their starting material. In their study, early crystallization of SiO$_2$-free phases (spinel) and also the relatively high SiO$_2$ content in the starting material compared to the experimentally produced *Plag* (and also *Cpx*) led to SiO$_2$ enrichment during progressive crystallization. In our study, *Mag* was produced only at *hydrous* conditions (late stage of crystallization), due to slightly higher fO$_2$. As *Mag* was also observed in the crystallized groundmass in the natural Shatsky Rise basalts (Husen et al., 2013), the *Mag* stability implies that our *hydrous* conditions more closely represent the natural system beneath Shatsky Rise, which is in agreement with the H$_2$O contents observed in the natural glasses.

Part II: The Role of H$_2$O and Pressure on Multiple Saturation and Liquid Lines of
Descent in Basalts from the Shatsky Rise
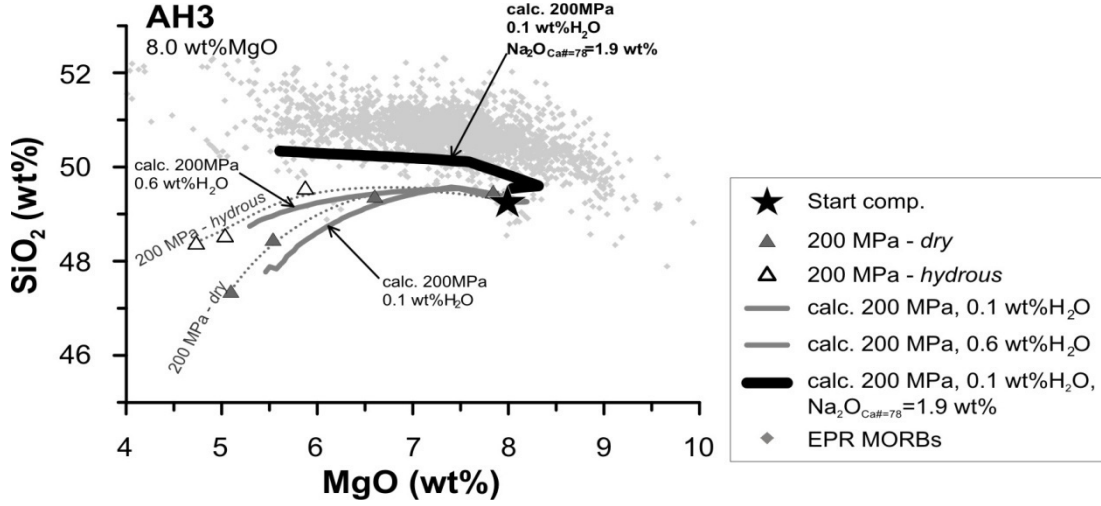
**Figure II.22:** Calculated LLDs for equilibrium crystallization at 200 MPa (solid lines) obtained using the COMAGMAT model (Ariskin & Barmina, 2004) in comparison to experimental 200 MPa liquids from *dry* (grey triangles) and *hydrous* (white triangles) conditions and natural EPR MORBs (PetDB, grey points). The difference between the thick black line (modified AH3 as starting composition) and grey lines (AH3 as starting composition) displays the effect of varying Ca# (Na$_2$O=1.9 wt%). Regarding simulation of *dry* and *hydrous* conditions, averages of experimental H$_2$O contents were used: 0.1 wt% H$_2$O for *dry* and 0.6 wt% H$_2$O for *hydrous* conditions. Due to overestimation of *Plag* stability by the COMAGMAT program, calculated LLDs display increasing MgO contents in the earliest stage of crystallization. However, this does not affect the general trend of SiO$_2$ contents in simulated liquids

.

6.6.   Composition of Coexisting Minerals

In the previous chapter (Mineral Compositions), we demonstrated that pressure

and small amounts of H$_2$O (up to 1.14 wt%) have minor or even no influence on the *Ol*

and *Plag* compositions when mineral compositions (Mg# of *Ol* and *Cpx*, An content in

Plag) are compared from runs of similar melt Mg#.

The deviations in *Plag* composition at given melt Mg# show a dependence on the

order of crystallization, because (1) the *Cpx* extracts CaO from the melt (leads to lower

melt Ca#) which results in lower anorthitic *Plag* and (2) the Mg# of the melt decreases

relatively less efficiently, if only one Fe-Mg-silicate is crystallizing. In contrast, the Mg#

Part II: The Role of H$_2$O and Pressure on Multiple Saturation and Liquid Lines of
Descent in Basalts from the Shatsky Rise

of *Cpx* is lowered with increasing pressure and also in the presence of small amounts of

H$_2$O. This is due to the relative stabilization of *Cpx* compared to *Ol* and *Plag* induced by

the increase of pressure and melt H$_2$O (see phase proportions), which also affects the

mineral compositions relative to each other. In Fig. II.23, we compare *Ol* and *Cpx*

compositions (expressed by Mg#) in our experimental products. Remarkably, the

different starting compositions and varying pressures have no effect on the mineral

cotectic compositions. In contrast, the addition of small amounts of H$_2$O results in

significantly lower Mg# in *Cpx* for the given *Ol* composition, e.g. at a Mg# of ~75 in *Ol*,

the *Cpx* Mg# is around 80 under *dry* conditions, whereas under *hydrous* conditions the

Mg# of *Cpx* is around 72 (Fig. II.23).
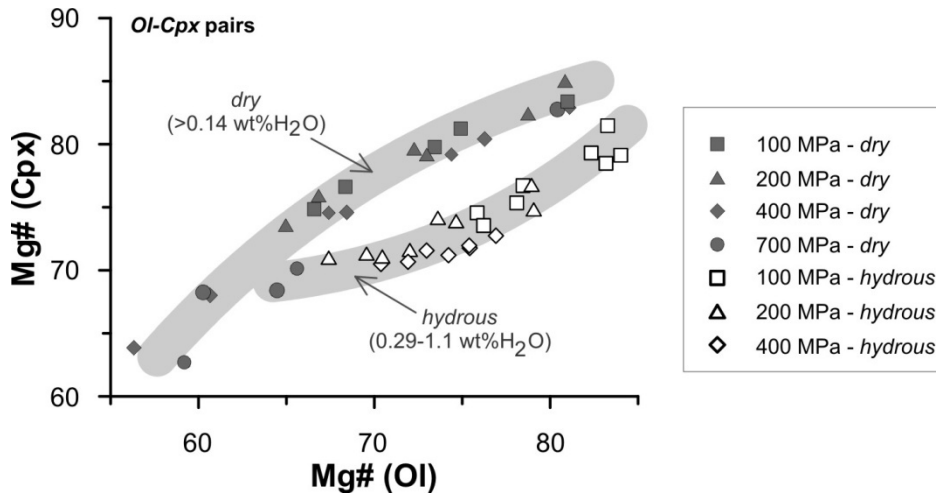
Figure II.23: Correlation of *Ol* and *Cpx* compositions represented by their Mg# (averages of 2-16 analyses). Different symbols represent experimental runs at different experimental pressures, grey and white symbols indicate *dry* and *hydrous* conditions respectively.

The comparison of *Plag* and *Cpx* compositions reveals to different systematics,

see Fig. II.24. The starting composition plays a major role, whereas our experiments show

no effect of pressure and the influence of H$_2$O is subordinate. The experimental *Plag*

produced under *hydrous* conditions, show slightly higher An contents in *Plag* for given

Mg# of *Cpx*. However, the *Plag* produced in the basalt AH6, exhibit the highest An contents in *Plag* for given *Cpx*; e.g. at a Mg# in *Cpx* of ~80 (*dry* conditions), a *Plag* in AH6 has ~73 mol% An in contrast to a *Plag* in AH3 having 68 mol% An. (Fig. II.24). Considering only the two more evolved compositions AH3 and AH5, the pairs of *Plag* and *Cpx* are on the same trend. As shown in Fig II.13a, higher An contents were observed in *Plag* at given Mg# in AH6, where *Cpx* is not the liquidus phase (see Fig. II.3). *Cpx* composition shows no variation with the different starting materials, which results in the great deviation of An in *Plag – Cpx* Mg# pairs of AH6 compared to the pairs in the other two basalts. Potential effects of pressure and H$_2$O on the relation of coexisting *Plag* and *Cpx* cannot be resolved in our experiments.

To sum up, systematics in cotectic mineral compositions revealed from our experiments can be useful to distinguish between different H$_2$O contents in magmas from the relations between natural *Cpx – Ol* pairs, whereas *Plag – Cpx* pairs can provide information on the crystallization sequence.

Part II: The Role of H₂O and Pressure on Multiple Saturation and Liquid Lines of Descent in Basalts from the Shatsky Rise
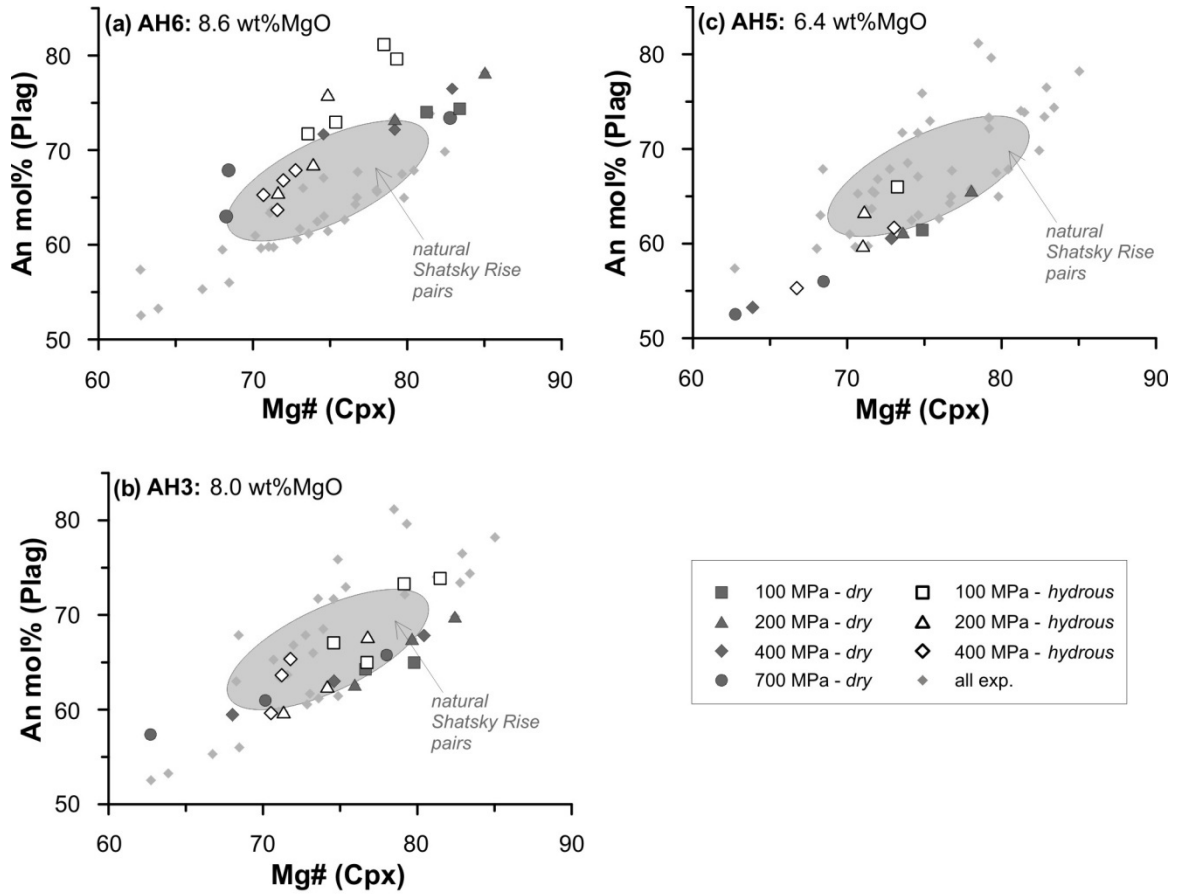
Figure II.24: Correlation of *Plag* and *Cpx* compositions represented by their An content and Mg# respectively (averages of 2-11 analyses) for each starting composition (a-c). Different symbols represent experimental runs at different experimental pressures, grey and white symbols indicate *dry* and *hydrous* conditions respectively. Additionally, the range of all experimental runs (light grey diamonds) and natural Shatsky Rise *Plag-Cpx* pairs (grey field, form Husen et al., 2013) are displayed.

6.7. Implications to Natural Shatsky Rise Basalts

The results of our experimental study confirm our previous constrains (Husen et al., 2013) of low pressure conditions during the magma differentiation beneath Shatsky Rise. The LLDs based on the intermediate starting material AH3 give evidence that the magma reservoir beneath Shatsky Rise was stored at pressures between 100 and 400 MPa; the 700 MPa LLD do not reproduce the natural trend of basaltic glass compositions. Considering, that our slightly *hydrous* experiments better represent the natural

Part II: The Role of H$_2$O and Pressure on Multiple Saturation and Liquid Lines of Descent in Basalts from the Shatsky Rise

---

differentiation processes in evolved MORBs (see previous chapter, SiO$_2$ depletion), the glasses produced in 100 MPa experiments best reproduce the natural trend of the Shatsky Rise lavas. 200-700 MPa LLDs lead to CaO/Al$_2$O$_3$ ratios systematically lower than that in the natural glasses. However, slightly lower amounts of H$_2$O would require higher pressures to reproduce the natural Shatsky Rise glasses.

In general, the natural trend shows a slight difference in the basaltic glasses from Tamu Massif (U1347A, Husen et al., 2013) and Ori Massif (U1350A, Sano et al., 2012). The basaltic glasses recovered on Ori Massif show a slightly steeper slope in the field of lower MgO concentrations (7-5.5 wt%) compared to those basaltic glasses from Tamu Massif. This leads to the assumption that the magmas beneath Ori Massif were stored at slightly higher pressures or were evolved in the presence of slightly higher melt H$_2$O. Husen et al. (2013) presented H$_2$O measurements (FTIR) of three more primitive natural glasses from Ori Massif (324 U1350 22R3 80–82, 324 U1350 24R1 135.5–137, 324 U1350 24R3 76–79), which show ~0.3 wt% H$_2$O. This H$_2$O content exceeds the minimum H$_2$O content (0.18 wt% H$_2$O) found in Tamu Massif basaltic glasses (Husen et al., 2013). Considering the incompatible character of H$_2$O, and that melt H$_2$O should always increase during differentiation, we assume that the parental Tamu Massif melts might have contained less H$_2$O compared to those from Ori Massif. Based on this, slight variations in the H$_2$O contents rather than variations in pressure might be responsible for the diversity of the evolved Shatsky Rise glass compositions.

Part II: The Role of H$_2$O and Pressure on Multiple Saturation and Liquid Lines of Descent in Basalts from the Shatsky Rise
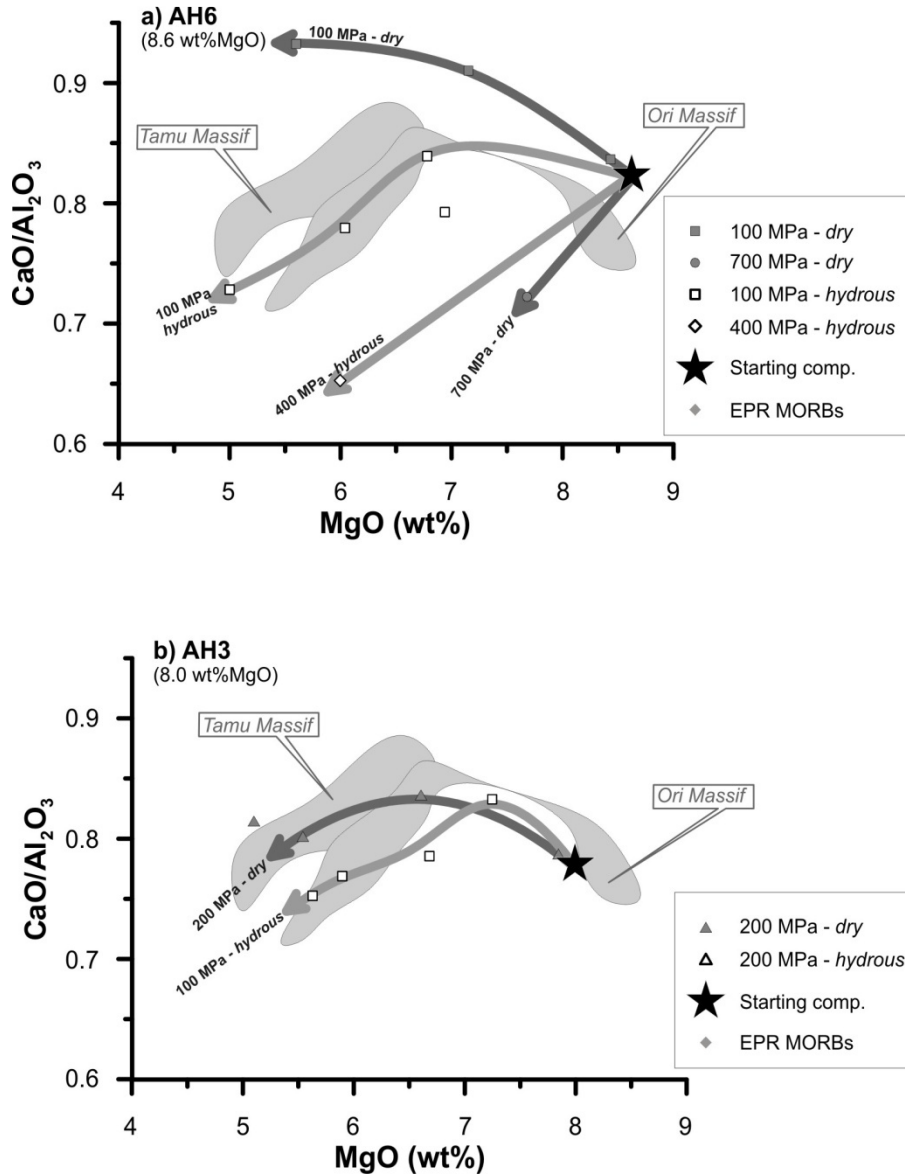
Figure II.25: Range of natural Shatsky Rise basaltic glasses (grey fields for Tamu Massif (324-U1347, Husen et al., 2013) and Ori Massif (324-U1350, Sano et al., 2012)) and experimental LLDs (dashed grey arrows) for the (a) most MgO-rich starting composition AH6 (8.6 wt% MgO) (b) intermediate starting composition AH3 (8 wt% MgO). Different symbols represent experimental liquid compositions obtained at different experimental pressures, grey and white symbols indicate *dry* and *hydrous* conditions respectively. Darker and lighter colors indicate *dry* and *hydrous* conditions respectively.

The melt trapped in an *Ol* with primitive composition may be assumed being parental for the suite of evolved basalts from the similar setting, if processes like e.g. magma mixing or assimilation can be excluded. The most primitive starting material

Part II: The Role of H_2O and Pressure on Multiple Saturation and Liquid Lines of
Descent in Basalts from the Shatsky Rise

AH6, which represents the composition of a melt inclusion in a high MgO *Ol* (Fo$_{87}$, Fo$_{90}$ would represent an *Ol* in equilibrium with a mantle melt), is assumed to be a parental melt of all Shatsky Rise magmas. For this composition the natural range of the Shatsky Rise basaltic glasses cannot be reproduced isobarically (Fig. II.6). Here, high pressures (400-700 MPa) are necessary to reproduce the high MgO (8-8.5 wt% MgO) Ori Massif glasses. In contrast to this, the group of more evolved glasses (5.5-7 wt% MgO) can be reproduced at lower pressures (100-400 MPa). As displayed in Fig. II.25, these observations lead to the conclusion that the more primitive Shatsky Rise (Ori Massif) lavas have been stored at greater depth. The differentiation of these magmas in deep crustal levels, was leading to the more primitive compositions found on Ori Massif reflected by the intermediate starting material AH3. This is in agreement with the data presented by Husen et al. (2013), who also described a multi level magma plumbing system beneath the Shatsky Rise. However, it should be noted that the starting material is based on an average of 15 compositions of re-homogenized melt inclusions, which were backtrack corrected (correction for post-entrapment crystallization). Thus, the composition obtained by this procedure, has an uncertainty and might not exactly represent the natural parental melt composition. Remarkably, the composition AH6 has a nepheline normative character and exhibits a very high CaO content, as well as CaO/Al_2O_3 higher than known for MORBs. Assuming an actual composition closer to the typical range of natural MORBs, the CaO/Al_2O_3 of AH6 should be lower. This results in the fact, that the pressures for magma storage indicated by our experiments might represent only maximum values, because the range of intermediate Shatsky Rise compositions could be reached by differentiation at lower pressures when the starting point was at lower CaO/Al_2O_3. However, the comparison to the typical range of EPR MORBs shows that a CaO/Al_2O_3 lower than that from the Ori Massif basaltic glasses

Dissertation of Anika Husen

Part II: The Role of H_2O and Pressure on Multiple Saturation and Liquid Lines of
Descent in Basalts from the Shatsky Rise

(AH3) is unlikely (would be lower than typical for MORB), which leads to the conclusion, that still higher pressures than 400 MPa at *dry* and 200 MPa at *hydrous* conditions would be necessary to reach constant or decreasing CaO/Al_2O_3 during differentiation to reproduce the Ori Massif glass compositions.

Our experimental data imply that in the deep magma reservoir beneath the Shatsky Rise (~650 MPa according to Husen et al., 2013), mainly *Cpx* and fewer *Plag* and *Ol* were fractionated similar to e.g. the run ShR611 (1:13:18 (*Ol*:*Plag*:*Cpx*)). Considering that ShR611 was conducted at *dry* conditions, the fraction of *Cpx* might be even higher under slightly *hydrous* conditions. In contrast, in the shallow magma reservoir, the fractionation of *Ol+Plag* is dominant while *Cpx* fractionation is subordinate.

7.   CONCLUSIONS

We presented an experimental study on tholeiitic basaltic glasses, which produced detailed information on the effect of pressure in a low pressure range between 100 and 700 MPa and the influence of small amounts of H_2O on the phase stabilities and LLDs for three different starting materials. The experimental pressure had a major influence on the *Cpx* stability whereas the melt H_2O depresses most efficiently the *Plag* liquidus, which is also shown by other studies (Bender et al., 1978; Michael & Chase, 1987; Danyushevsky, 2001; Almeev et al., 2012). With our experiments we demonstrated that pressure and H_2O have generally similar effects on the LLDs, due to *Cpx* stabilization and *Plag* destabilization. Considering that MORBs are generated under low pressure, and that they incorporate small amounts of H_2O, it is important to evaluate the role of pressure and H_2O in natural systems in relation to each other. The comparison showed that that the effect on the LLDs caused by a pressure increase from 100 to ~300 MPa can be reproduced by the addition of only small amounts of H_2O (0.4 wt%) at constant pressure. Taking into

account geophysical studies, which showed that magma chambers beneath MORs are expected between 1-3 km depth (Purdy et al., 1992), our data are in good agreement with this assumption. We showed that the H$_2$O content in basalts is a crucial factor for the evolution of MORBs and that it has to be taken into account in thermodynamic and experimental simulations of MORBs differentiation.

We observed a strong SiO$_2$ depletion during the crystallization in our experimental glasses. This is known by other studies (Grove et al., 1992; Whitaker et al., 2007) conducted in graphite containers. We assume that low Ca# and low SiO$_2$ contents in our starting glasses led to unusually high SiO$_2$ contents in the crystallized solid phase mainly caused by *Plag*. This in combination with extremely low H$_2$O contents in our *dry* experiments led to even stronger SiO$_2$ depletion due to high silicic/albitic *Plag*. The fact that SiO$_2$ depletion in experimental studies using other MORBs was observed when C-Pt containers (leading to almost dry conditions) were used, implies that MORB magmas generally incorporate more H$_2$O than gained in those experiments.

Regarding the Shatsky Rise magma evolution, our data support the study of Husen et al. (2013), because on the one hand, low pressure (100 MPa) LLDs reproduced best the natural differentiation trend of the Shatsky Rise glasses, whereas on the other hand, using the melt inclusion analogue starting composition, low pressures reproduce only the most evolved natural glass compositions and higher pressures (400-700 MPa) are necessary to produce the less evolved Shatsky Rise basalts. This is in agreement with the multi level magma plumbing system described by Husen et al. (2013).

Part II: The Role of H_2O and Pressure on Multiple Saturation and Liquid Lines of
Descent in Basalts from the Shatsky Rise

8.   ACKNOWLEDGEMENTS

9.   REFERENCES

Almeev, R. R., Holtz, F., Koepke, J., Parat, F. & Botcharnikov, R. E. (2007). The
effect of H2O on olivine crystallization in MORB: Experimental calibration at 200 MPa.
American Mineralogist 92, 670-674.

Almeev, R., Holtz, F., Koepke, J., Haase, K. & Devey, C. (2008). Depths of
partial crystallization of H_2O-bearing MORB: Phase equilibria simulations of basalts at
the MAR near Ascension Island (7-11 degrees S). Journal of Petrology 49, 25-45.

Almeev, R. R. & Ariskin, A. A. (1996). Mineral-melt equilibria in a hydrous
basaltic system: Computer modeling. Geokhimiya, 624-636.

Almeev, R., Portnyagin, M., Wengorsch, T., Sano, T., Natland, J.H., & Garbe-
Schönberg, D. (2011). Highly depleted melt inclusions in olivine from Shatsky Rise.
Mineralogical Magazine, Vol. 75 (3), 426

Almeev, R. R., Holtz, F., Koepke, J. & Parat, F. (2012). Experimental calibration
of the effect of H_2O on plagioclase crystallization in basaltic melt at 200 MPa. American
Mineralogist 97, 1234-1240.

Almeev, R. R., Holtz, F., Koepke, J., Parat, F. & Botcharnikov, R. E. (2007). The
effect of H_2O on olivine crystallization in MORB: Experimental calibration at 200 MPa.
American Mineralogist 92, 670-674.

Ariskin, A. A. (1999). Phase equilibria modeling in igneous petrology: use of
COMAGMAT model for simulating fractionation of ferro-basaltic magmas and the
genesis of high-alumina basalt. Journal of Volcanology and Geothermal Research 90,
115-162.

Ariskin, A. A. & Barmina, G. S. (2004). COMAGMAT: Development of a
magma crystallization model and its petrological Applications. Geochemistry
International 42, S1.

Behrens, H., Misiti, V., Freda, C., Vetere, F., Botcharnikov, R. E. & Scarlato, P.
(2009). Solubility of H_2O and CO_2 in ultrapotassic melts at 1200 and 1250 °C and
pressure from 50 to 500 MPa. American Mineralogist 94, 105-120.

Part II: The Role of H₂O and Pressure on Multiple Saturation and Liquid Lines of Descent in Basalts from the Shatsky Rise

Bender, J. F., Hodges, F. N. & Bence, A. E. (1978). Petrogenesis of basalts from the project FAMOUS area: experimental study from 0 to 15 kbars. Earth and Planetary Science Letters 41, 277-302.

Berndt, J., Liebske, C., Holtz, F., Freise, M., Nowak, M., Ziegenbein, D., Hurkuck, W. & Koepke, J. r. (2002). A combined rapid-quench and H₂-membrane setup for internally heated pressure vessels: Description and application for water solubility in basaltic melts. American Mineralogist 87, 1717-1726.

Berndt, J., Koepke, J. & Holtz, F. (2005). An Experimental Investigation of the Influence of Water and Oxygen Fugacity on Differentiation of MORB at 200 MPa. Journal of Petrology 46, 135-167.

Botcharnikov, R. E., Behrens, H. & Holtz, F. (2006). Solubility and speciation of C-O-H fluids in andesitic melt at T=1100-1300°C and P=200 and 500 MPa. Chemical Geology 229, 125-143.

Chekhmir, A. S., Persikov, M. B., Epel´baum, M. B. & Bukhtiyarov, P. G. (1985). Hydrogen transport through a model magma. Geokhimiya 5, 594-598.

Cross, W., Iddings, J. P., Pirsson, L. V. & Washington, H. S. (1902). A Quantitative Chemico-Mineralogical Classification and Nomenclature of Igneous Rocks. The Journal of Geology 10, 555-690.

Danyushevsky, L.V. and Plechov, P., 2011. Petrolog3: Integrated software for modeling crystallization processes. Geochemistry Geophysics Geosystems, 12(7): Q07021.

Danyushevsky, L. V. (2001). The effect of small amounts of H₂O crystallisation of mid-ocean ridge and backarc basin magmas. Journal of Volcanology and Geothermal Research 110, 265-280.

Danyushevsky, L. V., Eggins, S. M., Falloon, T. J. & Christie, D. M. (2000). H₂O Abundance in Depleted to Moderately Enriched Mid-ocean Ridge Magmas; Part I: Incompatible Behaviour, Implications for Mantle Storage, and Origin of Regional Variations. Journal of Petrology 41, 1329-1364.

Danyushevsky, L. V., Sobolev, A. V. & Dmitriev, L. V. (1996). Estimation of the pressure of crystallization and H₂O content of MORE and BABB glasses: Calibration of an empirical technique. Mineralogy and Petrology 57, 185-204.

Expedition 324 Scientists (2010). Testing plume and plate models of ocean plateau formation at Shatsky Rise, northwest Pacific Ocean. IODP Prel. Rept 324.

Feig, S., Koepke, J. r. & Snow, J. (2006). Effect of water on tholeiitic basalt phase equilibria: an experimental study under oxidizing conditions. Contributions to Mineralogy and Petrology 152, 611-638.

Fine, G. & Stolper, E. (1986). Dissolved carbon dioxide in basaltic glasses: concentrations and speciation. Earth and Planetary Science Letters 76, 263-278.

Part II: The Role of H_2O and Pressure on Multiple Saturation and Liquid Lines of Descent in Basalts from the Shatsky Rise

Freise, M., Holtz, F., Nowak, M., Scoates, J. & Strauss, H. (2009). Differentiation and crystallization conditions of basalts from the Kerguelen large igneous province: an experimental study. Contributions to Mineralogy and Petrology 158, 505-527.

French, B. M. & Eugster, H. P. (1965). Experimental Control of Oxygen Fugacities by Graphite-Gas Equilibriums. J. Geophys. Res. 70, 1529-1539.

Grove, T. (1993). Corrections to expressions for calculating mineral components in "Origin of calc-alkaline series lavas at medicine lake volcano by fractionation, assimilation and mixing" and "Experimental petrology of normal MORB near the kane fracture zone: 22°-25°N, mid-atlantic ridge". Contributions to Mineralogy and Petrology 114, 422-424.

Grove, T. L. & Bryan, W. B. (1983). Fractionation of pyroxene-phyric MORB at low pressure: An experimental study. Contributions to Mineralogy and Petrology 84, 293-309.

Grove, T. L., Kinzler, R. J. & Bryan, W. B. (1992). Fractionation of mid-ocean ridge basalt (MORB). Mantle Flow and Melt Generation at Mid-Ocean Ridges. Washington, DC: AGU, 281-310.

Hall, L. J., Brodie, J., Wood, B. J. & Carroll, M. R. (2004). Iron and water losses from hydrous basalts contained in $Au_{80}Pd_{20}$ capsules at high pressure and temperature. Mineralogical Magazine 68, 75-81.

Hamada, M. and Fujii, T., 2008. Experimental constraints on the effects of pressure and H_2O on the fractional crystallization of high-Mg island arc basalt. Contributions to Mineralogy and Petrology, 155(6): 767-790.

Herzberg, C. (2004). Partial crystallization of mid-ocean ridge basalts in the crust and mantle. Journal of Petrology 45, 2389-2405.

Holloway, J.R., Pan, V. and Gudmundsson, G., 1992. High-Pressure Fluid-Absent Melting Experiments in the Presence of Graphite - Oxygen Fugacity, Ferric Ferrous Ratio and Dissolved CO_2. European Journal of Mineralogy, 4(1): 105-114.

Holtz, F., Becker, A., Friese, M. & Johannes, W. (2001). The water-undersaturated and dry Qz-Ab-Or system revisited. Experimental results at very low water activities and geological implications. Contributions to Mineralogy and Petrology 141, 347-357.

Honma, U., 2012. Hydrous and anhydrous melting experiments of an alkali basalt and a transitional tholeiite from the Oginosen volcano, Southwest Japan: The possible influence of melt depolymerization on Ca-Na partitioning between plagioclase and the melt. Journal of Mineralogical and Petrological Sciences, 107(1): 8-32.

Husen, A., Almeev, R. R., Holtz, F., Koepke, J., Sano, T. & Mengel, K. (2013). Geothermobarometry of basaltic glasses from the Tamu Massif, Shatsky Rise oceanic plateau. Geochemistry, Geophysics, Geosystems 14, 3908–3928.

Jakobsson, S. & Oskarsson, N. (1994). The system C-O in equilibrium with graphite at high pressure and temperature: An experimental study. Geochimica Et Cosmochimica Acta 58, 9-17.

Part II: The Role of H$_2$O and Pressure on Multiple Saturation and Liquid Lines of Descent in Basalts from the Shatsky Rise

Jarosewich, E., Nelen, J. A. & Norberg, J. A. (1980). Reference Samples for Electron Microprobe Analysis. Geostandards Newsletter 4, 43-47.

Kinzler, R. J. & Grove, T. L. (1992). Primary magmas of mid-ocean ridge basalts 1. Experiments and methods. Journal of Geophysical Research: Solid Earth 97, 6885-6906.

Korenaga, J. and Sager, W.W., (2012), Seismic tomography of Shatsky Rise by adaptive importance sampling, Journal of Geophysical Research: Solid Earth, 117(B8), B08102, doi:10.1029/2012JB009248

Médard, E. & Grove, T. L. (2008). The effect of H$_2$O on the olivine liquidus of basaltic melts: experiments and thermodynamic models. Contributions to Mineralogy and Petrology 155, 417-432.

Michael, P. (1995). Regionally distinctive sources of depleted MORB: Evidence from trace elements and H$_2$O. Earth and Planetary Science Letters 131, 301-320.

Michael, P. J. & Cornell, W. C. (1998). Influence of spreading rate and magma supply on crystallization and assimilation beneath mid-ocean ridges: Evidence from chlorine and major element chemistry of mid-ocean ridge basalts. J. Geophys. Res. 103, 18325-18356.

Michael, P. J. & Chase, R. L. (1987). The influence of primary magma composition, H$_2$O and pressure on midocean ridge basalt differentiation. Contributions to Mineralogy and Petrology 96, 245-263.

Panjasawatwong, Y., Danyushevsky, L., Crawford, A. & Harris, K. (1995). An experimental study of the effects of melt composition on plagioclase-melt equilibria at 5 and 10 kbar: implications for the origin of magmatic high-An plagioclase. Contributions to Mineralogy and Petrology 118, 420-432.

Pouchou, J.-L. & Pichoir, F. o. (1991). Quantitative Analysis of Homogeneous or Stratified Microvolumes Applying the Model "PAP" . Electron Probe Quantitation: Springer US, 31-75.

Purdy, G. M., Kong, L. S. L., Christeson, G. L. & Solomon, S. C. (1992). Relationship between spreading rate and the seismic structure of mid-ocean ridges. Nature 355, 815-817.

Roeder, P. L. & Emslie, R. F. (1970). Olivine-liquid equilibrium. Contributions to Mineralogy and Petrology 29, 275-&.

Sager, W. W., Kim, J., Klaus, A., Nakanishi, M. & Khankishieva, L. M. (1999). Bathymetry of Shatsky Rise, northwest Pacific Ocean: Implications for ocean plateau development at a triple junction. J. Geophys. Res. 104, 7557-7576.

Sager, W. W., Zhang, J., Korenaga, J., Sano, T., Koppers, A. A. P., Widdowson, M. & Mahoney, J. J. (2013). An immense shield volcano within the Shatsky Rise oceanic plateau, northwest Pacific Ocean. Nature Geosci.

Part II: The Role of H_2O and Pressure on Multiple Saturation and Liquid Lines of Descent in Basalts from the Shatsky Rise

Sano, T., Shimizu, K., Ishikawa, A., Senda, R., Chang, Q., Kimura, J. I., Widdowson, M. & Sager, W. W. (2012). Variety and origin of magmas on Shatsky Rise, northwest Pacific Ocean. Geochemistry Geophysics Geosystems 13, 25.

Sano, T. & Yamashita, S. (2004). Experimental petrology of basement lavas from Ocean Drilling Program Leg 192: implications for differentiation processes in Ontong Java Plateau magmas. Geological Society, London, Special Publications 229, 185-218.

Schuessler, J. A., Botcharnikov, R. E., Behrens, H., Misiti, V. & Freda, C. (2008). Oxidation state of iron in hydrous phono-tephritic melts. American Mineralogist 93, 1493-1504.

Scientists, E. (2010). Testing plume and plate models of ocean plateau formation at Shatsky Rise, northwest Pacific Ocean. IODP Prel. Rept 324.

Shishkina, T. A., Botcharnikov, R. E., Holtz, F., Almeev, R. R. & Portnyagin, M. V. (2010). Solubility of H_2O- and CO_2-bearing fluids in tholeiitic basalts at pressures up to 500MPa. Chemical Geology 277, 115-125.

Sisson, T. W. & Grove, T. L. (1993). Experimental investigations of the role of H_2O in calc-alkaline differentiation and subduction zone magmatism. Contributions to Mineralogy and Petrology 113, 143-166.

Sobolev, A. V. & Chaussidon, M. (1996). H_2O concentrations in primary melts from supra-subduction zones and mid-ocean ridges: Implications for H_2O storage and recycling in the mantle. Earth and Planetary Science Letters 137, 45-55.

Stolper, E. (1982). Water in silicate glasses: An infrared spectroscopic study. Contributions to Mineralogy and Petrology 81, 1-17.

Stormer Jr, J.C. (1983). The effects of recalculation on estimates of temperature and oxygen fugacity from analyses of multi-component iron-titanium oxides. American Mineralogist 68 (5-6), 586-594.

Stormer, J. C. & Nicholls, J. (1978). XLFRAC: A program for the interactive testing of magmatic differentiation models. Computers and Geosciences 4, 143^159.

Takagi, D., Sato, H. and Nakagawa, M., 2005. Experimental study of a low-alkali tholeiite at 1-5 kbar: optimal condition for the crystallization of high-An plagioclase in hydrous arc tholeiite. Contributions to Mineralogy and Petrology, 149(5): 527-540.

Thompson, R. N. & Kushiro, I. (1972). The oxygen fugacity within graphite capsules in piston-cylinder apparatus at high pressure. Carnegie Institution of Washington Year Book 71, 615-616.

Tormey, D. R., Grove, T. L. & Bryan, W. B. (1987). Eexperimental petrology ofnormal MORB near the Kane Fracture-Zone - 22°-25°N, Mid-Atlantic Ridge. Contributions to Mineralogy and Petrology 96, 121-139.

Truckenbrodt, J. & Johannes, W. (1999). H_2O loss during piston-cylinder experiments. American Mineralogist 84, 1333-1335.

Ulmer, P. & Luth, R. (1991). The graphite-COH fluid equilibrium in P, T, & fO_2 space. Contributions to Mineralogy and Petrology 106, 265-272.

Part II: The Role of H$_2$O and Pressure on Multiple Saturation and Liquid Lines of Descent in Basalts from the Shatsky Rise

van der Laan, S. R. & Koster van Groos, A. F. (1991). Pt-Fe alloys in experimental petrology applied to high-pressure research on Fe-bearing systems. American Mineralogist 76, 1940-1949.

Villiger, S., Muentener, O. & Ulmer, P. (2007). Crystallization pressures of mid-ocean ridge basalts derived from major element variations of glasses from equilibrium and fractional crystallization experiments. Journal of Geophysical Research-Solid Earth 112.

Villiger, S., Ulmer, P., Muntener, O. & Thompson, A. B. (2004). The liquid line of descent of anhydrous, mantle-derived, tholeiitic liquids by fractional and equilibrium crystallization - an experimental study at 1 center dot 0 GPa. Journal of Petrology 45, 2369-2388.

Walker, D., Shibata, T. & Delong, S. E. (1979). Abyssal tholeiites from the Oceanographer Fracture-Zone .2. Phase-equilibria and mixing. Contributions to Mineralogy and Petrology 70, 111-125.

Whitaker, M. L., Nekvasil, H., Lindsley, D. H. & Difrancesco, N. J. (2007). The Role of Pressure in Producing Compositional Diversity in Intraplate Basaltic Magmas. Journal of Petrology 48, 365-393.

Yang, H. J., Kinzler, R. J. & Grove, T. L. (1996). Experiments and models of anhydrous, basaltic olivine-plagioclase-augite saturated melts from 0.001 to 10 kbar. Contributions to Mineralogy and Petrology 124, 1-18.

Part III: Evaluation of Thermodynamic (Petrological) Models and Geothermobarometers

1. INTRODUCTION

As discussed in the previous chapter, the compositional variety of basaltic rocks is mainly influenced by the variability in their crystallization conditions. Pressure, temperature, and water content as well as oxygen fugacity and bulk composition majorly influence phase stabilities and thus, the melt compositions which are produced during differentiation. Our and previous experimental studies showed the effect of pressure on the Liquid Lines of Descent (LLDs) (e.g. Part II; Bender et al, 1987; Grove et al, 1992; Villiger et al., 2004; Whitaker et al., 2007). Danyushevsky (2001), Berndt et al. (2005), Almeev et al. (2007), and Almeev et al. (2012), demonstrated the strong influence of H_2O on phase stabilities. In Part II, the relatively large effect of H_2O compared to pressure is discussed. Our experimental products demonstrated that especially the H_2O contents, even if they are below 1 wt%, are crucial to understand differentiation processes beneath mid-ocean ridges (MORs).

Many geothermobarometers and thermodynamic models are available to calculate and simulate potential magma storage conditions. Unfortunately, as discussed in the

Part III: Evaluation of Thermodynamic (Petrological) Models and Geothermobarometers

introduction of Part II, most models are calibrated on a narrow range of conditions (few high pressure experiments), especially regarding small amounts of H_2O, because the experimental data for the conditions, which are relevant for magmatic processes within the oceanic crust, are mainly underrepresented in the literature.

Following the approach presented in Putirka (2008) (and Putirka et al., 1996, Putirka, 2005, Putirka et al., 2007), we used our experimental products to evaluate recent models and equations for the calculation of magmatic pressures and temperatures. We will point out which advantages and disadvantages they have and where potential refinements are necessary. Special attention will be given on the problem of small amounts of H_2O, because we already showed in Part II that low H_2O contents are strongly controlling the mid-ocean ridge basalt (MORB) differentiation. To illustrate the increasing error of the pressure-temperature (*P-T*) calculations, which arises in the presence of small amounts of H_2O, we compare calculations for our almost anhydrous ("*dry*", <0.14 wt% H_2O, C-Pt double capsules) and H_2O-bearing ("*hydrous*", <0.14 wt% H_2O, Fe pre-saturated AuPd capsules) runs presented in Part II. We plot the calculated pressures and temperatures for each experiment against the corresponding experimental run conditions, assuming that the experimental phases are in equilibrium at those conditions (Part II, chapter 5.5). For all thermometers and barometers, we used only those of our experimental samples, where the melt H_2O could be determined. The corresponding measured H_2O content was applied in the calculations, in those cases where H_2O is taken into account. Only in the case of the simulations using the COMAGMAT program (Ariskin & Barmina, 2004), pressures and temperatures for all our multiple saturated (olivine+plagioclase+clinopyroxene (*Ol+Plag+Cpx*)) liquids were calculated, applying an average H_2O content of 0.1 wt% H_2O for *dry* and 0.6 wt% H_2O for *hydrous* conditions.

All our experimental run products were analyzed using a Cameca SX100 electron microprobe in the Institute of Mineralogy in Hannover. The water contents were determined via Fourier transformation infrared (FTIR) spectroscopy. The analytical methods are described in more detail in Part II, chapter 4. The data of this methodical test is reported in Tabs. AIII.1-AIII.3 (Appendix III).

2.   THERMODYNAMIC MODELING USING COMAGMAT

The COMAGMAT program (Almeev & Ariskin, 1996, Ariskin, 1999, Ariskin & Barmina, 2004) is a thermodynamic model based on a large set of experimental data. Recently, it was refined with new coefficients for the water induced liquidus depression for *Plag* and *Ol* in basaltic melts (Almeev et al., 2012; Almeev et al., 2007). COMAGMAT can be used to calculate mineral pseudoliquidus temperatures for given compositions and pressures or, more importantly, to simulate equilibrium or fractional crystallization at constant or variable pressures. The most important advantage is that the melt H_2O content is also taken into account in this model.

In Fig. III.1a, we present *Ol* pseudoliquidus temperature calculations for our experimental liquids saturated with *Ol*. The calculated values closely reproduce our measured temperatures, although the calculations for *dry* experiments are systematically underestimated of about 20°C. In the case of *hydrous* conditions, the experimental temperatures could be reproduced within an error of ±25°C, but the regression of the correlation of measured and calculated temperatures has a slope of 0.57, leading to an overestimation of lower temperatures and an underestimation of higher temperatures (Fig. III.1a).

Part III: Evaluation of Thermodynamic (Petrological) Models and
Geothermobarometers
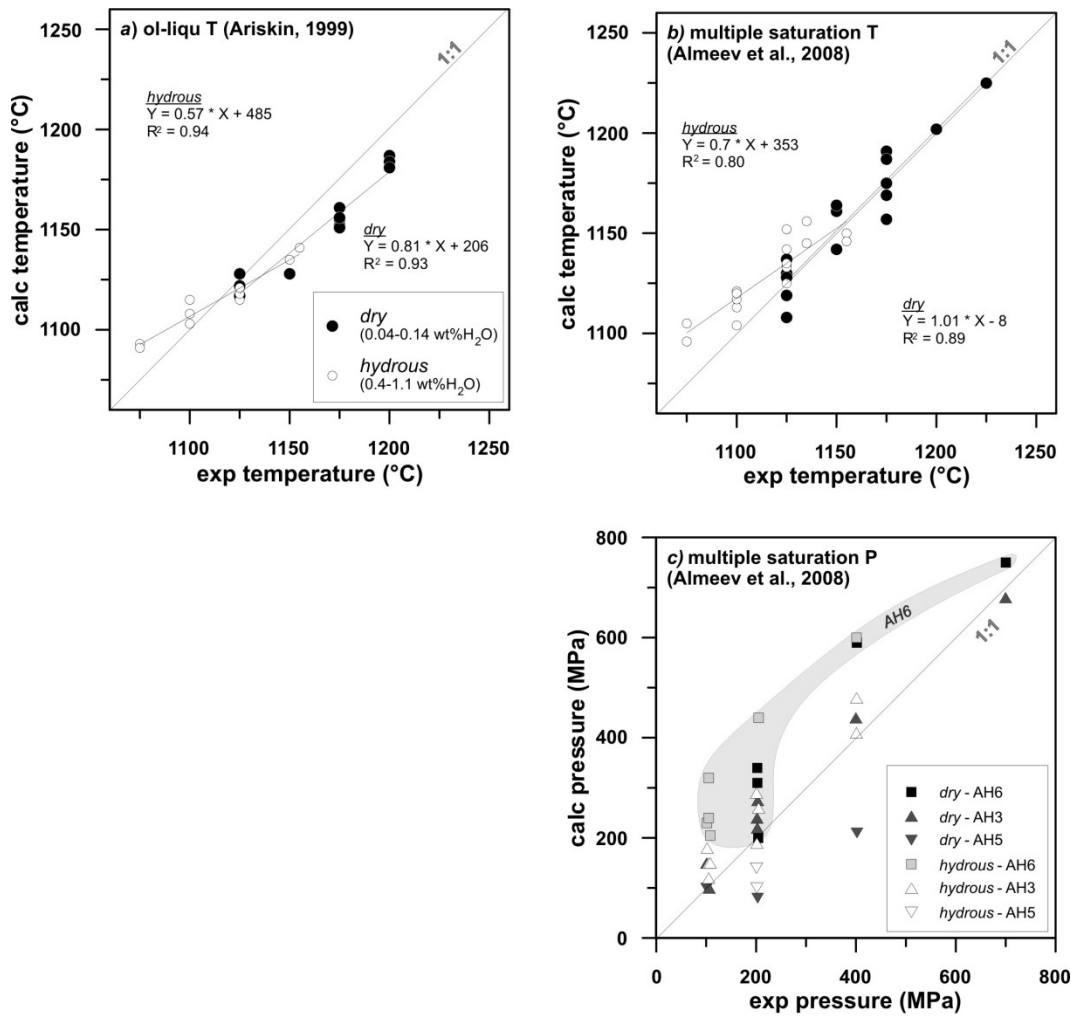
Figure III.1: Calculated temperatures and pressures for our experimental *dry* (black symbols) and *hydrous* (white symbols) liquid compositions compared with their measured counterparts. Temperatures were obtained using the COMAGMAT program (Ariskin & Barmina, 2004) with recently refined coefficients for the effect of H_2O on mineral stabilities (Almeev et al., 2012, Almeev et al., 2007). (a) *Ol* pseudoliquidus temperatures for given pressure and H_2O content. (b) calculation of temperatures and (c) pressures of multiple saturation (*Ol+Plag+Cpx*) at given H_2O conditions (average H_2O contents of 0.1 and 0.6 wt% H_2O for *dry* and *hydrous* conditions respectively were applied) following the approach of Almeev et al. (2008). For pressure calculation, the corresponding starting materials are indicated by different symbols, because the accuracy of the model is dependent on the starting material.

Almeev et al. (2008) and Husen et al. (2013) used the COMAGMAT program as a

geothermobarometer and calculated conditions of multiple saturation (*Ol+Plag+Cpx*) for

natural basaltic melt compositions (Part I). Besides the consideration of H_2O, this

approach has another important advantage, because only the liquid composition and the

measured H_2O contents are used. The method is independent on mineral compositions,

and thus it is not necessary to measure mineral compositions in equilibrium with the melt, which is sometimes problematic in natural samples (e.g. due to zoning of the minerals, alteration). However, the general assumption that the treated liquid is multiple saturated with all three mineral phases (*Ol+Plag+Cpx*) has to be true. It has to be noted that the determination and evaluation of the measured H_2O contents has to be done with caution, due to possible incorporation of H_2O during alteration, or degassing of the melts before quenching. This is discussed in detail in Part I, chapter 4.4. According to Husen et al. (2013), we slightly "adjusted" the *Cpx* crystallization temperature (-5°C, for the augite thermometer of Ariskin & Barmina, 2004) to avoid overestimation of *Cpx* stability.

The application to our experimental products led generally to a good agreement between the calculated and measured values (slope of regression: 1.01) in the case of *dry* experiments, although the precision is only ±20°C. Compared to *Ol*-temperatures, these calculations led to more accurate values for *dry* experiments, whereas the temperatures were stronger overestimated for *hydrous* experiments (Fig. III.1b). Additionally, the pressures for each liquid composition were calculated and are displayed in Fig. III.1c. The calculation of multiple saturation conditions for our experimental glasses reproduce the measured experimental pressures with a precision of ±100 MPa for the two more evolved starting materials (AH5, AH3). Remarkably, the calculations using experimental runs in the most MgO-rich starting composition (AH6) have a bigger deviation from to the measured values (up to 200 MPa). However, compared to other geobarometers, the COMAGMAT program leads to a more accurate simulation of crystallization conditions (see below).

3.   GEOTHERMOBAROMETRY

3.1.   Liquid Based Thermometers

As already reviewed by Putirka (2008), there are some simple geothermometers using only the melt composition for the calculation of crystallization temperatures (Fig. III.2). Helz & Thornber (1987) published two simple thermometers based on MgO and CaO contents respectively. The equations are based on experimental liquids produced via differentiation at 1 atm and fO_2=NNO (nickel-nickel oxide). Putirka (2008) also presented two modified equations after the MgO-thermometer of Helz & Thornber (1987) (Equation 13 and 14 in Putirka (2008)). Equation 14 contains a term for the influence of H_2O, which is not the case in the other equations.

The results of the application of the Helz & Thornber (1987) equations are shown in Fig. III.2a and b. Similarly to the *Ol* thermometry using COMAGMAT, the MgO-thermometer reproduced our *hydrous* experimental temperatures with higher precision (±30°C) compared to temperatures of *dry* experiments (systematically underestimated about 10-30°C). However, for *hydrous* experiments the slope of the regression is 0.52, thus, at lower temperatures the systematic error increases: e.g at 1125°C, the calculations reproduce our experimental temperatures with an accuracy of ±10°C, whereas at 1075°C, the calculated temperature is ~30°C too high (Fig. III.2a). The application of the CaO-thermometer showed generally similar results like the MgO-thermometer, although they have a larger scatter (±40°C) for both, *dry* and *hydrous* conditions. Remarkably, CaO-temperatures calculated for *dry* experiments lie more close to the 1:1 line.

Equation 13 presented in Putirka (2008) reproduced our experimental temperatures very good regarding *dry* experiments. The systematic error leading to underestimated temperatures is eliminated compared to Helz & Thornber (1987) and the

Part III: Evaluation of Thermodynamic (Petrological) Models and Geothermobarometers

slope of the correlation is 0.96 following closely the 1:1 line (Fig. III.2c). As it does not account for melt H_2O contents, this equation leads also to a systematic offset to higher calculated temperatures for the *hydrous* experiments (~30°C too high). In the case of our experiments, this misfit could not be solved using the Equation 14 (Putirka, 2008) although it takes the melt H_2O content into accout (Fig. III.2d).
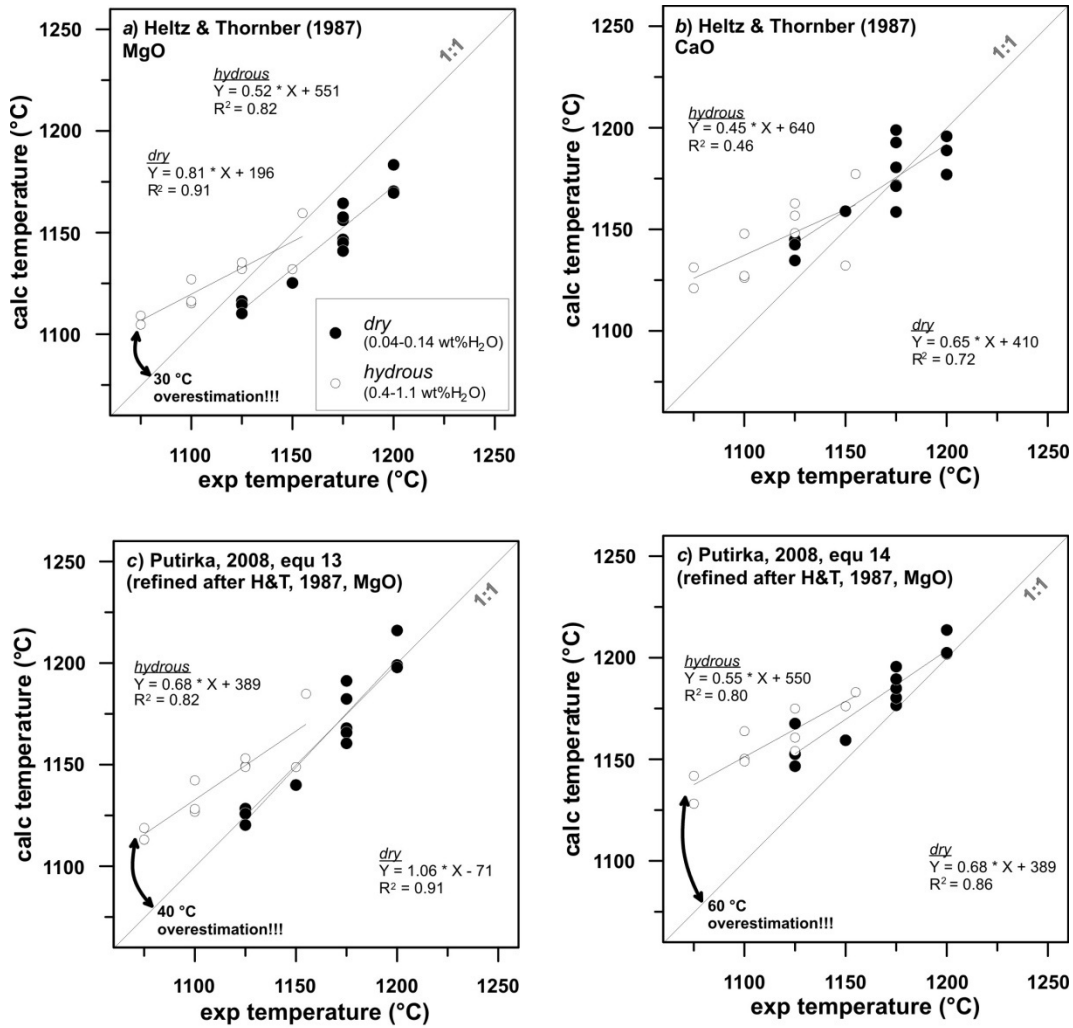
Figure III.2: Calculated temperatures for our experimental *dry* (black symbols) and *hydrous* (white symbols) liquid compositions compared with their measured counterparts. Temperatures were obtained using liquid-based geothermometers form (a) Heltz & Thornber (1987): referring only to the MgO content in the melt, (b) Heltz & Thornber (1987): referring only to the CaO content in the melt, (c) Putirka (2008, Equation 13): refinement of MgO-thermometer from Heltz & Thornber (1987), (d) Putirka (2008, Equation 14): refinement of MgO-thermometer from Heltz & Thornber (1987) which also includes a term referring to the melt H_2O content.

3.2.   Olivine-Melt Based Thermometers

In literature, different geothermometers based on *Ol*-melt equilibria are presented. In Fig. III.3, we compare temperatures obtained with different thermometers for our experimental liquids which were saturated in *Ol*. The model of Beattie (1993) is a melt composition based geothermometer for the calculation of *Ol* equilibration temperatures. According to Putirka (2008), it leads to valuable temperature estimations for anhydrous systems, but systematically overestimates the temperatures for hydrous compositions. As shown in Fig. III.3a, our observations using this thermometer are in agreement with those from Putirka (2008). Additionally, we show that, similar to the models discussed in the previous chapter, the calculations for lower temperature experiments are stronger overestimated than for intermediate and high temperatures, resulting in a tilt of the regression relative to the 1:1 line (slope: 0.53). The calculation of the temperatures for our *dry* experiments have a high precision ($\pm 20°C$) and show a good correlation with a slope of the regression close to the 1:1 line (slope: 0.79, R^2=0.89). We observed similar systematics using other models (Fig. III.3b to d): Ford et al. (1983), Herzberg & O'Hara (2002), Putirka (2008) (Equation 22), Danyushevsky (2001). Remarkably, the model presented by Ford et al. (1983), which is based on the partitioning of Mg and Fe between melt and *Ol*, led to almost perfect reproduction of our *dry* experimental temperatures (slope:1.06, R^2=0.95). The model presented by Danyushevsky (2001) is similar to the equation of the Ford et al. (1983) model with an additional correction factor for the melt H_2O content (Fig. III.3e). In contrast to the Ford et al. (1983) model, all calculations using the Danyushevsky (2001) model underestimate the experimental temperatures ($\sim 25°C$). However, the slope of regression is almost 1 (*dry*: 1.02 and *hydrous*: 0.79) and the data show small scatter (*dry*: R^2=0.95 and *hydrous*: R^2=0.86).

Part III: Evaluation of Thermodynamic (Petrological) Models and Geothermobarometers

a) Ol crystallization T (Beattie, 1993)

hydrous
Y = 0.53 * X + 567
R² = 0.91

dry
Y = 0.79 * X + 257
R² = 0.89

60 °C overestimation!!!

dry (0.04-0.14 wt%H₂O)
hydrous (0.4-1.1 wt%H₂O)

b) Ol crystallization T (Ford, 1983)

hydrous
Y = 0.73 * X + 333
R² = 0.91

dry
Y = 1.06 * X - 73
R² = 0.95

50 °C overestimation!!!

c) Ol crystallization T (Herzberg & O'Hara, 2002)

hydrous
Y = 0.67 * X + 414
R² = 0.88

dry
Y = 0.88 * X + 146
R² = 0.91

50 °C overestimation!!!

d) Ol crystallization T (Putirka, 2008, equ 22)

hydrous
Y = 0.56 * X + 517
R² = 0.85

dry
Y = 0.71 * X + 350
R² = 0.85

30 °C overestimation!!!

e) Ol crystallization T (Danyushevsky, 2001)

systematic underestimation!!!

hydrous
Y = 0.79 * X + 205
R² = 0.86

dry
Y = 1.02 * X - 60
R² = 0.95

Figure III.3: Calculated temperatures for our experimental *dry* (black symbols) and *hydrous* (white symbols) liquid compositions compared with their measured counterparts. Temperatures were obtained for *Ol* saturated runs using geothermometers based on *Ol*-liquid equilibria. (a) Beattie (1993), (b) Ford (1983), (c) Herzberg & O'Hara (2002) thermometers are calculating *Ol*-crystallization temperature for a given melt composition dependent on pressure. (d) Putirka (2008, Equation 22) is a refined version of the model of Beattie (1993) having an additional term which accounts for melt H₂O. (e) The equation of Danyushevsky (2001) is based on the Ford (1983) model with an additional correction for melt H₂O contents.

Part III: Evaluation of Thermodynamic (Petrological) Models and Geothermobarometers

Figure III.4: Calculated temperatures for our experimental *dry* (black symbols) and *hydrous* (white symbols) liquid compositions compared with their measured counterparts. Temperatures were obtained for *Plag* saturated runs using geothermometers based on *Plag*-liquid equilibria, which both account for melt H_2O contents. (a) Putirka (2008, Equation 24a) requires liquid and *Plag* compositions in equilibrium with each other, whereas (b) the model of Danyushevsky (2001) is based on the liquid composition only.

3.3. Plagioclase-Melt Based Thermometers

Regarding *Plag*-melt thermometry we compare two models in Fig. III.4. On the one hand, the *Plag*-melt thermometer of Putirka (2008) (Equation 24a, Equation 1 in Putirka (2005)), which is important, because it is a part of a geothermobarometer and takes the melt H_2O content into account. On the other hand, the model of Danyushevsky (2001), which also accounts for H_2O. We applied these calculations to all our samples where *Plag* and melt compositions as well as melt H_2O contents were measured. Although both models include H_2O in their calculation, again, temperatures of *dry* experiments were recalculated with significantly higher accuracy. They are ~20°C overestimated by the Putirka model (Fig. III.4a) and slightly underestimated by Danyushevsky (2001) (Fig. III.4b). However, regarding *dry* experiments they have a small scatter (±20°C, and R^2 close to 1) and the regression has a slope close to 1 in both cases (see Fig. III.4). The calculation of *hydrous* experimental temperatures showed that, Putirka (2008) leads to an overestimation of temperatures, which is more pronounced at

lower temperatures, e.g. at 1075°C, the offset of the calculated temperatures is ~70°C (Fig. III.4a). In contrast, the model of Danyushevsky (2001) leads to more reasonable results. The regression follows more closely the 1:1 line with a slope of 0.65, although the calculated temperatures have a higher scattering (±30°C) (Fig. III.4b).

3.4.   Clinopyroxene and Clinopyroxene-Melt Based Thermometers

As displayed in Fig. III.5, we tested the thermometers from Putirka (2008) and Danyushevsky (2001) by their application to our experimental runs which were saturated in *Cpx*. Only those samples with known melt composition and melt H_2O contents were used. Putirka (2008) presented one thermobarometer based on the *Cpx* and melt compositions (Equation 33) and one only based on the *Cpx* composition (Equation 32d). Especially thermobarometers based on only *Cpx* compositions (Equation 32d) are highly requested, because they can be applied to magmatic cumulates or other settings where no sufficient melt composition is available. As the Equation 32d is one part of a geothermobarometer presented by Putirka (2008), the calculations were tested first using measured experimental pressures as input parameters (Fig. III.5c), and afterwards using the calculated pressures (Equation 32b in Putirka, 2008) (Fig. III.5d).

The application of both Putirka equations led to temperatures in good agreement with the measured values, regarding *dry* experimental conditions (±25°C). The application of calculated pressures (using the geobarometer Equation 32b from Putirka, 2008) as pressure input in Equation 32d implies a much higher uncertainty, but noticeably, the calculated temperatures are still relatively close to the measured ones being slightly offset to higher values (~10°C). For *hydrous* conditions, similar systematics were observed like in the previously discussed models. Although all equations include a term which accounts for H_2O, the regressions are tilted and offset to higher temperatures.

Part III: Evaluation of Thermodynamic (Petrological) Models and Geothermobarometers

In contrast to the calculations using the Putirka (2008) models, again, the model of Danyushevsky (2001) leads to a systematic underestimation of the experimental temperatures for both, *dry* and *hydrous* conditions with similar extend. Besides this systematic shift, the data shows a close correlation almost parallel to the 1:1 line (slope of the regression: 0.7-0.66, R²=0,77-0,82) (Fig. III.5b).
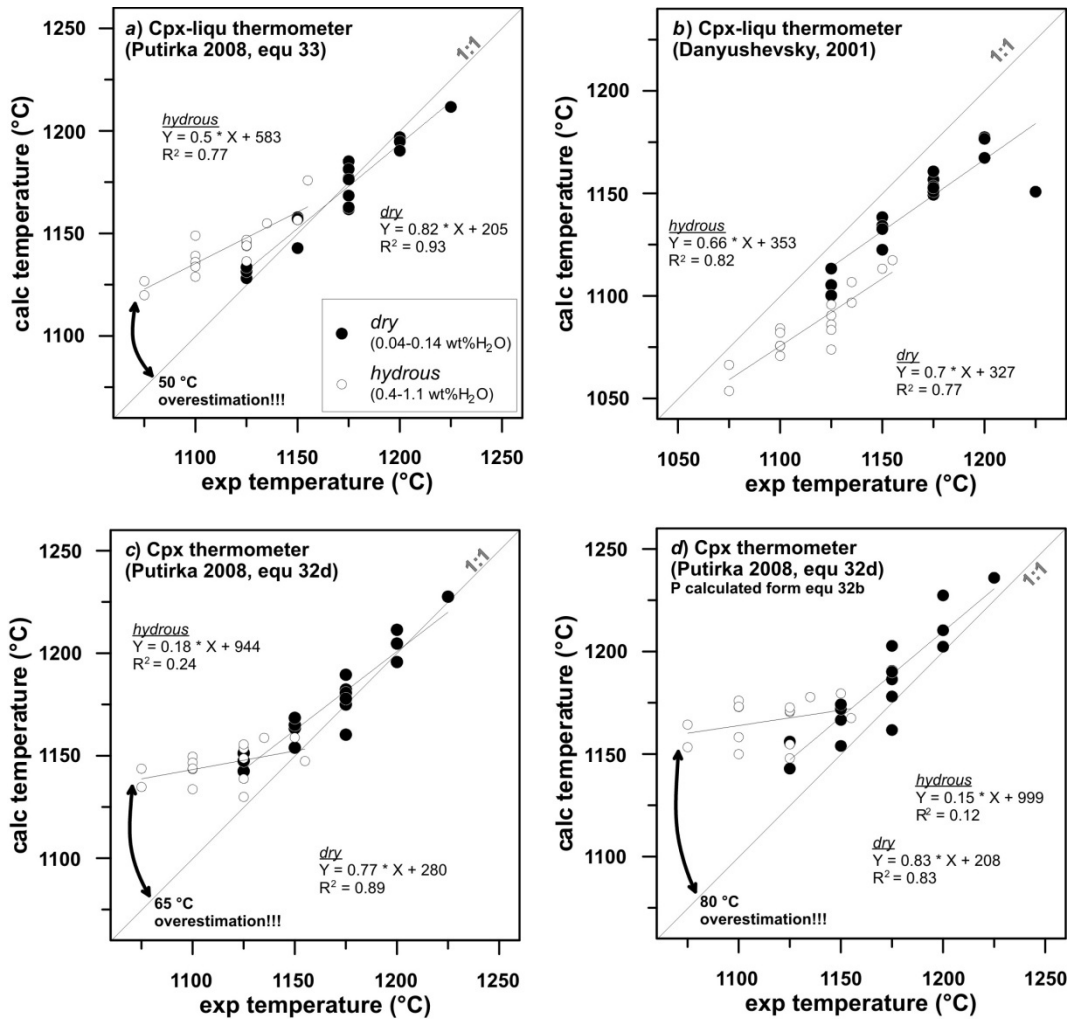
Figure III.5: Calculated temperatures for our experimental *dry* (black symbols) and *hydrous* (white symbols) liquid compositions compared with their measured counterparts. Temperatures were obtained for *Cpx* saturated runs using geothermometers based on *Cpx*-liquid equilibria, which all account for melt H$_2$O contents. (a) The equation of Putirka (2008, Equation 33) requires *Cpx* and liquid compositions in equilibrium with each other. (b) The model of Danyushevsky calculates *Cpx* pseudoliquidus for the given liquid composition. (c) In contrast Putirka (2008, Equation 32d) is based on *Cpx* compositions only; when combined with Equation 32b (Putirka, 2008), it can be used as a geothemobarometer as well.

3.5. Geobarometry

We used our experimental products to test recent geobarometers, which are shown in Fig. III.6. We present data obtained using models of Putirka (2008), which are based on *Plag*-melt (Equation 25a, Fig. III.6a) and *Cpx*-melt (Equation 31, Fig. III.6b) equilibria, and *Cpx* compositions only (Equation 32b, Fig. III.6c and d). Additionally we show calculations using the models of Herzberg (2004) (Fig. III.6e) and Yang et al. (1996) (Fig. III.6f), which are based on liquid compositions only, given that those liquids are multiple saturated with *Ol+Plag+Cpx*.

The application of the *Plag*-melt barometer (Fig. III.6.a) from Putirka (2008) led to a large spread of the data, with an uncertainty of the calculations up to 700 MPa in *dry* and 400 MPa in *hydrous* experiments. Thus, the error exceeds 100%, showing, that the barometer cannot be applied to our experimental products.

The *Cpx* barometers presented by Putirka (2008) (Equations 31, 32b) led to the best fit between the calculated and measured pressures, although they are slightly overestimated for both, *hydrous* and *dry* conditions (Fig. III.6b and c). In both cases, the calculated and measured values correlate almost parallel to the 1:1 line. The *Cpx*-melt barometer overestimated the pressures for *dry* conditions about ~100 MPa (slope: 1.03, $R^2=0.95$) and for *hydrous* conditions ~200 MPa (slope: 0.94, $R^2=0.59$) (Fig. III.6b). The barometry only based on *Cpx* compositions led to a slightly better match between calculated and measured values compared to *Cpx*-melt barometry. Pressures of *dry* experiments were overestimated about ~20 MPa (slope: 1.07, $R^2=0.97$) and those of *hydrous* experiments about ~150 MPa (slope: 0.8, $R^2=0.71$) (Fig. III.6c). When Equation 32b is used as a geothermobarometer in combination with Equation 32d (geothermometer), the deviation of the calculated and measured pressures increases.

However, the pressure estimations using this model still lead to systematic data being offset to higher pressures about 100 MPa and 300 MPa for *dry* and *hydrous* experiments respectively.

The geobarometers of Herzberg (2004) and Yang et al. (1996) (Fig. III.6e and f), which do not take the H_2O contents into account, have a higher uncertainty. Only in the case of *dry* conditions using the Herzberg (2004) barometer our 400 and 700 MPa experimental pressures were closely reproduced and the correlation follows the 1:1 line ±100 MPa (Fig. III.6d). In contrast to *dry* experimental conditions, the calculated pressures for *hydrous* experiments are more close to the actual values in the lower pressure region, whereas the overestimation increases towards higher pressures. This results in 100% (400 MPa) deviation for 400 MPa runs. The application of the barometer of Yang et al. (1996) (Fig. III.6f) led also to slightly better results in the case of *dry* experiments, but still the experimental pressures were systematically overestimated with a large spread in the calculated values (±250 MPa). Similar variety of calculated pressures was observed for the calculation of *hydrous* conditions (±250 MPa), but with higher offset to overestimated pressures (~200 MPa).

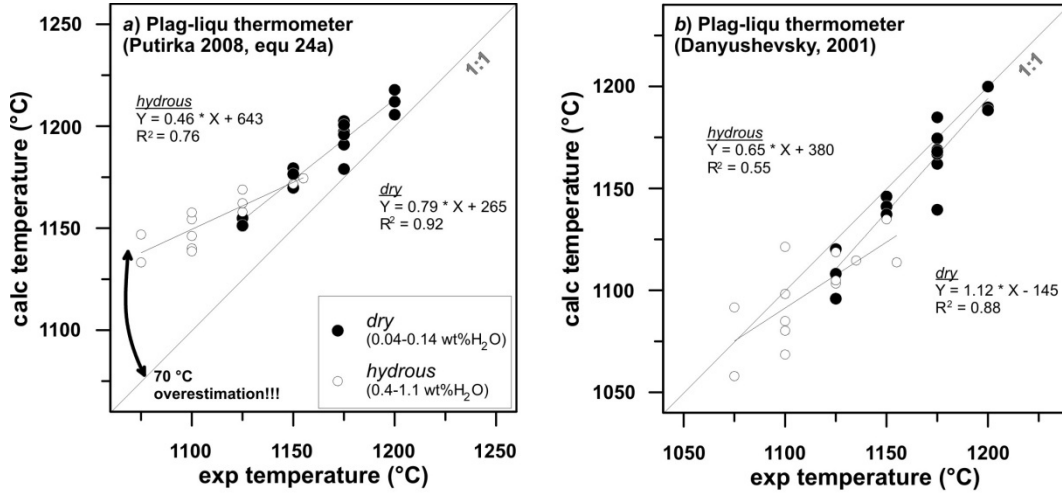**Figure III.6:** Calculated pressures for our experimental dry (black symbols) and hydrous (white symbols) liquid compositions compared with their measured counterparts. Pressures were obtained using different geobarometers: (a) The *Plag*-liquid geothermobarometer of Putirka (2008, Equation 25a) requires Plag and liquid compositions in equilibrium and also includes melt H_2O contents in pressure calculations, (b) the *Cpx*-liquid geothermobarometer of Putirka (2008, Equation 31) requires *Cpx* and liquid compositions in equilibrium and also includes melt H_2O contents in pressure calculations, (c) the *Cpx* geobarometer from Putirka (2008, Equation 32b) is based on *Cpx* compositions only and accounts for H_2O contents, (d) in combination with Equation 32d, it can be used as a geothermobarometer; (e) the model of Herzberg (2004) is based on liquid composition only (assuming that the liquid is multiple saturated with *Ol+Plag+Cpx*) but does not take H_2O contents into account, (f) the geobarometer of Yang et al. (1996) is based on liquid compositions, without accounting for melt H_2O contents

Part III: Evaluation of Thermodynamic (Petrological) Models and Geothermobarometers

a) Plag-liqu barometer (Putirka 2008, equ 25a)

b) Cpx-liqu barometer (Putirka 2008, equ 31)

hydrous
Y = 0.94 * X + 211
R² = 0.59

dry
Y = 1.03 * X + 91
R² = 0.95

dry
(0.04-0.14 wt% H₂O)

hydrous
(0.4-1.1 wt% H₂O)

c) Cpx barometer (Putirka 2008, equ 32b)

hydrous
Y = 0.80 * X + 148
R² = 0.71

dry
Y = 1.07 * X + 14
R² = 0.97

d) Cpx barometer (Putirka 2008, equ 32b)
T calculated form equ 32d

hydrous
Y = 0.89 * X + 267
R² = 0.72

dry
Y = 1.1 * X + 49
R² = 0.96

e) Geobarometer (Herzberg, 2004)

f) Geobarometer (Yang et al., 1996)
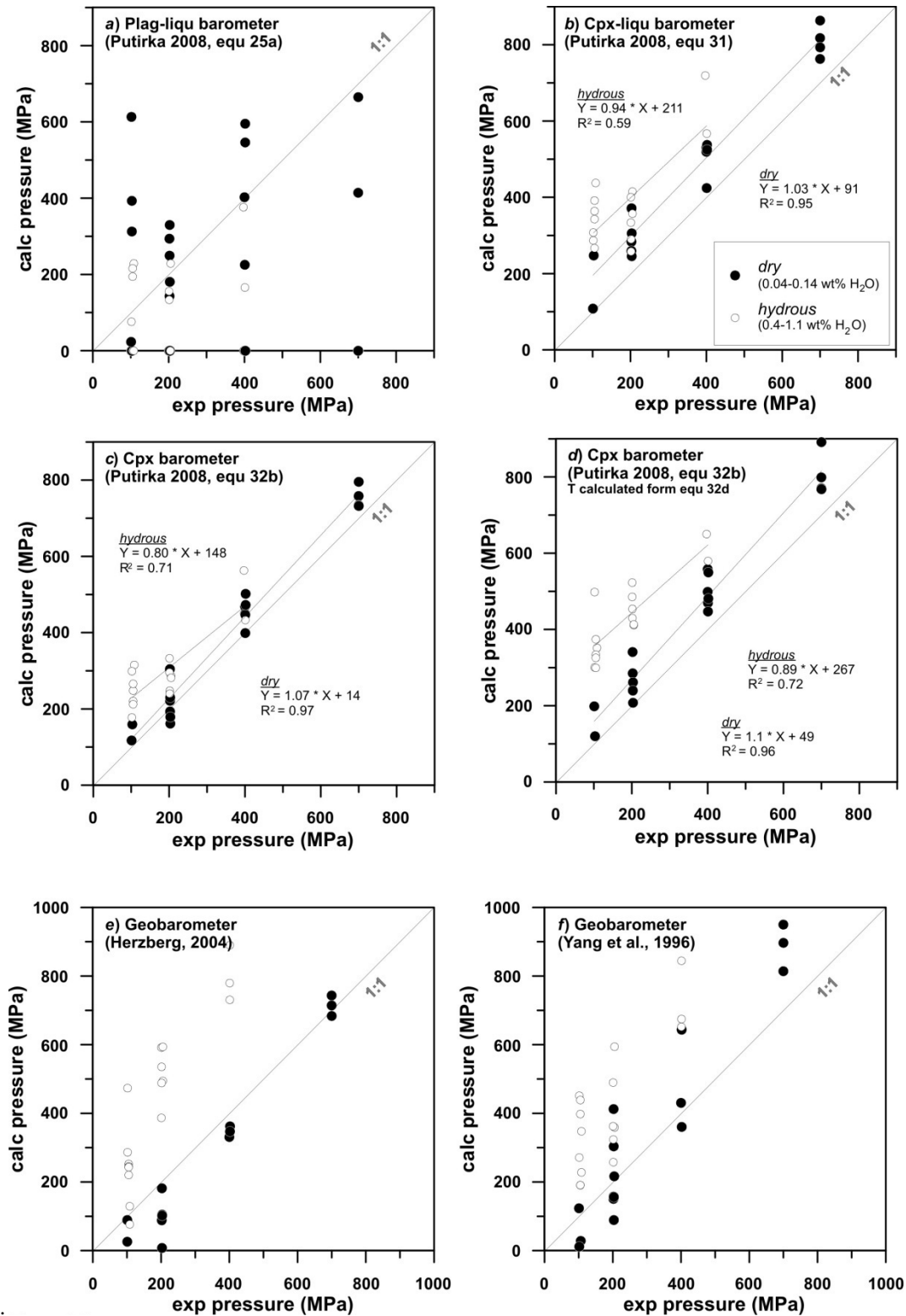
← caption

4.   DISCUSSION

4.1.   General Systematics

Considered collectively, most geothermometers and geobarometers work relatively well with a maximum uncertainty of 25°C and 150 MPa, when applying them on our anhydrous experimental products. Regarding H_2O bearing samples, most thermometers overestimate the crystallization temperatures especially in the lower temperature region. Regarding the correlation of calculated and measured temperatures, we observed a systematic deviation from the 1:1-line because the regression line is always tilted having a lower slope than one. Only models presented by Danyushevsky (2001) led to slightly lower calculated temperatures compared to their measured counterparts and did not show the tilted regression, but a correlation almost parallel to the 1:1 line. Note, that our measured pressures and temperatures have an uncertainty of ±5 MPa and ±10°C. However, since all calculations show systematic behavior, we assume that our observations are related to the inaccuracy of the models rather than to the precision of our *P-T* measurements.

4.1.1   Dry conditions

Generally, for our *dry* experiments, the best calculations were obtained using melt, *Ol*-melt and *Cpx*(-melt) thermometers. In contrast, the tested *Plag*-melt thermometers led to systematic overestimation and underestimation of the experimental temperatures using the models of Putirka (2008, Equation 24a) and Danyushevsky (2001) respectively. The most prcise melt composition based thermometer was the Equation 13 (±40°C) presented by Putirka (2008). Regarding *Ol*-melt thermometry, the Ford (1983) model led to the best fit between calculated and measured temperatures. Also, both models presented by Beattie (1993) and Herzberg & O'Hara (2002), led to relatively good fit between

measured and calculated values. *Cpx* thermobarometry after Putirka (2008) (Equations 33
and 32d) led to the best correlation of calculated and measured temperatures.
Remarkably, in the case when calculated pressures (Equation 32b) were used as pressure
input in Equation 32d, only a slight deviation from the measured temperatures was
observed.

This thermobarometer (Equation 32b) is also one of the most accurate in
recalculation of experimental pressures, leading to a correlation close to the 1:1 line and
only a slight (compared to other thermobarometers) systematic overestimation (~50
MPa). However, the best fit of calculated pressures could be obtained by the model of
Herzberg (2004).

4.1.2   *Hydrous conditions*

Regarding *hydrous* experiments, only the calculation of multiple saturation
(*Ol+Plag+Cpx*) conditions using the COMAGMAT program (after the approach
described by Almeev et al. (2008)) led to reasonable results for both, pressure and
temperature. However, our data show how the application of this model is limited to the
typical range of MORB compositions, because the calculations were less accurate for our
most MgO-rich basalt AH6. This starting material has a composition outside of the
typical range of MORBs (very high CaO and low SiO_2, see Fig II.1), which results in
systematic overestimation of the *Plag* stability. Thus, the calculated LLDs show an
interval of initial single *Plag* crystallization, which was not observed in our experiments
and is not representative for real crystallization processes. Due to this overestimation of
Plag stability, the *Plag* pseudoliquidus is too high in the simulation. In order to reach
multiple saturation of the given liquid composition, also the pseudoliquidus temperatures
of the other two minerals have to increase. Thus, to reach similar pseuduliquidus

temperatures for *Plag* and *Cpx*, higher pressures have to be applied. This, in turn, causes the overestimation of experimental pressures in this basaltic composition. A similar effect of overestimation of *Plag* stabilitiy was observed for AH3 glasses, but with smaller influence on the *P-T* estimates. Thus, in AH3 experimental glasses, pressures were mostly overestimated, whereas the pressures for AH5 glasses were always slightly underestimated.

4.2.   Impact of Temperature on Geobarometry

Although the relative error of the temperature calculations is generally low (25°C corresponds to only 2% of the absolute temperature), it has a large effect when those calculated temperatures are applied to further pressure calculations. As discussed in Part II, chapter 5.1, the pressure induced increase of the liquidus is 4-5°C/100 MPa for *Ol* and *Plag* and ~9°C/100 MPa for *Cpx*. Thus, an overestimation of the temperature about 20°C could correspond to an overestimation in pressure of about 200 to 400 MPa (related to *Cpx* or *Ol* and *Plag* respectively). This effect is visible in the geothermobarometer of Putirka (2008) using Equation 32b and Equation 32d, because here the temperature overestimation is clearly reflected in the misfit between calculated and measured pressures. When the measured experimental temperatures are applied in Equation 32b (geobarometer), the calculated pressures for *dry* and *hydrous* experiments are only 50 and 100 MPa overestimated respectively (Fig. III.5c). In contrast, when the systematically high calculated temperatures from Equation 32d (for *dry* experiments ~+15°C) are used, the deviation between calculated and measured pressures also increases (Fig. III.5d). This leads to an overestimation of ~100 MPa for *dry* experiments and ~250 MPa for *hydrous* experiments and is induced only by the ~15°C overestimated temperatures.

Part III: Evaluation of Thermodynamic (Petrological) Models and
Geothermobarometers
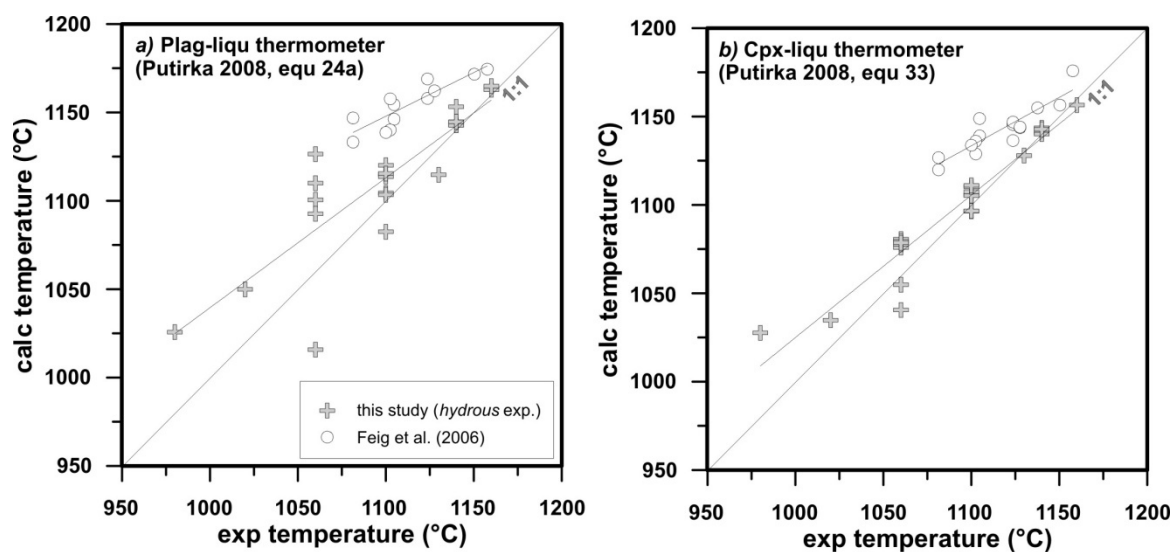
Figure III.7: Calculated temperatures for our experimental *hydrous* (open circles) runs and experiments conducted by Feig et al. (2006) (white symbols) compared to their measured counterparts. The two experimental studies are conducted in similar pressure range (100-400 MPa in this study, 200 and 500 MPa in Feig et al., 2006) but with different H_2O conditions (0.4-1.1 wt% H_2O in this study, 1-5wt% in Feig et al., 2006). Temperatures were obtained using geothermometers based on *Plag*-liquid and *Cpx*-liquid equilibria (Putirka, 2008), which both account for melt H_2O contents.

4.3. Impact of H_2O on Thermobarometry

As already discussed above (Part II), it should be noted, that the measured melt H_2O concentrations represent only minimum values for highly crystalline samples (F_{cryst}>30%). This might account for the higher uncertainty of calculated temperatures in the low temperature region. However, the big deviation of the calculated temperatures from their measured counterparts, which was consistently observed for our experimental runs, might be caused by neglecting the effect of H_2O on the liquidus and the composition of the crystallizing minerals. As shown in Part II, the effect of small amounts of H_2O on the liquidus of mineral phases is large. Almeev et al. (2012), Almeev et al. (2007), and Danyushevsky (2001) demonstrated that between 0 and 1 wt% H_2O the liquidus is most efficiently depressed. Therefore, the same systematic test of recent *Cpx*-melt and *Plag*-melt thermobarometers was made using experimental basalts presented by Feig et al.

Part III: Evaluation of Thermodynamic (Petrological) Models and
Geothermobarometers

(2006). The H_2O contents in their experimental runs range between 1-5 wt%. The direct

comparison with those experiments showed, that for their higher H_2O concentrations

slightly better results were obtained (even over a larger temperature range). As shown in

Fig. III.7, the calculations using the models of Putirka (2008) are less overestimating the

experimental temperatures for the experiments presented by Feig et al. (2006): e.g. the

highest temperatures (providing the most precise melt and H_2O measurements) at 1150°C

were reproduced in the case of Feig et al. (2006), whereas our experimental temperatures

were overestimated around 20°C. Additionally, the slope of the regression is slightly

higher for the Feig et al. (2006) experiments, resulting in a correlation being more close

to the 1:1 line. This observation supports the assumption that the influence of small

amounts of H_2O (>1 wt%) in the equations of Putirka (2008) is considered too small.

In contrast, the systematic underestimation of experimental temperatures using the

model of Danyushevsky (2001) implies that the effect of H_2O is considered too strong in

those models. The equation for *Ol* crystallization temperatures is based on the equation of

Ford (1983), which reproduces well the temperatures of our *dry* experiments. In

Danyshevsky (2001), the Ford (1983) temperatures are corrected with a H_2O dependent

term. This is too strong in the range of small amounts of H_2O, which results in the

systematic underestimation of our experimental temperatures. Similar effect was observed

for the *Plag* pseudoliquidus temperatures. These systematics support the recently

published models for the effect of H_2O on *Ol* and *Plag* by Almeev et al. (2007, 2012),

which are applied in the COMAGMAT program. They consider a slightly smaller

liquidus depression for *Ol* and *Plag* in the region of small amounts of H_2O.

5.   CONCLUSION

Small amounts of H_2O were often disregarded in previous studies of experimental and natural samples. Our experimental study (Part II) showed that H_2O has (especially compared to pressure) a large effect on the phase equilibria and thus the liquid evolution. Regarding this test of recent thermometers, we proved how already, and in particular, low H_2O contents lead to systematic deviation between predicted and measured temperatures and pressures. In contrast, the calculation of multiple saturation conditions (Almeev et al., 2008) was proven as a reliable tool for *P-T* estimates, although this is only true for basaltic compositions, where reliable simulation of differentiation can be obtained. Referring to the calculations presented in Part I, chapter 5.5, we can conclude, that the application of the simulation using COMAGMAT led to reliable calculations of *P-T* conditions. Only the temperatures of the natural basaltic melts might be slightly overestimated, especially regarding the most evolved Tamu Massif magmas, which have the highest H_2O contents (Group 2 and 4 in Part I, chapter 5.5).

6.   REFERENCES

Almeev, R., Holtz, F., Koepke, J., Haase, K. & Devey, C. (2008). Depths of partial crystallization of H_2O-bearing MORB: Phase equilibria simulations of basalts at the MAR near Ascension Island (7-11 degrees S). Journal of Petrology 49, 25-45.

Almeev, R. R. & Ariskin, A. A. (1996). Mineral-melt equilibria in a hydrous basaltic system: Computer modeling. Geokhimiya, 624-636.

Almeev, R. R., Holtz, F., Koepke, J. & Parat, F. (2012). Experimental calibration of the effect of H_2O on plagioclase crystallization in basaltic melt at 200 MPa. American Mineralogist 97, 1234-1240.

Almeev, R. R., Holtz, F., Koepke, J., Parat, F. & Botcharnikov, R. E. (2007). The effect of H_2O on olivine crystallization in MORB: Experimental calibration at 200 MPa. American Mineralogist 92, 670-674.

Ariskin, A. A. (1999). Phase equilibria modeling in igneous petrology: use of COMAGMAT program for simulating fractionation of ferro-basaltic magmas and the genesis of high-alumina basalt. Journal of Volcanology and Geothermal Research 90, 115-162.

Part III: Evaluation of Thermodynamic (Petrological) Models and Geothermobarometers

Ariskin, A. A. & Barmina, G. S. (2004). COMAGMAT: Development of a magma crystallization model and its petrological Applications. Geochemistry International 42, S1.

Beattie, P. (1993). Olivine-melt and orthopyroxene-melt equilibria. Contributions to Mineralogy and Petrology 115, 103-111.

Bender, J. F., Hodges, F. N. & Bence, A. E. (1978). Petrogenesis of basalts from the project FAMOUS area: experimental study from 0 to 15 kbars. Earth and Planetary Science Letters 41, 277-302.

Berndt, J., Koepke, J. & Holtz, F. (2005). An Experimental Investigation of the Influence of Water and Oxygen Fugacity on Differentiation of MORB at 200 MPa. Journal of Petrology 46, 135-167.

Danyushevsky, L. V. (2001). The effect of small amounts of H_2O crystallisation of mid-ocean ridge and backarc basin magmas. Journal of Volcanology and Geothermal Research 110, 265-280.

Feig, S., Koepke, J. r. & Snow, J. (2006). Effect of water on tholeiitic basalt phase equilibria: an experimental study under oxidizing conditions. Contributions to Mineralogy and Petrology 152, 611-638.

Ford, C. E., Russell, D. G., Craven, J. A. & Fisk, M. R. (1983). Olivine Liquid Equilibria - Temperature, Pressure, and Composition Dependence of the Crystal Liquid Cation Partition-Coefficientsfor Mg, Fe^{2+}, Ca and Mn. Journal of Petrology 24, 256-265.

Grove, T. L., Kinzler, R. J. & Bryan, W. B. (1992). Fractionation of mid-ocean ridge basalt (MORB). Mantle Flow and Melt Generation at Mid-Ocean Ridges. Washington, DC: AGU, 281-310.

Helz, R. & Thornber, C. (1987). Geothermometry of Kilauea Iki lava lake, Hawaii. Bulletin of Volcanology 49, 651-668.

Herzberg, C. & O'Hara, M. J. (2002). Plume-Associated Ultramafic Magmas of Phanerozoic Age. Journal of Petrology 43, 1857-1883.

Herzberg, C. (2004). Partial crystallization of mid-ocean ridge basalts in the crust and mantle. Journal of Petrology 45, 2389-2405.

Husen, A., Almeev, R. R., Holtz, F., Koepke, J., Sano, T. & Mengel, K. (2013). Geothermobarometry of basaltic glasses from the Tamu Massif, Shatsky Rise oceanic plateau. Geochemistry, Geophysics, Geosystems 14, 3908–3928.

Putirka, K., Johnson, M., Kinzler, R., Longhi, J. & Walker, D. (1996). Thermobarometry of mafic igneous rocks based on clinopyroxene-liquid equilibria, 0â€"30 kbar. Contributions to Mineralogy and Petrology 123, 92-108.

Putirka, K. D. (2005). Igneous thermometers and barometers based on plagioclase + liquid equilibria: Tests of some existing models and new calibrations. American Mineralogist 90, 336-346.

Putirka, K. D., Perfit, M., Ryerson, F. J. & Jackson, M. G. (2007). Ambient and excess mantle temperatures, olivine thermometry, and active vs. passive upwelling. Chemical Geology 241, 177-206.

Putirka, K. D. (2008). Thermometers and Barometers for Volcanic Systems. Reviews in Mineralogy and Geochemistry 69, 61-120.

Villiger, S., Ulmer, P., Muntener, O. & Thompson, A. B. (2004). The liquid line of descent of anhydrous, mantle-derived, tholeiitic liquids by fractional and equilibrium crystallization - an experimental study at 1 center dot 0 GPa. Journal of Petrology 45, 2369-2388.

Whitaker, M. L., Nekvasil, H., Lindsley, D. H. & Difrancesco, N. J. (2007). The Role of Pressure in Producing Compositional Diversity in Intraplate Basaltic Magmas. Journal of Petrology 48, 365-393.

Yang, H. J., Kinzler, R. J. & Grove, T. L. (1996). Experiments and models of anhydrous, basaltic olivine-plagioclase-augite saturated melts from 0.001 to 10 kbar. Contributions to Mineralogy and Petrology 124, 1-18.

Appendix

1. ABBREVIATIONS

$\sum R^2$	Residual sum of squares
AH3	Intermediate starting material
AH5	Most evolved starting material
AH6	Most MgO-rich starting material
Al#	Al/(Al+Si)
An	Anorthite content of plagioclase (mol%)
Ca#	Ca/(Ca+Na)
Ca_8/Al_8	CaO/Al_2O_3 fractionation back calculated to MgO=8 wt%
CCO	Carbon-Carbon oxide (oxygen buffer)
COMAGMAT	Simulation software
Cpx	Clinopxroxene
DFG	Deutsche Forschungsgemeinschaft (German Research Foundation)
Dur	Duration
En	Enstatite content of clinopyroxene (mol%)
EPMA	Electron beam micro analyzer
EPR	East Pacific Rise
F_{cryst}	Crystal fraction
Fe_8	FeO content fractionation back calculated to MgO=8 wt%
$fH2$	Hydrogen fugacity
$fH2O$	Water fugacity
Fig.	Figure
F_{melt}	Melt fraction
FMQ	Fayalite-Magnetite-Quartz (oxygen buffer)
Fo	Forsterite content of olivine (mol%)
$fO2$	Oxygen fugacity
F_{Plag}	Plagioclase fraction
Fs	Ferrosilite content of clinopyroxene (mol%)
FTIR	Fourier transformation infrared
Gl	Glass
HREE	Heavy rare earth elements
IHPV	Internally heated pressure vessel
IODP	Integrated Ocean Drilling Program
IR	Infrared
K_D	Crystal-liquid exchange coefficients

Appendix

$K_{DCa\text{-}Na}$	Crystal-liquid exchange coefficient for Ca and Na
$K_{DFe\text{-}Mg}$	Crystal-liquid exchange coefficient for Fe and Mg
LIP	Large Igneous Provinces
LLD	Liquid lines of descent
Lq	Liquid
Mag	Magnetite
MAR	Mid Atlantic Ridge
MELTS	Simulation software
Mg#	Mg/(Mg+Fe)
MIR	Mid-infrared
MOR	Mid-ocean ridge
MORB	Mid-ocean ridge basalt
Na_8	Na_2O content fractionation back calculated to MgO=8 wt%
NMORB	Normal-Mid-ocean ridge basalt
NNO	Nickel-Nickel oxide (oxygen buffer)
ODP	Ocean drilling Program
OJP	Ontong Java Plateau
Ol	Olivine
Plag	Plagioclase
Qz	Quartz
REE	Rare earth elements
Tab.	Table
U1347	IODP drilling site on Tamu Massif (Shatsky Rise)
U1350	IODP drilling site on Ori Massif (Shatsky Rise)
Wo	Wollastonite content of clinopyroxene (mol%)
Φ	Crystallization degree

2. APPENDIX PART I

2.1. Standard Reproducibility in Microprobe Analysis

The data presented here contains electron microprobe analysis of international standards (Jarosewich et al., 1980) and samples from a drilled core of the Shatsky Rise oceanic plateau, which was recovered during Expedition 234 at Site U1347. The data was obtained using the Cameca SX100 instruments at the Technical University of Clausthal and the Leibniz University of Hannover in the years from 2011 to 2013. The measurements are not listed here, the tables can be found in Husen et al. (2013). Mineral compositions are available from the PetDB database.
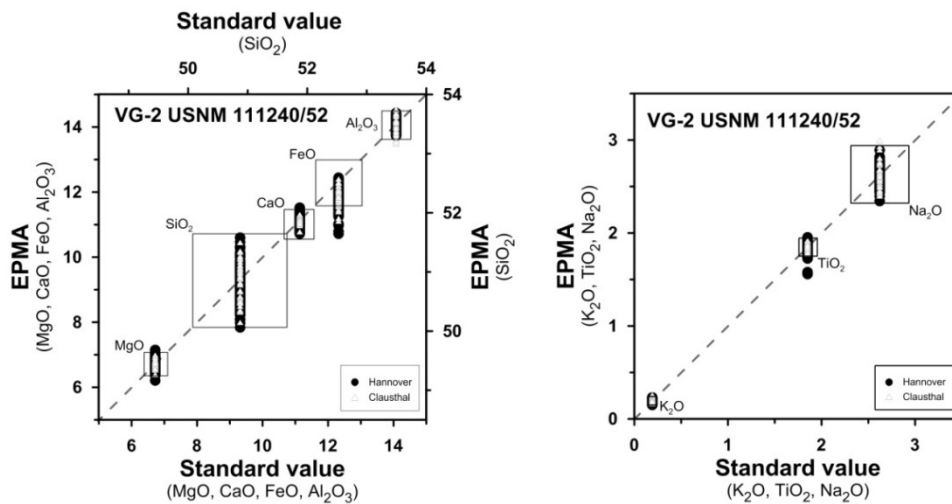
Figure AI.1: Analytical reproducibility during EPMA measurements shown for the basaltic glass standard VG-2 (USNM 111240/52) from the Juan de Fuca Ridge (Jarosewich et al., 1980). Literature values are compared to measured data. The black square shows the standard deviation of the EPMA measurements. Shown are measurements made during 34 EPMA sessions; in each session the glass standard was measured 3 to 10 times (10 nA, 10 µm defocused beam). The black solid circles represent data obtained at the Institute of Mineralogy at the Leibniz University of Hannover and the grey triangles show data produced at the Institute of Disposal Research at the University of Technology of Clausthal.

Appendix
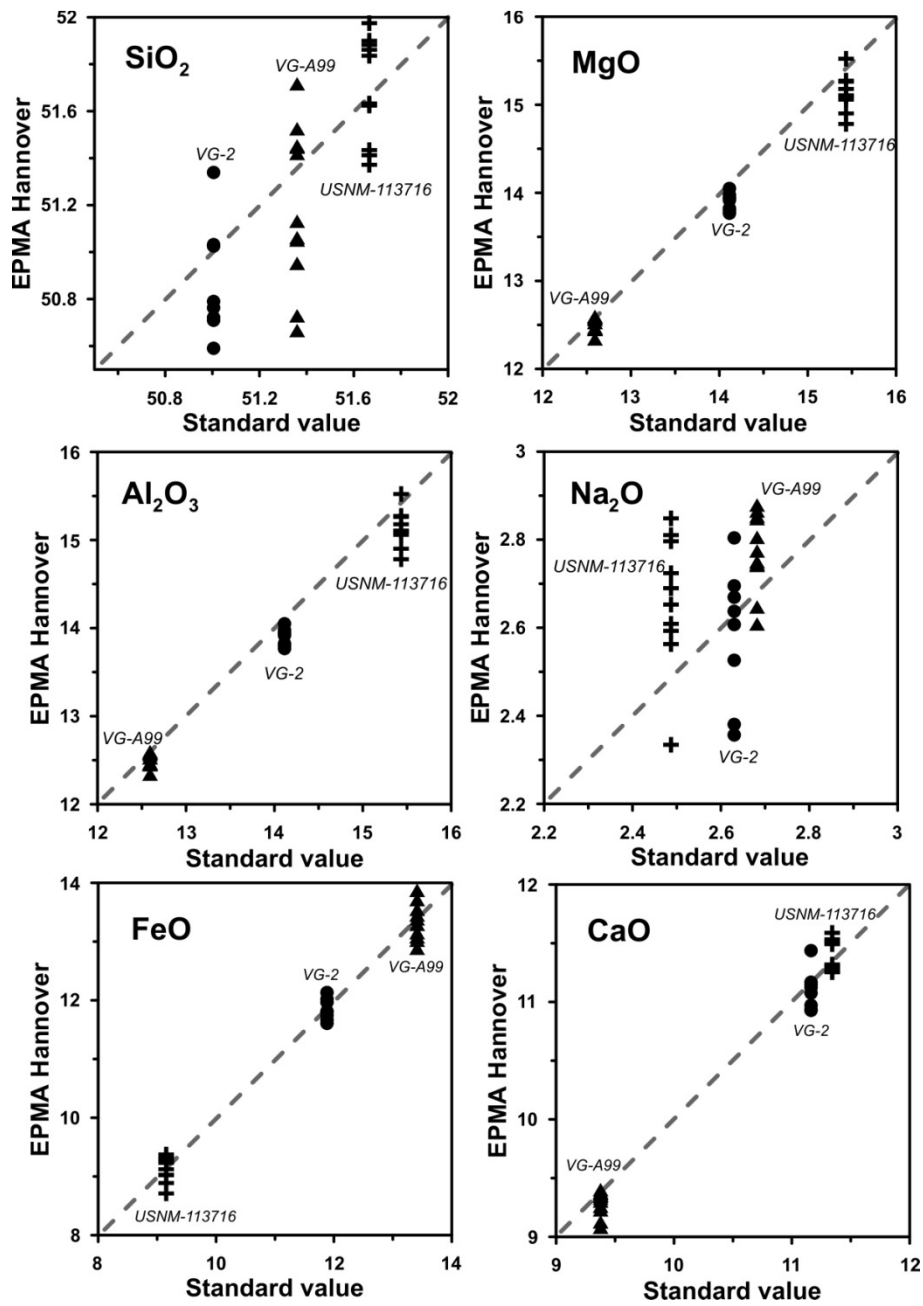
Figure AI.2: Standard reproducibility of three different standard glasses (Kilauea basalt glass: VG-A99 USNM 11134981; Indian ocean basalt glass: USNM 113716; Juan de Fuca basalt glass: USNM 111240/52) measured during one EPMA session. Each glass was measured 8 to 10 times (10 nA, 10 µm defocused beam).

Appendix
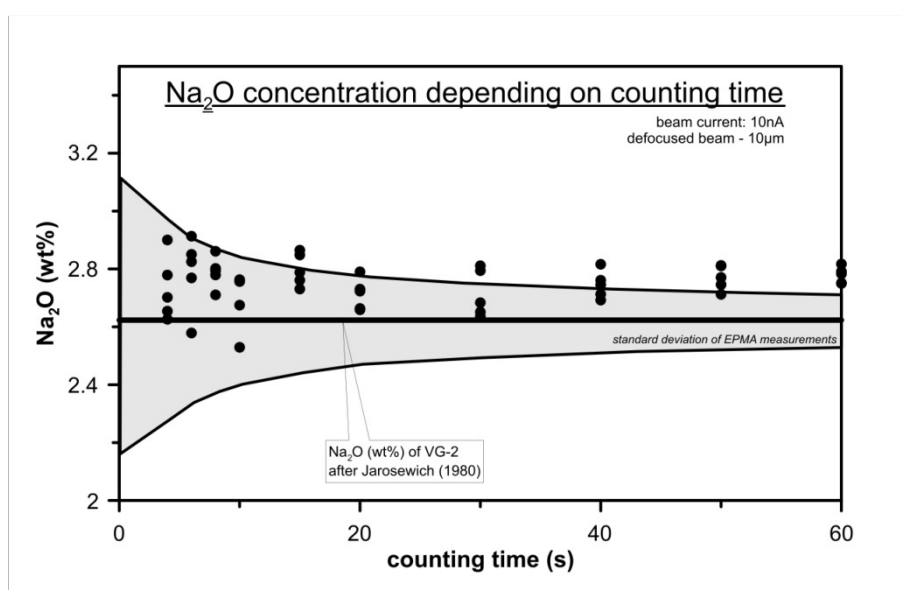
Figure AI.3: Na_2O content measured with different counting times. The basaltic glass has 2.62 wt% Na_2O (values of Jarosewich et al., 1980, normalized to 100 wt%). Beam current: 10 nA, acceleration power: 15 kV.

2.2. Mineral Analysis of Natural Shatsky Rise Basalts
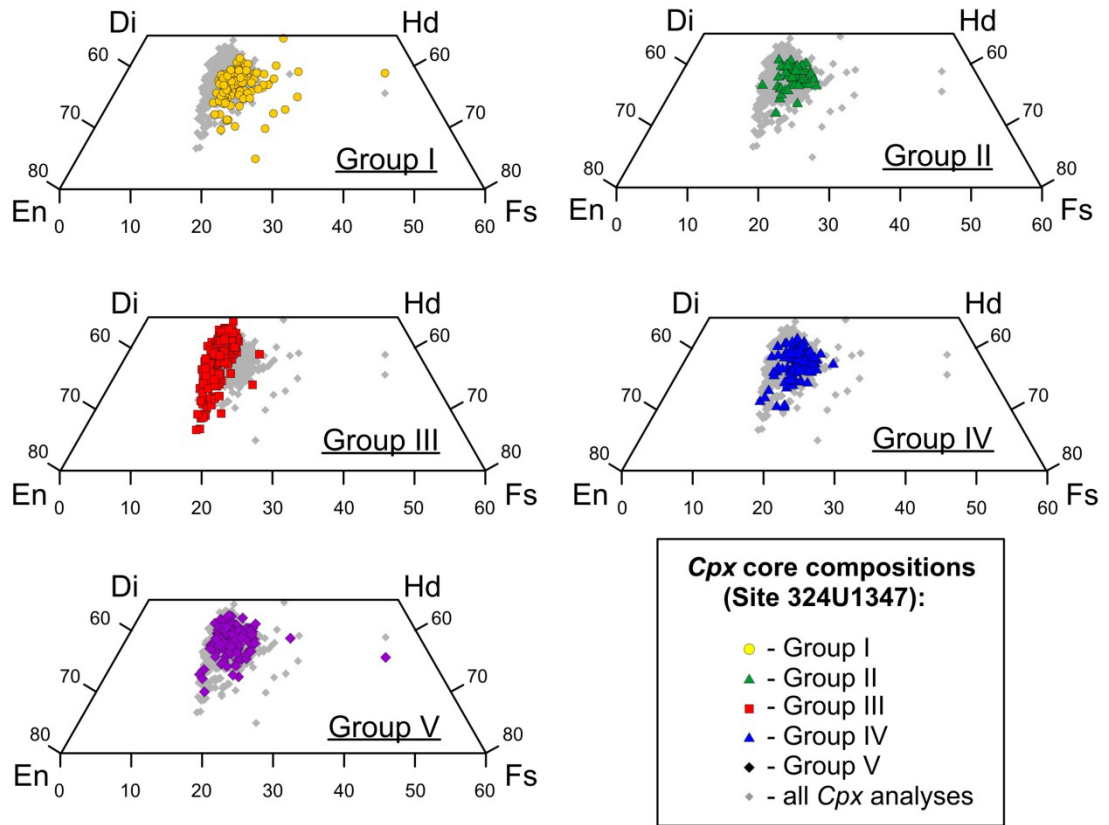
Figure AI.4: *Cpx* compositional variations in different chemical groups (I to V). Each triangular diagram displays the *Cpx* of one group (colored symbols) compared to the whole range of natural Shatsky Rise *Cpx* measured at Site 1347 (gray points).

2.3. References:

Jarosewich, E., Nelen, J.A., Norberg, J.A. (1980), Reference Samples for Electron Microprobe Analysis, Geostandards Newsletter, 4(1), 43-47.

Husen, A., Almeev, R. R., Holtz, F., Koepke, J., Sano, T. & Mengel, K. (2013). Geothermobarometry of basaltic glasses from the Tamu Massif, Shatsky Rise oceanic plateau. Geochemistry, Geophysics, Geosystems 14, 3908–3928.

3. APPENDIX PART II

The data in this chapter belongs to the experimental study of three synthetic basalts representing different evolutionary stages of the Shatsky Rise oceanic plateau basalts. Detailed discussion can be found in the main text of Part II. Experimental mineral compositions measured using the electron microprobe SX100 at the University of Hannover are presented. Additional figures support the observations and discussion above (Part II).

Dissertation of Anika Husen

Appendix

Table AII.1: Compositions of experimental olivines in *dry* experiments

Run	P (MPa)	T (°C)	n	SiO$_2$	TiO$_2$	Al$_2$O$_3$	FeOt	MnO	MgO	CaO	Total	Fo	K$_{DFe-Mg}$	Mg#
starting material: AH 6														
ShR603	102	1150	8	37.92 (.12)	0.06 (.02)	b.d.	22.66 (.32)	0.35 (.05)	37.97 (.21)	0.74 (.06)	100.21	73.85	0.25	74.9
ShR616	103	1175	4	39.22 (.31)	b.d.	b.d.	17.61 (.26)	0.29 (.03)	42.09 (.2)	0.63 (.03)	99.84	80.04	0.28	81
ShR609	102	1200	7	38.88 (.3)	b.d.	b.d.	14.46 (.23)	0.20 (.04)	46.08 (.49)	0.58 (.07)	100.45	84.22	0.28	85
ShR602	202	1150	5	37.53 (.15)	0.06 (.01)	0.20 (.03)	24.34 (.33)	0.41 (.04)	36.89 (.16)	0.72 (.08)	100.14	71.92	0.26	73
ShR615	203	1175	4	39.36 (.37)	b.d.	b.d.	17.69 (.14)	0.22 (.06)	41.89 (.27)	0.63 (.04)	99.79	79.95	0.29	80.8
ShR601	401	1150	5	36.72 (.2)	0.07 (.01)	0.33 (.32)	28.59 (.28)	0.43 (.03)	33.16 (.4)	0.77 (.12)	100.07	66.33	-	67.4
ShR619	402	1175	10	37.68 (.17)	0.05 (0)	0.21 (.05)	23.15 (.21)	0.40 (.04)	37.72 (.15)	0.63 (.04)	99.84	73.40	0.28	74.4
ShR605	402	1200	1	39.30 (.14)	b.d.	b.d.	17.67 (.08)	0.29 (.05)	42.53 (.13)	0.56 (.02)	100.34	80.24	0.29	81.1
ShR604	698	1150	4	36.39 (.57)	0.11 (.03)	1.34 (.55)	32.14 (.57)	0.46 (.02)	27.34 (.72)	1.26 (.46)	99.35	58.74	-	60.3
ShR606	700	1175	3	36.44 (.22)	0.08 (.01)	b.d.	30.35 (.66)	0.45 (.09)	30.89 (.18)	0.65 (.05)	99.16	63.50	-	64.5
ShR611	700	1225	4	38.86 (.29)	b.d.	b.d.	18.54 (.21)	0.25 (.05)	42.69 (.34)	0.44 (.05)	100.77	79.73	0.29	80.4
starting material: AH 3														
ShR322	101	1125	6	36.99 (.27)	0.08 (0)	b.d.	27.69 (.2)	0.51 (.06)	33.56 (.19)	0.70 (.01)	99.53	67.27	0.28	68.35
ShR318	106	1150	10	37.97 (.22)	0.07 (.02)	b.d.	23.87 (.19)	0.41 (.05)	37.02 (.27)	0.63 (.03)	100.26	72.45	0.27	73.43
ShR316	105	1175	10	39.40 (.17)	b.d.	b.d.	16.63 (.2)	0.25 (.04)	44.49 (.24)	0.50 (.03)	101.50	81.89	0.27	82.66
ShR315	102	1200				b.d.								
ShR324	203	1125	5	36.64 (.06)	0.08 (.01)	b.d.	28.90 (.29)	0.51 (.02)	32.67 (.16)	0.67 (.06)	99.48	65.79	0.29	66.83
ShR323	202	1150	8	37.43 (.24)	0.07 (.02)	b.d.	24.86 (.18)	0.41 (.04)	36.34 (.23)	0.62 (.03)	99.73	71.31	0.28	72.27
ShR305	202	1175	5	39.02 (.25)	0.05 (0)	b.d.	19.78 (.2)	0.31 (.05)	41.11 (.23)	0.60 (.05)	100.87	77.83	0.28	78.74
ShR326	402	1125	4	36.10 (.32)	0.11 (.01)	b.d.	33.34 (.12)	0.55 (.06)	28.84 (.27)	0.59 (.03)	99.53	59.73	-	60.66
ShR307	401	1150	6	36.77 (.17)	0.06 (.01)	b.d.	27.96 (.42)	0.45 (.05)	34.00 (.14)	0.58 (.05)	99.83	67.51	0.28	68.43
ShR304	402	1175	5	38.43 (.08)	0.06 (933)	b.d.	21.75 (.83)	0.36 (.34)	39.21 (.38)	0.53 (.41)	100.33	75.41	0.29	76.27
ShR311	402	1200	4	39.40 (.09)	b.d.	b.d.	16.62 (.46)	0.23 (.08)	43.34 (.29)	0.46 (.01)	100.11	81.57	0.30	82.29
ShR310	698	1150	6	35.91 (.42)	0.09 (.03)	b.d.	34.15 (.42)	0.48 (.05)	27.78 (.22)	0.56 (.04)	99.47	58.35	-	59.19
ShR312	700	1175	5	37.01 (.37)	0.15 (.17)	1.09 (.03)	29.14 (.02)	0.43 (.03)	31.17 (.86)	0.82 (.44)	100.12	64.46	0.28	65.60
starting material: AH 5														
ShR520	101	1125	7	36.51 (.2)	0.08 (.02)	b.d.	28.98 (.48)	0.80 (.06)	32.38 (.34)	0.63 (.13)	99.84	65.36	0.30	66.58
ShR519	203	1125	10	36.61 (.2)	0.07 (.01)	b.d.	30.20 (.27)	0.78 (.06)	31.41 (.28)	0.50 (.04)	99.57	63.90	0.30	64.96
ShR522	402	1125	8	35.32 (.26)	0.14 (.02)	b.d.	36.20 (.3)	0.93 (.04)	26.19 (.21)	0.59 (.07)	99.38	55.19	0.29	56.32

Olivine measurements in wt%, the standard deviations (1σ) are given in brackets

b.d. – below detection limit, *n* – number of analysis

Forsterite (Fo) is given in mol%

Mg# - molar ratio of (Mg/(Mg+Fe))

Table AII.2: Compositions of experimental olivines in *hydrous* experiments

Run	P (MPa)	T (°C)	*n*	SiO$_2$	TiO$_2$	Al$_2$O$_3$	FeOt	MnO	MgO	CaO	Total	Fo	K$_{DFe-Mg}$	Mg#
starting material: AH 3														
ShR360	102	1100	7	38.29 (.16)	0.06 (.01)	bd	21.94 (.33)	0.41 (.05)	38.64 (.23)	0.49 (.03)	100.05	74.98	0.27	75.84
ShR362	105	1125	7	38.59 (.32)	0.06 (.01)	bd	19.89 (.25)	0.38 (.04)	40.63 (.17)	0.47 (.03)	100.02	77.62	0.27	78.46
ShR361	105	1135	7	39.72 (.35)	0.05 (.01)	bd	15.86 (.2)	0.34 (.06)	44.29 (.12)	0.43 (.02)	100.69	82.49	0.28	83.27
ShR363	108	1155	5	39.59 (.14)	bd	bd	15.10 (.11)	0.27 (.04)	44.52 (.17)	0.51 (.04)	100.05	83.19	0.28	84.01
ShR358	202	1075	7	37.31 (.22)	0.06 (.01)	bd	26.80 (.2)	0.50 (.06)	34.34 (.46)	0.43 (.05)	99.44	68.72	0.29	69.55
ShR354	201	1100	6	38.08 (.17)	0.05 (.01)	bd	24.03 (.21)	0.44 (.04)	37.60 (.27)	0.41 (.02)	100.82	72.83	0.26	73.61
ShR350	205	1125	12	38.73 (.17)	0.05 (.01)	bd	19.64 (.23)	0.37 (.04)	41.30 (.26)	0.42 (.03)	100.52	78.17	0.27	78.94
ShR359	401	1100	11	37.54 (.49)	0.07 (.02)	0.53 (.35)	26.23 (.63)	0.45 (.06)	34.96 (.62)	0.61 (.62)	100.38	69.41	0.29	70.37
ShR357	401	1125	8	38.07 (.34)	0.06 (.01)	bd	23.43 (.31)	0.40 (.04)	37.83 (.19)	0.41 (.1)	100.43	73.46	0.27	74.21
ShR366	397	1150	5	37.94 (.2)	0.04 (.01)	0.09 (.03)	22.45 (.18)	0.42 (.03)	38.65 (.12)	0.39 (.06)	100.03	74.67	0.27	75.42
starting material: AH 5														
ShR558	202	1075	4	37.08 (.21)	0.05 (0)	bd	28.35 (.19)	0.75 (.08)	32.89 (.25)	0.37 (.03)	99.48	66.47	0.31	67.41
ShR554	201	1100	5	37.21 (.35)	0.05 (0)	bd	26.42 (.52)	0.77 (.05)	35.35 (.29)	0.33 (.03)	100.13	69.51	0.29	70.45
starting material: AH 6														
ShR660	102	1100	6	38.26 (.38)	0.07 (.04)	bd	21.62 (.17)	0.40 (.06)	38.86 (.9)	0.63 (.08)	100.54	75.20	0.22	76.21
ShR662	105	1125	5	38.52 (.13)	bd	bd	20.23 (.21)	0.31 (.02)	40.46 (.19)	0.57 (.07)	100.09	77.22	0.27	78.09
ShR661	105	1135	7	39.35 (.23)	bd	bd	16.53 (.23)	0.26 (.05)	43.24 (.43)	0.52 (.03)	99.96	81.53	0.26	82.34
ShR663	108	1155	6	39.22 (.29)	bd	bd	15.86 (.2)	0.30 (.06)	44.00 (.41)	0.58 (.05)	100.21	82.26	0.23	83.18
ShR658	202	1075	7	37.68 (.25)	0.07 (.03)	0.39 (.13)	24.83 (.31)	0.50 (.04)	35.85 (.29)	0.58 (.06)	99.91	71.01	0.00	72.01
ShR654	201	1103	6	38.06 (.19)	0.06 (.01)	0.43 (.33)	23.09 (.35)	0.50 (.03)	38.14 (.3)	0.59 (.12)	100.87	73.63	0.00	74.65
ShR650	205	1125	16	38.54 (.21)	0.05 (.01)	0.19 (.01)	19.44 (.4)	0.33 (.06)	41.17 (.25)	0.48 (.06)	100.21	78.25	0.28	79.06
ShR659	401	1100	5	37.60 (.26)	0.08 (.02)	0.20 (.05)	25.10 (.16)	0.49 (.09)	36.06 (.13)	0.50 (.04)	100.02	71.02	0.00	71.92
ShR657	401	1125	9	38.00 (.2)	0.06 (.01)	0.24 (.06)	22.38 (.37)	0.41 (.05)	38.47 (.57)	0.50 (.07)	100.05	74.53	0.25	75.39
ShR666	397	1150	5	37.92 (.45)	0.04 (.03)	0.15 (.1)	21.20 (.36)	0.39 (.07)	39.63 (.23)	0.42 (.04)	99.78	76.14	0.26	76.91

Olivine measurements in wt%, the standard deviations (1σ) are given in brackets

b.d. – below detection limit, *n* – number of analysis

Forsterite (Fo) is given in mol%

Mg# - molar ratio of (Mg/(Mg+Fe))

Table AII.3: Compositions of experimental plagioclases in *dry* experiments

Run	P (MPa)	T (°C)	*n*	SiO$_2$	TiO$_2$	Al$_2$O$_3$	FeOt	MgO	CaO	Na$_2$O	K$_2$O	Total	An	KD$_{Ca-Na}$
starting material: AH 6														
ShR603	102	1150	4	50.22 (.83)	0.15 (.06)	31.38 (.76)	0.96 (.24)	0.51 (.23)	15.08 (.41)	2.88 (.2)	0.06 (.01)	101.25	74.04	1.19
ShR616	103	1175	2	51.17 (.03)	0.11 (.06)	29.78 (.97)	0.79 (.28)	0.85 (.77)	15.65 (.3)	2.98 (.24)	b.d.	101.00	74.39	0.92
ShR609	102	1200	4	48.48 (.58)	0.06 (.01)	33.24 (.49)	0.57 (.08)	0.34 (.06)	16.47 (.47)	2.11 (.31)	b.d.	101.27	81.18	1.26
ShR602	202	1150	3	50.38 (.38)	0.15 (.07)	30.08 (.76)	1.10 (.34)	0.67 (.24)	14.79 (.21)	2.91 (.13)	0.10 (.01)	100.18	73.3	1.38
ShR615	203	1175	4	49.00 (.4)	0.07 (.02)	32.78 (.42)	0.65 (.07)	0.33 (.11)	15.99 (.35)	2.46 (.2)	b.d.	101.29	78.22	1.20
ShR601	401	1150	6	50.05 (.15)	0.11 (.03)	30.80 (.23)	0.82 (.16)	0.29 (.14)	14.46 (.24)	3.10 (.05)	0.08 (.01)	99.70	71.7	-
ShR619	402	1175	9	50.03 (.33)	0.08 (.03)	31.56 (.38)	0.69 (.09)	0.21 (.06)	14.57 (.23)	3.07 (.15)	0.05 (.01)	100.27	72.18	1.31
ShR605	402	1200	3	49.60 (.28)	0.06 (.02)	31.92 (.64)	0.74 (.19)	0.41 (.17)	15.55 (.32)	2.64 (.07)	b.d.	100.92	76.51	1.06
ShR604	698	1150	4	52.69 (.59)	0.11 (.01)	30.08 (.42)	0.62 (.11)	0.14 (.06)	12.76 (.25)	3.95 (.13)	0.29 (.02)	100.64	63.01	-
ShR606	700	1175	4	51.87 (.49)	0.08 (.02)	31.26 (.41)	0.73 (.07)	0.14 (.05)	13.82 (.46)	3.54 (.3)	0.12 (.02)	101.57	67.89	-
ShR611	700	1225	8	50.27 (.6)	0.06 (.01)	32.01 (.35)	0.59 (.04)	0.20 (.08)	14.93 (.36)	2.95 (.15)	b.d.	101.07	73.42	1.05
starting material: AH 3														
ShR322	101	1125	6	52.20 (.36)	0.13 (.02)	30.15 (.19)	0.70 (.05)	0.18 (.04)	13.07 (.23)	3.95 (.17)	0.10 (.01)	100.48	64.28	1.05
ShR318	106	1150	6	52.30 (.51)	0.14 (.02)	29.91 (.31)	0.71 (.06)	0.27 (.05)	13.62 (.15)	4.00 (.23)	0.09 (.01)	101.03	64.98	0.87
ShR316	105	1175	7	50.21 (.31)	0.07 (.02)	31.98 (.27)	0.58 (.1)	0.26 (.07)	15.35 (.26)	2.80 (.18)	0.05 (.01)	101.32	74.91	1.13
ShR324	203	1125	7	53.05 (.44)	0.13 (.03)	29.56 (.36)	0.75 (.13)	0.23 (.08)	12.64 (.24)	4.09 (.11)	0.11 (.01)	101.00	62.65	1.03
ShR323	202	1150	8	51.32 (.7)	0.11 (.04)	30.56 (.54)	0.74 (.12)	0.20 (.12)	13.50 (.44)	3.53 (.22)	0.09 (.01)	100.06	67.49	1.04
ShR305	202	1175	4	51.40 (.24)	0.10 (.03)	30.11 (.57)	0.77 (.13)	0.37 (.16)	14.34 (.19)	3.38 (.15)	b.d.	100.54	69.85	0.98
ShR326	402	1125	4	54.01 (.42)	0.18 (.05)	29.37 (.54)	0.86 (.09)	0.32 (.05)	11.78 (.41)	4.30 (.13)	0.20 (.02)	100.27	59.49	-
ShR307	401	1150	5	52.25 (0.4)	0.11 (.01)	29.85 (.18)	0.59 (.06)	0.18 (.05)	12.58 (.33)	4.00 (.17)	0.12 (.01)	99.68	63.03	0.82
ShR304	402	1175	5	51.60 (.9)	0.08 (.91)	31.40 (.53)	0.59 (.37)	0.16 (.87)	13.79 (.76)	3.54 (.7)	0.10 (.09)	101.27	67.86	0.97
ShR310	698	1150	5	54.58 (.5)	0.16 (.06)	28.77 (.3)	0.69 (.21)	0.26 (.19)	11.54 (.23)	4.57 (.11)	0.25 (.02)	100.82	57.39	-
ShR312	700	1175	5	53.49 (.36)	0.12 (.04)	29.83 (.25)	0.72 (.09)	0.14 (.04)	12.24 (.15)	4.22 (.1)	0.16 (.02)	100.91	60.99	0.98
ShR314	700	1200	2	52.43 (.07)	0.08 (.01)	31.04 (.01)	0.71 (.11)	0.19 (.09)	13.32 (.18)	3.77 (.17)	0.09 (.01)	101.62	65.79	1.03
starting material: AH 5														
ShR520	101	1125	5	53.01 (.2)	0.12 (.04)	29.28 (.31)	0.80 (.12)	0.21 (.06)	12.29 (.2)	4.20 (.07)	0.09 (.01)	100.01	61.45	0.91
ShR519	203	1125	10	53.29 (.37)	0.09 (.02)	29.44 (.33)	0.60 (.07)	0.17 (.04)	12.17 (.4)	4.19 (.2)	0.10 (.01)	101.00	61.2	0.87
ShR505	202	1150	6	52.61 (.7)	0.11 (.01)	29.96 (.53)	0.69 (.08)	0.21 (.02)	13.19 (.42)	3.76 (.16)	0.10 (.01)	100.63	65.61	0.90
ShR522	402	1125	4	55.72 (.81)	0.17 (.03)	28.30 (.4)	0.87 (.07)	0.23 (.09)	10.53 (.34)	4.97 (.12)	0.20 (.02)	100.27	53.27	0.68
ShR504	401	1150	8	53.52 (.27)	0.11 (.02)	29.29 (.23)	0.71 (.09)	0.17 (.05)	12.21 (.12)	4.32 (.08)	0.11 (.01)	100.44	60.57	0.85
ShR507	698	1150	4	55.92 (.38)	0.14 (.02)	27.92 (.37)	0.82 (.11)	0.11 (.03)	10.48 (.25)	5.02 (.1)	0.32 (.01)	100.73	52.55	0.70
ShR509	700	1175	2	54.60 (.34)	0.10 (.02)	29.01 (.27)	0.74 (.07)	0.13 (.02)	11.38 (.21)	4.84 (.12)	0.15 (.01)	100.95	56.02	0.72

Plagioclase measurements in wt%, the standard deviations (1σ) are given in brackets

b.d. – below detection limit, *n* – number of analysis

Anorthite (An) is given in mol%

Table AII.4: Compositions of experimental plagioclases in *hydrous* experiments

Run	P (MPa)	T (°C)	*n*	SiO$_2$	TiO$_2$	Al$_2$O$_3$	FeOt	MgO	CaO	Na$_2$O	K$_2$O	Total	An	K$_{DCa-Na}$
starting material: AH 6														
ShR660	102	1100	4	50.63 (.46)	0.08 (.01)	31.41 (.16)	1.20 (.07)	0.21 (.06)	14.52 (.18)	3.12 (.22)	0.06 (.01)	101.22	71.74	1.44
ShR662	105	1125	3	50.29 (.59)	0.07 (.01)	31.63 (.57)	1.21 (.06)	0.24 (.09)	14.98 (.75)	3.03 (.43)	b.d.	101.49	72.97	1.43
ShR661	105	1135	7	48.30 (.8)	0.10 (.04)	32.18 (.77)	1.16 (.11)	0.46 (.21)	16.31 (.66)	2.30 (.33)	b.d.	100.81	79.65	1.88
ShR663	108	1155	6	47.46 (.57)	0.07 (.01)	32.40 (.54)	1.19 (.08)	0.29 (.09)	16.53 (.49)	2.10 (.21)	0.03 (.01)	100.09	81.18	1.88
ShR658	202	1075	4	51.47 (.38)	0.10 (.03)	30.62 (.2)	1.15 (.06)	0.20 (.11)	13.70 (.13)	3.92 (.15)	0.09 (.01)	101.25	65.55	-
ShR654	201	1103	6	51.65 (.49)	0.13 (.03)	30.55 (.39)	1.46 (.18)	0.24 (.07)	13.71 (.26)	3.41 (.07)	0.11 (.02)	101.26	68.53	-
ShR650	205	1125	3	49.30 (.79)	0.09 (.02)	31.98 (.27)	1.25 (.04)	b.d.	15.47 (.52)	2.72 (.31)	b.d.	101.00	75.89	1.58
ShR659	401	1100	2	52.28 (.08)	0.12 (.02)	29.74 (.27)	1.22 (.09)	0.53 (.19)	13.20 (.12)	3.79 (.1)	0.13 (.01)	101.03	65.29	-
ShR657	401	1125	8	51.72 (.64)	0.07 (.02)	30.84 (.32)	1.09 (.11)	0.18 (.06)	13.78 (.34)	3.73 (.32)	0.07 (.01)	101.49	66.83	1.33
ShR666	397	1150	6	50.96 (.18)	0.08 (.02)	30.60 (.56)	1.11 (.04)	0.24 (.28)	13.64 (.14)	3.50 (.08)	0.09 (.01)	100.30	67.89	1.23
starting material: AH 3														
ShR360	102	1100	5	51.66 (.62)	0.14 (.03)	30.49 (.41)	1.29 (.09)	0.28 (.08)	13.75 (.5)	3.68 (.3)	0.07 (.01)	101.37	67.08	1.16
ShR362	105	1125	2	52.92 (.13)	0.13 (.05)	29.51 (.3)	1.29 (.17)	0.38 (.09)	13.11 (.4)	3.86 (.21)	0.07 (.01)	101.27	65.00	0.96
ShR361	105	1135	4	50.48 (.6)	0.12 (.05)	31.32 (.52)	1.11 (.09)	0.47 (.12)	15.00 (.53)	2.89 (.31)	0.05 (.01)	101.44	73.88	1.27
ShR363	108	1155	7	49.70 (.1)	0.09 (.03)	30.98 (.9)	1.04 (.06)	0.30 (.06)	15.06 (.9)	2.99 (.42)	0.06 (.01)	100.22	73.31	1.06
ShR358	202	1075	9	52.80 (.45)	0.18 (0.1)	29.49 (.42)	1.25 (.32)	0.28 (.16)	12.38 (.25)	4.54 (.25)	0.11 (.02)	101.02	59.76	0.94
ShR354	201	1100	5	53.15 (.75)	0.12 (.02)	29.96 (.41)	1.31 (.15)	0.17 (.02)	12.45 (.54)	4.07 (.25)	0.10 (.01)	101.34	62.46	1.03
ShR350	205	1125	4	51.40 (.31)	0.11 (.03)	29.94 (.42)	1.11 (.09)	0.26 (0.1)	14.08 (0.4)	3.67 (.22)	0.06 (.01)	100.63	67.72	1.10
ShR359	401	1100	4	53.69 (.22)	0.11 (.01)	29.60 (.33)	0.97 (.01)	0.15 (.04)	11.97 (.14)	4.40 (.03)	0.11 (.01)	100.98	59.66	0.96
ShR357	401	1125	6	53.02 (.51)	0.10 (.01)	30.05 (.45)	1.07 (.06)	0.18 (.05)	12.78 (.47)	3.98 (.27)	0.09 (.01)	101.26	63.65	1.14
ShR366	397	1150	5	51.75 (.26)	0.10 (.02)	30.35 (.39)	1.17 (.08)	0.11 (.03)	13.10 (.29)	3.78 (.19)	0.09 (.01)	100.46	65.36	1.10
starting material: AH 5														
ShR560	102	1100	3	52.36 (.72)	0.10 (.03)	30.29 (.06)	1.18 (.05)	0.23 (.04)	13.33 (.39)	3.75 (.09)	0.07 (.01)	101.32	66.00	1.05
ShR558	202	1075	3	53.09 (.38)	0.10 (.01)	29.90 (.18)	1.19 (.06)	0.10 (.01)	12.51 (.27)	4.60 (.13)	0.07 (.01)	101.55	59.80	0.95
ShR554	201	1100	4	53.00 (.45)	0.11 (.03)	29.82 (.45)	1.33 (.16)	0.18 (.07)	12.64 (.37)	3.99 (.18)	0.07 (.01)	101.14	63.38	1.02
ShR559	401	1100	6	54.64 (.74)	0.11 (.01)	28.76 (.44)	1.09 (.09)	0.13 (.02)	11.00 (.38)	4.84 (.3)	0.10 (.01)	100.67	55.32	0.82
ShR566	397	1150	3	52.90 (.41)	0.10 (.01)	29.54 (.33)	1.28 (.16)	0.15 (.03)	12.21 (.12)	4.14 (.19)	0.08 (.01)	100.42	61.69	0.89

Plagioclase measurements in wt%, the standard deviations (1σ) are given in brackets

b.d. – below detection limit, *n* – number of analysis

Anorthite (An) is given in mol%

Table AII.5: Compositions of experimental clinopyroxenes in *dry* experiments

Run	P (MPa)	T (°C)	n	SiO$_2$	TiO$_2$	Al$_2$O$_3$	FeOt	MnO	MgO	CaO	Na$_2$O	Cr$_2$O$_3$	Total	Mg#	En	Wo	Fs	K$_{DFe-Mg}$
starting material: AH 6																		
ShR603	102	1150	6	52.09 (.56)	0.68 (.06)	3.04 (.32)	6.31 (.22)	0.18 (.03)	15.33 (.28)	21.84 (.19)	0.23 (.02)	0.40 (.06)	100.10	81.25	44.36	45.41	10.23	0.17
ShR616	103	1175	6	51.93 (.48)	0.63 (.14)	3.56 (.48)	5.68 (.58)	0.11 (.05)	16.00 (.31)	21.96 (.31)	0.20 (.06)	0.54 (.09)	100.60	83.40	45.75	45.14	9.11	0.23
ShR602	202	1150	9	51.17 (.81)	0.79 (.13)	3.90 (.79)	7.01 (.39)	0.17 (.03)	14.98 (.43)	21.55 (.25)	0.30 (.06)	0.34 (.04)	100.20	79.20	43.54	45.03	11.43	0.18
ShR615	203	1175	6	51.27 (.63)	0.49 (.07)	4.05 (.88)	5.11 (.25)	0.16 (.01)	16.30 (.57)	21.81 (.36)	0.26 (.03)	0.71 (.17)	100.16	85.03	46.78	44.99	8.23	0.22
ShR601	401	1150	5	49.80 (.4)	1.13 (.08)	5.51 (.48)	8.24 (.42)	0.22 (.01)	13.56 (.23)	20.95 (.56)	0.49 (.17)	b.d.	100.27	74.57	40.79	45.30	13.91	-
ShR619	402	1175	9	50.56 (.5)	0.75 (.08)	5.08 (.59)	6.96 (.41)	0.18 (.02)	14.86 (.26)	20.85 (.43)	0.37 (.04)	0.36 (.02)	99.98	79.19	44.03	44.40	11.57	0.22
ShR605	402	1200	7	50.94 (.96)	0.47 (.03)	5.47 (.73)	5.89 (.76)	0.16 (.03)	16.03 (.34)	21.05 (.4)	0.28 (.1)	0.56 (.07)	100.85	82.91	46.51	43.90	9.59	0.26
ShR604	698	1150	4	47.31 (.33)	1.77 (.13)	8.70 (.63)	9.58 (.14)	0.24 (.01)	11.57 (.18)	20.11 (.22)	0.70 (.01)	b.d.	99.99	68.27	36.83	46.04	17.12	-
ShR606	700	1175	5	47.55 (.13)	1.48 (.15)	8.87 (.26)	9.90 (.46)	0.21 (.07)	12.03 (.38)	19.56 (.25)	0.80 (.15)	b.d.	100.44	68.42	38.03	44.42	17.55	-
ShR611	700	1225	7	50.81 (.26)	0.48 (.02)	7.01 (.52)	5.99 (.17)	0.19 (.03)	16.16 (.15)	19.46 (.19)	0.41 (.03)	b.d.	100.83	82.77	48.22	41.75	10.04	0.25
starting material: AH 3																		
ShR322	101	1125	6	52.05 (.04)	0.97 (0)	2.28 (.18)	8.31 (.02)	0.25 (.05)	15.29 (.23)	20.94 (.43)	0.28 (.05)	-	100.38	76.64	43.69	42.99	13.32	0.19
ShR318	106	1150	8	52.57 (.39)	0.77 (.12)	2.06 (.37)	7.35 (.33)	0.21 (.04)	16.28 (.34)	20.97 (.25)	0.22 (.02)	-	100.44	79.79	45.90	42.48	11.62	0.19
ShR324	203	1125	8	51.88 (.42)	1.13 (.05)	2.50 (.2)	8.41 (0.4)	0.21 (.02)	14.90 (.21)	20.86 (.42)	0.32 (.04)	-	100.21	75.95	43.05	43.32	13.63	0.19
ShR323	202	1150	5	52.51 (.53)	0.76 (.12)	2.42 (.5)	7.36 (.29)	0.20 (.02)	16.17 (.51)	20.54 (.29)	0.26 (.04)	-	100.22	79.66	46.12	42.10	11.78	0.19
ShR305	202	1175	1	52.67 (.59)	0.6 (.05)	3.16 (.66)	6.37 (.33)	0.17 (.03)	16.78 (.46)	20.75 (.64)	0.26 (.08)	-	100.77	82.44	47.57	42.29	10.14	0.22
ShR326	402	1125	2	50.03 (.44)	1.89 (.04)	4.73 (.98)	10.86 (.74)	0.29 (.01)	12.96 (.39)	19.64 (.01)	0.50 (.03)	-	100.90	68.03	39.07	42.57	18.36	-
ShR307	401	1150	5	51.00 (.68)	1 (.13)	3.75 (.73)	9.28 (.36)	0.20 (.05)	15.30 (.29)	19.22 (.48)	0.36 (.09)	-	100.12	74.61	44.57	40.26	15.17	0.21
ShR304	402	1175	5	52.72 (.13)	0.66 (935)	3.77 (412)	7.21 (.1)	0.24 (.22)	16.62 (.50)	19.92 (.11)	0.35 (.28)	-	101.48	80.43	47.51	40.93	11.56	0.23
ShR310	698	1150	6	50.44 (.56)	0.95 (.16)	3.65 (.51)	15.18 (.36)	0.62 (.09)	14.33 (.34)	14.17 (.25)	0.40 (.07)	-	99.72	62.71	43.38	30.83	25.79	-
ShR312	700	1175	5	49.80 (.56)	1.28 (.21)	6.18 (.75)	10.68 (.52)	0.32 (.05)	14.08 (.72)	17.44 (.56)	0.69 (.14)	-	100.53	70.15	43.18	38.45	18.37	0.23
ShR314	700	1200	3	51.31 (.46)	0.74 (.11)	5.53 (.78)	8.14 (.18)	0.20 (.03)	16.20 (.74)	18.22 (.46)	0.52 (.12)	-	100.87	78.01	47.85	38.67	13.49	0.26
ShR317	700	1225	7	52.07 (.34)	0.54 (.06)	5.23 (.54)	5.84 (.27)	0.18 (.02)	16.81 (.22)	19.92 (.37)	0.40 (.03)	-	100.98	83.70	48.86	41.62	9.52	0.25
starting material: AH 5																		
ShR520	101	1125	5	52.34 (.54)	0.79 (0.1)	1.81 (.49)	9.64 (.53)	0.5 (.04)	16.11 (.27)	18.44 (.71)	0.21 (.03)	-	99.84	74.86	46.33	38.11	15.56	0.20
ShR506	102	1150	1	53.12	0.65	2.26	7.96	0.36	17.12	19.28	0.28	-	101.03	79.32	48.31	39.09	12.59	0.25
ShR519	203	1125	7	52.20 (.38)	0.83 (.08)	2.05 (.3)	10.17 (.4)	0.49 (.05)	15.92 (.22)	18.38 (.58)	0.25 (.03)	-	100.29	73.61	45.69	37.92	16.38	0.20
ShR505	202	1150	8	52.14 (.77)	0.76 (.12)	2.72 (.56)	8.25 (.44)	0.41 (.07)	16.46 (.29)	19.12 (.74)	0.23 (.02)	-	100.10	78.05	47.26	39.45	13.29	0.25
ShR522	402	1125	4	51.17 (.23)	1.21 (.02)	2.70 (.11)	14.41 (.83)	0.64 (.12)	14.29 (.19)	15.50 (.69)	0.33 (.04)	-	100.25	63.87	42.64	33.24	24.12	0.21
ShR504	401	1150	6	51.49 (.75)	0.82 (.15)	3.12 (.79)	10.79 (.22)	0.53 (.08)	16.26 (.43)	16.68 (.22)	0.29 (.03)	-	99.99	72.87	47.40	34.95	17.65	0.23
ShR501	402	1175	8	52.07 (.9)	0.85 (539)	3.85 (.08)	8.22 (.83)	0.35 (.08)	16.71 (948)	18.82 (.03)	0.33 (.03)	-	101.20	78.37	47.94	38.82	13.24	0.25
ShR507	698	1150	11	50.25 (.34)	1.06 (.12)	3.89 (.35)	14.76 (.38)	0.57 (.08)	13.95 (.39)	14.93 (.5)	0.47 (.08)	-	99.89	62.75	42.32	32.55	25.13	0.19
ShR509	700	1175	4	50.82 (.31)	0.89 (0.1)	4.10 (.32)	12.20 (.15)	0.53 (.05)	14.86 (.09)	16.23 (.15)	0.48 (.05)	-	100.11	68.47	44.52	34.97	20.51	0.24
ShR511	700	1200	4	51.76 (.06)	0.67 (.12)	4.18 (.87)	8.41 (.1)	0.29 (.07)	15.49 (.61)	19.23 (.19)	0.49 (.12)	-	100.51	76.66	45.53	40.61	13.86	0.25

Clinopyroxene measurements in wt%, the standard deviations (1σ) are given in brackets

b.d. – below detection limit, *n* – number of analysis

Enstatite (En), Wollastonite (Wo), and Ferrosilite (Fs) are given in mol%

Mg# - molar ratio of (Mg/(Mg+Fe))

Table AII.6: Compositions of experimental clinopyroxenes in *hydrous* experiments

Run	P (MPa)	T (°C)	n	SiO$_2$	TiO$_2$	Al$_2$O$_3$	FeOt	MnO	MgO	CaO	Na$_2$O	Cr$_2$O$_3$	Total	mg#	En	Wo	Fs	K$_{DFe-Mg}$
starting material: AH 6																		
ShR660	102	1100	3	49.63 (.62)	0.95 (.04)	4.79 (.76)	8.92 (.12)	0.21 (.04)	13.93 (.4)	21.23 (0.2)	0.44 (.11)	b.d.	100.10	73.57	40.74	44.62	14.64	0.26
ShR662	105	1125	4	49.65 (.29)	0.85 (.07)	4.94 (.44)	8.26 (.12)	0.18 (.03)	14.18 (.21)	21.68 (.32)	0.40 (.06)	0.42 (.11)	100.55	75.36	41.22	45.30	13.48	0.31
ShR661	105	1135	7	49.92 (.75)	0.69 (0.1)	4.78 (.35)	6.97 (.77)	0.18 (.04)	15.00 (.29)	21.63 (.5)	0.32 (.03)	0.50 (.12)	100.01	79.32	43.53	45.12	11.35	0.32
ShR663	108	1155	6	49.38 (.49)	0.64 (.05)	5.02 (.49)	7.40 (.6)	b.d.	15.14 (.4)	21.39 (.59)	0.30 (.03)	0.64 (.15)	100.08	78.49	43.68	44.35	11.97	0.32
ShR658	202	1075	6	48.77 (.5)	1.09 (.08)	5.18 (.33)	9.55 (.53)	0.20 (.03)	13.53 (.21)	20.72 (.65)	0.47 (.02)	b.d.	99.52	71.63	40.05	44.08	15.86	-
ShR654	201	1103	6	49.42 (.77)	0.96 (.09)	4.94 (.84)	9.17 (.75)	0.27 (.03)	14.58 (.3)	20.57 (.72)	0.48 (.05)	b.d.	100.39	73.91	42.24	42.84	14.91	-
ShR650	205	1125	11	49.04 (.52)	0.87 (.09)	5.72 (.57)	8.55 (.46)	0.19 (.03)	14.27 (.39)	20.88 (.7)	0.41 (.06)	0.35 (.05)	100.27	74.85	41.88	44.05	14.07	0.35
ShR659	401	1100	5	48.26 (.73)	1.08 (.07)	6.28 (.46)	9.92 (.38)	0.27 (.07)	13.42 (.23)	19.71 (.37)	0.61 (.03)	b.d.	99.55	70.68	40.48	42.73	16.79	-
ShR657	401	1125	7	49.00 (.55)	0.96 (.04)	5.90 (.33)	9.65 (.23)	0.23 (.04)	13.90 (.34)	19.85 (.47)	0.48 (.06)	b.d.	99.97	71.97	41.40	42.48	16.12	0.30
ShR666	397	1150	6	48.66 (.37)	0.93 (.05)	6.44 (.17)	9.44 (.25)	0.23 (.05)	14.15 (.66)	19.25 (.5)	0.59 (.1)	0.06 (.03)	99.76	72.76	42.51	41.58	15.91	0.33
starting material: AH 3																		
ShR360	102	1100	5	50.32 (.59)	0.96 (.03)	3.46 (.22)	9.18 (.35)	0.23 (.06)	15.10 (.6)	20.29 (.95)	0.41 (.05)	-	99.96	74.58	43.36	41.86	14.78	0.29
ShR362	105	1125	6	50.32 (.31)	0.90 (.05)	4.07 (.2)	8.27 (.3)	0.21 (.04)	15.31 (.24)	20.91 (.42)	0.37 (.03)	-	100.37	76.73	43.76	42.97	13.27	0.30
ShR361	105	1135	7	52.36 (.53)	0.62 (0.1)	2.99 (.6)	6.71 (.55)	0.20 (.03)	16.55 (.23)	21.13 (.58)	0.31 (.04)	-	100.87	81.48	46.63	42.78	10.60	0.32
ShR363	108	1155	6	50.27 (.41)	0.83 (.07)	4.31 (.45)	7.29 (.58)	0.20 (.03)	15.51 (.48)	20.95 (.49)	0.35 (.06)	-	99.69	79.14	44.75	43.45	11.79	0.39
ShR358	202	1075	7	50.03 (.08)	1.15 (.06)	3.85 (.09)	10.28 (.81)	0.27 (.09)	14.36 (.13)	19.41 (.03)	b.d.	-	99.77	71.34	42.14	40.93	16.93	0.27
ShR354	201	1100	4	51.11 (.25)	0.90 (.02)	3.55 (.28)	9.58 (.07)	0.27 (.06)	15.44 (.24)	19.11 (.63)	0.41 (.03)	-	100.39	74.17	44.69	39.75	15.56	0.25
ShR350	205	1125	6	50.53 (.64)	0.86 (.07)	4.13 (.35)	8.40 (.24)	0.22 (.02)	15.59 (.36)	20.17 (.77)	0.37 (.03)	-	100.28	76.79	44.79	41.66	13.54	0.31
ShR359	401	1100	8	49.41 (.72)	1.06 (.12)	4.72 (.36)	10.95 (.26)	0.31 (.04)	14.70 (.37)	18.02 (.57)	0.56 (.07)	-	99.72	70.52	43.50	38.32	18.18	0.29
ShR357	401	1125	7	49.83 (.32)	1.04 (.09)	5.12 (.47)	10.81 (.6)	0.29 (.04)	15.00 (.47)	17.83 (.77)	0.52 (.04)	-	100.45	71.21	44.27	37.83	17.90	0.31
ShR366	397	1150	9	49.09 (.32)	1.01 (.05)	5.96 (.27)	10.06 (.32)	0.23 (.06)	14.36 (.39)	18.83 (.62)	0.52 (.05)	-	100.11	71.78	42.81	40.36	16.83	0.33
starting material: AH 5																		
ShR560	102	1100	6	51.19 (.43)	0.73 (.09)	2.71 (.36)	10.43 (.61)	0.52 (.06)	16.03 (.75)	17.65 (.35)	0.42 (.1)	-	99.69	73.25	46.36	36.71	16.93	0.31
ShR562	105	1125	6	51.12 (.57)	0.78 (.11)	3.40 (.35)	8.51 (.37)	0.38 (.04)	15.87 (.43)	19.86 (.43)	0.35 (.04)	-	100.27	76.88	45.46	40.88	13.67	0.30
ShR561	105	1135	6	52.57 (.97)	0.67 (.24)	2.76 (.02)	7.42 (.89)	0.30 (.06)	16.39 (.54)	20.44 (.58)	0.27 (.03)	-	100.83	79.74	46.50	41.69	11.81	0.30
ShR558	202	1075	7	50.91 (.64)	0.82 (.15)	2.89 (.47)	11.21 (.55)	0.49 (.05)	15.41 (.52)	17.80 (.9)	0.37 (.03)	-	99.90	71.02	44.67	37.10	18.23	0.26
ShR554	201	1100	4	51.43 (.35)	0.76 (.08)	3.10 (.3)	11.46 (.36)	0.50 (.04)	15.83 (.49)	17.24 (.74)	0.36 (.04)	-	100.69	71.11	45.68	35.76	18.56	0.28
ShR550	205	1125	9	51.21 (.52)	0.75 (.11)	3.11 (.44)	9.46 (.55)	0.42 (.04)	15.98 (.41)	18.89 (.69)	0.34 (.04)	-	100.16	75.07	45.83	38.95	15.22	0.31
ShR559	401	1100	6	49.52 (.25)	1.04 (.09)	3.79 (.37)	12.81 (.27)	0.55 (.06)	14.42 (.18)	16.88 (.3)	0.51 (.04)	-	99.52	66.73	42.74	35.96	21.30	0.31
ShR566	397	1150	6	50.23 (.54)	0.78 (.09)	4.12 (.43)	9.99 (.47)	0.44 (.06)	15.18 (.31)	18.55 (.27)	0.48 (.05)	-	99.81	73.04	44.49	39.09	16.42	0.30

Clinopyroxene measurements in wt%, the standard deviations (1σ) are given in brackets

b.d. – below detection limit, *n* – number of analysis

Enstatite (En), Wollastonite (Wo), and Ferrosilite (Fs) are given in mol%

Mg# - molar ratio of (Mg/(Mg+Fe))

Table AII.7: Compositions of experimental magnetites in *hydrous* experiments

Run	P (MPa)	T (°C)	*n*	SiO_2	TiO_2	Al_2O_3	Fe_2O_3	FeO	MnO	MgO	CaO	Cr_2O_3	Total	X^{USP}
starting material: AH 6														
ShR660	102	1100	4	0.56 (.24)	5.96 (.07)	8.62 (.12)	44.42	28.53	0.15 (.37)	5.87 (.07)	b.d.	3.63 ()	98.29	0.21
ShR658	202	1075	4	0.8 (.56)	9.04 (.11)	6.96 (.07)	42.3	32.88	0.33 (.04)	4.86 (.05)	0.65 (.26)	1.25 (.04)	99.09	0.30
ShR654	201	1103	7	0.27 (.17)	7.41 (.28)	7.26 (0.1)	46.84	30.7	0.33 (.08)	5.14 (.04)	0.42 (.08)	1.2 (.32)	99.57	0.23
ShR659	401	1100	3	0.89 (.33)	7.98 (.38)	9.62 (.08)	40.82	32.15	0.31 (.02)	4.96 (.04)	0.65 (.14)	1.06 (.08)	98.42	0.29
ShR657	401	1125	7	0.75 (.58)	5.57 (.06)	12.94 (.26)	42.58	28.79	0.21 (.04)	6.35 (.11)	0.57 (.18)	2.06 (.08)	99.83	0.22
ShR666	397	1150.3	6	0.42 (.18)	5.84 (.06)	10.67 (.19)	45	28.14	0.26 (.06)	6.08 (.17)	0.5 (.08)	1.29 (.04)	98.19	0.20
starting material: AH 3														
ShR354	201	1100	6	0.28 (.08)	9.4 (.08)	6.29 (.08)	44.98	32.46	0.35 (.08)	5.02 (0.1)	0.37 (.03)	b.d.	99.14	0.28
ShR359	401	1100	11	0.19 (.08)	11.57 (.28)	7.49 (.18)	38.1	35.21	0.29 (.05)	4.81 (.08)	0.28 (.13)	1.59 (1.1)	99.54	0.39

Magnetite measurements in wt%, the standard deviations (1σ) are given in brackets

b.d. – below detection limit, *n* – number of analysis

Fe_2O_3, FeO, and X^{USP} are calculated after Stormer (1983)

Appendix

3.2. Figures
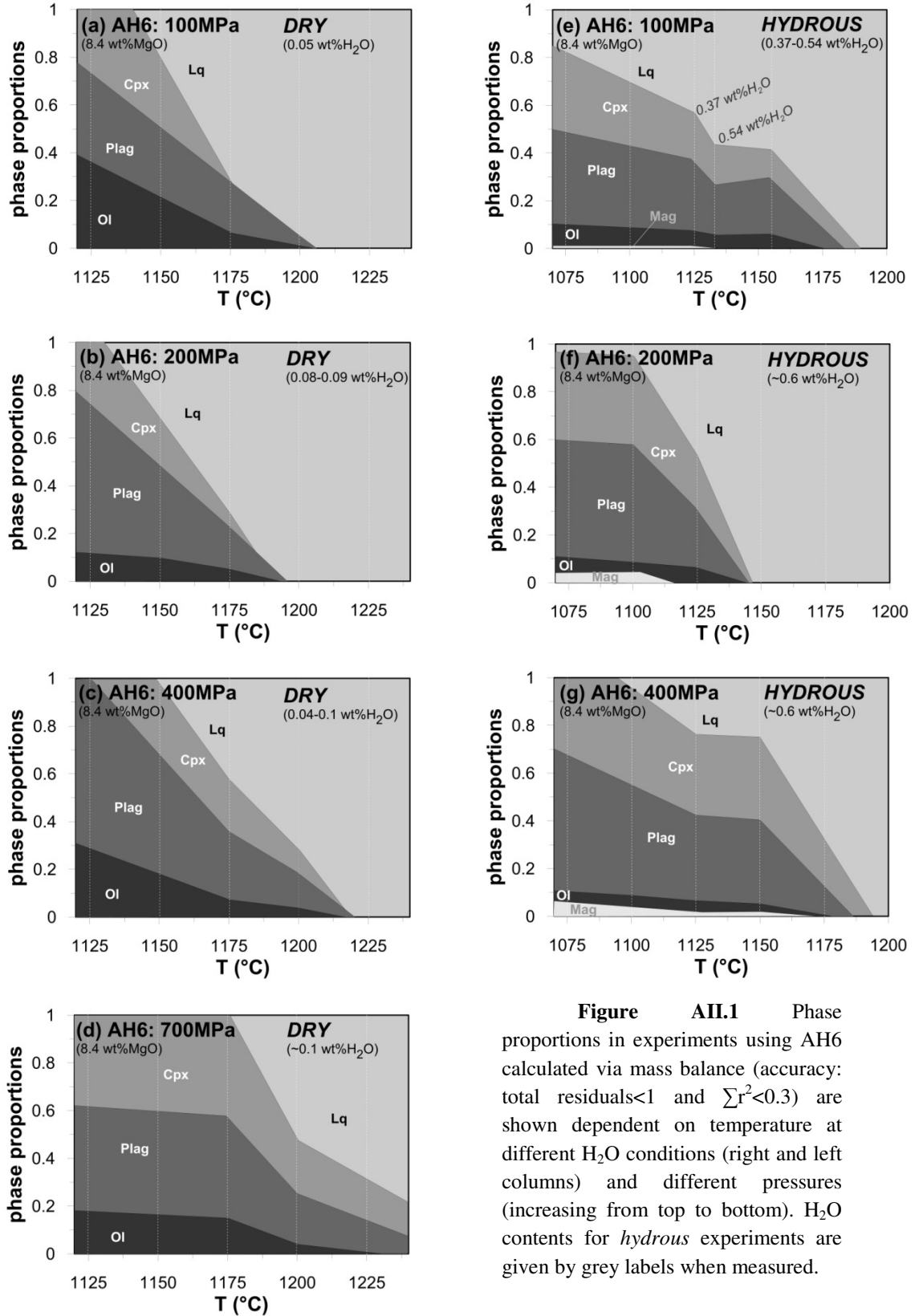
Figure AII.1 Phase proportions in experiments using AH6 calculated via mass balance (accuracy: total residuals<1 and $\sum r^2$<0.3) are shown dependent on temperature at different H_2O conditions (right and left columns) and different pressures (increasing from top to bottom). H_2O contents for *hydrous* experiments are given by grey labels when measured.

Appendix
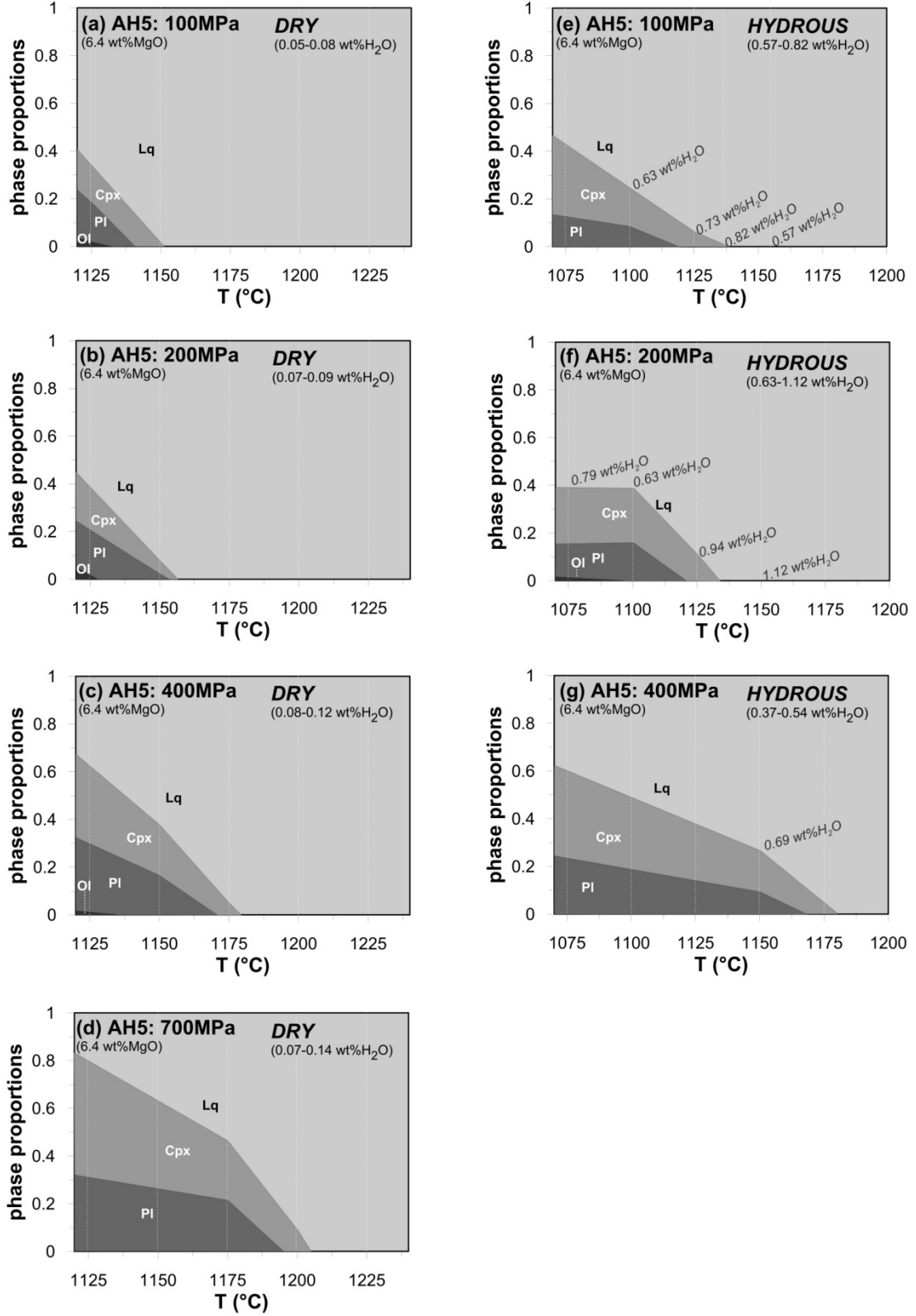
Figure AII.2: Phase proportions in experiments using AH5 calculated via mass balance (accuracy: total residuals<1 and $\sum r^2 <0.3$) are shown dependent on temperature at different H_2O conditions (right and left columns) and different pressures (increasing from top to bottom). H_2O contents for *hydrous* experiments are given by grey labels when measured.

Appendix
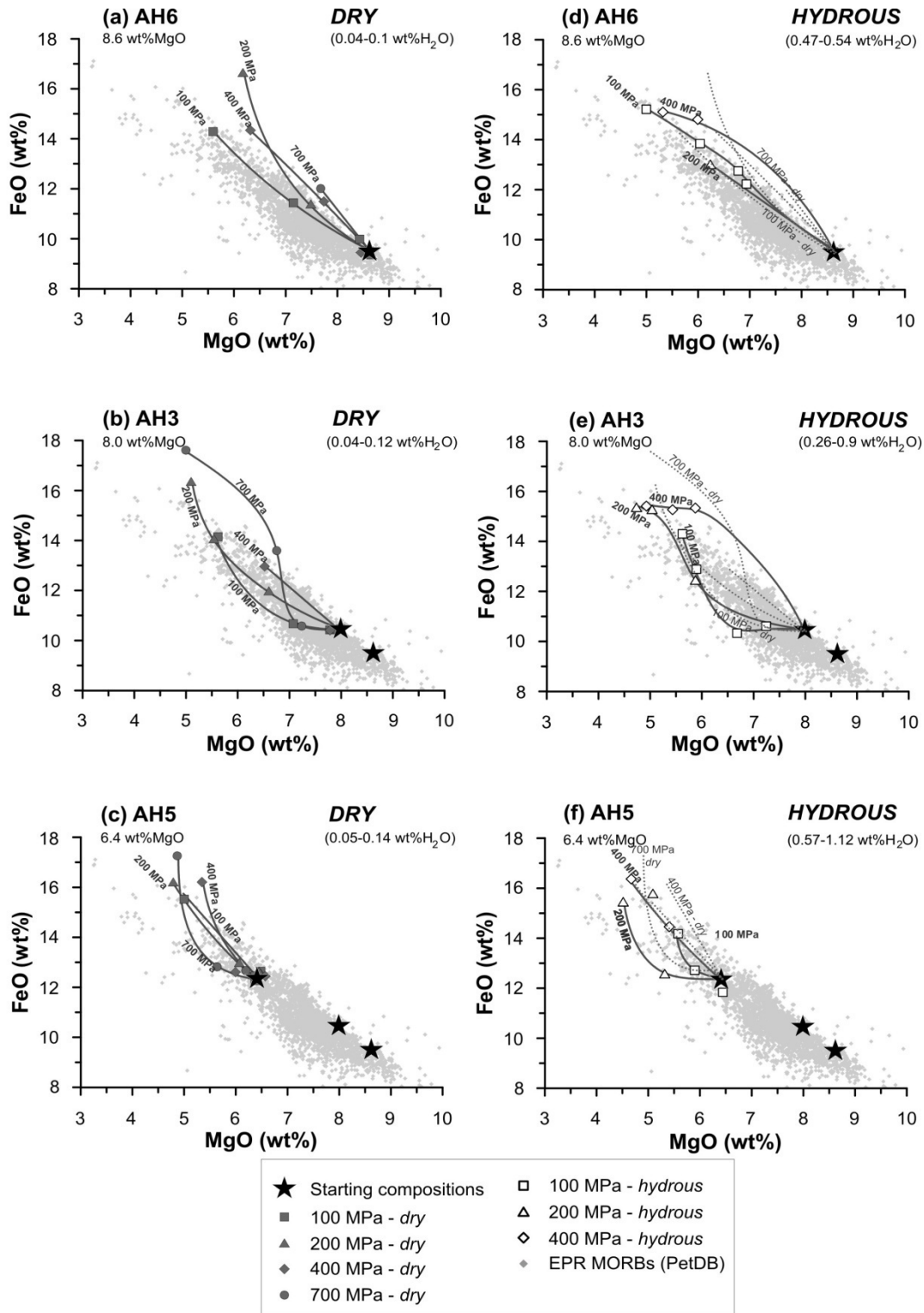
Figure AII.3: The experimentally produced Liquid Lines of Descent (LLDs, dark grey solid lines) for FeO (wt%) for the three different starting materials (black stars) are shown in comparison to the range of natural EPR MORBs (grey points, PetDB). Different columns show different H_2O contents (left: *dry*, right: *hydrous*) and starting compositions vary from top to bottom (AH6 - AH3 - AH5). Different pressures are indicated by symbols. In diagrams displaying *hydrous* conditions, also *dry* LLDs are shown for comparison (light grey dashed lines).

Appendix
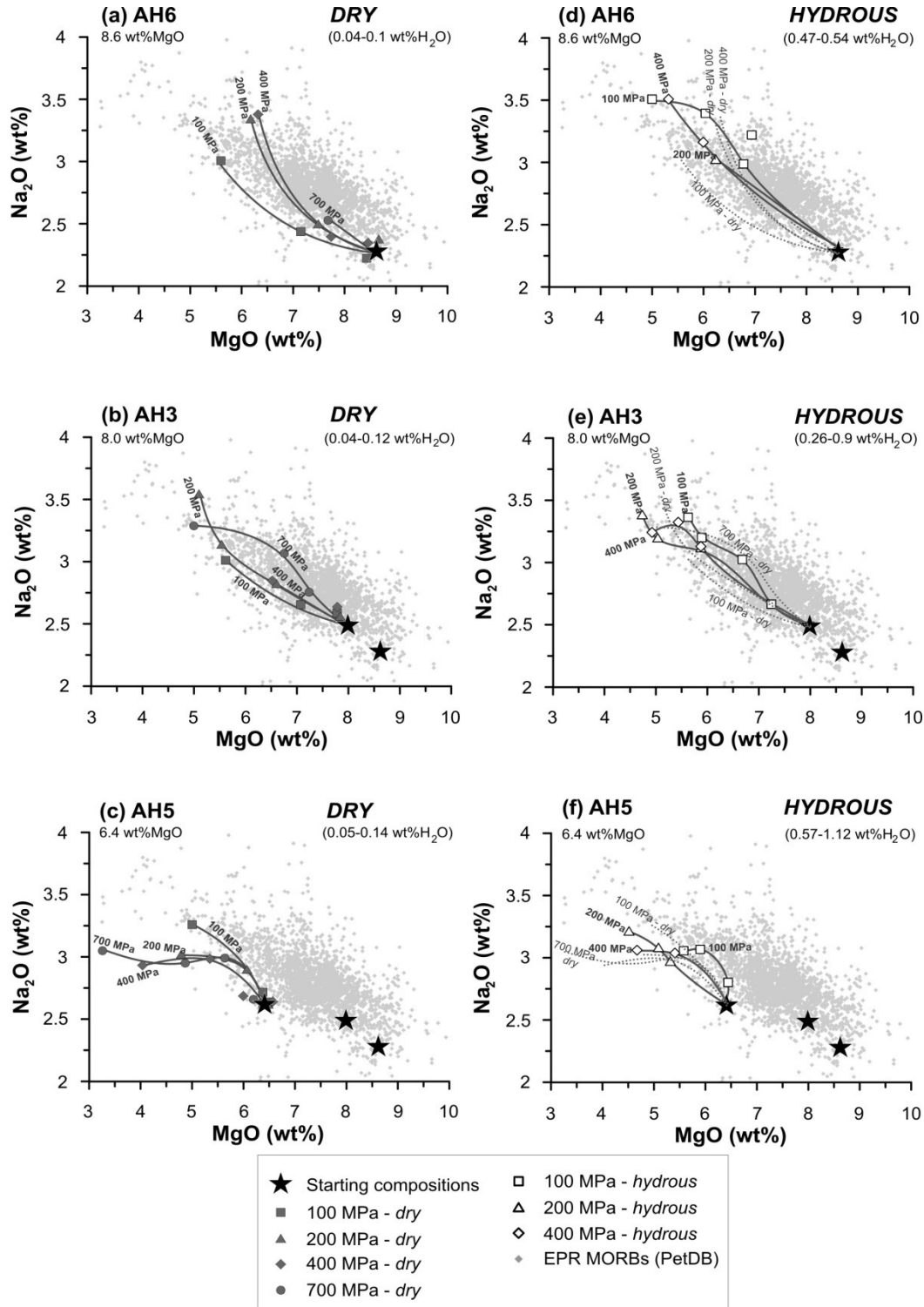
Figure AII.4: The experimentally produced LLDs (dark grey solid lines) for Na_2O (wt%) for the three different starting materials (black stars) are shown in comparison to the range of natural EPR MORBs (grey points, PetDB). Different columns show different H_2O contents (left: *dry*, right: *hydrous*) and starting compositions vary from top to bottom (AH6 - AH3 - AH5). Different pressures are indicated by symbols. In diagrams displaying *hydrous* conditions, also *dry* LLDs are shown for comparison (light grey dashed lines).

Appendix
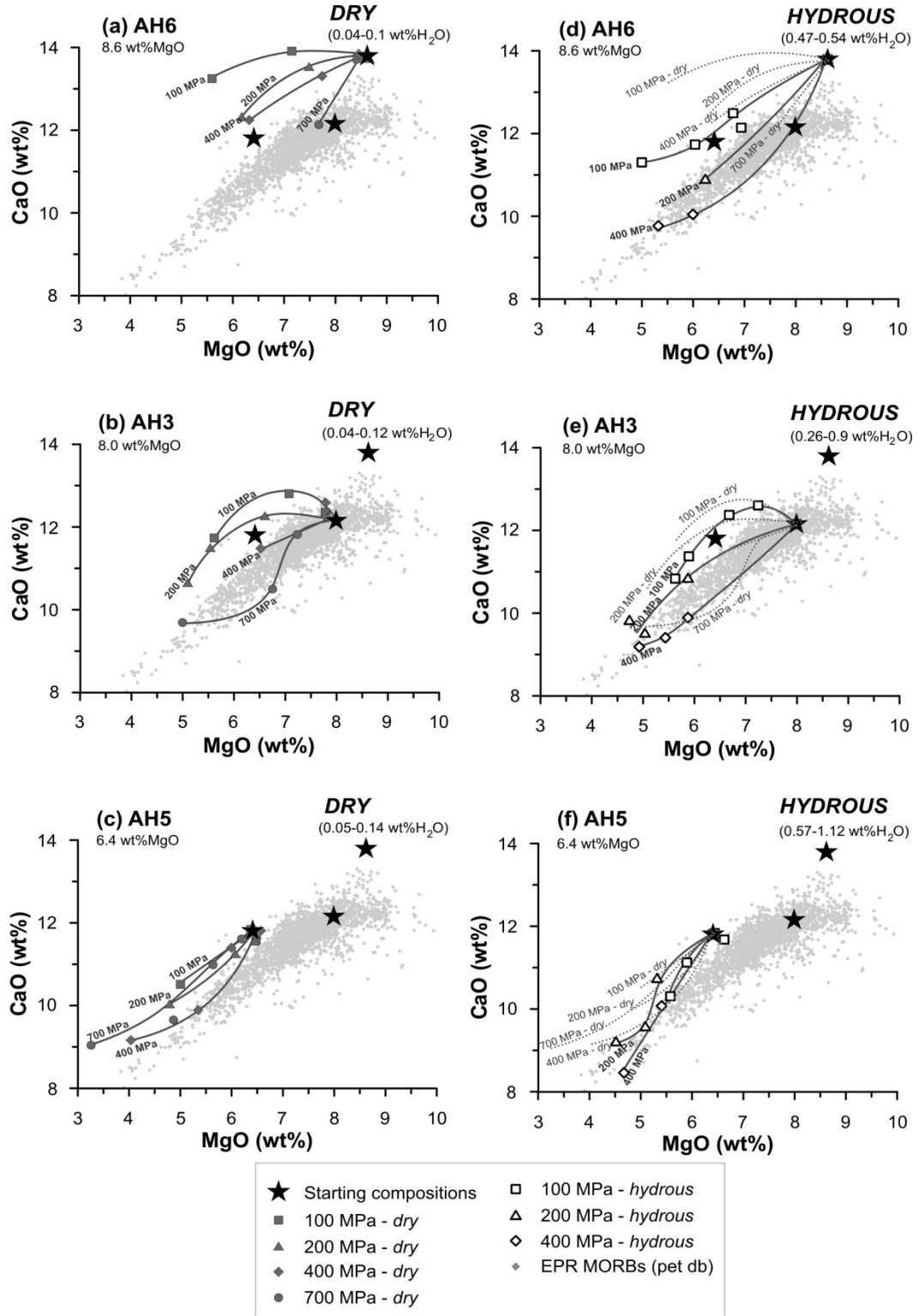
Figure AII.5: The experimentally produced LLDs (dark grey solid lines) for CaO (wt%) for the three different starting materials (black stars) are shown in comparison to the range of natural EPR MORBs (grey points, PetDB). Different columns show different H_2O contents (left: *dry*, right: *hydrous*) and starting compositions vary from top to bottom (AH6 - AH3 - AH5). Different pressures are indicated by symbols. In diagrams displaying *hydrous* conditions, also *dry* LLDs are shown for comparison (light grey dashed lines).

Appendix
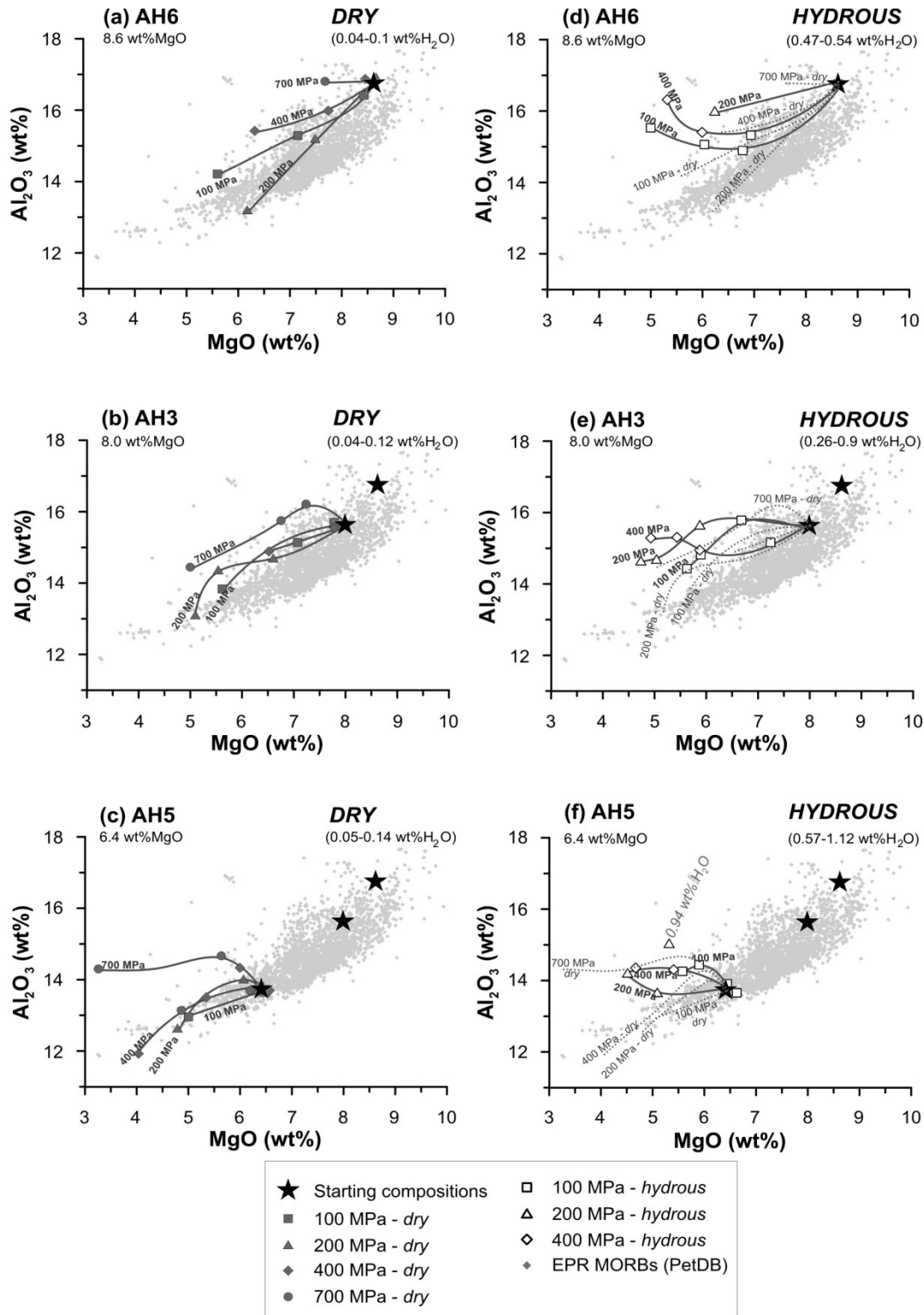
Figure AII.6: The experimentally produced LLDs (dark grey solid lines) for Al_2O_3 (wt%) for the three different starting materials (black stars) are shown in comparison to the range of natural EPR MORBs (grey points, PetDB). Different columns show different H_2O contents (left: *dry*, right: *hydrous*) and starting compositions vary from top to bottom (AH6 - AH3 - AH5). Different pressures are indicated by symbols. In diagrams displaying *hydrous* conditions, also *dry* LLDs are shown for comparison (light grey dashed lines).

Appendix
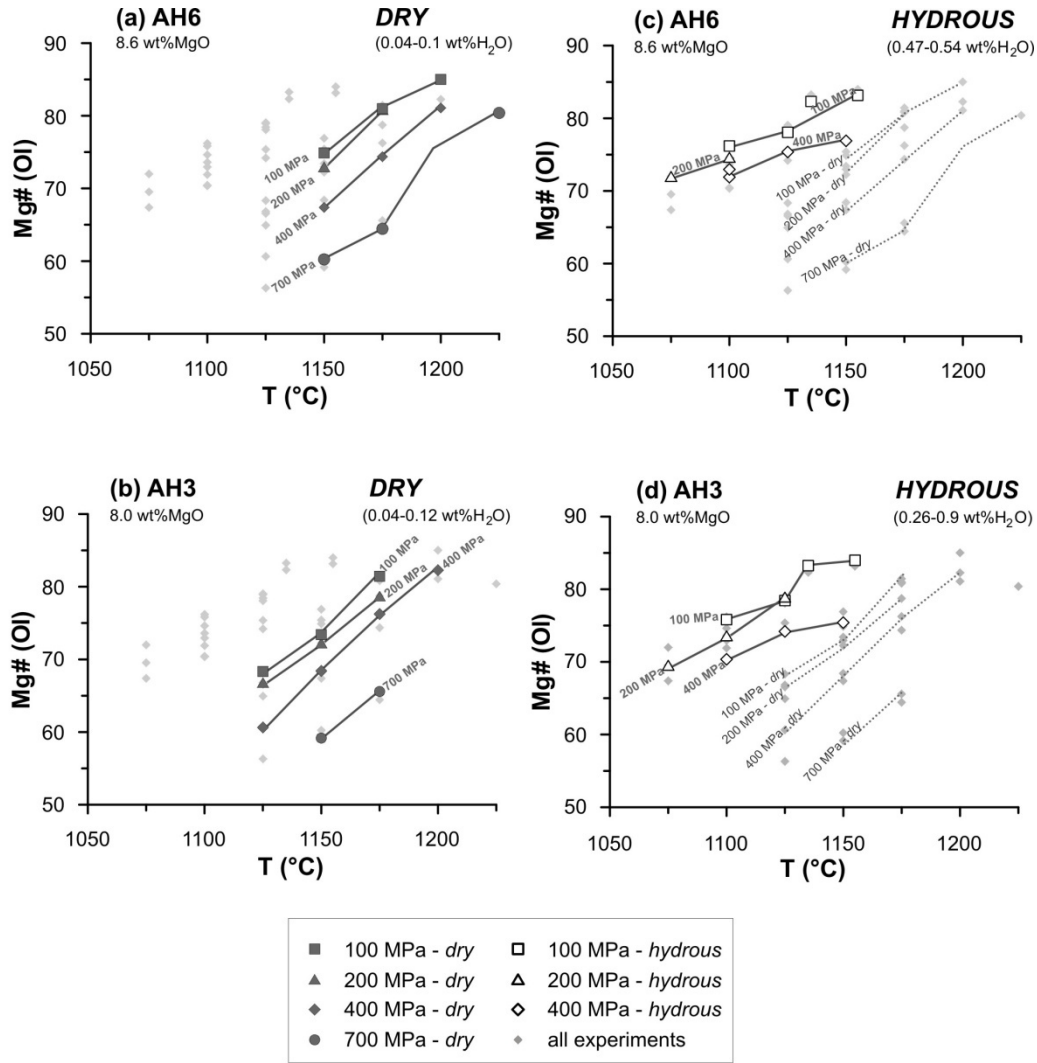
Figure AII.7: *Ol* composition represented by the Mg# (averages of 3-16 analyses) is shown dependent on temperature. Isobaric experiments are connected by solid lines. Left and right column show diagrams for *dry* and *hydrous* conditions respectively. From top to bottom different starting compositions are displayed (AH6 - AH3). In diagrams for *hydrous* experiments also results of *dry* experiments are shown for comparison (light dashed lines). The range of *Ol* compositions in all experiments is shown for comparison (light grey diamonds).

Appendix
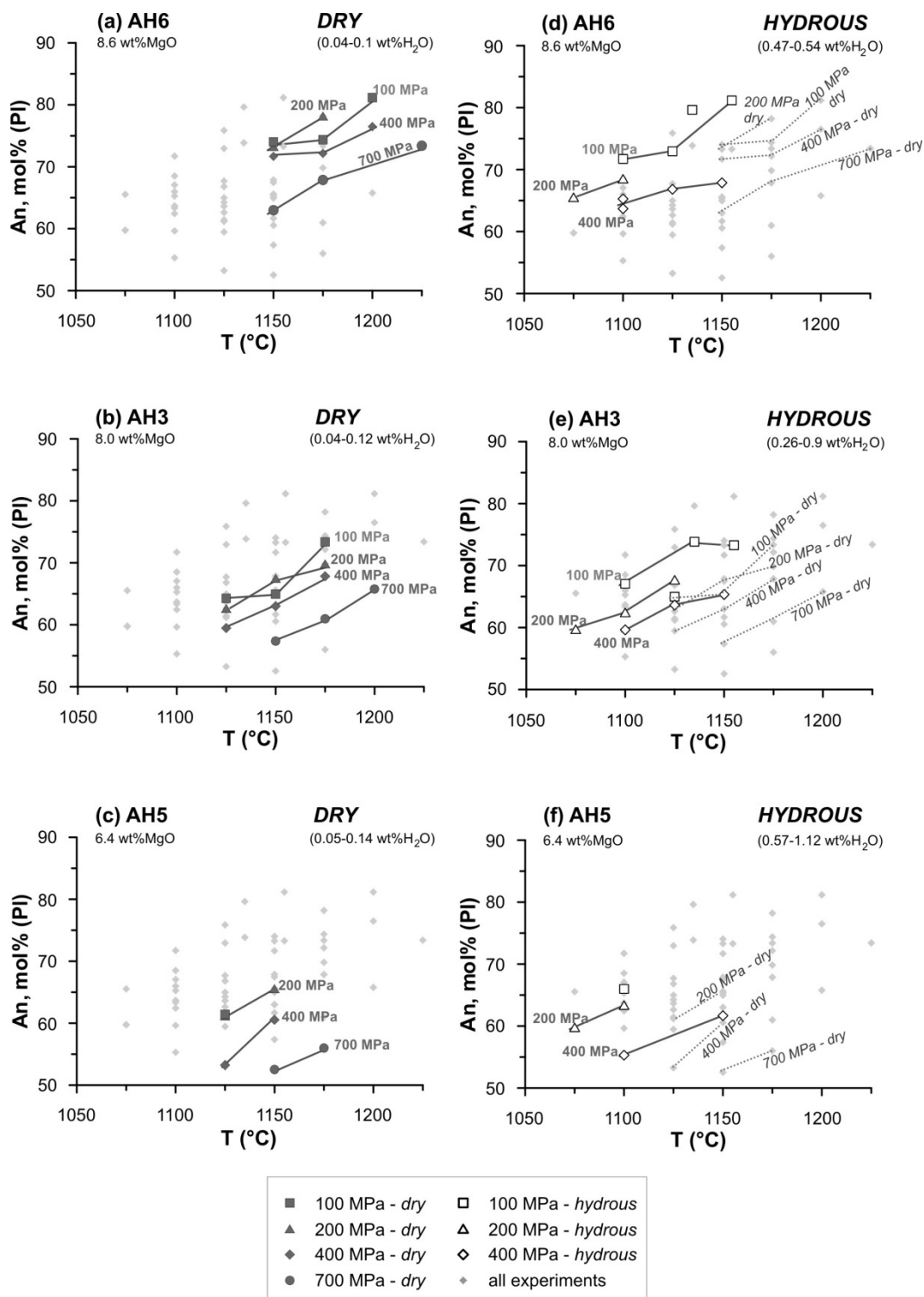
Figure AII.8: *Plag* composition represented by the An content (mol%) (averages of 2-10 analyses) is shown dependent on temperature. Isobaric experiments are connected by solid lines. Left and right column show diagrams for *dry* and *hydrous* conditions respectively. From top to bottom different starting compositions are displayed (AH6 - AH3 - AH5). In diagrams for *hydrous* experiments also results of *dry* experiments are shown for comparison (light dashed lines). The range of *Plag* compositions in all experiments is shown for comparison (light grey diamonds).

Figure AII.9: *Cpx* composition represented by the Mg# (averages of 2-11 analyses) is shown dependent on temperature. Isobaric experiments are connected by solid lines. Left and right column show diagrams for *dry* and *hydrous* conditions respectively. From top to bottom different starting compositions are displayed (AH6 - AH3 - AH5). In diagrams for *hydrous* experiments also results of *dry* experiments are shown for comparison (light dashed lines). The range of *Cpx* compositions in all experiments is shown for comparison (light grey diamonds).

4. APPENDIX PART III

The evaluation of recent geothermobarometers is described in Part III. This Appendix contains the calculated temperatures and pressures discussed and shown in the main text of Part III. The temperatures were obtained using the equations provided by Putirka (2008) (Putirka, 2008, Beattie et al., 1993and by the application of the COMAGMAT program (Ariskin & Barmina, 2004) and the PETROLOG program (Danyushevsky & Plechov, 2011). PETROLOG was used for calculations according to the model of Ford et al. (1983), Herzberg & O'Hara (2002) and Danyushevsky (2001).

Table AIII.1: Calculated temperatures for *dry* runs

Run	P	T	Dur	H₂O	Phase Assemblage	COMAGMAT multiple sat	H&T '87 (MgO)	H&T '87 (CaO)	P '08 Eq13	P '08 Eq14	B '93	Ford '83	H&O '02	P '08 Eq22	D '01 (Ol)	P '08 Eq24a	D '01 (Pl)	P '08 Eq33	D '01 (Cpx)	P '08 Eq32d	P '08 Eq32d (calc P)
	(MPa)	(°C)	(h)	(wt%)		(°C)	(°C)	(°C)	(°C)	(°C)	(°C)	(°C)	(°C)	(°C)	(°C)	(°C)	(°C)	(°C)	(°C)	(°C)	(°C)
ShR616	103	1175	46	0.05	Ol, Plag, Cpx, Gl		1158	1199	1182	1185	1170	1166	1172	1173	1140	1196	1169	1162	1151	1160	1162
ShR609	102	1200	46	0.05	Ol, Plag, Gl		1183	1196	1216	1214	1198	1200	1202	1195	1175	1206	1190				
ShR602	202	1150	108		Ol, Plag, Cpx, Gl	1161															
ShR615	203	1175	71	0.08	Ol, Plag, Cpx, Gl	1191	1164	1193	1191	1196	1186	1183	1189	1191	1153	1203	1168	1176	1161	1175	1178
ShR619	402	1175	64	0.06	Ol, Plag, Cpx, Gl	1187	1141	1171	1161	1190	1187	1173	1188	1188	1145	1201	1185	1163	1153	1178	1190
ShR605	402	1200	63	0.10	Ol, Plag, Cpx, Gl		1170	1189	1198	1203	1204	1199	1207	1207	1167	1218	1188	1190	1177	1196	1202
ShR611	700	1225	60		Ol, Plag, Cpx, Gl	1225															
ShR322	101	1125	48		Ol, Plag, Cpx, Gl	1130															
ShR318	106	1150	65		Ol, Plag, Cpx, Gl	1142															
ShR324	203	1125	108	0.04	Ol, Plag, Cpx, Gl	1137	1116	1145	1128	1168	1152	1131	1149	1155	1106	1155	1120	1128	1113	1143	1143
ShR323	202	1150	73	0.06	Ol, Plag, Cpx, Gl	1149	1125	1159	1140	1159	1151	1136	1149	1152	1109	1180	1146	1143	1123	1163	1167
ShR305	202	1175	68	0.04	Ol, Plag, Cpx, Gl	1169	1147	1172	1168	1177	1169	1164	1171	1170	1140	1191	1167	1169	1151	1175	1187
ShR307	401	1150	91			1127															
ShR304	400	1175	89	0.07	Ol, Plag, Cpx, Gl	1175	1145	1159	1166	1180	1184	1174	1187	1186	1145	1197	1175	1177	1157	1190	1203
ShR311	402	1200	63	0.12	Ol, Gl		1170	1177	1199	1202	1205	1205	1209	1206	1170						
ShR314	700	1200	60	0.12	Plag, Cpx, Gl											1212	1200	1197	1178	1211	1227
ShR317	700	1225	60	0.11	Cpx, Gl													1212	1151	1228	1236
ShR520	101	1125	48	0.05	Ol, Plag, Cpx, Gl	1128	1115	1143	1126	1153	1139	1120	1135	1147	1094	1151	1108	1131	1105	1148	1156
ShR506	102	1150	60	0.05	Cpx, Gl													1139			
ShR519	203	1125	108	0.09	Ol, Plag, Cpx, Gl	1119	1110	1135	1120	1147	1140	1116	1137	1147	1084	1151	1096	1134	1100	1151	1156
ShR505	202	1150	73	0.08	Plag, Cpx, Gl											1177	1141	1158	1134	1165	1172
ShR522	402	1125	66		Ol, Plag, Cpx, Gl	1108															
ShR504	401	1150	91	0.08	Plag, Cpx, Gl											1170	1137	1157	1133	1169	1174
ShR501	400	1175	89	0.10	Cpx, Gl													1185	1149	1182	1191
ShR509	700	1175	60	0.07	Plag, Cpx, Gl											1179	1140	1181	1154	1181	1186
ShR511	700	1200	60	0.14	Cpx, Gl													1195	1167	1205	1210
ShR660	102	1100	64		Ol, Plag, Cpx, Gl	1120															
ShR662	105	1125	65	0.37	Ol, Plag, Cpx, Gl	1135	1135	1163	1153	1175	1163	1150	1162	1143	1098	1169	1119	1136	1096	1130	1148
ShR661	105	1135	89	0.54	Ol, Plag, Cpx, Gl	1156						1175	1182		1115		1115		1107		
ShR663	108	1155	64		Ol, Plag, Cpx, Gl	1146															
ShR657	401	1125	62		Ol, Plag, Cpx, Gl	1142															

The used glass compositions are presented in Tab. II.3 and II.4. Mineral compositions are listed in Tab. AII.1-AII.6

COMAGMAT (Ariskin & Barmina, 2004) is applied using the coefficients for the effect of H₂O published by Almeev et al. (2007 and 2012).

H&T'87 – Helz & Thornber (1987)

P'08 – Putirka (2008)

B'93 – Beattie (1993)

Ford'83 – Ford et al. (1983)

H&O'02 – Herzberg & O'Hara (2002)

D'01 – Danyushevsky (2001)

Ol – olivine, Plag – plagioclase, Cpx – clinopyroxene, Gl – glass, Dur – duration

Table AIII.2: Calculated temperatures for *hydrous* runs

Run	P (MPa)	T (°C)	Dur (h)	H₂O (wt%)	Phase Assemblage	COMAGMAT multiple sat (°C)	H&T '87 (MgO) (°C)	H&T '87 (CaO) (°C)	P '08 Eq13 (°C)	P '08 Eq14 (°C)	B '93 (°C)	Ford '83 (°C)	H&O '02 (°C)	P '08 Eq22 (°C)	D '01 (Ol) (°C)	P '08 Eq24a (°C)	D '01 (Pl) (°C)	P '08 Eq33 (°C)	D '01 (Cpx) (°C)	P '08 Eq32d (°C)	P '08 Eq32d (calc P) (°C)
ShR360	102	1100	64	0.43	Ol, Plag, Cpx, Gl	1121	1127	1148	1142	1164	1153	1141	1152	1135	1085	1154	1098	1139	1084	1134	1150
ShR362	105	1125	65	0.48	Ol, Plag, Cpx, Gl	1125	1132	1157	1149	1161	1153	1144	1152	1134	1087	1158	1103	1146	1091	1139	1155
ShR361	105	1135	89		Ol, Plag, Cpx, Gl	1145															
ShR363	108	1155	64	0.51	Ol, Plag, Cpx, Gl	1150	1160	1177	1185	1183	1176	1175	1178	1160	1117	1175	1114	1176	1118	1147	1168
ShR358	202	1075	64	0.48	Ol, Plag, Cpx, Gl	1105	1109	1131	1119	1142	1137	1120	1132	1121	1061	1147	1092	1127	1066	1135	1153
ShR354	201	1100	70	0.26	Ol, Plag, Cpx, Gl	1113	1115	1126	1127	1150	1147	1130	1145	1125	1083	1158	1121	1129	1082	1150	1173
ShR350	205	1125	65	0.75	Ol, Plag, Cpx, Gl	1134	1132	1148	1149	1154	1157	1150	1156	1132	1083	1162	1105	1144	1086	1154	1171
ShR359	401	1100	70		Ol, Plag, Cpx, Gl	1117															
ShR357	401	1125	62		Ol, Plag, Cpx, Gl	1133															
ShR366	397	1150	63	0.37	Ol, Plag, Cpx, Gl		1132	1132	1149	1176	1182	1167	1183	1160	1114	1172	1135	1157	1113	1159	1180
ShR560	102	1100	64	0.63	Plag, Cpx, Gl											1146	1080	1149	1076	1143	1176
ShR562	105	1125	65	0.73	Cpx, Gl													1147	1084	1149	1171
ShR561	105	1135	89	0.82	Cpx, Gl													1155	1097	1159	1178
ShR558	202	1075	64	0.79	Ol, Plag, Cpx, Gl	1096	1105	1121	1113	1128	1132	1115	1125	1106	1045	1133	1058	1120	1054	1144	1164
ShR554	201	1100	70	0.63	Ol, Plag, Cpx, Gl	1104	1116	1127	1128	1149	1150	1130	1149	1130	1067	1140	1069	1136	1071	1147	1173
ShR550	205	1125	65	0.94	Cpx, Gl													1144	1074	1156	1173
ShR559	401	1100	70	0.69	Plag, Cpx, Gl											1139	1085	1134	1076	1144	1158

The used glass compositions are presented in Tab. II.3 and II.4. Mineral compositions are listed in Tab. AII.1-AII.6

COMAGMAT (Ariskin & Barmina, 2004) is applied using the coefficients for the effect of H₂O published by Almeev et al. (2007 and 2012).

H&T'87 – Helz & Thornber (1987)

P'08 – Putirka (2008)

B'93 – Beattie (1993)

Ford'83 – Ford et al. (1983)

H&O'02 – Herzberg & O'Hara (2002)

D'01 – Danyushevsky (2001)

Ol – olivine, Plag – plagioclase, Cpx – clinopyroxene, Gl – glass, Dur – duration

Appendix

Table AIII.3: Calculated pressures for *dry* and *hydrous* runs

Run	P (MPa)	T (°C)	Dur (h)	H₂O (wt%)	Phase Assemblage	P '08 Eq25a (MPa)	P '08 Eq32b (MPa)	P '08 Eq32b (calc T) (MPa)	YKG '96 (MPa)	Herz '04 (MPa)	Villiger '07 (MPa)	COM mult. sat (MPa)
DRY												
ShR603	102	1150	65		Ol, Plag, Cpx, Gl				12	-251	-1279	
ShR616	103	1175	46	0.05	Ol, Plag, Cpx, Gl	393	160	120	205	-68	-832	
ShR609	102	1200	46	0.05	Ol, Plag, Gl	613						
ShR602	202	1150	108		Ol, Plag, Cpx, Gl				413	-351	-1001	340
ShR615	203	1175	71	0.08	Ol, Plag, Cpx, Gl	330	230	240	304	8	-602	310
ShR619	402	1175	64	0.06	Ol, Plag, Cpx, Gl	546	502	550	644	348	-684	590
ShR605	402	1200	63	0.10	Ol, Plag, Cpx, Gl	595	473	481	602	289	-455	
ShR611	700	1225	60		Ol, Plag, Cpx, Gl				950	715	-120	810
ShR322	101	1125	48		Ol, Plag, Cpx, Gl				124	89	-697	150
ShR318	106	1150	65		Ol, Plag, Cpx, Gl				29	-17	-649	100
ShR324	203	1125	108	0.04	Ol, Plag, Cpx, Gl	181	162	208	156	105	-556	275
ShR323	202	1150	73	0.06	Ol, Plag, Cpx, Gl	249	194	241	158	182	-573	220
ShR305	202	1175	68	0.04	Ol, Plag, Cpx, Gl	294	305	341	151	89	-429	240
ShR307	401	1150	91		Ol, Plag, Cpx, Gl				368	-48	-430	150
ShR304	400	1175	89	0.07	Ol, Plag, Cpx, Gl	403	469	558	431	331	-219	440
ShR314	700	1200	60	0.12	Plag, Cpx, Gl	665	796	892				
ShR317	700	1225	60	0.11	Cpx, Gl		759	799				
ShR520	101	1125	48	0.05	Ol, Plag, Cpx, Gl	23	118	199	-7	26	-462	100
ShR519	203	1125	108	0.09	Ol, Plag, Cpx, Gl	-2	179	262	89	103	-399	80
ShR505	202	1150	73	0.08	Plag, Cpx, Gl	143	222	285				
ShR522	402	1125	66		Ol, Plag, Cpx, Gl				361	362	-490	210
ShR504	401	1150	91	0.08	Plag, Cpx, Gl	226	399	470				
ShR501	400	1175	89	0.10	Cpx, Gl		450	499				
ShR509	700	1175	60	0.07	Plag, Cpx, Gl	414	735	770				
ShR511	700	1200	60	0.14	Cpx, Gl		733	768				
HYDROUS												
ShR660	102	1100	64		Ol, Plag, Cpx, Gl				452	474	-759	230
ShR662	105	1125	65	0.37	Ol, Plag, Cpx, Gl	216	266	326	398	243	-475	240
ShR661	105	1135	89	0.54	Ol, Plag, Cpx, Gl				439	221	-235	320
ShR663	108	1155	64		Ol, Plag, Cpx, Gl				348	77	-532	205
ShR657	401	1125	62		Ol, Plag, Cpx, Gl				845	890	-6	600
ShR666	397	1150	63		Ol, Plag, Cpx, Gl				778	688	104	
ShR360	102	1100	64	0.43	Ol, Plag, Cpx, Gl	76	178	301	272	287	-285	180
ShR362	105	1125	65	0.48	Ol, Plag, Cpx, Gl	195	221	300	191	246	-280	120
ShR361	105	1135	89		Ol, Plag, Cpx, Gl				191	253	-160	150
ShR363	108	1155	64	0.51	Ol, Plag, Cpx, Gl	229	316	352	228	129	-151	150
ShR358	202	1075	64	0.48	Ol, Plag, Cpx, Gl	134	248	430	324	536	-197	190
ShR354	201	1100	70	0.26	Ol, Plag, Cpx, Gl	156	296	486	490	592	-18	290
ShR350	205	1125	65	0.75	Ol, Plag, Cpx, Gl	229	287	412	359	495	-23	260
ShR359	401	1100	70		Ol, Plag, Cpx, Gl				652	780	69	410
ShR357	401	1125	62		Ol, Plag, Cpx, Gl				675	731	150	480
ShR366	397	1150	63	0.37	Ol, Plag, Cpx, Gl	376	563	650				
ShR366	397	1150	63		Ol, Plag, Cpx, Gl				712	651	108	
ShR560	102	1100	64	0.63	Pl, Cpx, Gl	-17	299	498				
ShR562	105	1125	65	0.73	Cpx, Gl		248	374				
ShR561	105	1135	89	0.82	Cpx, Gl		212	334				
ShR558	202	1075	64	0.79	Ol, Plag, Cpx, Gl	-34	240	454	258	489	-22	100
ShR554	201	1100	70	0.63	Ol, Plag, Cpx, Gl	-26	333	523	362	387	-79	140
ShR550	205	1125	65	0.94	Cpx, Gl		282	413				
ShR559	401	1100	70	0.69	Plag, Cpx, Gl	166	433	580				

The used glass compositions are presented in Tab. II.3 and II.4. Mineral compositions are listed in Tab. AII.1-AII.6

P'08 – Putirka (2008)

YKG'96 – Yang et al. (1996)

Herz'04 – Herzberg (2004)

Villiger'07 – Villiger et al. (2007)

COM – COMAGMAT (Ariskin & Barmina, 2004), applied using the coefficients for the effect of H_2O published by Almeev et al. (2007 and 2012).

Ol – olivine, Plag – plagioclase, Cpx – clinopyroxene, Gl – glass, Dur – duration

Appendix

4.1.   References

Almeev, R., Holtz, F., Koepke, J., Haase, K. & Devey, C. (2008). Depths of partial crystallization of H_2O-bearing MORB: Phase equilibria simulations of basalts at the MAR near Ascension Island (7-11 degrees S). Journal of Petrology 49, 25-45.

Almeev, R. R. & Ariskin, A. A. (1996). Mineral-melt equilibria in a hydrous basaltic system: Computer modeling. Geokhimiya, 624-636.

Almeev, R. R., Holtz, F., Koepke, J. & Parat, F. (2012). Experimental calibration of the effect of H_2O on plagioclase crystallization in basaltic melt at 200 MPa. American Mineralogist 97, 1234-1240.

Almeev, R. R., Holtz, F., Koepke, J., Parat, F. & Botcharnikov, R. E. (2007). The effect of H_2O on olivine crystallization in MORB: Experimental calibration at 200 MPa. American Mineralogist 92, 670-674.

Ariskin, A. A. (1999). Phase equilibria modeling in igneous petrology: use of COMAGMAT model for simulating fractionation of ferro-basaltic magmas and the genesis of high-alumina basalt. Journal of Volcanology and Geothermal Research 90, 115-162.

Ariskin, A. A. & Barmina, G. S. (2004). COMAGMAT: Development of a magma crystallization model and its petrological Applications. Geochemistry International 42, S1.

Beattie, P. (1993). Olivine-melt and orthopyroxene-melt equilibria. Contributions to Mineralogy and Petrology 115, 103-111.

Danyushevsky, L. V. (2001). The effect of small amounts of H_2O crystallisation of mid-ocean ridge and backarc basin magmas. Journal of Volcanology and Geothermal Research 110, 265-280.

Danyushevsky, L.V. and Plechov, P., 2011. Petrolog3: Integrated software for modeling crystallization processes. Geochemistry Geophysics Geosystems, 12(7): Q07021.

Ford, C. E., Russell, D. G., Craven, J. A. & Fisk, M. R. (1983). Olivine Liquid Equilibria - Temperature, Pressure, and Composition Dependence of the Crystal Liquid Cation Partition-Coefficientsfor Mg, Fe^{2+}, Ca and Mn. Journal of Petrology 24, 256-265.

Helz, R. & Thornber, C. (1987). Geothermometry of Kilauea Iki lava lake, Hawaii. Bulletin of Volcanology 49, 651-668.

Herzberg, C. & O'Hara, M. J. (2002). Plume-Associated Ultramafic Magmas of Phanerozoic Age. Journal of Petrology 43, 1857-1883.

Herzberg, C. (2004). Partial crystallization of mid-ocean ridge basalts in the crust and mantle. Journal of Petrology 45, 2389-2405.

Putirka, K. D. (2008). Thermometers and Barometers for Volcanic Systems. Reviews in Mineralogy and Geochemistry 69, 61-120.

Appendix

Yang, H. J., Kinzler, R. J. & Grove, T. L. (1996). Experiments and models of anhydrous, basaltic olivine-plagioclase-augite saturated melts from 0.001 to 10 kbar. Contributions to Mineralogy and Petrology 124, 1-18.

Appendix

---

5.   CURRICULUM VITAE

PERSONAL DETAILS

Name:	**Anika Husen**
E-Mail:	Anika.Husen@gmx.de
Date of Birth:	27/02/86
Nationality	German

SHORT PROFILE

10/2014	PhD Geosciences (Dr. rer.nat., Leibniz University of Hannover)
11/2010	Diploma Geosciences (Dipl.-Geow., Leibniz University of Hannover)
05/2005	Secondary school (Abitur, Gymnasium Trittau, Schleswig-Holstein)

GRANTS	DAAD travel Grant for international conferences (Kongressreisestipendium)

PROFESSIONAL EXPERIENCE

since 11/2010	PhD (Dr. rer. nat.) at the Institue of Mineralogy at Leibniz University Hannover „Magma differentiation processes and volatile contents in Shatsky Rise oceanic Plateau basalts: constraints from mineral, glass and melt inclusion compositions combined with experimental and thermodynamic modeling"
10/2009 – 01/2010	Student assistant at the „Bundesanstalt für Geowissenschaften und Rohstoffe" (BGR) in Hannover Public relations for GeneSys (Geothermal energy drilling project)
03/10 – 12/12/2009	Internship at Ri-Con in Hannover Sampling and documentation of dilapidations caused by salt minerals; writing articles for www.salzwiki.de (German encyclopedia of salts)
11/2007 - 10/2010	Student assistant at the Institute of Mineralogy at Leibniz University Hannover Besides other analytical methods, colorimetric determination of Fe^{2+}/Fe^{3+} ratio in rock and glass samples, IR spectroscopic measurements of H_2O concentrations is glasses

Appendix

PUBLIKATIONS

Journals (peer-reviewed):

- Husen, A., Almeev, R. R., Holtz, F., Koepke, J., Sano, T. & Mengel, K. (2013). Geothermobarometry of basaltic glasses from the Tamu Massif, Shatsky Rise oceanic plateau. *Geochemistry, Geophysics, Geosystems* 14, 3908–3928.

Conference Abstracts:

- Husen, A., Almeev, R. R., Holtz, F. (2013): Cyclic fractionation processes beneath the Shatsky Rise oceanic plateau, Tagungsband AGU Fall Meeting 2013

- Husen, A., Almeev, R. R., Holtz, F.: Experimental simulation of the magma differentiation beneath Shatsky Rise oceanic plateau. *Tagungsband DMG GV 2013*

- Fanara, S., Botcharnikov, R., Palladino, D.M., Husen, A., Righi, S., Ceccarani, G.M., Stranghöner, M., Behrens, H. (2013): Phase equilibria experiments on a trachyte and a trachybasalt from the Campi Phlegrei Volcanic District (Italy). *Tagungsband DMG GV 2013*

- Fanara, S., Botcharnikov, R., Palladino, D.M., Husen, A., Righi,S., Ceccarani, G.M., Behrens, H. (2013): New constraints on the pre-eruptive storage conditions of the Campanian Ignimbrite (Campi Flegrei, IT). *Mineralogical Magazine*, 77(5) 1063, Goldschmidt Conference 2013

- Husen, A., Almeev, R. R., Holtz, F., Koepke, J., Mengel, K., Sano, T. (2013): Petrological and experimental study of Basalts from Tamu Massif, Shatsky Rise Oceanic Plateau (IODP Expedition 324). *Tagungsband ICDP/IODP Kolloquium 2013*

- Husen, A., Almeev, R. R., Natland, J. H., Holtz, F., Koepke, J., Mengel, K. (2012): Liquid evolution beneath Shatsky Rise oceanic plateau - experimental and thermodynamic simulations of the magma differentiation. *European Mineralogical Conference* Vol. 1, EMC2012-487-2, 2012.

Appendix

- Husen, A., Almeev, R. R., Holtz, F., Koepke, J., Shimizu, K., Sano, T., Natland, J.H. (2012): Petrological study of Basalts from Shatsky Rise Oceanic Plateau (Site U1347, IODP Expedition 324). *Tagungsband ICDP/IODP Kolloquium 2012*

- Husen, A., Almeev, R. R., Shimizu, K., Sano, T., Natland, J.H., Koepke, J., Holtz, F. (2011): Geothermobarometry of basaltic glasses from Tamu massif, Shatsky Rise oceanic plateau. *Mineralogical Magazine*, Vol. 75 (3), 1073, Goldschmidt Conference 2011

- Almeev, R. R., Husen, A., Koepke, J., Holtz, F. (2011): Magma differentiation processes in Shatsky Rise oceanic Plateau basalts: constraints from mineral, glass and melt inclusions. *Tagungsband ICDP/IODP Kolloquium 2011*

- Behrens, H., Botsharnikov, R. E., Husen, A. (2011): Pre-eruptive conditions of the Campanian Ignimbrite eruption: Experimental constraints from phase equilibria and volatile solubility studies and its implication for the Campi Flegrei drilling project. *Tagungsband ICDP/IODP Kolloquium 2011*